

論文 / 著書情報  
Article / Book Information

題目(和文)	
Title(English)	Study of two-plane couplers having arbitrary power ratio and their applications to two-dimensional beam switching matrices
著者(和文)	LIQi
Author(English)	Qi Li
出典(和文)	学位:博士(学術), 学位授与機関:東京工業大学, 報告番号:甲第12586号, 授与年月日:2023年9月22日, 学位の種別:課程博士, 審査員:廣川 二郎,阪口 啓,西方 敦博,青柳 貴洋,TRAN GIA KHANH,高橋 徹
Citation(English)	Degree:Doctor (Academic), Conferring organization: Tokyo Institute of Technology, Report number:甲第12586号, Conferred date:2023/9/22, Degree Type:Course doctor, Examiner:,,,,,
学位種別(和文)	博士論文
Type(English)	Doctoral Thesis

Doctoral Dissertation

**Study of two-plane couplers having  
arbitrary power ratio and their  
applications to two-dimensional beam  
switching matrices**

September, 2023

Under the Supervision of

**Professor Jiro Hirokawa**

Presented by

**Qi Li**

Department of Electrical and Electronic Engineering

Tokyo Institute of Technology

# Contents

<b>Chapter 1</b>	<b>Introduction</b> .....	1
1.1	Applications of multi-beam antenna technologies.....	1
1.2	Beam forming networks.....	2
1.2.1	Beam-switching matrices.....	2
1.2.2	Lens-based antenna.....	4
1.2.3	2-D beam-switching.....	6
1.2.4	Beam-switching matrices by different transmission line technologies.....	7
1.2.5	Miniaturization of beam-switching matrices.....	7
1.3	Motivation of this dissertation.....	8
1.4	Outline of this dissertation.....	10
<b>Chapter 2</b>	<b>Two-plane Waveguide Coupler with Arbitrary Coupling Ratios in the H-plane and E-plane Directions</b> .....	27
2.1	Introductory remarks.....	27
2.2	One-plane couplers.....	28
2.3	General analysis of two-plane coupler.....	30
2.4	Coupling mechanisms of two-plane coupler.....	33
2.5	Mode matching-FEM analysis.....	40
2.6	Designing of a two-plane coupler with different coupling ratio in H-plane and E-plane directions.....	41
2.7	Conclusion Remarks.....	46
<b>Chapter 3</b>	<b>Two-dimensional One-body 3×3-way Hollow-waveguide Nolen Matrix using Two-plane Couplers</b> .....	61
3.1	Introductory remarks.....	61
3.2	1-D 3-way Nolen matrix.....	62
3.3	Configuration of 2-D 3×3-way Nolen matrix.....	63
3.4	Design of constituent two-plane coupler.....	64
3.5	Design of constituent one-plane coupler.....	68
3.6	Design of waveguide phase shifters.....	69

3.7	Experimental results of 2-D 3×3-way Nolen matrix.....	69
3.8	Conclusion remarks.....	76
<b>Chapter 4</b>	<b>Two-dimensional hollow waveguide 6×4-way beam-switching matrix .....</b>	<b>102</b>
4.1	Introduction remarks.....	102
4.2	1-D 6-way and 4-way matrices .....	103
4.3	Configuration of 2-D 6×4-way matrix.....	104
4.4	Experimental results of 2-D 6×4-way matrix.....	106
4.5	Conclusion remarks .....	111
<b>Chapter 5</b>	<b>Conclusion.....</b>	<b>140</b>
5.1	Summary of preceding chapters .....	140
5.2	Remarks for future study.....	142
<b>Appendix A</b> .....		<b>144</b>
<b>Appendix B</b> .....		<b>147</b>
<b>Appendix C</b> .....		<b>152</b>
<b>Appendix D</b> .....		<b>156</b>
<b>Appendix E</b> .....		<b>158</b>
<b>Acknowledgement</b> .....		<b>163</b>
<b>List of Publications</b> .....		<b>165</b>

# Chapter 1 Introduction

## 1.1 Applications of multi-beam antenna technologies

Multi-beam technologies have garnered significant interest and attention in recent times, owing to their ability to create antennas with spatially orthogonal multiple beams. This innovative approach has found extensive applications in various domains such as broadband satellite communications, massive MIMO systems, terrestrial and non-terrestrial 5G/6G wireless networks [1-1]-[1-4], and more. The widespread adoption of multi-beam technologies can be attributed to their remarkable potential in revolutionizing communication systems and facilitating enhanced connectivity. According to the current development tendency, in order to further expand the communication capacity and disciplinaries, a large number of airborne and space-borne nodes will be added in the future sixth-generation communication system network or other application scenarios. For example, [1-5] has proposed a 60GHz drone-ground communication system by employing drones as air-borne nodes to act as small cell base stations, as depicted in Fig.1.1.

For the time being, the digital signal process MIMO is deemed as a reliable approach in the current terrestrial 5G communication system, particularly applicable in extensive reflection circumstances [1-6]. However, digital MIMO containing bulk plenty of components will generate large power consumption, which is reckoned to be not proper for most non-terrestrial communication systems with very limited power supply. Instead, analogue beam-forming technology, including active and passive beamforming can be more adequately for target applications. Analog active beamforming generally incorporates phase shifters and amplifiers to steer and shape the beam pattern. While passive beam-forming technologies, including circuits type beam forming networks (BFNs), as well known as beam-switching circuits, and quasi-optical devices, like lens antenna, generates multi-beam with fixed beam direction with spatial orthogonality. Passive beam-forming, despite its larger antenna size and higher cost, offers unparalleled potential when it comes to low-loss multi-beam antenna technologies. In comparison to

active beam-forming and digital beamforming, passive beam-forming boasts the significant advantage of the lowest power consumption, as it eliminates the need for amplifiers. This becomes especially crucial in non-terrestrial communication systems, which often involve numerous air-borne or space-borne nodes operating under strict power constraints. Consequently, the undeniable suitability of analogue passive beam-forming technologies arises, ensuring optimal performance in scenarios where efficiency and limited power supply are paramount considerations.

## **1.2 Beam forming networks**

Beam-switching matrices [1-3] and lens-based antennas [1-4] are widely utilized for the purpose of multi-beam applications. In general, most lens antenna will be more applicable to higher frequencies to the THz band, due to electromagnetic wave can be simplified as the behavior of light of sight at those frequencies. Beam-switching circuits, consisting of microwave components like couplers and phase shifters, are more efficient in the microwave frequency bandwidth.

### **1.2.1 Beam-switching matrices**

A beam-switching matrix is to divide the input signal into identical signals and produces an equal phase difference between adjacent output ports to determine the main direction of the radiation beam in dependence on input ports. Conventional well-known 1-D beam-switching matrices include Blass matrix [1-7], Butler matrix [1-8] and Nolen matrix [1-9][1-10]. In [1-11], a new way of designing generalized matrices with an arbitrary number of beams was put forward, which combines some of the advantages of the Butler and the Nolen matrices, thus broadening the range of 1-D beam-switching matrices.

Fig.1.2 shows the general configuration of a Blass matrix, incorporating M-input and N-output ports. The Blass matrix contains MN nodes, which is composed of a Hybrid coupler and phase shifters. Meanwhile, M+N termination leads are uploaded at the edge

of matrix network for the purpose of generating traveling wave. The advantages of Blass matrix mainly reflect on the flexibility in design to designate beam direction and number of beams, as well as crossover levels among each beam. However, due to the employment of termination loads to match, Blass matrix usually behaves with low efficiency, restricting its application in most scenarios.

Fig. 1.3 shows a general configuration of 4-way Butler matrix. Butler matrix comprises Hybrid couplers, crossovers and phase shifters. Butler matrix is limited to identical number of both input and output ports as  $2^N$ . Each signal path of Butler matrix is independent, and theoretically without interactions, thus, Butler matrix is always deemed as most wideband-enabled beam-switching matrices. Meanwhile, attributed to its symmetrical configuration, the design complexity of Butler matrix is reduced in half. For a conventional 1-D  $2^N$ -way. Some new conceptions of Butler matrices with unequal number of input and output ports are put forward [1-12], but it could be regarded as simply oversizing matrices configuration, simultaneously utilizing some matching loads.

Nolen matrix, as shown in Fig.1.4, has improved the topology progressively compared with Blass matrix, in discarding all the match loads, and decreasing number of nodes. Parallel configuration of Nolen matrix can be proposed in lieu of a conventional diagonal-shape network [1-13], which as well indicates that a lossless Nolen matrix should have identical number of input ports as output ports. Similar to Blass matrix, each node of Nolen matrix contains a quadrature coupler and a phase shifter. A parallel  $N$ -way Nolen matrix is composed of  $N(N-1)2$  units with the couplers having several different values, leading to a complicated design process. In addition, the Nolen matrix in its original form is usually not wideband, as a direct consequence of the series-fed configuration.

The new generalized 1-D matrix with an arbitrary number of beams introduced in [1-11], generates output phase difference between adjacent ports as

$$p_k = \frac{2k\pi}{N} - \frac{(N+1)\pi}{N} \quad k = 1, 2 \dots N \quad (1-1)$$

Here  $N$  signifies the number of beams and  $k$  means input port number. It combines merits of both the Butler matrix and the Nolen matrix, especially reflected on even number of beams case, which is originated from two mirror-like Nolen matrix connected by crossover network. As such, this kind of matrices are deemed to be enhanced bandwidth performance compared with Nolen matrix. According to the methodology in [1-11], a 1-D  $2n$ -way matrix having all  $(2n)!$  permutations of the beam assignments and associated adjacent output phase differences can be obtained by adjusting the values of the phase shifters. Fig.1.5 (a) and (b) present a general configuration of 4-way and 5-way 1-D beam switching matrices, which can be a reference to broaden its disciplinary to any even or odd number of beams cases. It could be induced that for both an even and an odd number of beam, the matrix will comprise  $2N$  layers and  $(N-1)N/2$  nodes, which is same as Nolen matrix. The most meaningful contribution of [1-11] turns on even number ways of matrix, as shown the general configuration in Fig.1.5 (c). The  $2N$ -way matrix comprises Hybrid coupler layer, two pyramid shape crossover networks and two  $N$ -way Nolen matrix. In this manner, it is deemed that this  $2N$ -way matrix will have a wider bandwidth than a normal  $2N$ -way Nolen matrix, as its close-knit depth is reduced in half. Meanwhile, some solutions to a  $2N$ -way matrix proposed by [1-11], will possess a completely symmetrical configuration by properly adjusting value of couplers and phase shifters, leading to diminished complexity of design. Furthermore, retrofitted configuration of  $2^N$ -way matrices will manifest fewer layers than Butler matrices, which may contribute to miniaturization of some target application.

Table. 1.1 lists a comparison table for above mentioned beam-switching matrices in the case of  $N$ -input and  $N$ -output. Overall, Butler matrix will manifest a simple design complexity and widest bandwidth, but limited to its beam number as  $N = 2^n$ . The newly proposed matrix configuration [1-11] will have a wider bandwidth than Nolen matrix, and have liberty in number of beams, which is superior to Butler matrix.

## 1.2.2 Lens-based antenna

Lens antenna is deemed to be a proper candidate for spatially orthogonal beams generator in very high frequency like Terahertz bandwidth to support dynamic and long-



range communication [1-4]. Owing to the high frequency and short wavelength, lens antennas are generally quasi-optical natures. Rotman lenses [1-14] and Luneburg lens [1-15] have very wide applications in high-frequency multi-beam demanded systems. In recent years, due to fast development of meta-surface related conception, many multi-beam antenna, such as transmit array [1-16]-[1-19] and reflect array [1-20]-[1-22] based on meta-surface structure are proposed and investigated in-depth. As these meta-surface antennas, theoretically have same physical mechanism with lens antenna, to generate difference of physical path to attain phase distribution at aperture, thus generating beams in desired directions.

Rotman lens is initially proposed by Rotman and Turner [1-14]. The general topology and a layout of Rotman lens by planar transmission line is shown in Fig.1.6 (a). Rotman lens contains a focal arc where input ports are loaded, an inner contour and an outer contour where radiation elements are placed. The mechanism of Rotman lens is ascribed to difference of propagation path independence of input ports, which generates different phase intervals at inner contour. And these physical length differences are theoretically keeping unchanged with the frequency variation, thus, Rotman lens manifest very wide bandwidth. However, performances of Rotman lens are impaired due to its spillover path, which is out of expectation, and will lead to higher side lobe levels and low efficiency. And the condition degrades more when feeding is more far away from the center of focal arc.

Luneburg lens [1-15] is optical devices with spherical [1-23] or cylindrical shape [1-24], counterpart to different applications. Luneburg lens is a dielectric compound with varying dielectric constant  $\epsilon_r(r) = 2 - (r/R)^2$  from center to edge, as Fig1.6 (b) shows. Luneburg lens greatly decreases the designing complexity compared with beam-switching circuits and other lens-based antennas, also with less network loss. However, the most concerned disadvantages of Luneburg lens reflect on its varying dielectric constants. In practical design, it is achieved by stacking different dielectric materials layer by layer. Some investigation has put efforts in designing Luneburg lens based on meta-

surface cells, which might potentially improve the fabrication complexity of Luneburg lens.

Overall, in a perspective view of comparison of beam-switching matrices and lens-based antennas, lens antenna will have a wider bandwidth and more compact physical layout comparing with beam-switching matrices when number of ports turns out to be larger, however, beam-switching matrices will manifest to be more effective in microwave frequency, as a consequence of natures for quasi-optical characteristics of lens-based antenna is not dominant at this frequency [1-3][1-4], which may lead to low antenna efficiency and high side lobe levels. This could be reflected on Fig.1.6(a), as there will be reflection between inner surface of lens and outer surface of lens, which will generate undesired propagation path and spillover, thus leading to increasing side lobe levels. And this phenomenon degrades the performance more when feeding point deviates from center. A solution for this is to upload some matching load or absorber surrounding Rotman lens, and at the same time bring about more decreased efficiency and realized gain, as a matter of this, to level up efficiency of Rotman lens in microwave frequency band is always a challenging topic. Besides, considering fabrication complexity, beam-switching matrices are obviously simpler than lens-based antennas, as lens antenna generally incorporates curvature shape or varying dielectric constants, with higher difficulty on high precision and low-cost manufacturing. Another challenge for lens antenna is the integration with feeding or radiation ports, which can inherently be equipped by beam-switching matrices.

### **1.2.3 2-D beam-switching**

As anticipated in [1-8], 2-D beam switching can be achieved by direct cascading 1-D multi-beam matrices in two directions. For instance, as Fig.1.7 (a1) shows, a 2-D 4×4-way Butler matrix is attained by cascading horizontally-stacked 4-way Butler matrices and vertically-stacked 4-way Butler matrices. And a 2-D 4×4-way one-body Butler matrix is developed instead of a directly cascading structure, as depicted in Fig.1.7 (a2) Similarly, a 2-D beam-switching Rotman lens can be attained by cascading stacked 1-D Rotman lens at two orthogonal directions, as Fig1.7 (b1) shows. And a 2-D one-body

Rotman lens is proposed in [1-25], which significantly reduces the physical size of the network as shown in Fig.1.7 (b2). For a spherical Luneburg lens, it can achieve 2-D beam-switching inherently by placing input incidence as per 2-D distribution.

## **1.2.4 Beam-switching matrices by different transmission line technologies**

Various transmission line technologies, as shown in Fig.1.8, like microstrip line [1-26]-[1-31], substrate integrated waveguide (SIW) [1-32]-[1-37], also known as post-wall waveguide, and metal-wall waveguide [1-38]-[1-40], have been applied to beam-switching networks. Among them, the low loss of hollow-waveguide in high frequencies is undeniably superior to other planar transmission lines or dielectric-filled waveguides [1-41]. As shown in Fig.1.8(d), the transmission loss by waveguide around 25.6GHz is only 0.003dB/cm, which is deemed to be extremely minor compared to microstrip line and SIW, as for metal-wall waveguide, ideally only conductor loss will exist, but for microstrip line and SIW, there will be accompanying dielectric loss and radiation loss, which will be dominant in the very high-frequency bandwidth.

Table. 1.2 lists a comparison of some 2-D beam-switching matrices with comparable network complexity with some normal indexes, and it could be perceived, for hollow-waveguide matrix, its low insertion loss is much more conspicuous than SIW and transmission line when it comes to over 20GHz band.

## **1.2.5 Miniaturization of beam-switching matrices**

Generally, the number of elementary components and thus the volume of beam-switching matrices tend to increase with the number of ports [1-42], and this is more notable for 2-D beam-switching matrices, which impelled researchers to investigate miniaturization techniques. Some of the applied methodologies include improving the layout of the matrices or planarization [1-43]-[1-46]. Another method is to capitalize two-plane couplers instead of traditional one-plane couplers in a hollow waveguide structure

to be assembled in a complete matrix configuration in lieu of cascading of H-plane couplers and E-plane couplers, which can be referred in Fig.1.9. The design of 2-D hollow-waveguide hybrid coupler and crossover components was first proposed in [1-47], and subsequently applied to 2-D 4×4-way [1-39] and 2-D 8×8-way Butler matrices [1-40]. This design approach has extensively facilitated the development of miniaturized waveguide-based multibeam feeding matrices. Compared to conventional one-plane couplers, two-plane couplers have remarkable merits in reducing physical dimensions and optimizing the spatial deployment of constituent components in 2-D multibeam matrices. [1-48] has significantly improved designing method of two-plane couplers by FEM-Mode matching joint computations. Moreover, [1-49] greatly enhance the bandwidth performance of two-plane couplers by introducing several coupled regions with arbitrary shapes. The two-plane couplers reported in the literature to date are all hybrid couplers, i.e. balanced couplers, and crossovers. Nolen matrices as well as the newly put forward matrix [1-11], however, normally consist of couplers splitting power unevenly, the unbalance increasing with the number of ports. As a consequence, the configuration of 2-D hollow-waveguide Nolen matrices may inevitably incorporate some unbalanced two-plane couplers which have never been proposed before, which is exactly main motivation of this dissertation.

### **1.3 Motivation of this dissertation**

As elaborated in section 1.2, the superiority of beam-switching matrices particularly in microwave frequency is embodied. Compared with other transmission line technologies, hollow waveguide is undoubtedly superior in low loss, as there are no dielectric loss and radiation loss, but only with extremely minor conductor loss, this feature will be fully advantageous in microwave frequency applications and high-power transmission scenarios.

As emphasized in section 1.2, large volume is a dominant drawback of beam-switching matrices, and this might be more notable when the number of beams increase and broaden

in 2-D beam-switching applications. Rather than approach of improvement for layout or planarization utilized in most planar transmission line technologies, waveguide-type beam-switching matrices is to capitalize two-plane couplers instead of traditional one-plane couplers in a hollow waveguide structure. Two-plane couplers have remarkably brought about promotion and stimulation of the development of miniaturized waveguide-based multibeam feeding matrices. Compared to conventional one-plane couplers, two-plane couplers have remarkable merits in reducing physical dimensions and optimizing the spatial deployment of constituent components in 2-D multibeam matrices. However, up to days, those reported two-plane couplers [1-39], [1-40], [1-47]-[1-49] are equal power splitter or crossover only, the mechanism to enable arbitrary coupling ratio for two-plane coupler still needs to be explored, as they are in all likelihood to be adopted in more complex beam-switching networks composed of 1-D matrices with arbitrary number of beams containing unbalanced coupler.

On the other hand, up to days, for 2-D hollow waveguide beam-switching applications, there are only reported works on Butler matrices, such as 2-D 4×4-way and 8×8-way Butler matrix, with their port numbers restricted as identical in either of the dimension and limited to  $2^n$ . Solutions for 2-D hollow waveguide beam-switching matrices, with beam numbers other than  $2^n$  or with different number of beams in two orthogonal directions still need to be explored, particularly there might be possibilities to bring about utilizing of two-plane coupler following arbitrary coupling ratios.

Overall, the motivation of this doctoral dissertation can be summarized as below two items:

1. To find out the coupling mechanism of two-plane coupler capable of achieving arbitrary coupling ratios in H-plane and E-plane directions. This motivation will be corresponding to subsequent Chapter.2 of this dissertation, to drastically elaborate working mechanism of two-plane couplers.
2. To design 2-D hollow waveguide beam-switching matrices with a number of beams other than  $2^n$  and with different number of beams in two orthogonal directions. This motivation will be a counterpart to Chapter.3 and Chapter.4 of this

dissertation, which introduce designs of a 2-D  $3 \times 3$ -way Nolen matrix and a 2-D  $6 \times 4$ -way dually symmetrical matrix.

## 1.4 Outline of this dissertation

This dissertation is split into 5 chapters in total. The flow chart of the dissertation is presented in Fig.1.10.

Chapter 1 gives a brief introduction concerning the background, application and development of beam forming networks, including beam-switching matrices and lens-based antennas. And the motivation of this dissertation comes up, which focuses on the exploration of two-plane coupler realizing arbitrary coupling ratios and 2-D beam-switching matrices with beam numbers other than  $2^n$  and with different number of beams in two orthogonal directions.

Chapter 2 will present a profound theoretical analysis of two-plane coupler following arbitrary coupling ratios in H-plane and E-plane directions. In addition to usual coupling mechanism with equivalence to cascading of H-plane coupler and E-plane couplers, other two coupling mechanisms will also be introduced. Subsequently with above-mentioned theory part, a designing instance of two-plane coupler following  $1:\sqrt{2}$  in H-plane direction and  $\sqrt{2}:1$  in E-plane direction will be exhibited to verify the theoretical analysis.

Chapter 3 will propose a two-dimensional (2-D) one-body  $3 \times 3$ -way hollow-waveguide Nolen matrix employing two-plane couplers working from 27.65 GHz to 28.85 GHz, corresponding to a 4.1% fractional bandwidth. This chapter corresponds to the motivation to propose 2-D one-body beam-switching matrix having a number of beams other than  $2^n$ .

Chapter 4 will present a design of a two-dimensional (2-D)  $6 \times 4$ -way hollow waveguide beam-switching matrix working at 28.25 GHz, with a fractional bandwidth of 7.1%. This chapter is counterpart to the motivation to propose a 2-D one-body hollow waveguide beam-switching matrix different numbers of beams in two orthogonal directions.

Chapter 5 will give summarize the complete dissertation and give some perspective views on future works.

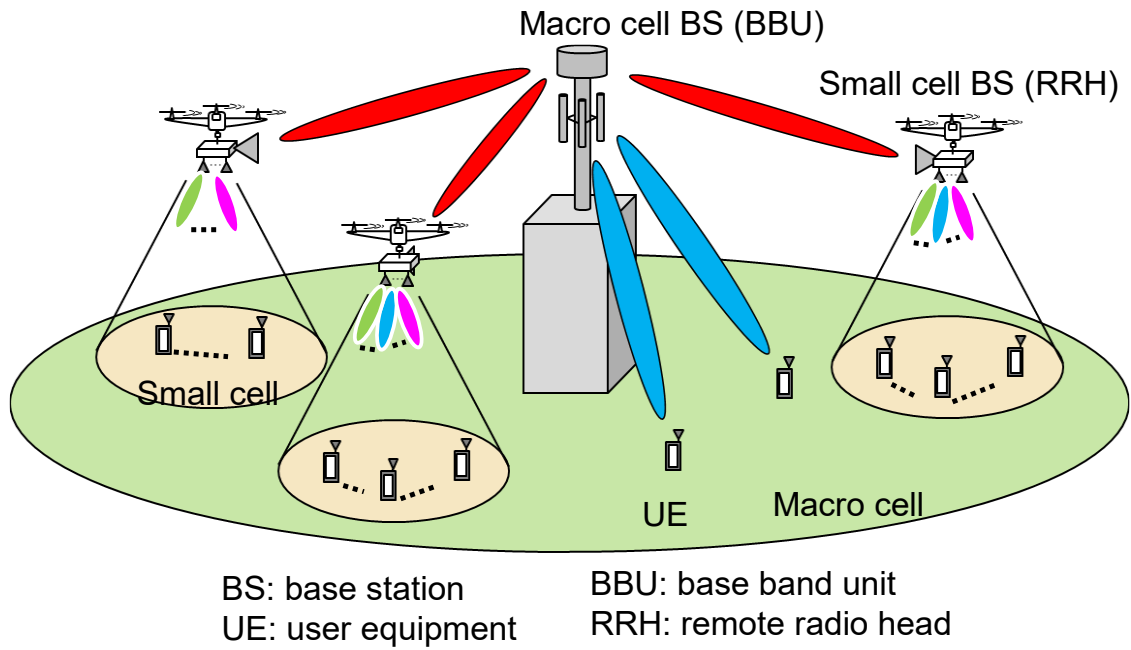


**Fig. 1.1.** Novel Unmanned Aerial Vehicle-Based Line-of-Sight MIMO Configuration Independent of Transmitted Distance Using Millimeter Wave [1-5].

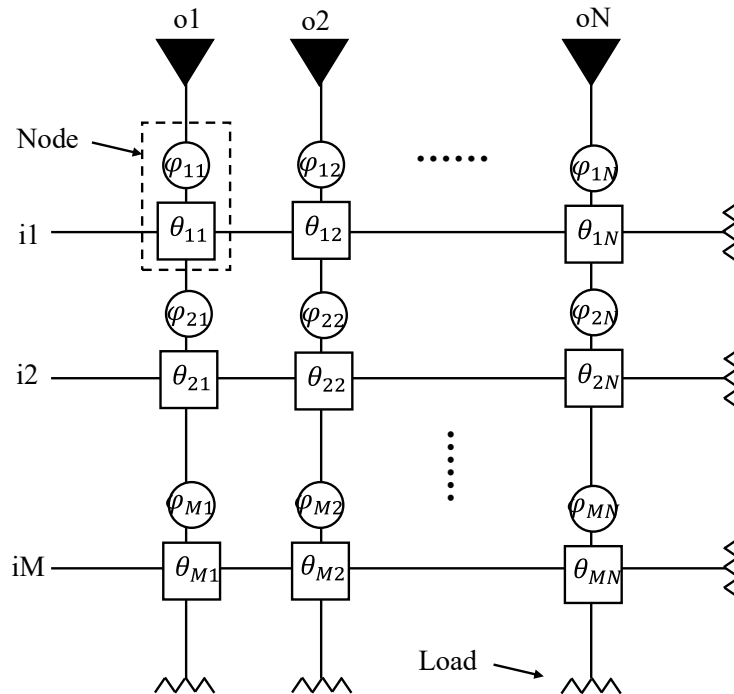


**Fig. 1.2.** Normal configuration of a Blass matrix.



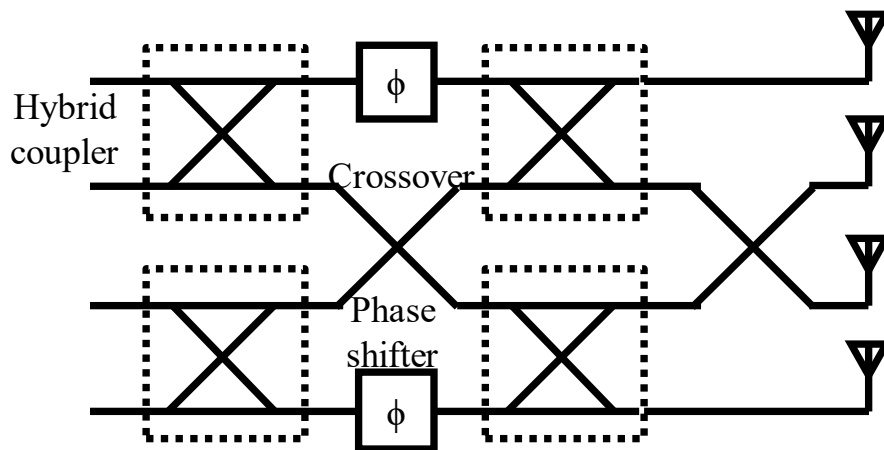


**Fig. 1.3.** Configuration of a 4-way Butler matrix

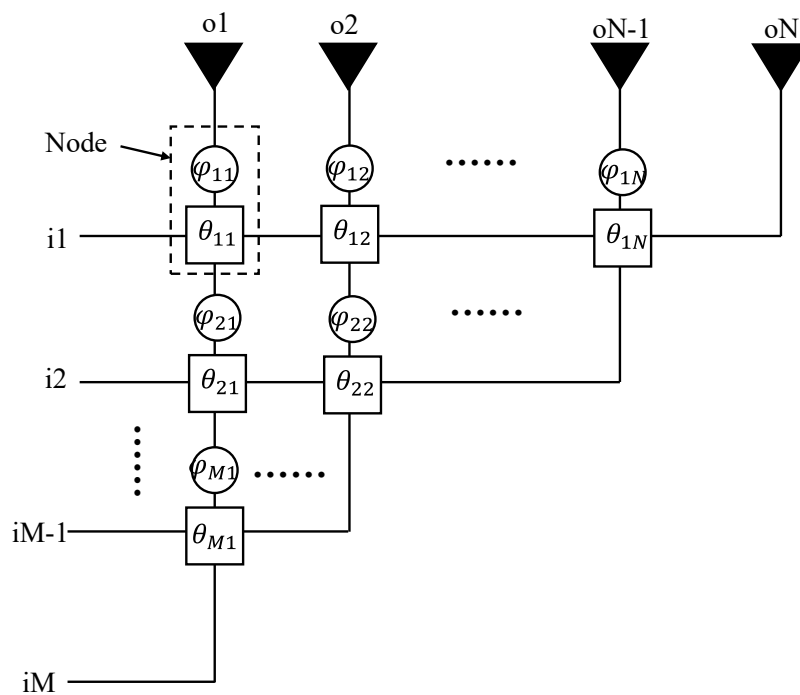
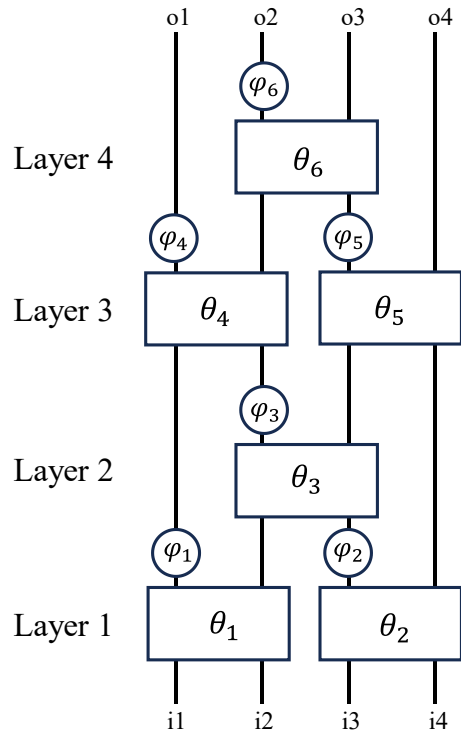
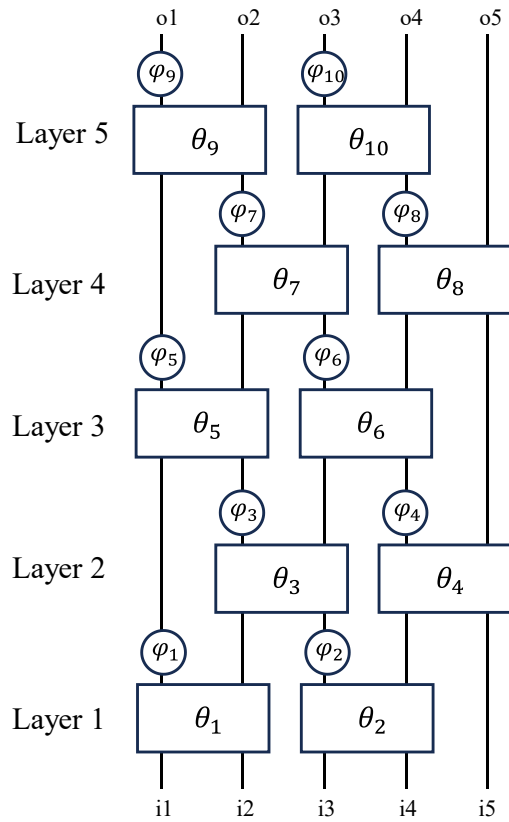


**Fig. 1.4.** Normal configuration of a Nolen matrix.



(a) 4-way matrix



(b) 5-way matrix

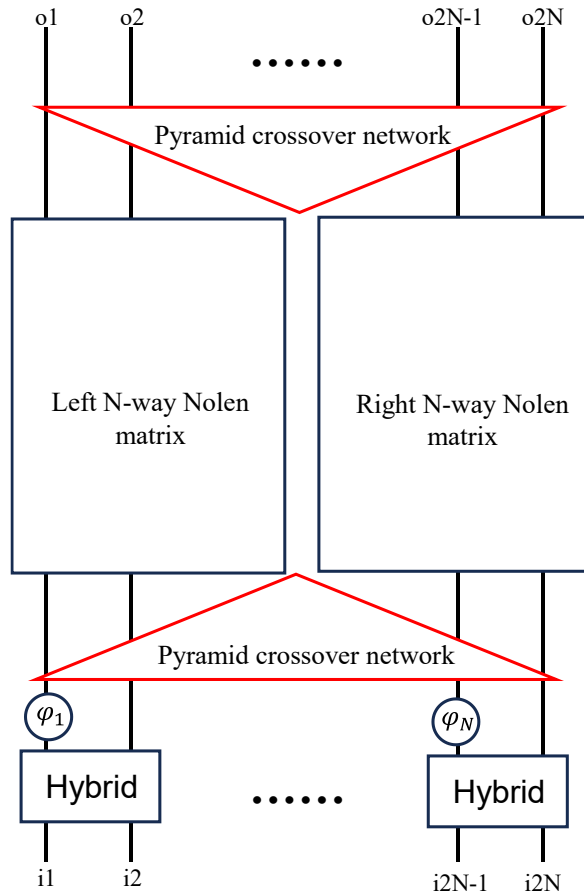
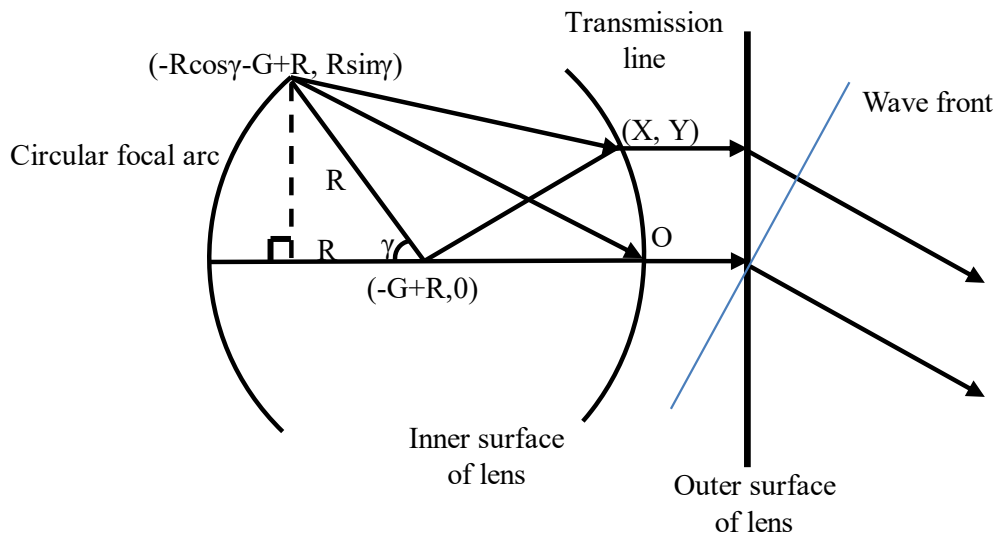


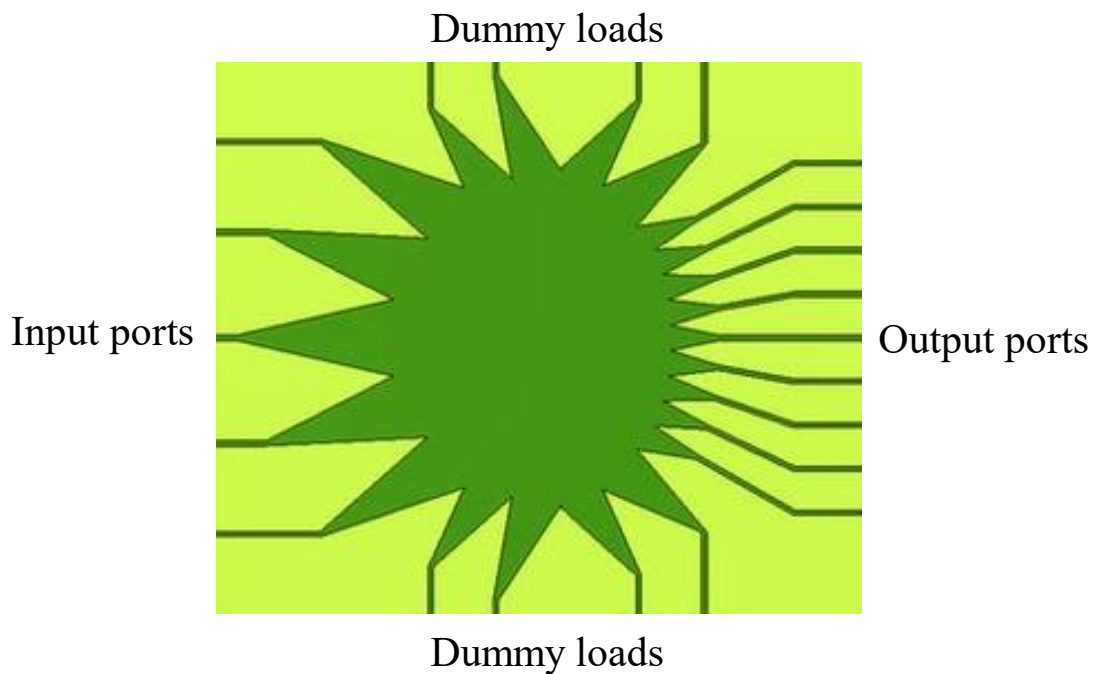
**Fig. 1.5.** Configuration of proposed matrix in [1-11].

**TABLE 1.1**  
**Comparison among 1-D beam-switching matrices**

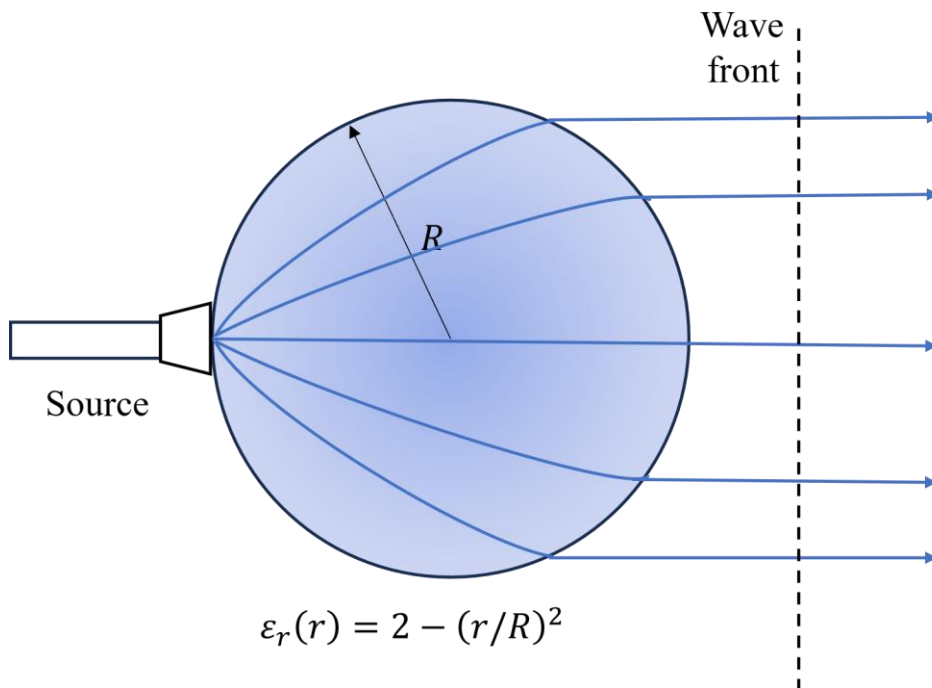
Project ( $N \times N$ -way)	Blass matrix	Nolen matrix	Butler matrix ( $N=2^n$ )	[1-11]
Number of couplers	$N^2$	$N(N-1)/2$	$Nn/2$	$N(N-1)/2$
Number of phase shifters	$N^2$	$N(N-1)/2$	$N(n-1)/2$	$N(N-1)/2$
Lossless	No	Yes	Yes	Yes
Bandwidth	Narrow	Narrow	Widest	Wider
Symmetry	No	No	Yes	Some solutions



(a1) Rotman lens working mechanism

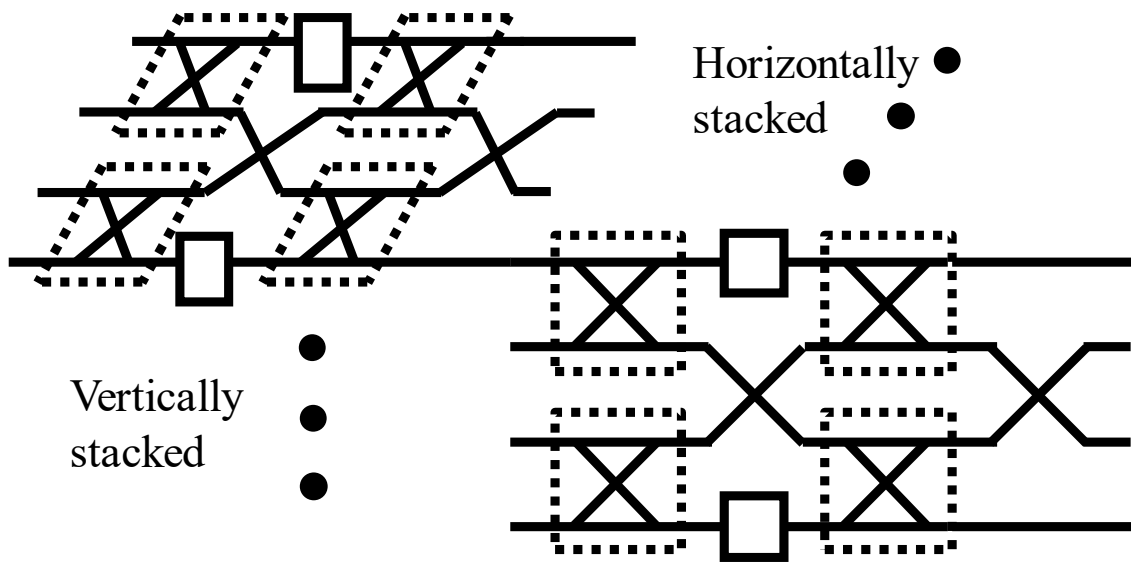


(a2) Layout of a Rotman lens by microstrip line

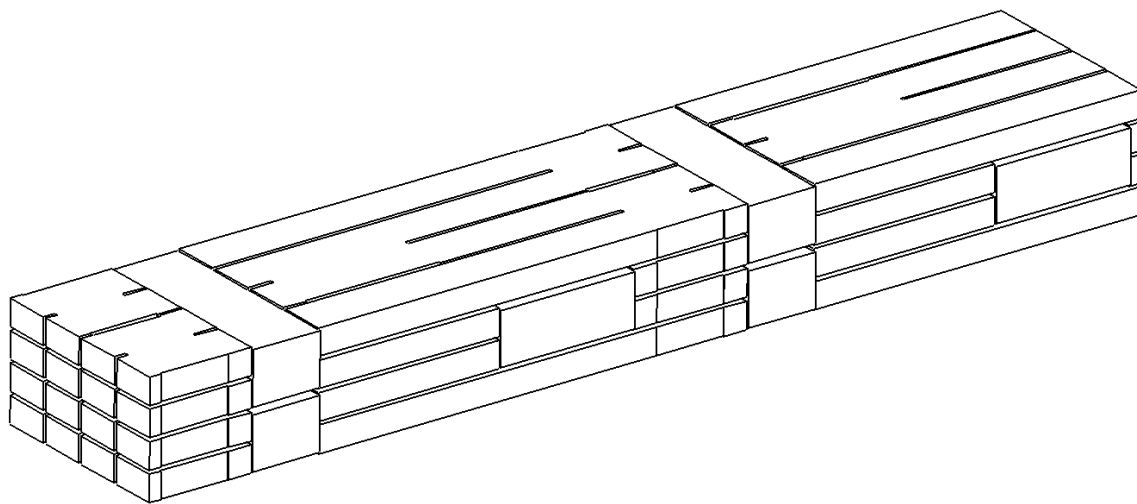


(b) Luneburg lens

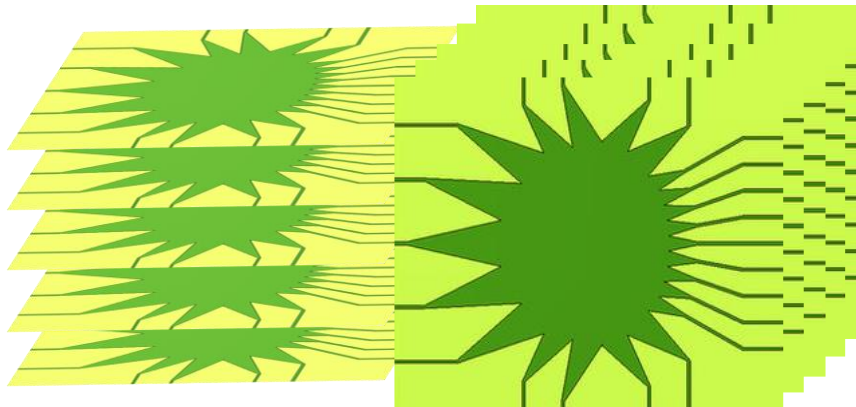
**Fig. 1.6.** Lens type antennas.



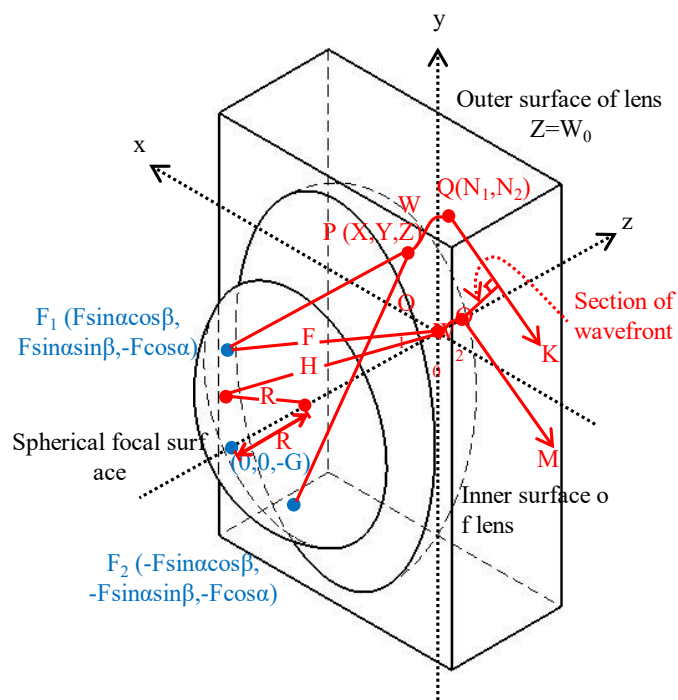
(a1) 2-D 4x4-way Butler matrix by direct cascading



(a2) 2-D one-body hollow waveguide 4x4-way Butler matrix.



(b1) 2-D beam-switching Rotman lens by direct cascading.



(b2) One-body 2-D beam-switching Rotman lens.

**Fig. 1.7.** 2-D beam-switching networks.

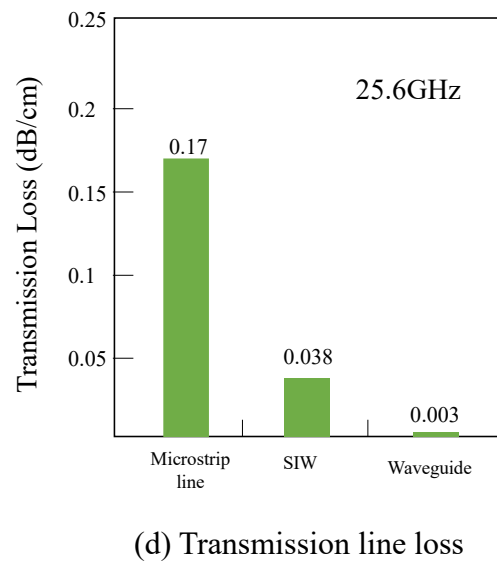
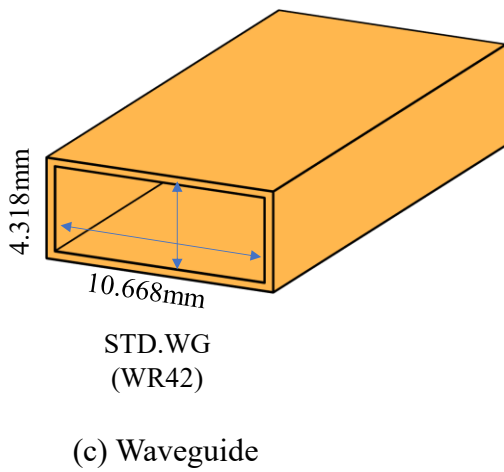
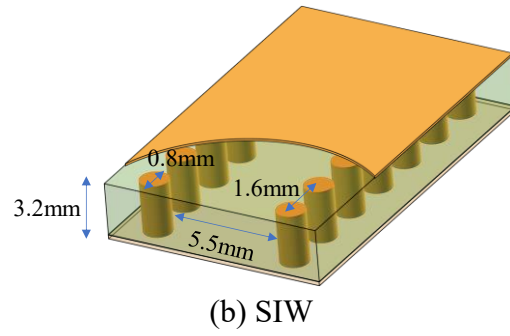
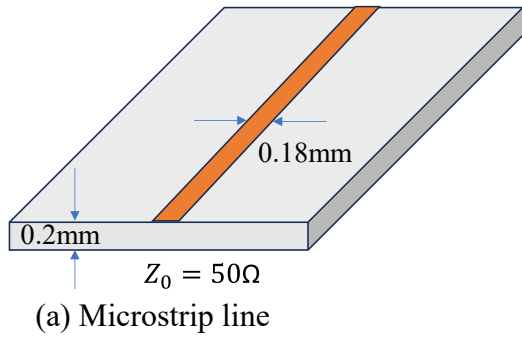


**Fig. 1.8.** Normal transmission line technologies.



**TABLE 1.2**  
**Comparison among 2-D beam-switching matrices**  
**by different transmission line technologies**

	2-D 3×3	2-D 3×3	2-D 4×4 Butler	2-D 4×4 Butler	2-D 4×4
<b>Performance</b>	Nolen matrix	matrix	matrix	matrix	Butler matrix
	[1-31]	[1-37]	[1-26]	[1-46]	[1-39]
<b>Frequency</b>	6GHz	28GHz	2.4GHz	10GHz	22GHz
<b>Transmission</b>	Microstrip line	SIW	Microstrip line	SIW	Waveguide
<b>Insertion loss (IL)</b>	N.A.	N.A.	1.8dB	4dB	1.5dB
<b>Output amplitude imbalance (IL included)</b>	N.A.	N.A.	3dB	>6dB	4.8dB
<b>Bandwidth</b>	N.A.	7.1%	16.7%	N.A.	2%
<b>Physical size (<math>\lambda^3</math>)</b>	N.A.	N.A.	1.6*1.6*0.004	22*16.7*0.03	3.45*3.45*14.0

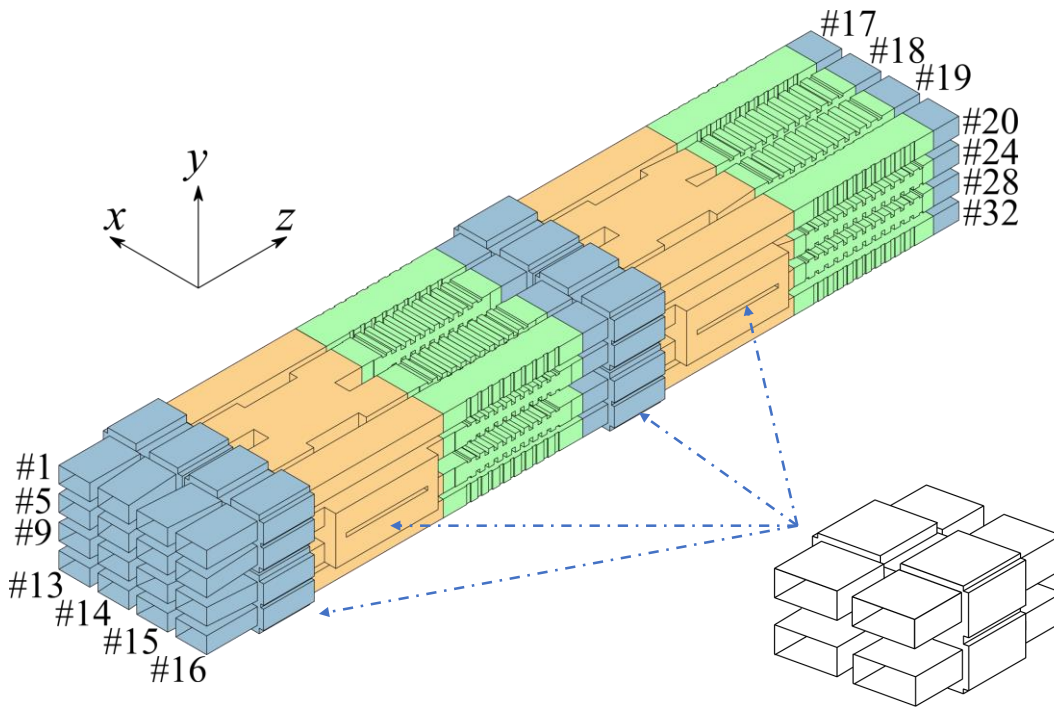


**Fig. 1.9.** Two-plane couplers assembled in a 2-D 4×4-way Butler matrix.

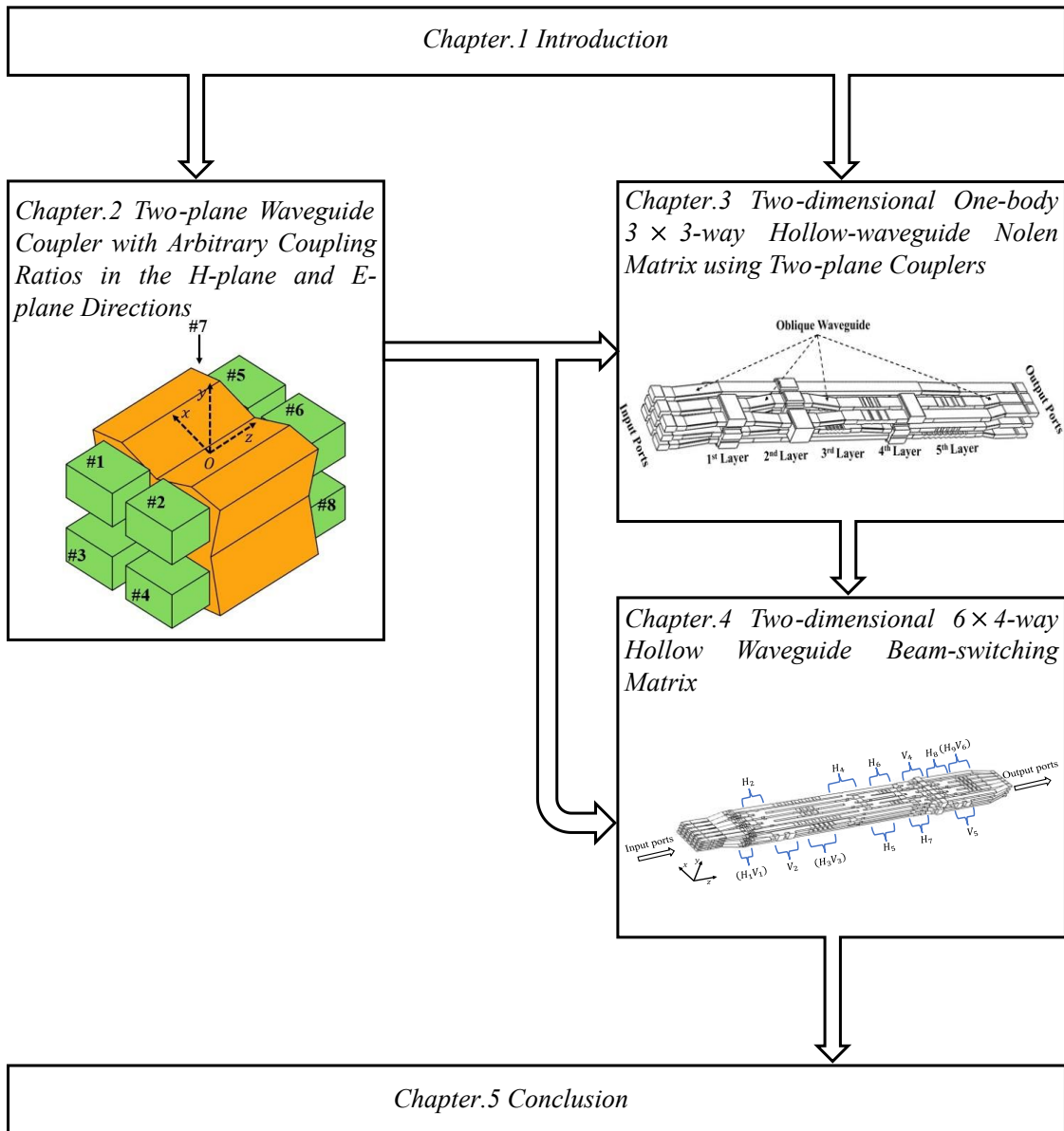


**Fig. 1.10.** Flow chart of dissertation structure.

## References

- [1-1] H. Papadopoulos, C. Wang, O. Bursalioglu, X. Hou, and Y. Kishiyama, "Massive MIMO technologies and challenges towards 5G," *IEICE Trans. Commun.*, vol. 99, no. 3, pp. 602–621, Mar. 2015.
- [1-2] Y. Yamasa, K. Hariu, T. Okamoto and Y. Otsu, "Study on feed systems of multibeam antennas for S-band mobile satellite communications," *IEEE Int. Antennas Propag. Symp.. 1996 Digest*, 1996, pp. 1688-1691 vol.3.
- [1-3] Y. J. Guo, M. Ansari and N. J. G. Fonseca, "Circuit Type Multiple Beamforming Networks for Antenna Arrays in 5G and 6G Terrestrial and Non-Terrestrial Networks," *IEEE J. Microwaves*, vol. 1, no. 3, pp. 704-722, July 2021.
- [1-4] Y. J. Guo, M. Ansari, R. W. Ziolkowski and N. J. G. Fonseca, "Quasi-Optical Multi-Beam Antenna Technologies for B5G and 6G mmWave and THz Networks: A Review," in *IEEE Open Journal of Antennas and Propagation*, vol. 2, pp. 807-830, 2021
- [1-5] N. Matsumura, K. Nishimori, R. Taniguchi, T. Hiraguri, T. Tomura and J. Hirokawa, *IEEE Access*, vol. 1, pp. 2169-3536, Jan. 2020.
- [1-6] Y. J. Guo and R.W. Ziolkowsk, *Advanced Antenna Array Engineering for 6G and Beyond Wireless Communications*. Hoboken, NJ, USA: Wiley, 2021.
- [1-7] J. Blass, "Multidirectionnal antenna, a new approach to stacked beams," *IRE Int. Conf. Record*, vol. 8, pt. 1, pp. 48-50, 1960.
- [1-8] J. Butler and R. Lowe, "Beam-forming matrix simplifies design of electronically scanned antennas," *Electron. Des.*, vol. 9, pp. 170–173, Apr. 1961.
- [1-9] J. Nolen, "Synthesis of multiple beam networks for arbitrary illuminations" Bendix Corp, 1965.
- [1-10] N. J. G. Fonseca, "Printed S-Band  $4 \times 4$  Nolen Matrix for Multiple Beam Antenna Applications," *IEEE Trans. Antennas Propag.*, vol. 57, no. 6, pp. 1673-1678, June 2009.
- [1-11] J. Hirokawa and N. J. G. Fonseca, "Generalized one-dimensional parallel switching matrices with an arbitrary number of beams," *IEEE J. Microwaves*, vol. 1, no. 4, pp. 975-988, Oct. 2021.
- [1-12] P. Angeletti and M. Lisi, "Multimode beamforming networks for space applications," *IEEE Antennas Propag. Mag.*, vol. 56, no. 1, pp. 62–78, Feb. 2014.
- [1-13] T. Djerafi, N. J. G. Fonseca and K. Wu, "Planar Ku-Band  $4 \times 4$  Nolen Matrix in SIW Technology," *IEEE Trans. Microw. Theory Techn.*, vol. 58, no. 2, pp. 259-266, Feb. 2010.

- [1-14] W. Rotman and R. Turner, "Wide-angle microwave lens for line source applications," *IEEE Trans. Antennas Propag.*, vol. AP-11, no. 6, pp. 623–632, Nov. 1963.
- [1-15] R. K. Luneburg, *Mathematical Theory of Optics*. Providence, RI, USA: Univ. California Press, 1964.
- [1-16] J. R. Reis et al., "FSS-inspired transmitarray for two-dimensional antenna beamsteering," *IEEE Trans. Antennas Propag.*, vol. 64, no. 6, pp. 2197–2206, Jun. 2016.
- [1-17] N. Kou, S. Yu, Z. Ding, and Z. Zhang, "One-dimensional beam scanning transmitarray lens antenna fed by microstrip linear array," *IEEE Access*, vol. 7, pp. 90731–90740, 2019.
- [1-18] Z.-W. Miao et al., "140 GHz high-gain LTCC-integrated transmitarray antenna using a wideband SIW aperture-coupling phase delay structure," *IEEE Trans. Antennas Propag.*, vol. 66, no. 1, pp. 182–190, Jan. 2017.
- [1-19] X. Liu et al., "Ultra-broadband all dielectric transmitarray designing based on genetic algorithm optimization and 3D print technology," *IEEE Trans. Antennas Propag.*, vol. 69, no. 4, pp. 2003–2012, Apr. 2021.
- [1-20] D. Berry, R. Malech, and W. Kennedy, "The reflectarray antenna," *IEEE Trans. Antennas Propag.*, vol. AP-11, no. 6, pp. 645–651, Nov. 1963.
- [1-21] J. Huang, "Reflectarray antenna," in *Encyclopedia of RF and Microwave Engineering*. Hoboken, NJ, USA: Wiley, 2005.
- [1-22] Y. Rahmat-Samii and R. Haupt, "Reflector antenna developments: A perspective on the past, present and future," *IEEE Antennas Propag. Mag.*, vol. 57, no. 2, pp. 85–95, Apr. 2015.
- [1-23] M. Ansari, B. Jones, H. Zhu, N. Shariati, and Y. J. Guo, "A highly efficient spherical Luneburg lens for low microwave frequencies realized with a metal-based artificial medium," *IEEE Trans. Antennas Propag.*, early access, 2021.
- [1-24] C. A. Fernandes, E. B. Lima, and J. R. Costa, "Dielectric lens antennas," in *Handbook of Antenna Technology*. Singapore: Springer, 2016, pp. 1001–1064.
- [1-25] D. -H. Kim, J. Hirokawa, K. Tekkouk, M. Ando and R. Sauleau, "Comparison between one-body 2-D beam-switching Butler matrix and 2-D beam-switching Rotman lens," 2016 International Symposium on Antennas and Propagation (ISAP), Okinawa, Japan, 2016, pp. 300-301
- [1-26] K. Ding and A. A. Kishk, "2-D Butler matrix and phase-shifter group," *IEEE Trans. Microw. Theory Techn.*, vol. 66, no. 12, pp. 5554-5562, Dec. 2018
- [1-27] Y. Li, J. Wang, and K.-M. Luk, "Millimeter-wave multibeam aperturecoupled magnetoelectric dipole array with planar substrate integrated beamforming network for 5G applications," *IEEE Trans. Antennas Propag.*, vol. 65, no. 12, pp. 6422–6431, Dec. 2017.
- [1-28] C.-W. Wang, T.-G. Ma, and C.-F. Yang, "A new planar artificial transmission line and its applications to a miniaturized Butler matrix," *IEEE Trans. Microw. Theory Techn.*, vol. 55, no. 12, pp. 2792–2801, Dec. 2007.

- [1-29] C. A. Guo, Y. J. Guo, H. Zhu, W. Ni and J. Yuan, "Optimization of Multibeam Antennas Employing Generalized Joined Coupler Matrix," *IEEE Trans. Antennas Propag.*, vol. 71, no. 1, pp. 215-224, Jan. 2023.
- [1-30] M. Bona, L. Manholm, J. P. Starski, and B. Svensson, "Low-loss compact Butler matrix for a microstrip antenna," *IEEE Trans. Microw. Theory Techn.*, vol. 50, no. 9, pp. 2069–2075, Sep. 2002.
- [1-31] H. Ren, H. Zhang, Y. Jin, Y. Gu, and B. Aridong, "A novel 2-D  $3 \times 3$  Nolen matrix for 2-D beamforming applications," *IEEE Trans. Microw. Theory Techn.*, vol. 67, no. 11, pp. 4622–4631, Nov. 2019.
- [1-32] A. A. M. Ali, N. J. G. Fonseca, F. Coccetti, and H. Aubert, "Design and implementation of two-layer compact wideband butler matrices in SIW technology for Ku-band applications," *IEEE Trans. Antennas Propag.*, vol. 59, no. 2, pp. 503–512, Feb. 2011.
- [1-33] T. Djerafi and K. Wu, "A Low-Cost Wideband 77-GHz Planar Butler Matrix in SIW Technology," *IEEE Trans. Antennas Propag.*, vol. 60, no. 10, pp. 4949-4954, Oct. 2012.
- [1-34] E. T. Der, T. R. Jones and M. Daneshmand, "Miniaturized  $4 \times 4$  Butler Matrix and Tunable Phase Shifter Using Ridged Half-Mode Substrate Integrated Waveguide," *IEEE Trans. Microw. Theory Techn.*, vol. 68, no. 8, pp. 3379-3388, Aug. 2020.
- [1-35] Q. Sun, Y. -L. Ban, Y. -X. Che and Z. Nie, "Coexistence-Mode CRLH SIW Transmission Line and Its Application for Longitudinal Miniaturized Butler Matrix and Multibeam Array Antenna," *IEEE Trans. Antennas Propag.*, vol. 69, no. 11, pp. 7593-7603, Nov. 2021.
- [1-36] J. -W. Lian, X. -Y. Zhao, Y. -L. Ban, Y. Liu and Z. Nie, "Compact SIW 2-D Butler Matrix and Its Multibeam Application," *IEEE Antennas Wireless Propag. Lett.*, vol. 20, no. 3, pp. 386-390, Mar. 2021.
- [1-37] J.-W. Lian, Y.-L. Ban, J.-Q. Zhu, K. Kang, and Z. Nie, "Compact 2-D scanning multibeam array utilizing the SIW three-way couplers at 28 GHz," *IEEE Antennas Wireless Propag Lett.*, vol. 17, no. 10, pp. 1915–1919, Oct. 2018.
- [1-38] S. Yamamoto, J. Hirokawa, and M. Ando, "A single-layer hollow waveguide 8-way Butler matrix," *IEICE Trans. Electron.*, vol. 89, no. 7, pp. 1080–1088, Jul. 2006.
- [1-39] D.-H. Kim, J. Hirokawa, and M. Ando, "One-body 2-D Beam-switching Butler Matrix with Waveguide Short-slot 2-plane Couplers," *IEICE Trans. Electron.*, vol. E100-C, no.10, pp.-, Oct. 2017.
- [1-40] T. Tomura, D. -H. Kim, M. Wakasa, Y. Sunaguchi, J. Hirokawa and K. Nishimori, "A 20-GHz-Band  $64 \times 64$  Hollow waveguide Two-Dimensional Butler Matrix," *IEEE Access*, vol. 7, pp. 164080-164088, 2019.
- [1-41] T. Djerafi, N. J. G. Fonseca and K. Wu, "Broadband Substrate Integrated Waveguide  $4 \times 4$  Nolen Matrix Based on Coupler Delay Compensation," *IEEE Trans. Microw. Theory Techn.*, vol. 59, no. 7, pp. 1740-1745, July 2011.

- [1-42] M. Bozzi and N. J. G. Fonseca, "Substrate Integrated Transmission Lines: Review and Applications," *IEEE J. Microwaves*, vol. 1, no. 1, pp. 345-363, Jan. 2021.
- [1-43] W. F. Moulder, W. Khalil, and J. L. Volakis, "60-GHz two-dimensionally scanning array employing wideband planar switched beam network," *IEEE Antennas Wireless Propag. Lett.*, vol. 9, pp. 818–821, 2010.
- [1-44] I. M. Mohamed and A.-R. Sebak, "60 GHz 2-D scanning multibeam cavity-backed patch array fed by compact SIW beamforming network for 5G applications," *IEEE Trans. Antennas Propag.*, vol. 67, no. 4, pp. 2320–2331, Apr. 2019.
- [1-45] X. Wang, X. Fang, M. Laabs, and D. Plettemeier, "Compact 2-D multibeam array antenna fed by planar cascaded Butler matrix for millimeterwave communication," *IEEE Antennas Wireless Propag. Lett.*, vol. 18, no. 10, pp. 2056–2060, Oct. 2019.
- [1-46] J. -W. Lian, Y. -L. Ban, H. Zhu and Y. J. Guo, "Uniplanar Beam-Forming Network Employing Eight-Port Hybrid Couplers and Crossovers for 2-D Multibeam Array Antennas," *IEEE Trans. Microw. Theory Techn.*, vol. 68, no. 11, pp. 4706-4718, Nov. 2020.
- [1-47] D.-H. Kim, J. Hirokawa, and M. Ando, "Design of waveguide shortslot two-plane couplers for one-body 2-D beam-switching Butler matrix application," *IEEE Trans. Microw. Theory Techn.*, vol. 64, no. 3, pp. 776–784, Mar. 2016.
- [1-48] M. Wakasa, D.-H. Kim, T. Tomura, and J. Hirokawa, "Wideband Design of a Short-Slot 2-Plane Coupler by the Mode Matching/FEM Hybrid Analysis considering the Structural Symmetry," *IEICE Trans. Commun.*, vol. E102-B, No.5, pp.1019-1026, May 2019.
- [1-49] S. Chen, T. Tomura, J. Hirokawa, K. Ito, M. Suga, Y. Shirato, D. Uchida, and N. Kita, "Design for Operation in Two Frequency Bands by Division of the Coupled Region in a Waveguide 2-Plane Coupler," *IEICE Trans. Commun.*, vol. E105-C, No.12, pp.729-739, Dec. 2022.

# Chapter 2 Two-plane Waveguide Coupler with Arbitrary Coupling Ratios in the H-plane and E-plane Directions

## 2.1 Introductory remarks

Two-plane coupler following arbitrary coupling ratios in H-plane and E-plane directions, which is reckoned as most principal and notable contribution of this doctor thesis, its working mechanism will be elaborated in this chapter.

To begin, a comprehensive explanation of the theory behind conventional one-plane couplers will be presented, establishing a solid foundation for understanding the subsequent discussion. This thorough exploration will ensure a clear understanding of the principles governing these couplers and their established mechanisms. Following that, the theoretical analysis of two-plane couplers accommodating arbitrary coupling ratios will be utterly demonstrated. This in-depth exploration will delve into the intricacies of these couplers, showcasing their versatility in achieving various coupling ratios. Moreover, beyond the commonly employed coupling mechanism, two additional distinct coupling mechanisms will be discussed. The utilization of Mode Matching-FEM computation, a crucial computational method for analyzing two-plane couplers with irregular shapes, will be introduced and discussed. This computational technique plays a pivotal role in accurately evaluating and optimizing the performance and characteristics of two-plane couplers featuring non-standard geometries. A detailed demonstration of this computation method will be included in the Appendix section, providing a comprehensive understanding of its implementation and its significance in the analysis of two-plane couplers.

Building upon the aforementioned theoretical framework, a practical design example of a two-plane coupler with specific coupling ratios will be presented. This particular coupler follows a ratio of  $1:\sqrt{2}$  in the H-plane direction and  $\sqrt{2}:1$  in the E-plane

direction. To demonstrate its feasibility, the coupler has been successfully fabricated and its performance has been verified through meticulous VNA (Vector Network Analyzer) measurements. The results obtained from both simulations and measurements will be extensively discussed to provide a comprehensive evaluation of its performance characteristics. Furthermore, in order to emphasize the advantages of utilizing two-plane couplers in terms of miniaturization when compared to the conventional cascading of one-plane couplers, a separate design sample consisting of an H-plane coupler and an E-plane coupler will be presented. The cascading of these individual couplers is equivalent to the proposed two-plane coupler in terms of functionality. A detailed comparison between the performance of the cascaded one-plane couplers and the proposed two-plane coupler will be conducted through simulation analysis. By conducting this comparative study, it is anticipated that a clear understanding of the benefits and limitations of the two-plane coupler design will be achieved. This comprehensive analysis, incorporating both simulation and measurement data, will shed light on the performance characteristics and potential advantages of the proposed two-plane coupler over the traditional approach of cascading one-plane couplers.

## **2.2 One-plane couplers**

One-plane couplers, incorporating H-plane couplers and E-plane couplers are very conventional microwave components those have been widely employed in various applications.

As Fig.2.1 shows, H-plane coupler and E-plane coupler are symmetrical 4-port structure. They are comprised of input or output waveguides and coupled region. Input or output port are rigorously complying to single-mode condition, while coupled region should at least contain odd higher modes like  $TE_{20}$  mode to act desired coupling mechanism. Take H-plane coupler as an example, based on even-odd method analysis, the output S-parameter of H-plane coupler, could be synthesized by parameter of two-port half structure accompanying with associated PEC/PMC boundary in correspondence of mode polarity.

Hence, the output of a 4-port H-plane coupler turns out to be,



$$S_{31} = \frac{1}{2}S_{21}^M + \frac{1}{2}S_{21}^E \quad (2-1a)$$

$$S_{41} = \frac{1}{2}S_{21}^M - \frac{1}{2}S_{21}^E \quad (2-1b)$$

Here M and E stand for PMC and PEC, respectively.  $S_{21}$  represents transmission of half structure. Similarly, the reflection or isolation of a H-plane coupler can be expressed as,

$$S_{11} = \frac{1}{2}S_{11}^M + \frac{1}{2}S_{11}^E \quad (2-2a)$$

$$S_{21} = \frac{1}{2}S_{11}^M - \frac{1}{2}S_{11}^E \quad (2-2b)$$

For equation (2-1), in favor of an ideally matching condition, literally  $|S_{21}^M| = |S_{21}^E| = 1$ , and  $|S_{11}^M| = |S_{11}^E| = 0$ , then  $e^{jP_M}$  and  $e^{jP_E}$  can alternatively incarnate transition of half structure with PMC and PEC symmetrical plane, where  $P_M$  and  $P_E$  signify transition phase. Then equation (2-1) can be converted into

$$S_{31} = e^{j\frac{P_M+P_E}{2}} \cos\left(\frac{P_E - P_M}{2}\right) \quad (2-3a)$$

$$S_{41} = -je^{j\frac{P_M+P_E}{2}} \sin\left(\frac{P_E - P_M}{2}\right) \quad (2-3b)$$

From equation (2-3), it could be perceived amplitude of  $S_{31}$  and  $S_{41}$  are manipulated by variable  $(P_E - P_M)/2$ , and phase of  $S_{41}$  is always lagged 90 degree by  $S_{31}$  when  $(P_E - P_M)/2$  varies from 0 to  $\pi/2$ . That is also why symmetrical coupler is commonly referred to as quadrature coupler. PMC boundary is counterpart to all even mode along H-plane in coupled region, including  $TE_{mn}$  and  $TM_{mn}$  mode, when m is even. PEC boundary corresponds to all existing odd mode along H-plane, covering all  $TE_{mn}$  and

TM<sub>mn</sub> mode in coupled region, when m is odd. The analysis of 2-port model is exerted by Mode matching-FEM joint calculation, which will be demonstrated in latter section.

The output of E-plane coupler, is similarly to be given as,

$$S_{31} = e^{j\frac{P_M+P_E}{2}} \cos\left(\frac{P_M - P_E}{2}\right) \quad (2 - 4a)$$

$$S_{41} = -je^{j\frac{P_M+P_E}{2}} \sin\left(\frac{P_M - P_E}{2}\right) \quad (2 - 4b)$$

But just as opposed to H-plane coupler, for E-plane coupler, PMC boundary is counterpart to all odd mode along E-plane in coupled region, including TE<sub>mn</sub> and TM<sub>mn</sub> mode, when n is odd. PEC boundary corresponds to all even mode along E-plane, covering all TE<sub>mn</sub> and TM<sub>mn</sub> mode in coupled region, when n is even.

Generally, E-plane coupler will manifest narrower bandwidth than H-plane coupler, since main mode for PMC boundary is TE<sub>01</sub> mode which has an orthogonal direction of electrical field against TE<sub>10</sub> mode at input or output region, which lead to difficult matching.

### 2.3 General analysis of two-plane coupler

Two-plane hollow waveguide coupler is equivalent to concatenation unit including two vertically-stacked H-plane couplers cascading with two horizontally-stacked E-plane couplers, as Fig.2.2 shows. The prerequisite of composing a two-plane coupler would be for commutativity between uniform stacked components in the H-plane and E-plane directions, and the sequence order of each layer of component can be swapped, then interleaved H-plane and E-plane coupler units will occur, and provide the base to construct a two-plane coupler.

The groundbreaking concept of designing 2-D hollow-waveguide hybrid coupler and crossover components was initially introduced in [2-1]. This innovative approach paved the way for its subsequent application in the development of impressive 2-D 4×4-way [2-

2] and 2-D  $8 \times 8$ -way Butler matrices [2-3]. These remarkable advancements in waveguide technology have propelled the 2-D waveguide beam-switching matrices forward. Moreover, a notable breakthrough was achieved in [2-4], where an effective method was demonstrated to significantly enhance the bandwidth performance of two-plane couplers. This was accomplished by introducing an arbitrary shape for the coupled region, resulting in improved performance characteristics. This breakthrough has had a profound impact on the application of two-plane couplers. The utilization of two-plane couplers has generated immense excitement and has acted as a catalyst for the development of compact waveguide-based multibeam feeding matrices. In comparison to traditional one-plane couplers, the adoption of two-plane couplers presents distinct advantages, including the reduction of physical dimensions and the optimization of spatial deployment of constituent components within 2-D multibeam matrices. These merits have revolutionized the related field, opening up new avenues for exploration and advancement.

The previous literature primarily focused on two-plane hybrid coupler and crossover as the predominant types of two-plane couplers for application on 2-D Butler matrices. However, it is important to note that Nolen matrices, and the recently published literature pursuing general 1-D beam-switching matrices [2-5] to accommodate arbitrary numbers of beams, differing from the Butler matrix, normally consist of couplers splitting power unevenly, this power imbalance tends to increase as the number of ports within the matrix grows. Consequently, when constructing 2-D hollow-waveguide matrices utilizing these 1-D beam-switching matrices, it becomes inevitable to incorporate two-plane couplers that adopt arbitrary coupling ratios. Remarkably, this particular configuration, featuring two-plane couplers with arbitrary coupling ratios, has never been proposed or explored in prior research.

A general two-plane coupler containing 4 input ports and 4 output ports, as well as a coupled region, as depicted in Fig.2.3. Usually, a two-plane coupler equivalent to cascading two vertically-stacked H-plane couplers and two horizontally-stacked E-plane couplers should be symmetric about the x-axis and y-axis. Moreover, here to impose symmetry about the z-axis can reduce the number of variables in the design process and

thereby diminish complexity. The quarter model of two-plane coupler with only two ports can be extracted exclusively and assigned perfect electric conductor (PEC) or perfect magnetic conductor (PMC) boundary conditions at the symmetry planes in accordance with the polarity of the coupling region modes to analyze the overall output characteristics of the complete two-plane coupler, based on two-dimensionally even-odd method.

The output of an 8-port two-plane coupler corresponding to incidence from port 1, can be synthesized as

$$S_{51} = \frac{1}{4}S_{21}^{ME} + \frac{1}{4}S_{21}^{EE} + \frac{1}{4}S_{21}^{MM} + \frac{1}{4}S_{21}^{EM} \quad (2-5a)$$

$$S_{61} = \frac{1}{4}S_{21}^{ME} - \frac{1}{4}S_{21}^{EE} + \frac{1}{4}S_{21}^{MM} - \frac{1}{4}S_{21}^{EM} \quad (2-5b)$$

$$S_{71} = \frac{1}{4}S_{21}^{ME} + \frac{1}{4}S_{21}^{EE} - \frac{1}{4}S_{21}^{MM} - \frac{1}{4}S_{21}^{EM} \quad (2-5c)$$

$$S_{81} = \frac{1}{4}S_{21}^{ME} - \frac{1}{4}S_{21}^{EE} - \frac{1}{4}S_{21}^{MM} + \frac{1}{4}S_{21}^{EM} \quad (2-5d)$$

Here  $S_{21}$  means transition of a quarter model with regard to different boundary in symmetrical plane. In addition, the reflection and isolation can be expressed as,

$$S_{11} = \frac{1}{4}S_{11}^{ME} + \frac{1}{4}S_{11}^{EE} + \frac{1}{4}S_{11}^{MM} + \frac{1}{4}S_{11}^{EM} \quad (2-6a)$$

$$S_{21} = \frac{1}{4}S_{11}^{ME} - \frac{1}{4}S_{11}^{EE} + \frac{1}{4}S_{11}^{MM} - \frac{1}{4}S_{11}^{EM} \quad (2-6b)$$

$$S_{31} = \frac{1}{4}S_{11}^{ME} + \frac{1}{4}S_{11}^{EE} - \frac{1}{4}S_{11}^{MM} - \frac{1}{4}S_{11}^{EM} \quad (2-6c)$$

$$S_{41} = \frac{1}{4}S_{11}^{ME} - \frac{1}{4}S_{11}^{EE} - \frac{1}{4}S_{11}^{MM} + \frac{1}{4}S_{11}^{EM} \quad (2-6d)$$

In order to achieve an ideally matching condition for a quarter 2-port model, where  $|S_{21}^{ME}| = |S_{21}^{EE}| = |S_{21}^{MM}| = |S_{21}^{EM}| = 1$ , the transmission coefficients can be incarnated as

$e^{jP_{ME}}$ ,  $e^{jP_{EE}}$ ,  $e^{jP_{MM}}$ , and  $e^{jP_{EM}}$ . Here,  $P_{ME}$ ,  $P_{EE}$ ,  $P_{MM}$ , and  $P_{EM}$  denote the transmission phase, which is defined as the phase part of the ratio of the TE<sub>10</sub> mode at the output ports to the TE<sub>10</sub> mode at the input ports. These phase values determine the relative phase shift experienced by the signals passing through the model. By expressing the transmission coefficients as complex exponentials with the transmission phases, we can effectively describe the phase characteristics of the quarter 2-port model under the ideally matching condition. Hence, Eq. (2-5a)-(2-5d) can be alternatively expressed as

$$S_{51} = \frac{1}{4}e^{jP_{ME}} + \frac{1}{4}e^{jP_{EE}} + \frac{1}{4}e^{jP_{MM}} + \frac{1}{4}e^{jP_{EM}} \quad (2-7a)$$

$$S_{61} = \frac{1}{4}e^{jP_{ME}} - \frac{1}{4}e^{jP_{EE}} + \frac{1}{4}e^{jP_{MM}} - \frac{1}{4}e^{jP_{EM}} \quad (2-7b)$$

$$S_{71} = \frac{1}{4}e^{jP_{ME}} + \frac{1}{4}e^{jP_{EE}} - \frac{1}{4}e^{jP_{MM}} - \frac{1}{4}e^{jP_{EM}} \quad (2-7c)$$

$$S_{81} = \frac{1}{4}e^{jP_{ME}} - \frac{1}{4}e^{jP_{EE}} - \frac{1}{4}e^{jP_{MM}} + \frac{1}{4}e^{jP_{EM}} \quad (2-7d)$$

## 2.4 Coupling mechanisms of two-plane coupler

Upon initial inspection, equations (2-6a) to (2-6d) may not reveal straightforward information at first glance. However, by imposing specific conditions, these equations can provide valuable insights and become more informative. Through careful investigation, it becomes evident that there are three distinct coupling mechanism cases that can be applied to two-plane couplers. These cases will be individually and thoroughly discussed below, highlighting their unique characteristics and implications.

- ***Mechanism case 1***

When following condition is exerted,

$$P_{ME} + P_{EM} = P_{MM} + P_{EE} \quad (2-8)$$

From equation (2-8), two variables can be defined,

$$P_{EE} - P_{ME} = P_{EM} - P_{MM} = \Delta P_x \quad (2-9a)$$

$$P_{MM} - P_{ME} = P_{EM} - P_{EE} = \Delta P_y \quad (2-9b)$$

$$P_{EM} - P_{ME} = \Delta P_x + \Delta P_y \quad (2-9c)$$

Then equation (2-7) can be converted to

$$\begin{aligned} S_{51} &= \frac{1}{4} e^{\frac{1}{4}j(P_{ME}+P_{EM}+P_{EE}+P_{MM})} \left\{ e^{\frac{1}{2}j(P_{ME}-P_{EM})} + e^{\frac{1}{2}j(P_{EM}-P_{ME})} + e^{\frac{1}{2}j(P_{EE}-P_{MM})} \right. \\ &\quad \left. + e^{\frac{1}{2}j(P_{MM}-P_{EE})} \right\} \\ &= \frac{1}{4} e^{\frac{1}{2}j(P_{ME}+P_{EM})} \left\{ e^{-\frac{1}{2}j(\Delta P_x+\Delta P_y)} + e^{\frac{1}{2}j(\Delta P_x+\Delta P_y)} + e^{\frac{1}{2}j(\Delta P_x-\Delta P_y)} + e^{-\frac{1}{2}j(\Delta P_x-\Delta P_y)} \right\} \\ &= \frac{1}{2} e^{\frac{1}{2}j(P_{ME}+P_{EM})} \left\{ \cos\left(\frac{\Delta P_x + \Delta P_y}{2}\right) + \cos\left(\frac{\Delta P_x - \Delta P_y}{2}\right) \right\} \\ &= e^{\frac{1}{2}j(P_{ME}+P_{EM})} \cos\left(\frac{\Delta P_x}{2}\right) \cos\left(\frac{\Delta P_y}{2}\right) \end{aligned} \quad (2-10a)$$

$$\begin{aligned} S_{61} &= \frac{1}{4} e^{\frac{1}{2}j(P_{ME}+P_{EM})} \left\{ e^{-\frac{1}{2}j(\Delta P_x+\Delta P_y)} - e^{\frac{1}{2}j(\Delta P_x+\Delta P_y)} - e^{\frac{1}{2}j(\Delta P_x-\Delta P_y)} + e^{-\frac{1}{2}j(\Delta P_x-\Delta P_y)} \right\} \\ &= -\frac{j}{2} e^{\frac{1}{2}j(P_{ME}+P_{EM})} \left\{ \sin\left(\frac{\Delta P_x + \Delta P_y}{2}\right) + \sin\left(\frac{\Delta P_x - \Delta P_y}{2}\right) \right\} \\ &= -je^{\frac{1}{2}j(P_{ME}+P_{EM})} \sin\left(\frac{\Delta P_x}{2}\right) \cos\left(\frac{\Delta P_y}{2}\right) \end{aligned} \quad (2-10b)$$

$$\begin{aligned} S_{71} &= \frac{1}{4} e^{\frac{1}{2}j(P_{ME}+P_{EM})} \left\{ e^{-\frac{1}{2}j(\Delta P_x+\Delta P_y)} - e^{\frac{1}{2}j(\Delta P_x+\Delta P_y)} + e^{\frac{1}{2}j(\Delta P_x-\Delta P_y)} - e^{-\frac{1}{2}j(\Delta P_x-\Delta P_y)} \right\} \\ &= -\frac{j}{2} e^{\frac{1}{2}j(P_{ME}+P_{EM})} \left\{ \sin\left(\frac{\Delta P_x + \Delta P_y}{2}\right) - \sin\left(\frac{\Delta P_x - \Delta P_y}{2}\right) \right\} \\ &= -je^{\frac{1}{2}j(P_{ME}+P_{EM})} \cos\left(\frac{\Delta P_x}{2}\right) \sin\left(\frac{\Delta P_y}{2}\right) \end{aligned} \quad (2-10c)$$

$$\begin{aligned}
S_{81} &= \frac{1}{4} e^{\frac{1}{2}j(P_{ME}+P_{EM})} \left\{ e^{-\frac{1}{2}j(\Delta P_x+\Delta P_y)} + e^{\frac{1}{2}j(\Delta P_x+\Delta P_y)} - e^{\frac{1}{2}j(\Delta P_x-\Delta P_y)} - e^{-\frac{1}{2}j(\Delta P_x-\Delta P_y)} \right\} \\
&= \frac{1}{2} e^{\frac{1}{2}j(P_{ME}+P_{EM})} \left\{ \cos\left(\frac{\Delta P_x + \Delta P_y}{2}\right) - \cos\left(\frac{\Delta P_x - \Delta P_y}{2}\right) \right\} \\
&= -e^{\frac{1}{2}j(P_{ME}+P_{EM})} \sin\left(\frac{\Delta P_x}{2}\right) \sin\left(\frac{\Delta P_y}{2}\right) \quad (2-10d)
\end{aligned}$$

Equations (2-9a) to (2-9d) serve as a powerful representation of the coupling mechanism inherent in two-plane waveguide couplers with equivalence to the cascading of two vertically stacked H-plane couplers and two horizontally stacked E-plane couplers. The output phases of the two-plane coupler comparatively locate at  $0^\circ$ ,  $-90^\circ$ ,  $-90^\circ$  and  $180^\circ$ , and the coupling ratio of the varying output signals is manipulated by  $\Delta P_x$  and  $\Delta P_y$ , which presents the phase difference of the EE and MM boundaries-assigned quarter model compared with the ME boundaries-assigned quarter model.

The coupling ratio in the H-plane direction is

$$\frac{|S_{51}|}{|S_{61}|} = \frac{|S_{71}|}{|S_{81}|} = \cot\left(\frac{\Delta P_x}{2}\right) \quad (2-11)$$

While the coupling ratio in the E-plane direction is

$$\frac{|S_{51}|}{|S_{71}|} = \frac{|S_{61}|}{|S_{81}|} = \cot\left(\frac{\Delta P_y}{2}\right) \quad (2-12)$$

By adjusting values of  $\Delta P_x$  and  $\Delta P_y$ , the two-plane coupler can attain arbitrary proportion of signal splitting in principle. When two different two-plane couplers are defined by  $(\Delta P_{x1}, \Delta P_{y1})$  and  $(\Delta P_{x2}, \Delta P_{y2})$  to denote their coupling ratio in the transmission matrices separately as

$$T_1 = T(\Delta P_{x1}, \Delta P_{y1}) = \begin{pmatrix} \cos\left(\frac{\Delta P_{x1}}{2}\right)\cos\left(\frac{\Delta P_{y1}}{2}\right) & -j\sin\left(\frac{\Delta P_{x1}}{2}\right)\cos\left(\frac{\Delta P_{y1}}{2}\right) & -j\cos\left(\frac{\Delta P_{x1}}{2}\right)\sin\left(\frac{\Delta P_{y1}}{2}\right) & -\sin\left(\frac{\Delta P_{x1}}{2}\right)\sin\left(\frac{\Delta P_{y1}}{2}\right) \\ -j\sin\left(\frac{\Delta P_{x1}}{2}\right)\cos\left(\frac{\Delta P_{y1}}{2}\right) & \cos\left(\frac{\Delta P_{x1}}{2}\right)\cos\left(\frac{\Delta P_{y1}}{2}\right) & -\sin\left(\frac{\Delta P_{x1}}{2}\right)\sin\left(\frac{\Delta P_{y1}}{2}\right) & -j\cos\left(\frac{\Delta P_{x1}}{2}\right)\sin\left(\frac{\Delta P_{y1}}{2}\right) \\ -j\cos\left(\frac{\Delta P_{x1}}{2}\right)\sin\left(\frac{\Delta P_{y1}}{2}\right) & -\sin\left(\frac{\Delta P_{x1}}{2}\right)\sin\left(\frac{\Delta P_{y1}}{2}\right) & \cos\left(\frac{\Delta P_{x1}}{2}\right)\cos\left(\frac{\Delta P_{y1}}{2}\right) & -j\sin\left(\frac{\Delta P_{x1}}{2}\right)\cos\left(\frac{\Delta P_{y1}}{2}\right) \\ -\sin\left(\frac{\Delta P_{x1}}{2}\right)\sin\left(\frac{\Delta P_{y1}}{2}\right) & -j\cos\left(\frac{\Delta P_{x1}}{2}\right)\sin\left(\frac{\Delta P_{y1}}{2}\right) & -j\sin\left(\frac{\Delta P_{x1}}{2}\right)\cos\left(\frac{\Delta P_{y1}}{2}\right) & \cos\left(\frac{\Delta P_{x1}}{2}\right)\cos\left(\frac{\Delta P_{y1}}{2}\right) \end{pmatrix}$$

$$T_2 = T(\Delta P_{x2}, \Delta P_{y2}) = \begin{pmatrix} \cos\left(\frac{\Delta P_{x2}}{2}\right)\cos\left(\frac{\Delta P_{y2}}{2}\right) & -j\sin\left(\frac{\Delta P_{x2}}{2}\right)\cos\left(\frac{\Delta P_{y2}}{2}\right) & -j\cos\left(\frac{\Delta P_{x2}}{2}\right)\sin\left(\frac{\Delta P_{y2}}{2}\right) & -\sin\left(\frac{\Delta P_{x2}}{2}\right)\sin\left(\frac{\Delta P_{y2}}{2}\right) \\ -j\sin\left(\frac{\Delta P_{x2}}{2}\right)\cos\left(\frac{\Delta P_{y2}}{2}\right) & \cos\left(\frac{\Delta P_{x2}}{2}\right)\cos\left(\frac{\Delta P_{y2}}{2}\right) & -\sin\left(\frac{\Delta P_{x2}}{2}\right)\sin\left(\frac{\Delta P_{y2}}{2}\right) & -j\cos\left(\frac{\Delta P_{x2}}{2}\right)\sin\left(\frac{\Delta P_{y2}}{2}\right) \\ -j\cos\left(\frac{\Delta P_{x2}}{2}\right)\sin\left(\frac{\Delta P_{y2}}{2}\right) & -\sin\left(\frac{\Delta P_{x2}}{2}\right)\sin\left(\frac{\Delta P_{y2}}{2}\right) & \cos\left(\frac{\Delta P_{x2}}{2}\right)\cos\left(\frac{\Delta P_{y2}}{2}\right) & -j\sin\left(\frac{\Delta P_{x2}}{2}\right)\cos\left(\frac{\Delta P_{y2}}{2}\right) \\ -\sin\left(\frac{\Delta P_{x2}}{2}\right)\sin\left(\frac{\Delta P_{y2}}{2}\right) & -j\cos\left(\frac{\Delta P_{x2}}{2}\right)\sin\left(\frac{\Delta P_{y2}}{2}\right) & -j\sin\left(\frac{\Delta P_{x2}}{2}\right)\cos\left(\frac{\Delta P_{y2}}{2}\right) & \cos\left(\frac{\Delta P_{x2}}{2}\right)\cos\left(\frac{\Delta P_{y2}}{2}\right) \end{pmatrix} \quad (2-13)$$

Then their cascaded transmission matrix can be expressed as

$$T_{1-2} = T(\Delta P_{x1}, \Delta P_{y1})T(\Delta P_{x2}, \Delta P_{y2}) = T(\Delta P_{x1} + \Delta P_{x2}, \Delta P_{y1} + \Delta P_{y2}) = \begin{pmatrix} \cos\left(\frac{\Delta P_{x1} + \Delta P_{x2}}{2}\right)\cos\left(\frac{\Delta P_{y1} + \Delta P_{y2}}{2}\right) & -j\sin\left(\frac{\Delta P_{x1} + \Delta P_{x2}}{2}\right)\cos\left(\frac{\Delta P_{y1} + \Delta P_{y2}}{2}\right) & -j\cos\left(\frac{\Delta P_{x1} + \Delta P_{x2}}{2}\right)\sin\left(\frac{\Delta P_{y1} + \Delta P_{y2}}{2}\right) & -\sin\left(\frac{\Delta P_{x1} + \Delta P_{x2}}{2}\right)\sin\left(\frac{\Delta P_{y1} + \Delta P_{y2}}{2}\right) \\ -j\sin\left(\frac{\Delta P_{x1} + \Delta P_{x2}}{2}\right)\cos\left(\frac{\Delta P_{y1} + \Delta P_{y2}}{2}\right) & \cos\left(\frac{\Delta P_{x1} + \Delta P_{x2}}{2}\right)\cos\left(\frac{\Delta P_{y1} + \Delta P_{y2}}{2}\right) & -\sin\left(\frac{\Delta P_{x1} + \Delta P_{x2}}{2}\right)\sin\left(\frac{\Delta P_{y1} + \Delta P_{y2}}{2}\right) & -j\cos\left(\frac{\Delta P_{x1} + \Delta P_{x2}}{2}\right)\sin\left(\frac{\Delta P_{y1} + \Delta P_{y2}}{2}\right) \\ -j\cos\left(\frac{\Delta P_{x1} + \Delta P_{x2}}{2}\right)\sin\left(\frac{\Delta P_{y1} + \Delta P_{y2}}{2}\right) & -\sin\left(\frac{\Delta P_{x1} + \Delta P_{x2}}{2}\right)\sin\left(\frac{\Delta P_{y1} + \Delta P_{y2}}{2}\right) & \cos\left(\frac{\Delta P_{x1} + \Delta P_{x2}}{2}\right)\cos\left(\frac{\Delta P_{y1} + \Delta P_{y2}}{2}\right) & -j\sin\left(\frac{\Delta P_{x1} + \Delta P_{x2}}{2}\right)\cos\left(\frac{\Delta P_{y1} + \Delta P_{y2}}{2}\right) \\ -\sin\left(\frac{\Delta P_{x1} + \Delta P_{x2}}{2}\right)\sin\left(\frac{\Delta P_{y1} + \Delta P_{y2}}{2}\right) & -j\cos\left(\frac{\Delta P_{x1} + \Delta P_{x2}}{2}\right)\sin\left(\frac{\Delta P_{y1} + \Delta P_{y2}}{2}\right) & -j\sin\left(\frac{\Delta P_{x1} + \Delta P_{x2}}{2}\right)\cos\left(\frac{\Delta P_{y1} + \Delta P_{y2}}{2}\right) & \cos\left(\frac{\Delta P_{x1} + \Delta P_{x2}}{2}\right)\cos\left(\frac{\Delta P_{y1} + \Delta P_{y2}}{2}\right) \end{pmatrix} \quad (2-14)$$

Equation (2-14) reveals an important observation regarding the regulation for cascading two-plane couplers. It indicates that the coupling ratios of the cascaded couplers can be represented by a linear superposition of angles denoting their coupling ratio, which aligns with how H-plane or E-plane couplers are cascaded. This finding holds significant practical implications, particularly in cases where broadening the bandwidth of the two-plane coupler is desired or when eliminating undesired resonances or fluctuations within the operational bandwidth is necessary. When a two-plane coupler possesses a long coupled region area, typically associated with large  $(\Delta P_x, \Delta P_y)$  values, it becomes more prone to excite higher modes within the operational bandwidth abruptly. This can lead to unwanted fluctuations in the performance of the complete two-plane coupler's S-parameters. However, utilizing equation (2-14), it becomes possible to dismantle a two-plane coupler and replaced by cascading multiple shorter two-plane couplers. This approach results in a significant enhancement of the bandwidth performance.

By leveraging this insight, the bandwidth of the two-plane coupler can be effectively



broadened, and issues related to undesired resonances or fluctuations can be mitigated. This finding offers a practical solution to optimize the performance of two-plane couplers, enhancing their suitability for a wide range of applications.

In practical scenarios, a two-plane crossover can be effectively substituted by cascading two two-plane couplers with equal coupling ratios. This cascaded configuration offers the advantage of a significantly wider bandwidth compared to a single two-plane crossover. The use of multiple couplers in this arrangement allows for enhanced frequency response and improved performance across a broader range of frequencies. However, it is important to note that the connection of multiple two-plane couplers can introduce additional reflections in the system. This is a trade-off that needs to be carefully considered, taking into account the specific requirements of the application at hand.

- *Mechanism case 2*

The second mechanism case is based on below condition,

$$P_{ME} + P_{MM} = P_{EM} + P_{EE} \quad (2 - 15)$$

Then following variables could be defined,

$$P_{EE} - P_{ME} = P_{MM} - P_{EM} = \Delta P_x \quad (2 - 16a)$$

$$P_{EM} - P_{ME} = P_{MM} - P_{EE} = \Delta P_y \quad (2 - 16b)$$

$$P_{MM} - P_{ME} = \Delta P_x + \Delta P_y \quad (2 - 16c)$$

With same operation and computation with equation (2-10), the equation (2-7) can be induced to below

$$S_{51} = e^{\frac{1}{2}j(P_{ME}+P_{MM})} \cos\left(\frac{\Delta P_x}{2}\right) \cos\left(\frac{\Delta P_y}{2}\right) \quad (2 - 17a)$$

$$S_{61} = -e^{\frac{1}{2}j(P_{ME}+P_{MM})} \sin\left(\frac{\Delta P_x}{2}\right) \sin\left(\frac{\Delta P_y}{2}\right) \quad (2 - 17b)$$

$$S_{71} = -je^{\frac{1}{2}j(P_{ME}+P_{MM})} \cos\left(\frac{\Delta P_x}{2}\right) \sin\left(\frac{\Delta P_y}{2}\right) \quad (2-17c)$$

$$S_{81} = -je^{\frac{1}{2}j(P_{ME}+P_{MM})} \sin\left(\frac{\Delta P_x}{2}\right) \cos\left(\frac{\Delta P_y}{2}\right) \quad (2-17d)$$

From equation (2-16a) to (2-16d), the output distribution is different from equation (2-9). The output phases of the two-plane coupler comparatively locate at  $0^\circ$ ,  $180^\circ$ ,  $-90^\circ$  and  $-90^\circ$ . And the relationship among four output ports is

$$\frac{|S_{51}|}{|S_{81}|} = \frac{|S_{71}|}{|S_{61}|} = \cot\left(\frac{\Delta P_x}{2}\right) \quad (2-18)$$

And

$$\frac{|S_{51}|}{|S_{71}|} = \frac{|S_{81}|}{|S_{61}|} = \cot\left(\frac{\Delta P_y}{2}\right) \quad (2-19)$$

Meanwhile, same with two-plane coupler following mechanism case 1, the cascading of two-plane coupler following mechanism case 2 also abides by superposition of angle to denote their coupling ratio,

$$T_{1-2} = T(\Delta P_{x1}, \Delta P_{y1})T(\Delta P_{x2}, \Delta P_{y2}) = T(\Delta P_{x1} + \Delta P_{x2}, \Delta P_{y1} + \Delta P_{y2}) =$$

$$\begin{pmatrix} \cos\left(\frac{\Delta P_{x1} + \Delta P_{x2}}{2}\right) \cos\left(\frac{\Delta P_{y1} + \Delta P_{y2}}{2}\right) & -\sin\left(\frac{\Delta P_{x1} + \Delta P_{x2}}{2}\right) \sin\left(\frac{\Delta P_{y1} + \Delta P_{y2}}{2}\right) & -j \cos\left(\frac{\Delta P_{x1} + \Delta P_{x2}}{2}\right) \sin\left(\frac{\Delta P_{y1} + \Delta P_{y2}}{2}\right) & -j \sin\left(\frac{\Delta P_{x1} + \Delta P_{x2}}{2}\right) \cos\left(\frac{\Delta P_{y1} + \Delta P_{y2}}{2}\right) \\ -\sin\left(\frac{\Delta P_{x1} + \Delta P_{x2}}{2}\right) \sin\left(\frac{\Delta P_{y1} + \Delta P_{y2}}{2}\right) & \cos\left(\frac{\Delta P_{x1} + \Delta P_{x2}}{2}\right) \cos\left(\frac{\Delta P_{y1} + \Delta P_{y2}}{2}\right) & -j \sin\left(\frac{\Delta P_{x1} + \Delta P_{x2}}{2}\right) \cos\left(\frac{\Delta P_{y1} + \Delta P_{y2}}{2}\right) & -j \cos\left(\frac{\Delta P_{x1} + \Delta P_{x2}}{2}\right) \sin\left(\frac{\Delta P_{y1} + \Delta P_{y2}}{2}\right) \\ -j \cos\left(\frac{\Delta P_{x1} + \Delta P_{x2}}{2}\right) \sin\left(\frac{\Delta P_{y1} + \Delta P_{y2}}{2}\right) & -j \sin\left(\frac{\Delta P_{x1} + \Delta P_{x2}}{2}\right) \cos\left(\frac{\Delta P_{y1} + \Delta P_{y2}}{2}\right) & \cos\left(\frac{\Delta P_{x1} + \Delta P_{x2}}{2}\right) \cos\left(\frac{\Delta P_{y1} + \Delta P_{y2}}{2}\right) & -\sin\left(\frac{\Delta P_{x1} + \Delta P_{x2}}{2}\right) \sin\left(\frac{\Delta P_{y1} + \Delta P_{y2}}{2}\right) \\ -j \sin\left(\frac{\Delta P_{x1} + \Delta P_{x2}}{2}\right) \cos\left(\frac{\Delta P_{y1} + \Delta P_{y2}}{2}\right) & -j \cos\left(\frac{\Delta P_{x1} + \Delta P_{x2}}{2}\right) \sin\left(\frac{\Delta P_{y1} + \Delta P_{y2}}{2}\right) & -\sin\left(\frac{\Delta P_{x1} + \Delta P_{x2}}{2}\right) \sin\left(\frac{\Delta P_{y1} + \Delta P_{y2}}{2}\right) & \cos\left(\frac{\Delta P_{x1} + \Delta P_{x2}}{2}\right) \cos\left(\frac{\Delta P_{y1} + \Delta P_{y2}}{2}\right) \end{pmatrix} \quad (2-20)$$

- **Mechanism case 3**

The third mechanism case is based on below condition,

$$P_{ME} + P_{EE} = P_{EM} + P_{MM} \quad (2-21)$$

Then following variables can be defined,

$$P_{MM} - P_{ME} = P_{EE} - P_{EM} = \Delta P_x \quad (2-22a)$$

$$P_{EM} - P_{ME} = P_{EE} - P_{MM} = \Delta P_y \quad (2-22b)$$

$$P_{EE} - P_{ME} = \Delta P_x + \Delta P_y \quad (2-22c)$$

As a consequence, the equation (2-7) turns to be,

$$S_{51} = e^{\frac{1}{2}j(P_{ME}+P_{EE})} \cos\left(\frac{\Delta P_x}{2}\right) \cos\left(\frac{\Delta P_y}{2}\right) \quad (2-23a)$$

$$S_{61} = -je^{\frac{1}{2}j(P_{ME}+P_{EE})} \cos\left(\frac{\Delta P_x}{2}\right) \sin\left(\frac{\Delta P_y}{2}\right) \quad (2-23b)$$

$$S_{71} = -e^{\frac{1}{2}j(P_{ME}+P_{EE})} \sin\left(\frac{\Delta P_x}{2}\right) \sin\left(\frac{\Delta P_y}{2}\right) \quad (2-23c)$$

$$S_{81} = -je^{\frac{1}{2}j(P_{ME}+P_{EE})} \sin\left(\frac{\Delta P_x}{2}\right) \cos\left(\frac{\Delta P_y}{2}\right) \quad (2-23d)$$

From equation (2-22a) to (2-22d), the output distribution is also different from equation (2-9). The output phases of the two-plane coupler comparatively locate at  $0^\circ$ ,  $-90^\circ$ ,  $180^\circ$  and  $-90^\circ$ . And the relationship among four output ports is

$$\frac{|S_{51}|}{|S_{81}|} = \frac{|S_{61}|}{|S_{71}|} = \cot\left(\frac{\Delta P_x}{2}\right) \quad (2-24)$$

And

$$\frac{|S_{51}|}{|S_{61}|} = \frac{|S_{81}|}{|S_{71}|} = \cot\left(\frac{\Delta P_y}{2}\right) \quad (2-25)$$

Same with two-plane coupler following mechanism case 1 and 2, the cascading of two-plane coupler following mechanism case 3 also abides by superposition of angle to denote their coupling ratio,

$$\begin{aligned}
T_{1-2} &= T(\Delta P_{x1}, \Delta P_{y1})T(\Delta P_{x2}, \Delta P_{y2}) = T(\Delta P_{x1} + \Delta P_{x2}, \Delta P_{y1} + \Delta P_{y2}) = \\
&\begin{pmatrix} \cos\left(\frac{\Delta P_{x1} + \Delta P_{x2}}{2}\right) \cos\left(\frac{\Delta P_{y1} + \Delta P_{y2}}{2}\right) & -j \cos\left(\frac{\Delta P_{x1} + \Delta P_{x2}}{2}\right) \sin\left(\frac{\Delta P_{y1} + \Delta P_{y2}}{2}\right) & -\sin\left(\frac{\Delta P_{x1} + \Delta P_{x2}}{2}\right) \sin\left(\frac{\Delta P_{y1} + \Delta P_{y2}}{2}\right) & -j \sin\left(\frac{\Delta P_{x1} + \Delta P_{x2}}{2}\right) \cos\left(\frac{\Delta P_{y1} + \Delta P_{y2}}{2}\right) \\ -j \cos\left(\frac{\Delta P_{x1} + \Delta P_{x2}}{2}\right) \sin\left(\frac{\Delta P_{y1} + \Delta P_{y2}}{2}\right) & \cos\left(\frac{\Delta P_{x1} + \Delta P_{x2}}{2}\right) \cos\left(\frac{\Delta P_{y1} + \Delta P_{y2}}{2}\right) & -j \sin\left(\frac{\Delta P_{x1} + \Delta P_{x2}}{2}\right) \cos\left(\frac{\Delta P_{y1} + \Delta P_{y2}}{2}\right) & -\sin\left(\frac{\Delta P_{x1} + \Delta P_{x2}}{2}\right) \sin\left(\frac{\Delta P_{y1} + \Delta P_{y2}}{2}\right) \\ -\sin\left(\frac{\Delta P_{x1} + \Delta P_{x2}}{2}\right) \sin\left(\frac{\Delta P_{y1} + \Delta P_{y2}}{2}\right) & -j \sin\left(\frac{\Delta P_{x1} + \Delta P_{x2}}{2}\right) \cos\left(\frac{\Delta P_{y1} + \Delta P_{y2}}{2}\right) & \cos\left(\frac{\Delta P_{x1} + \Delta P_{x2}}{2}\right) \cos\left(\frac{\Delta P_{y1} + \Delta P_{y2}}{2}\right) & -j \cos\left(\frac{\Delta P_{x1} + \Delta P_{x2}}{2}\right) \sin\left(\frac{\Delta P_{y1} + \Delta P_{y2}}{2}\right) \\ -j \sin\left(\frac{\Delta P_{x1} + \Delta P_{x2}}{2}\right) \cos\left(\frac{\Delta P_{y1} + \Delta P_{y2}}{2}\right) & -\sin\left(\frac{\Delta P_{x1} + \Delta P_{x2}}{2}\right) \sin\left(\frac{\Delta P_{y1} + \Delta P_{y2}}{2}\right) & -j \cos\left(\frac{\Delta P_{x1} + \Delta P_{x2}}{2}\right) \sin\left(\frac{\Delta P_{y1} + \Delta P_{y2}}{2}\right) & \cos\left(\frac{\Delta P_{x1} + \Delta P_{x2}}{2}\right) \cos\left(\frac{\Delta P_{y1} + \Delta P_{y2}}{2}\right) \end{pmatrix} \\
&\hspace{15em} (2 - 26)
\end{aligned}$$

Among above-mentioned three coupling mechanism cases, only case 1 is corresponding to cascading of vertically-stacked H-plane coupler and horizontally-stacked E-plane coupler. The physical meaning of case 2 and case 3 are in all likelihood to be explained as cross-stacked couplers cascading with horizontally-stacked or vertically-stacked couplers. Even though it is not of practical significance, but it is expected to be meaningful and applicable in future applications.

## 2.5 Mode matching-FEM analysis

In preceding sections, an 8-port two-plane coupler is always analyzed by exclusively extracting its quarter 2-port model. And in most case, for a better performance, shape of coupled region is irregular shape, either a rectangular with several notches or just an irregular shape. As Fig.2.4(a) shows, normal electromagnetic simulator like HFSS adopting 3D-FEM as analyzer, are not proper to optimize two-plane coupler as there are a great deal of variables. Considering uniformity along the longitudinal direction of waveguide and just several discrete discontinuous planes as depicted in Fig.2.4(b), Mode matching-FEM is undoubtedly more superior by converting a 3-D model analysis into 2-D perspective, with less time consumed and better capabilities of targeted optimizations [2-6]. The theoretical fundamentals of FEM/MM hybrid calculation can be refer to the Appendix section of this dissertation.

In practical designing, to further diminish the complexity, in most cases, two-plane coupler will be additionally conceived symmetry about longitudinal direction, as such, totally three symmetry axes are authenticated to a two-plane model shown in Fig.2.5, also indicating exactly identical parameter and positions of input and output waveguides. As

a matter of this, only 1/8 of the complete two-plane model needs to be extracted to be analyzed with accompanied PEC or PMC boundaries at symmetrical plane “B” and “C”, and electrical performance of 1/4 model can be induced by directly cascading two back-to-back 1/8 model.

Overall, the analysis as well as optimization of two-plane coupler with additionally imposed symmetry about longitudinal direction are expounded in Fig.2.6, as four steps:

1. With given initial generation of parameters, including shape of coupled regions, position as well as dimension of input(output) waveguides, then performances of 1/8 model with in total 4 sorts of boundaries assigned at symmetrical planes can be analyzed in a way that 2-D FEM is capitalized to calculate eigen mode inside coupled region, and mode matching is utilized to compute connection between input(output) waveguide with coupled region.
2. With derived parameters of 1/8 model assigned with four sorts of boundaries, the S-parameter of 1/4 model can be deduced by directly connecting two back-to-back 1/8 models, through phase continuity condition at interface. This is a very fast calculation, which will decrease almost half of time compared with those two-plane couplers without symmetry in longitudinal directions.
3. With S-parameter of 1/4 model with 4 sorts of boundaries, the full S-parameters of complete two-plane coupler can be synthesized as Eq.(2-5).
4. Then the parameters together with performance of two-plane coupler will be undergoing evolutionary selection and elimination by Genetic algorithm to realize global optimization, until desired design is obtained.

## **2.6 Designing of a two-plane coupler with different coupling ratio in H-plane and E-plane directions**

This section will give a designing example of two-plane coupler following different coupling ratios in H-plane and E-plane directions. As emphasized in section 2.3,

compelled symmetry along longitudinal direction will significantly mitigate designing complexity, here without exception, this rule is also adopted in proposed two-plane coupler.

The proposed prototype of the two-plane coupler is depicted in Fig.2.7. This prototype exemplifies the design configuration that implements a coupling ratio of  $1:\sqrt{2}$  in the H-plane direction and  $\sqrt{2}:1$  in the E-plane direction, with the overall output coupling ratio being

$$|S_{51}|:|S_{61}|:|S_{71}|:|S_{81}| = \sqrt{2}:2:1:\sqrt{2} \quad (2 - 20)$$

The center frequency of the designed two-plane coupler has been established at 28.25GHz. However, it is important to note that the design can be theoretically converted to operate at any desired frequency by proportionally adjusting its dimensions. This flexibility allows for versatility and adaptability in different frequency applications. As highlighted in section 2.4, enforcing symmetry along the longitudinal direction of the coupler plays a pivotal role in simplifying the design complexity. In alignment with this principle, the two-plane coupler under consideration has been intentionally conceived with symmetry relative to the z-axis. This deliberate symmetry choice simplifies the optimization process by reducing the number of variables involved. Consequently, the output ports of the coupler exhibit identical physical dimensions, mirroring each other, as do the input ports. This deliberate symmetry ensures a balanced configuration and facilitates the optimization and analysis of the coupler's performance. By adopting this approach, the design process is streamlined and the overall complexity is mitigated, enabling more efficient and effective optimization.

To ensure optimal performance across the bandwidth, the input and output ports of the two-plane coupler are meticulously aligned with the single mode ( $TE_{10}$ ) condition. The coupled region of the two-plane coupler comprises five distinct points, including the coordinate origin. These points, along with their specific details, are illustrated in Fig. 2.7(c). The irregular-shaped design of the coupled region offers advantages over

conventional rectangular waveguides or ridged waveguides with regular notches or dislodgements. By incorporating this irregular shape, the coupler is better positioned to achieve the desired performance characteristics, particularly in enhancement of bandwidth.

Throughout the designing and optimization processes, it is imperative to consider certain restrictions imposed by fabrication technologies. One such restriction pertains to the position of the input or output waveguide, denoted as  $x_0$  and  $y_0$  in Fig.2.7 (c). It is crucial for these positions to surpass a threshold value in order to prevent the metal thickness from becoming excessively thin. This limitation is inherent to the fabrication technology and must be acknowledged. Furthermore, it is advisable to avoid incorporating sharp wedge shapes in the coupled region, as this would increase the complexity of the manufacturing process. Additionally, when employing a drill to shape the coupler, rounded fillets are naturally formed at each corner. These fillets should be taken into consideration when investigating their impact on the performance of the full two-plane coupler.

In the presence of the coupling ratio as equation (2-20), following phase restriction can be deduced

$$P_{EE} - P_{ME} = \Delta P_x = 2 \cot^{-1} \frac{1}{\sqrt{2}} \quad (2 - 21a)$$

$$P_{MM} - P_{ME} = \Delta P_y = 2 \cot^{-1} \sqrt{2} \quad (2 - 21b)$$

$$P_{EM} - P_{ME} = \Delta P_x + \Delta P_y = \pi \quad (2 - 21c)$$

In accordance with equation (2-21), a significant observation can be made regarding the transition phase between the EM boundary-assigned and ME boundary-assigned quarter sections, as that the transition phase of the EM boundary-assigned section is in an out-of-phase relationship with the ME boundary-assigned section. This phase relationship holds true when the coupling ratios in both the H-plane and E-plane directions are reciprocal.

Fig.2.8 demonstrates the transition characteristics of the proposed quarter model (shown in Fig.2.7(b)) when assigned with four different types of boundaries. The analysis focuses on the amplitude, reflection, and relative phase behavior compared to the ME boundary-assigned section within the frequency range of 27GHz to 29.5GHz. From Fig.2.8(a), it can be observed that  $|S_{21}^{EE}|$ ,  $|S_{21}^{MM}|$ , and  $|S_{21}^{EM}|$  tend to approach the 0dB level, indicating an excellent lossless condition. This corresponds to their reflections,  $|S_{11}^{EE}|$ ,  $|S_{11}^{MM}|$ , and  $|S_{11}^{EM}|$ , being suppressed below -15dB. On the other hand,  $|S_{21}^{ME}|$  exhibits an adverse trend starting from 29.0GHz and experiences a sharp decline around 29.5GHz, resulting in a loss of more than 0.5dB. This behavior aligns with  $|S_{11}^{ME}|$  exceeding -15dB at the same frequency. Furthermore, the relative phase of the EE, MM, and EM quarter models closely approaches their respective ideal values of  $109.5^\circ$ ,  $70.5^\circ$ , and  $180^\circ$ , as defined by equation (2-21). This close alignment validates the matching characteristics of the quarter models against the desired phase values.

Fig.2.9 showcases a photograph of the fabricated two-plane coupler, manufactured using high-precision CNC (Computer Numerical Control) technology. The coupler body is constructed using three separate blocks, comprising the coupled region and two straightforward waveguide blocks. The blocks are meticulously assembled using screws, ensuring a secure and stable structure. Two coaxial-waveguide transformers are assembled in order to impel VNA measurements.

Fig.2.10 illustrates the S-parameters of the fabricated two-plane coupler across a bandwidth ranging from 27.0GHz to 29.5GHz, which corresponds to an 8.85% fractional bandwidth, in terms of the output amplitudes, reflections, and phase differences over Port 5, counterpart to incidence from Port 1. To ensure accurate measurements, post-operation calibration has been conducted to eliminate the insertion loss of the transformers used in the measurement setup. Detailed information on the calibration process can be referred to the Appendix section of this dissertation.

The measured results, as shown in Fig.2.10, generally align well with the simulation results, with a few discrepancies observed. Notably, there is a sharp dip around 28.8GHz



in the measured  $S_{41}$  parameter. Additionally, the measured  $S_{81}$  parameter deviates from the simulated  $S_{81}$  by approximately 2dB at 27.5GHz. These discrepancies can be attributed to fabrication and assembly errors, as well as uncertainties in the measurement process. The degradation observed in  $S_{51}$  and  $S_{81}$  close to 29.5GHz can be attributed to the corresponding deterioration of  $|S_{21}^{ME}|$  at that frequency, as depicted in Fig.2.8(a). Overall, both the simulation and measurement results demonstrate reflections below -15dB, power imbalance within 2dB, and phase deviations of at most 20 degrees. While these results may not be considered perfect, they are sufficient to validate and demonstrate the concept of a two-plane coupler following arbitrary coupling ratios in the H-plane and E-plane directions. Moreover, it is worth noting that the performance of the two-plane coupler can potentially be further enhanced by introducing multiple segments of the coupled regions, as discussed in [2-4]. This offers a potential avenue for improving the performance and expanding the capabilities of the coupler design.

To accentuate the advantages of the two-plane coupler in terms of size reduction compared to the conventional approach of concatenating vertically-stacked H-plane couplers with horizontally-stacked E-plane couplers, Fig.2.11 presents design examples of one-plane couplers. In order to ensure a fair and meaningful comparison, these one-plane couplers are designed with the same dimensions for the input and output waveguides as the two-plane coupler depicted in Fig.2.7. In Fig.2.11(a), the H-plane coupler is configured with a  $1:\sqrt{2}$  coupling ratio, while in Fig.2.11(b), the E-plane coupler follows a  $\sqrt{2}:1$  coupling ratio, both operating within the 28.25GHz band. Consequently, cascading two vertically-stacked H-plane couplers as depicted in Figure Fig.2.11(a) with two horizontally-stacked E-plane couplers as shown in Figure Fig.2.11(b) will result in the same functionality as the proposed two-plane coupler.

If we focus solely on the coupled region and exclude the input and output waveguides, the miniaturization rate of the two-plane coupler compared to the cascading of a conventional H-plane coupler with an E-plane coupler in terms of longitudinal length can be calculated as follows:

$$m = 1 - \frac{L_T}{L_H + L_E} = 58.4\% \quad (2 - 22)$$

Where  $L_T$ ,  $L_H$  and  $L_E$  represent the length of the coupled region of the two-plane coupler, H-plane coupler and E-plane coupler, respectively. Meanwhile, the ratio of volumetric downsizing can be calculated as,

$$n = 1 - \frac{v_T}{2(v_H + v_E)} = 50.1\% \quad (2 - 23)$$

Where  $v_T$ ,  $v_H$  and  $v_E$  correspond to the volume of the coupled region of the two-plane coupler, H-plane coupler and E-plane coupler. Both  $m$  and  $n$  will demonstrate the significant downsizing effect achieved by the two-plane coupler design. It is noteworthy that normal connection should be introduced among the cascaded H-plane coupler and E-plane coupler to suppress higher modes and maintain the dominance of the TE<sub>10</sub> mode. As a matter of this, the miniaturization ratio represented by  $m$  and  $n$  can be further increased. The S-parameters of above two models are provided in Fig.2.12. Overall, it could be perceived that cascading of one-plane couplers will manifest flatter imbalance over the considered bandwidth, by setting aside the resonance close to 29.5GHz. However, two-plane coupler possesses lower reflection and isolations, which can be reflected on insertion loss all under 0.1dB, while cascading of one-plane couplers showcase more than 0.2dB loss. Even though the effect to suppress insertion loss by a single two-plane coupler is not obvious, but considering for a vast beam-switching matrix network, the reflection can be superimposed, as such, the lower insertion loss by two-plane coupler over cascading of one-plane couplers is still meaningful.

## 2.7 Conclusion Remarks

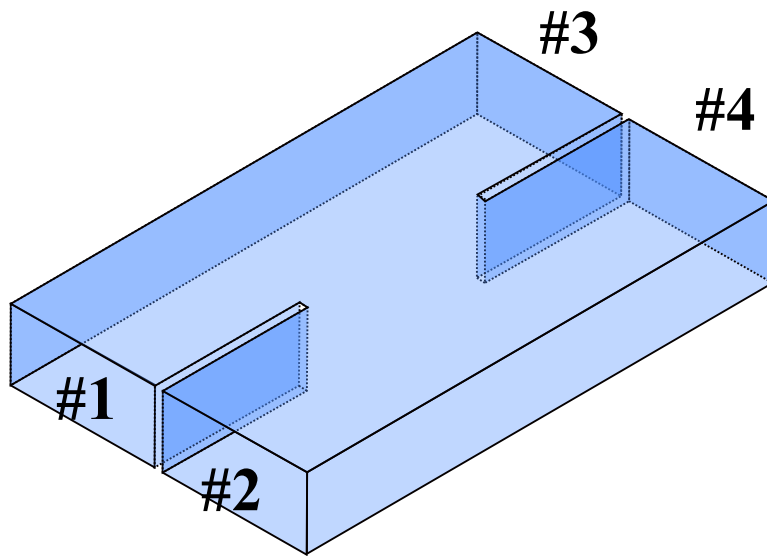
This chapter has successfully accomplished the theoretical analysis of the two-plane coupler, which complies with arbitrary coupling ratios in the H-plane and E-plane directions. Equation (2-7) is unveiled as the core equation governing the coupling mechanism of the two-plane coupler. In addition to the coupling mechanism enabling equivalence with cascaded H-plane and E-plane couplers, two other coupling

mechanisms are introduced, laying the foundation for future explorations and developments. To validate the proposed theoretical analysis, a specific two-plane coupler operating at 28.25GHz is designed and measured. This coupler follows a  $\sqrt{2}:2:1:\sqrt{2}$  coupling ratio, which can be dismantled into  $1:\sqrt{2}$  in the H-plane direction and  $\sqrt{2}:1$  in the E-plane direction. The performance of this two-plane coupler is evaluated through simulation and measurement, covering a frequency range from 27GHz to 29.5GHz with an 8.85% fractional bandwidth. Throughout the entire bandwidth, reflections are effectively suppressed below -15dB, the deviation in output amplitude is kept within 2dB, and phase digressions remain below 20 degrees. This study marks the first proposal of a two-plane coupler operating with different coupling ratios in the H-plane and E-plane directions. Furthermore, future works can explore the potential enhancement of performance by incorporating multiple coupled regions, as discussed in [2-4].

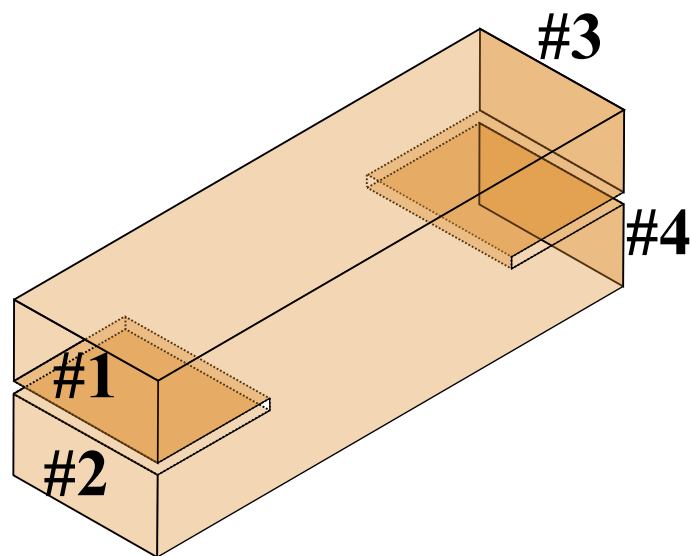
Additionally, design samples of an H-plane coupler and an E-plane coupler are provided, which, when cascaded, achieve equivalence to the proposed two-plane coupler. A comparison is made between cascaded one-plane couplers and the two-plane coupler in terms of performance, size, and volume. The two-plane coupler exhibits an impressive downsizing rate, with a reduction of 58.4% in length and 50.1% in volume compared to the cascaded one-plane couplers. While the cascaded one-plane couplers show flatter imbalance, they also exhibit higher reflections and subsequent insertion loss compared to the two-plane coupler.

The theoretical analysis presented in this chapter establishes the foundation for the utilization of two-plane couplers with arbitrary coupling ratios in the H-plane and E-plane directions. It is anticipated that two-plane couplers will play an increasingly crucial role in the miniaturization of 2-D hollow waveguide beam-switching matrices, and thus expanding application of 2-D hollow-waveguide-based beam-switching matrices.

Overall, this chapter contributes valuable insights into the theoretical analysis, design, and potential applications of two-plane couplers. The findings pave the way for further research and advancements in the field of waveguide technology.



(a)



(b)

**Fig. 2.1.** One-plane coupler. (a) H-plane coupler. (b) E-plane couler

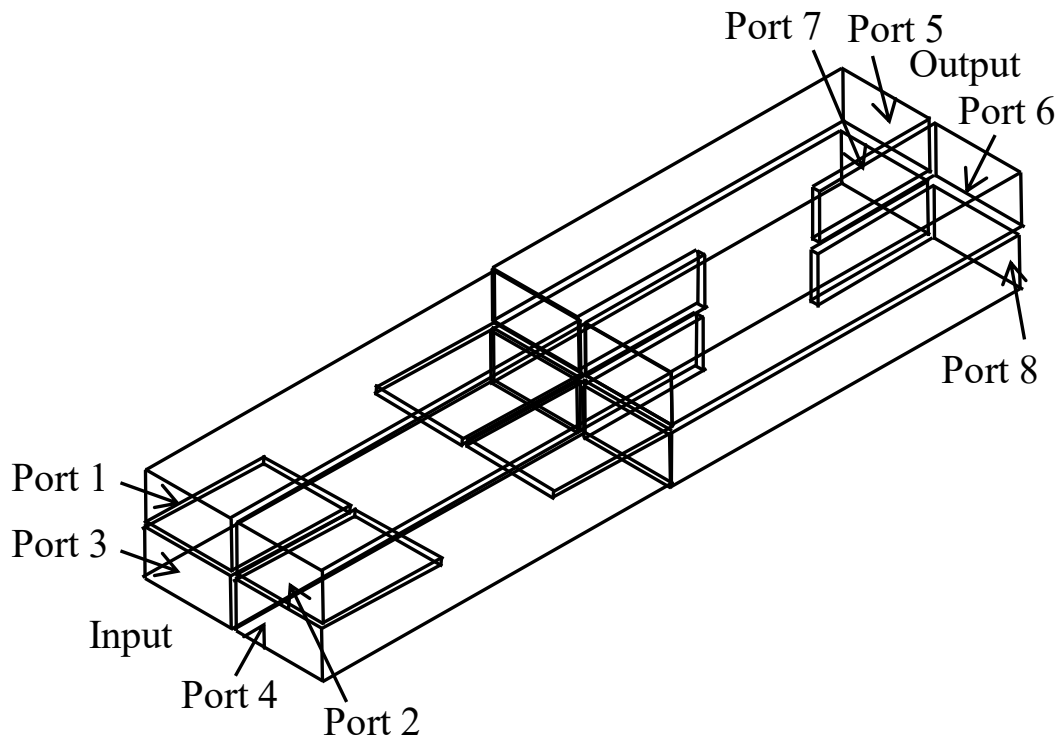


**Fig. 2.2.** Cascading of H-plane and E-plane couplers

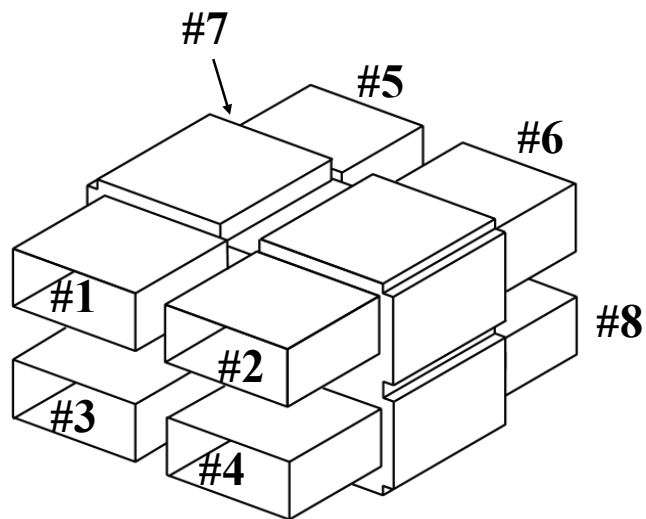
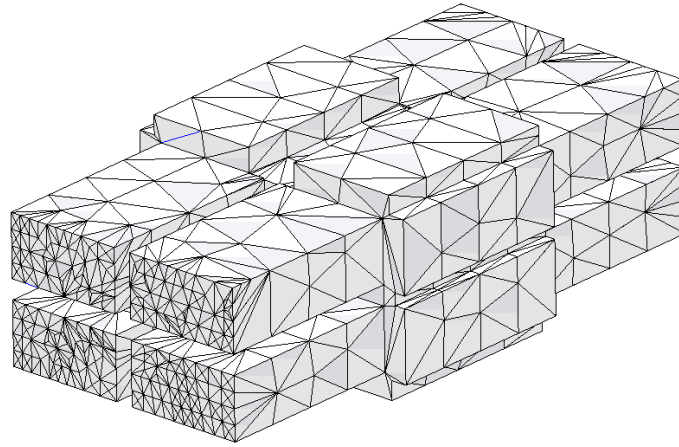
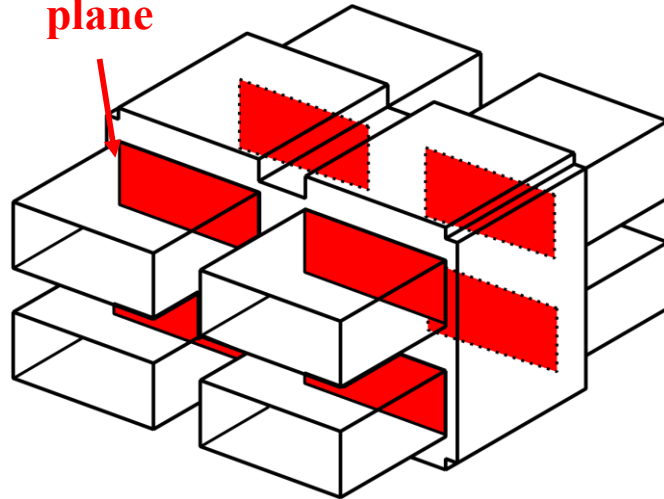


**Fig. 2.3.** Normal configuration of a two-plane coupler.



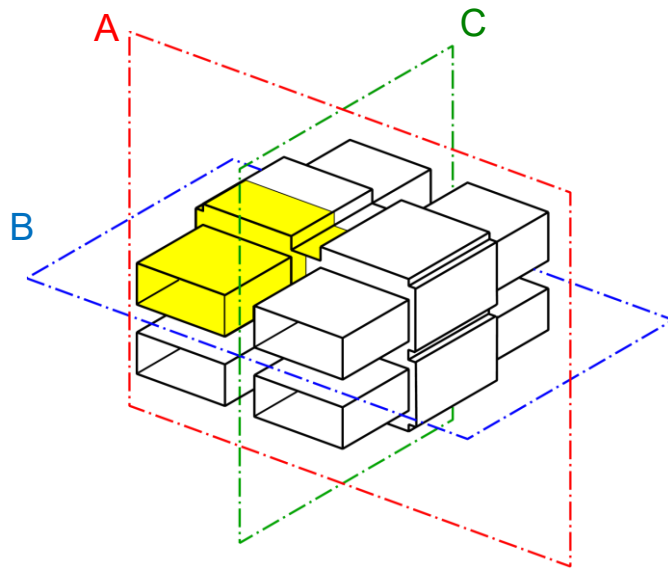
(a)

**Discontinuous  
plane**

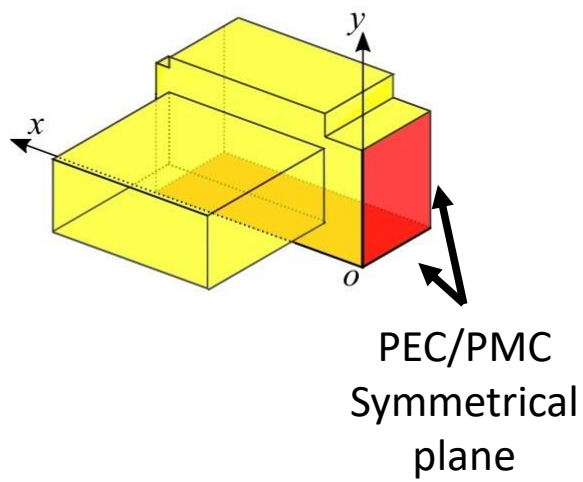


(b)

**Fig. 2.4.** (a) 3-D mesh for 3-D FEM analysis in HFSS. (b) Two-dimensionalized perspective of two-plane coupler model.



(a)



(b)

**Fig. 2.5.** (a) Symmetrical plane of two-plane coupler with additionally imposed symmetry in longitudinal direction. (b) 1/8 model of two-plane coupler.

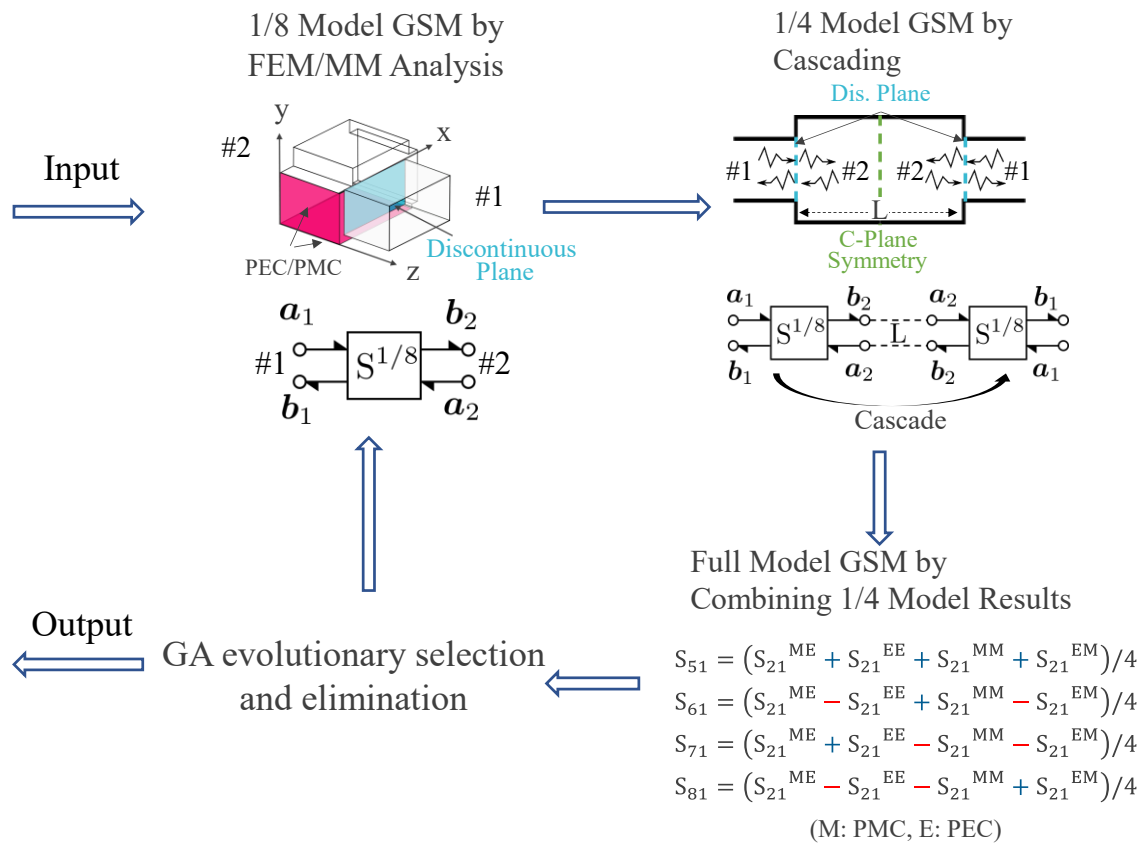
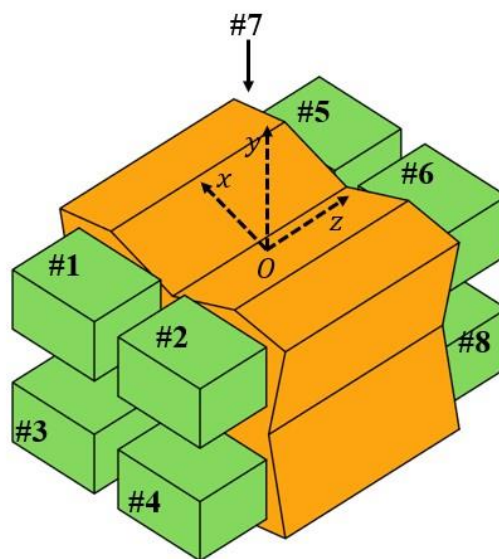
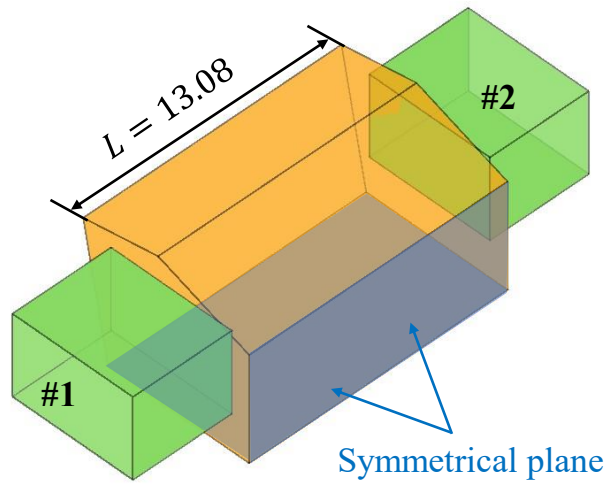


**Fig. 2.6.** Step-by-step analysis and optimization of two-plane coupler with imposed symmetry in longitudinal direction.

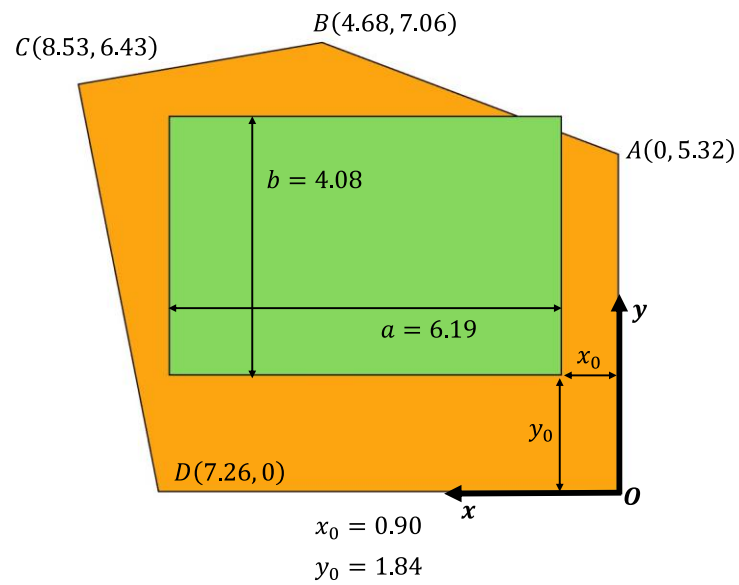


(a) Side view of the full model.



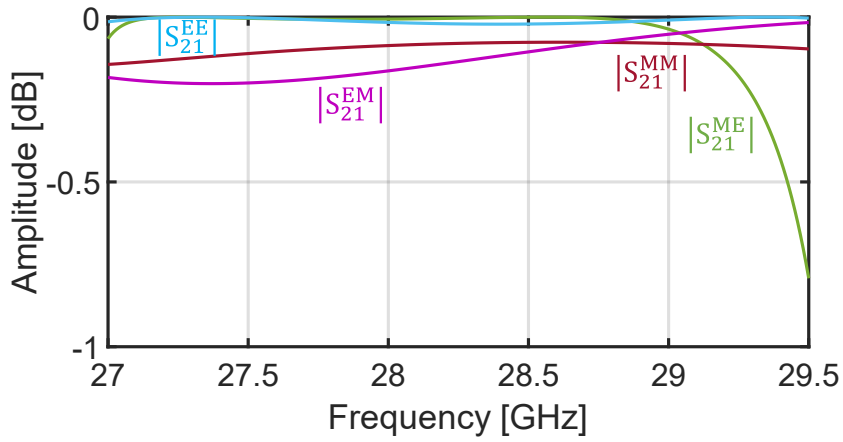


(b) Perspective view of the quarter model in the first quadrature.

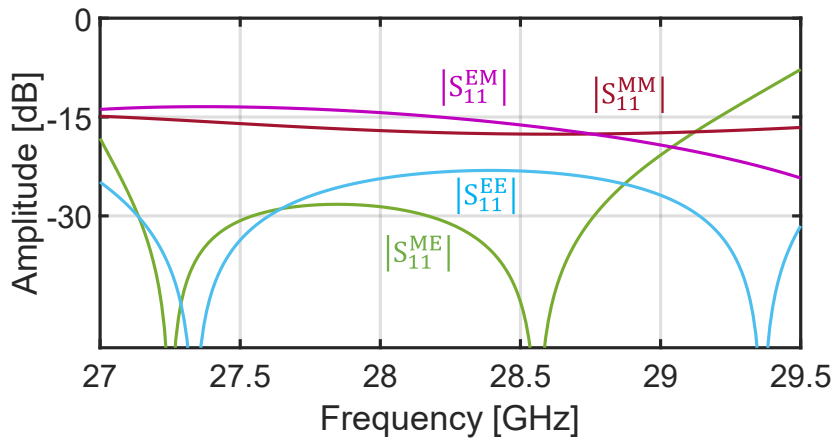


(c) Cross section of the quarter model.

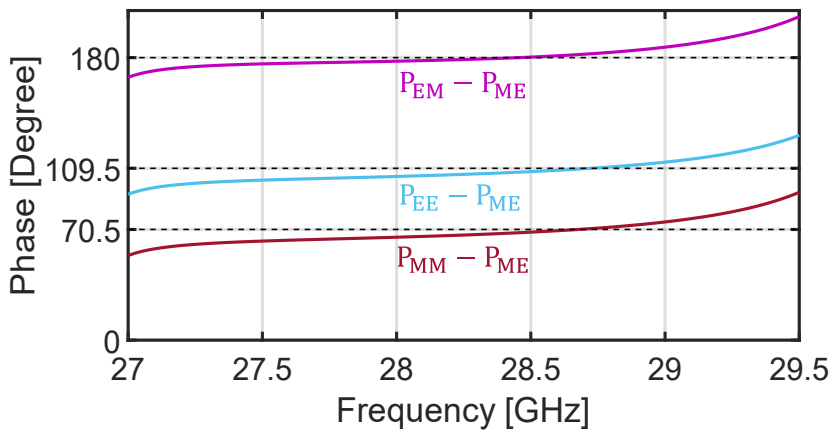
**Fig. 2.7.** Two-plane coupler model. Unit: mm.



(a) Amplitude

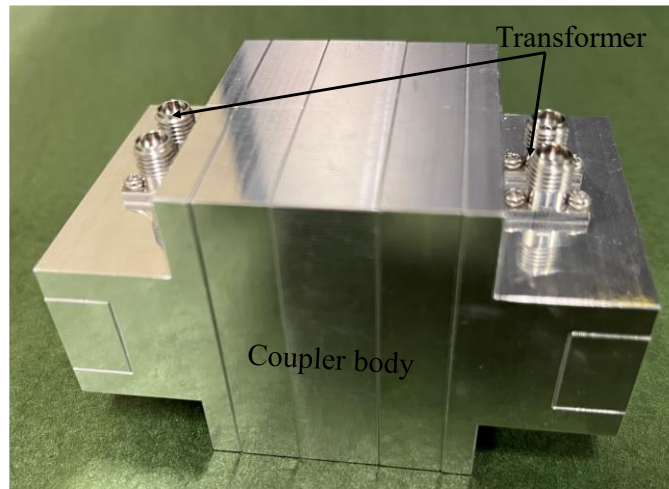


(b) Reflection

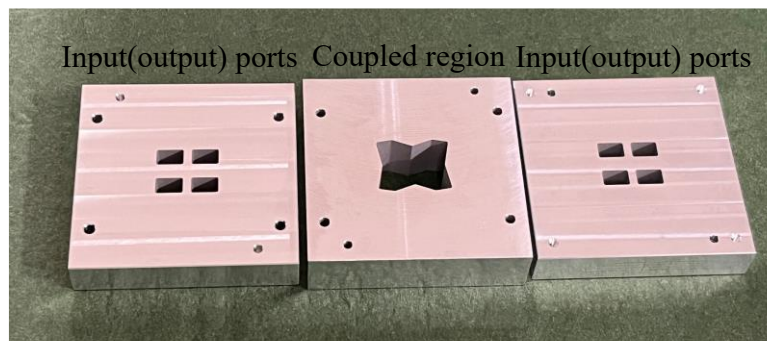


(c) Relative phase against the ME boundary-assigned quarter section.

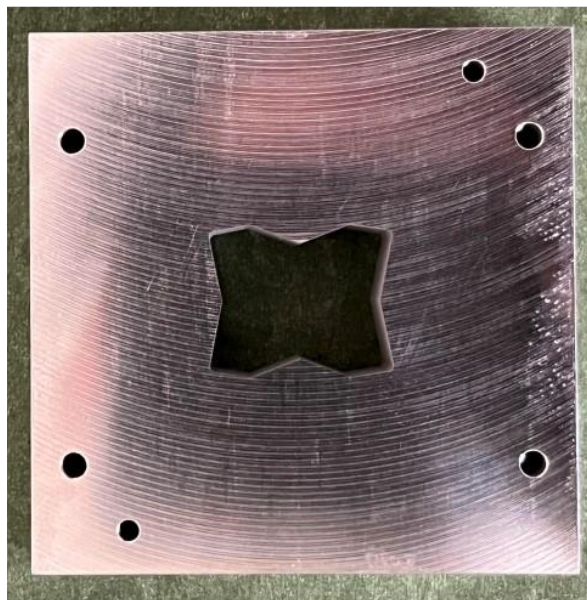
**Fig. 2.8.** Transition of the quarter model assigned with different boundaries.



(a)

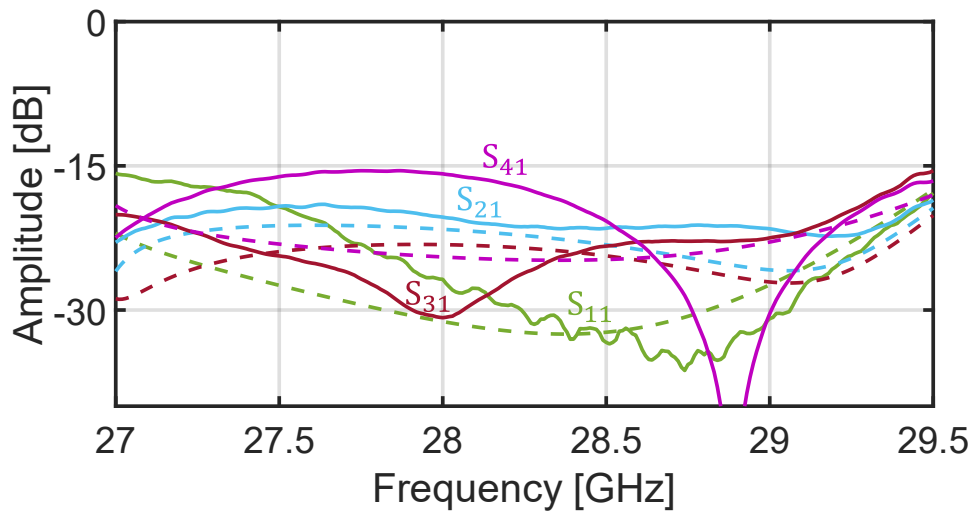


(b)

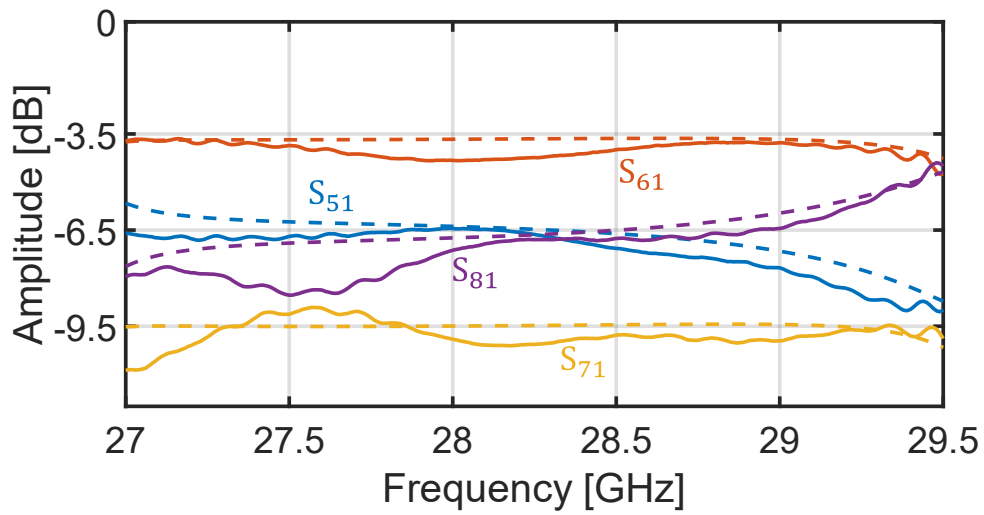


(c)

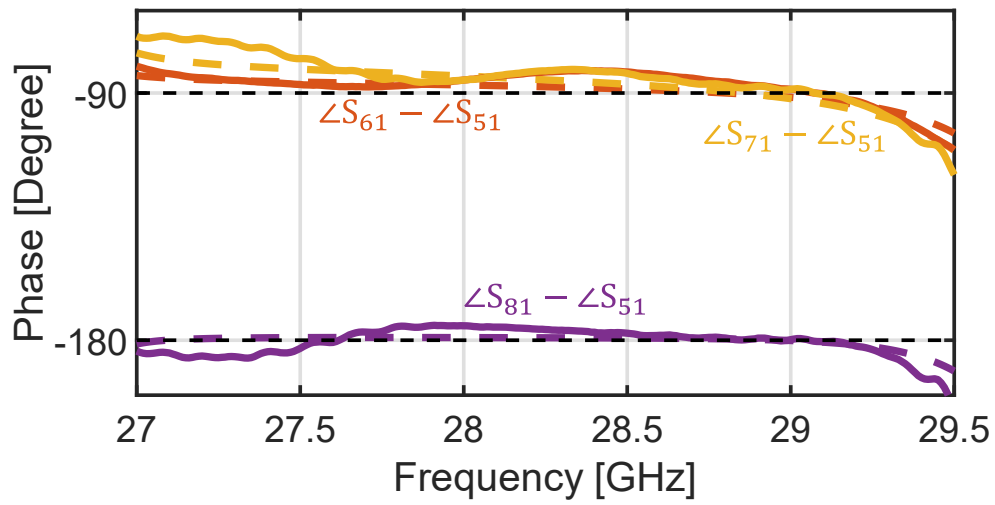
**Fig. 2.9.** Photographs of the manufactured two-plane coupler. (a) Overall structure including two transformers. (b) Three segments of coupler body. (c) Cross section of the coupled region.



(a) Reflection.

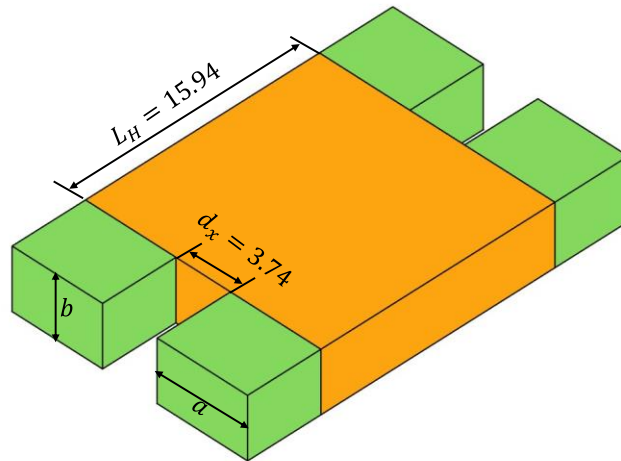


(b) Output amplitudes.

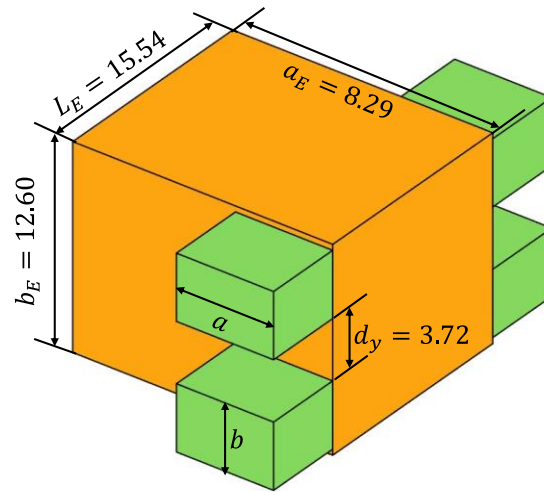


(c) Phase differences compared with Port 5.

**Fig. 2.10.** S-parameters of the proposed two-plane coupler corresponding to incidence from Port 1. Solid lines: Measurement results. Dotted lines: Simulation results.

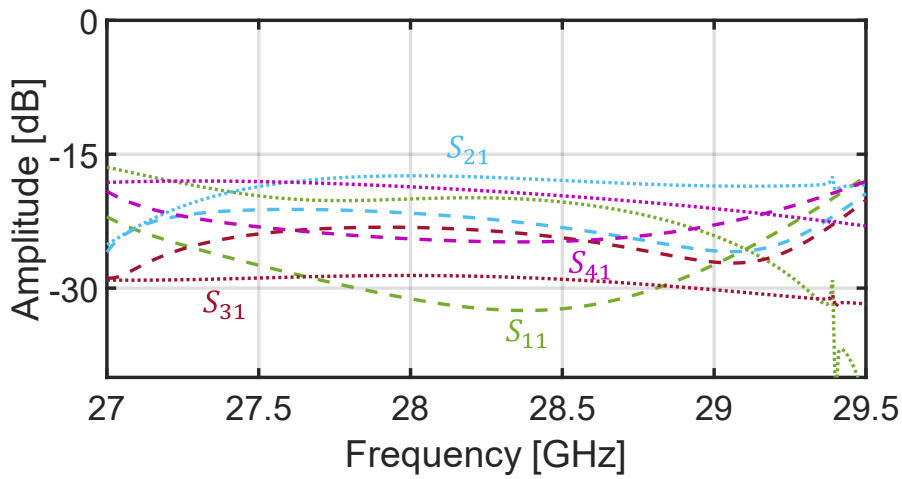


(a) H-plane coupler with a  $1:\sqrt{2}$  coupling ratio.



(b) E-plane coupler with a  $\sqrt{2}:1$  coupling ratio.

**Fig. 2.11.** Designing samples of conventional one-plane couplers working at 28.25GHz possessing identical dimension of input or output waveguide with proposed two-plane coupler. Unit: mm.



(a) Reflections

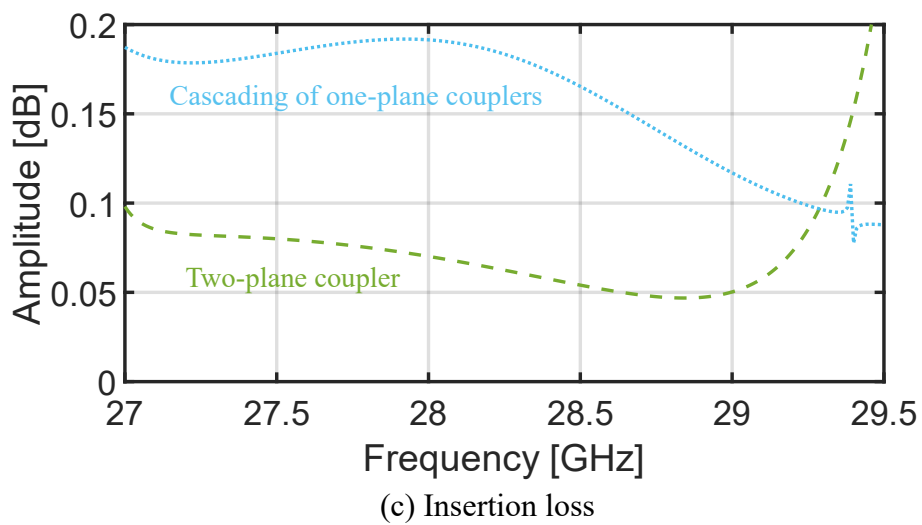
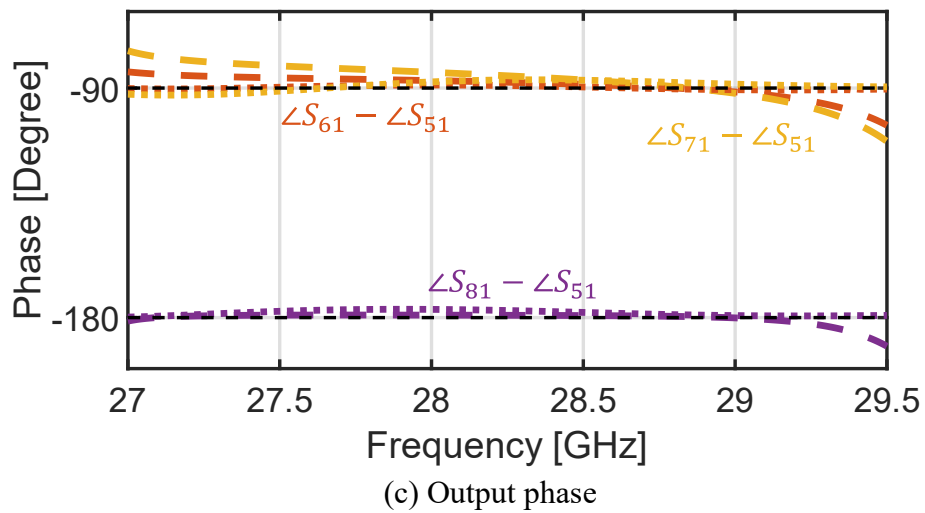
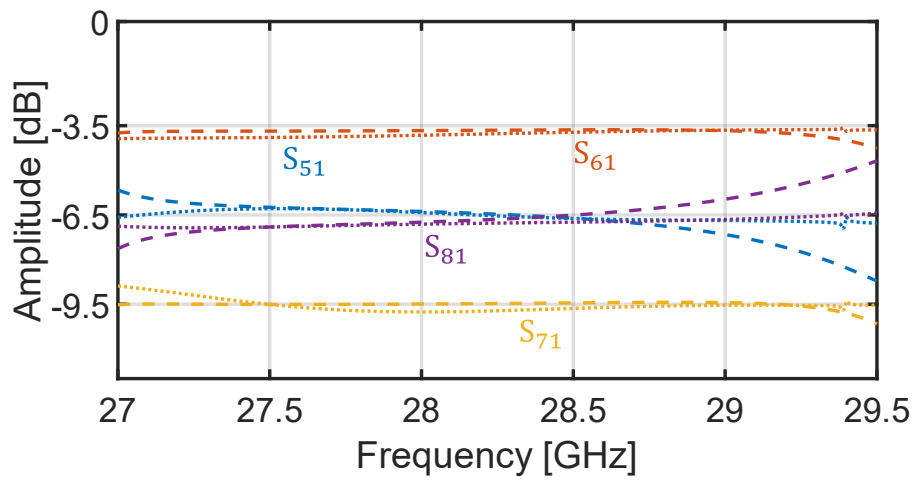


**Fig. 2.12.** Comparison between two-plane coupler and cascaded one-plane couplers.

## References

- [2-1] D.-H. Kim, J. Hirokawa, and M. Ando, "Design of waveguide shortslot two-plane couplers for one-body 2-D beam-switching Butler matrix application," *IEEE Trans. Microw. Theory Techn.*, vol. 64, no. 3, pp. 776–784, Mar. 2016.
- [2-2] D.-H. Kim, J. Hirokawa, and M. Ando, "One-body 2-D Beam-switching Butler Matrix with Waveguide Short-slot 2-plane Couplers," *IEICE Trans. Electron.*, vol. E100-C, no.10, pp.-, Oct. 2017.
- [2-3] T. Tomura, D. -H. Kim, M. Wakasa, Y. Sunaguchi, J. Hirokawa and K. Nishimori, "A 20-GHz-Band 64×64 Hollow waveguide Two-Dimensional Butler Matrix," *IEEE Access*, vol. 7, pp. 164080-164088, 2019.
- [2-4] S. Chen, T. Tomura, J. Hirokawa, K. Ito, M. Suga, Y. Shirato, D. Uchida, and N. Kita, "Design for Operation in Two Frequency Bands by Division of the Coupled Region in a Waveguide 2-Plane Coupler," *IEICE Trans. Commun.*, vol. E105-C, No.12, pp.729-739, Dec. 2022.
- [2-5] J. Hirokawa and N. J. G. Fonseca, "Generalized one-dimensional parallel switching matrices with an arbitrary number of beams," *IEEE J. Microwaves*, vol. 1, no. 4, pp. 975-988, Oct. 2021.
- [2-6] M. Wakasa, D.-H. Kim, T. Tomura, and J. Hirokawa, "Wideband Design of a Short-Slot 2-Plane Coupler by the Mode Matching/FEM Hybrid Analysis considering the Structural Symmetry," *IEICE Trans. Commun.*, vol. E102-B, No.5, pp.1019-1026, May 2019.



# Chapter 3 Two-dimensional One-body 3×3-way Hollow-waveguide Nolen Matrix using Two-plane Couplers

## 3.1 Introductory remarks

This chapter presents the proposal of a two-dimensional (2-D) one-body 3×3-way hollow-waveguide Nolen matrix operating from 27.65 GHz to 28.85 GHz, corresponding to a 4.1% fractional bandwidth. The novelty of this project lies in being the first to propose a 2-D one-body beam-switching matrix with a number of beams other than  $2^n$ , differing from Butler matrix. Additionally, it introduces the utilization of a two-plane unequal division coupler in the matrix configuration, which adds to its uniqueness. The chapter provides a comprehensive overview of the diagram and working principle of the entire 2-D 3×3-way Nolen matrix, which comprises two-plane couplers, an H-plane coupler, E-plane couplers, and phase shifters. The reflection and port-to-port isolation coefficients of this 2-D 3×3-way Nolen matrix, as well as the realized gain, are verified through measurements with the output ports directly radiating into free space.

The simulation results reveal that the maximum insertion loss of the 2-D 3×3-way Nolen matrix is 0.86 dB, while the maximum power imbalance is 2.5 dB, both within the operating bandwidth. The maximum realized gain, measured at the boresight beam, is 15.5 dBi, closely aligned with the simulated value of 15.7 dBi. The minimum realized gain, observed for Beam 6, which represents a 2-D tilted beam at an angle of 42 degrees with respect to the boresight, is 12.0 dBi with a scan loss of 3.5 dB in the measurements. The simulated minimum realized gain is 12.7 dBi, obtained for Beam 9 at an angle of 36 degrees with respect to the boresight, with a 3 dB scan loss.

The matrix demonstrates significant superiority in terms of low insertion loss when compared to state-of-the-art designs. The chapter concludes by discussing future perspectives and potential improvements for the 2-D 3×3-way Nolen matrix, exploring possibilities for enhancing its performance and capabilities.

### 3.2 1-D 3-way Nolen matrix

The Nolen matrix, as described in references [3-1] and [3-2], stands out for its ability to accommodate any integer number of beams. This is in stark contrast to the Butler matrix [3-3], which is limited to a port number that is  $2^n$ . In a Nolen matrix, there are  $n(n+1)/2$  nodes, each consisting of a quadrature coupler and a phase shifter. Unlike the independent signal paths of the Butler matrix, multiple signals in a Nolen matrix converge at a node, undergo vector superposition, and then exit the node as a combined signal. Due to this nature, the Nolen matrix is often considered to be mechanically narrowband. However, the fact that the Nolen matrix supports a diverse range of beam numbers gives it significant practical applications, even in situations where the Butler matrix would not suffice. This versatility makes the Nolen matrix an attractive choice for various applications that require a non-power-of-2 number of beams.

In reference [3-4], a new generalized 1-D beam-switching matrix was introduced, expanding the realm of possibilities for 1-D beam-switching matrices. This innovative concept allows for greater flexibility and versatility in designing 1-D beam-switching matrices. Specifically, when the beam number is set to 3, the configuration of the matrix aligns with that of a standard parallel 3-way Nolen matrix, as depicted in Fig.3.1. Supposing the phase differences between adjacent output ports, when considering incidence from Ports 1, 2, and 3, as  $\varphi_1$ ,  $\varphi_2$ , and  $\varphi_3$ , respectively, and taking into account the properties of a lossless 6-port network as discussed in reference [3-5], the following restrictions can be derived,

$$1 + e^{j(\varphi_2 - \varphi_1)} + e^{j2(\varphi_2 - \varphi_1)} = 0 \quad (3-1a)$$

$$1 + e^{j(\varphi_3 - \varphi_1)} + e^{j2(\varphi_3 - \varphi_1)} = 0 \quad (3-1b)$$

When  $\varphi_2 \neq \varphi_3$ , equation (3-1) will give,

$$\varphi_2 - \varphi_1 = \pm 2\pi/3 \quad (3-2a)$$

$$\varphi_3 - \varphi_1 = \mp 2\pi/3 \quad (3-2b)$$

In observation of incidence from Port 1 and progressive phase difference prescription:  $\angle S_{51} - \angle S_{41} = \angle S_{61} - \angle S_{51}$ , the following constraint needs to be satisfied:

$$\theta_2 = \theta_3 \quad (3-3)$$

Table 3.1 presents all six permutations of port assignments for the phase shifters  $\theta_1$  and  $\theta_2$  or  $\theta_3$ . These assignments result in one of the phase differences, denoted as  $\varphi_1$ ,  $\varphi_2$ , and  $\varphi_3$  in radians, being 0, while the other two phase differences are  $-2\pi/3$  and  $2\pi/3$ , respectively. It is important to note that one particular set of parameters corresponds to a phase shifter that introduces no relative phase difference. This simplifies the corresponding layer in the matrix configuration, offering a more streamlined and efficient design.

### 3.3 Configuration of 2-D 3×3-way Nolen matrix

Based on the introduction of the 1-D 3-way Nolen matrix in Section 3.2, the construction of the 2-D 3×3-way Nolen matrix follows a three-step procedure, as described in reference [3-6].

Step 1: The first step involves connecting vertically-stacked H-plane 1-D 3-way matrices with horizontally-stacked E-plane 1-D 3-way matrices. This establishes the initial framework of the 2-D matrix.

Step 2: The second step capitalizes on the commutativity between the H-plane and E-plane components, allowing for the interchange of their sequences and cascading. This results in the consecutive concatenation of the H-plane couplers with the E-plane couplers. Additionally, the phase shifters in two dimensions are merged.

Step 3: In the final step, the two vertically-stacked H-plane couplers and two horizontally-stacked E-plane couplers are combined into a two-plane coupler. This integration completes the construction of the 2-D 3×3-way Nolen matrix.

These three steps can be applied to construct 2-D beam-switching matrices that are

originally composed of 1-D beam-switching matrices. The schematic diagram of the retrofitted 2-D 3×3-way Nolen matrix is presented in Fig.3.2. It is worth noting that, due to the theoretical distribution of phase shifters at  $0^\circ$ , one layer of phase shifters can be omitted in the selected port assignment, resulting in a reduction of the entire matrix to only five layers, with the 1st and 4th layers being identical.

The 1<sup>st</sup>, 2<sup>nd</sup>, and 4<sup>th</sup> layers of the 2-D 3×3-way Nolen matrix consist of H-plane couplers, E-plane couplers, and two-plane couplers. The 1<sup>st</sup> and 4<sup>th</sup> layers consist of two-plane couplers that divide the output power equally. In contrast, the two-plane coupler in the 2nd layer provides an output division ratio of  $1:\sqrt{2}:\sqrt{2}:2$ . The phase shifters in the 3<sup>rd</sup> and 5<sup>th</sup> layers are assigned angles of  $0^\circ$ ,  $90^\circ$ , and  $180^\circ$  relative to a designated reference port at each layer and these phase shifters should additionally compensate for the transition phase of the couplers they are connecting to, as the premise that no transition phases are introduced to each coupler model.

The overall matrix configuration comprises 9 input ports and 9 output ports, as indicated in Fig.3.2. Incidence from Port 1 generates a boresight beam, while Ports 2, 3, 4, and 7 correspond to 1-D tilted beams, Ports 5, 6, 8, and 9 provide 2-D tilted beams with respect to the main axes of the array. To further illustrate the behavior of the matrix, Fig.3.3 presents the ideal signals obtained at the output of each layer, including both amplitude and phase information. In this illustration, a unitary input signal is applied to Ports 1 and 5 as examples. The signal propagates through the couplers and phase shifters of each layer, resulting in its division into 9 signals of identical amplitude at the output ports of the 5th layer. Incidence from Port 1 results in all outputs being in phase, corresponding to a boresight beam. Conversely, incidence from Port 5 yields output signals with a phase difference of  $-2\pi/3$  between adjacent ports in the two orthogonal directions, creating a 2-D tilted beam scenario.

### 3.4 Design of constituent two-plane coupler

Different from the two-plane coupler proposed in Chapter.2, the two-plane couplers

deployed in this 2-D 3×3-way Nolen matrix adopts normal rectangular shape with several notches, which is deemed simpler than the two-plane coupler with arbitrary shape of coupled region, also less hardware-cost considering fabrication.

The diagram of the proposed two-plane coupler working from 27.65 GHz to 28.85 GHz, covering the working bandwidth of 2-D 3×3-way Nolen matrix, is depicted in Fig. 3.4. The coupler is symmetric along the three main axes. It comprises four input and four output rectangular waveguide ports and a ridge-shaped coupling region. The input and output ports are required to satisfy single-mode condition throughout the operating frequency band. The ridge-shape coupling region including three notches, and dimensions as well as the position of input and output waveguides, are purposely designed to achieve desired output amplitude and phase distributions.

Fig.3.4 illustrates the diagram of the proposed two-plane coupler, designed to operate within the frequency range of 27.65 GHz to 28.85 GHz, matching the working bandwidth of the 2-D 3×3-way Nolen matrix. Exactly same with the design of two-plane coupler in Chapter.2, imposing symmetry about the z-axis can reduce the number of variables in the design process and thereby decrease complexity. It consists of four input and four output rectangular waveguide ports, along with a ridge-shaped coupling region. To ensure optimal functionality, the input and output ports are carefully designed to satisfy the single-mode condition across the entire operating frequency band. The ridge-shaped coupling region, featuring three notches as well as dimensions and positioning of the input and output waveguides, is specifically designed in line with target performance.

It won't be difficult to perceive that coupling ratio of two-plane coupler along two orthogonal directions employed in this 2-D 3×3-way Nolen matrix are identical, as it is originally composed by H-plane and E-plane couplers with same coupling ratios in two orthogonal directions as well. Based on (2-10)-(2-12), the coupling mechanism of the two-plane coupler following identical coupling ratio in H-plane and E-plane directions can be obtained as,

$$P_{MM} = P_{EE} = \frac{P_{ME} + P_{EM}}{2} \quad (3-4)$$

As a consequence, equations (2-7) can be converted as,

$$S_{51} = \frac{1}{2} e^{j\left(\frac{P_{ME}+P_{EM}}{2}\right)} \left\{ 1 + \cos\left(\frac{P_{EM}-P_{ME}}{2}\right) \right\} \quad (3-5a)$$

$$S_{61} = S_{71} = \frac{-j}{2} e^{j\left(\frac{P_{ME}+P_{EM}}{2}\right)} \sin\left(\frac{P_{EM}-P_{ME}}{2}\right) \quad (3-5b)$$

$$S_{81} = \frac{-1}{2} e^{j\left(\frac{P_{ME}+P_{EM}}{2}\right)} \left\{ 1 - \cos\left(\frac{P_{EM}-P_{ME}}{2}\right) \right\} \quad (3-5c)$$

The amplitude ratios of the outputs, namely  $S_{51}$ ,  $S_{61}$ ,  $S_{71}$ , and  $S_{81}$ , are determined by three distinct function curves that are dependent on the angular variable  $(P_{EM} - P_{ME})/2$ . Remarkably, regardless of the specific combinations of these output signals, they consistently fulfill the following criteria:

$$|S_{61}|^2 = |S_{71}|^2 = |S_{51}||S_{81}| \quad (3-6)$$

Fig. 3.5 illustrates the variation of the three dependent curves as a function of  $(P_{EM} - P_{ME})/2$  over the full period from 0 to  $2\pi$ . When  $(P_{EM} - P_{ME})/2$  is equal to  $\pi/2$  and  $\pi$ , the resulting transmission coefficients correspond to an equal division hybrid coupler and a crossover, respectively. To realize the  $1:\sqrt{2}:\sqrt{2}:2$  output division, which corresponds to Point B, the following constraint needs to be satisfied:

$$\cos\left(\frac{P_{EM}-P_{ME}}{2}\right) = -\frac{1}{3} \quad (3-7)$$

Taking the two-plane coupler in 2<sup>nd</sup> layer of entire configuration of 2-D 3×3-way Nolen matrix in Fig. 3.2 as an example, its physical parameters are presented in Table.3.2, corresponding to the quarter model in Fig.3.4(b)(c).

In Fig.3.6(a), the amplitude transmission coefficients of the proposed quarter coupler under different boundary conditions (ME, EE, MM, and EM) at the symmetry planes are presented. These coefficients demonstrate low insertion losses, all below 0.3 dB, indicating efficient power transfer. The reflection coefficients, shown in Figure 3.6(b),

are almost entirely suppressed, with values below -15 dB, indicating excellent impedance matching. Fig.3.6(c) showcases the relative phases of the quarter coupler model assigned with EE, MM, and EM boundary conditions, with reference to the model assigned with ME boundary conditions. According to (3-4), relative phases should follow the expression,

$$P_{EE} - P_{ME} = P_{MM} - P_{ME} = \frac{P_{EM} - P_{ME}}{2} \quad (3-8)$$

Fig. 3.6(c) reveals that  $P_{EE}$  and  $P_{MM}$  exhibit nearly identical values across the considered frequency range. Additionally, the phase differences  $P_{EE} - P_{ME}$  and  $P_{MM} - P_{ME}$  closely approximate  $109.5^\circ$ , which corresponds to the  $\arccos(-1/3)$  angle measurement in degrees, all of which are well aligned with (3-8). The optimization process of this two-plane unequal division coupler is performed using Finite Element Method (FEM) - Mode Matching computations, as described in Chapter 2 and referenced in [3-7]. The FEM approach is employed to calculate the eigenmodes within the non-rectangular coupled region, enabling a comprehensive understanding of the electromagnetic behavior in this specific geometry. On the other hand, mode matching techniques are utilized to establish the connection between the input or output waveguides and the coupled region. This combination of FEM and mode matching computations ensures accurate analysis and optimization of the two-plane coupler's performance characteristics.

The performance of the proposed two-plane unequal division coupler is evaluated through the S-parameters corresponding to incidence from Port 1, as shown in Fig. 3.7. Across the frequency bandwidth of 27.65 GHz to 28.85 GHz, which corresponds to a fractional bandwidth of 4.1%, the coupler exhibits satisfactory performance based on the desired criteria outlined in [3-8]. The deviation of amplitudes from the theoretical values remains within  $\pm 0.5$  dB, indicating accurate power transfer. The reflections and isolations between input ports are all effectively suppressed below -15 dB, ensuring excellent impedance matching. Moreover, the phase differences of each output port

relative to Port 5 do not exceed  $\pm 10^\circ$ , signifying consistent phase behavior.

While the bandwidth of the proposed two-plane coupler in this design is limited, it still serves as a significant step towards realizing a 2-D one-body hollow-waveguide Nolen matrix. This configuration represents an advancement over previously reported designs that rely on the more conventional approach of two orthogonal stacks of 1-D matrices [3-9], [3-10]. Ongoing related developments has indicate potential future bandwidth enhancements for the two-plane coupler. Notably, Ref. [3-8] demonstrates the realization of a two-plane coupler with a single bandwidth of 7.3%, as well as two-plane couplers with dual bandwidths of 6.3% and 2.2% by incorporating multiple segments of the coupled region with arbitrary shapes in the couplers. These advancements open up exciting possibilities for further improving the performance and bandwidth capabilities of the two-plane coupler in this 2-D  $3 \times 3$ -way Nolen matrix.

Utilizing the same design approach as the unequal division two-plane coupler, the physical dimensional parameters of the quarter model for the two-plane coupler with equal output division, which is employed in the 1<sup>st</sup> and 4<sup>th</sup> layers of Fig. 3.2, are presented in Table II(B).

### **3.5 Design of constituent one-plane coupler**

The complete 2-D  $3 \times 3$ -way Nolen matrix depicted in Fig. 3.2 consists of three H-plane couplers and three E-plane couplers, each with a coupling ratio of 1:1 or  $1:\sqrt{2}$ . Since all quadrature couplers possess symmetrical structures, they can be represented by half models, as illustrated in Fig. 3.8. However, it should be noted that the symmetrical axis differs between the H-plane coupler, which is symmetrical about the vertical axis, and the E-plane coupler, which is symmetrical about the horizontal axis.

The physical parameters of all quadrature couplers are listed in Table 3.3. The electrical performance of the 1<sup>st</sup>, 2<sup>nd</sup>, and 4<sup>th</sup> layers is illustrated in Fig. 3.9. Since the 1<sup>st</sup>, 2<sup>nd</sup>, and 4<sup>th</sup> layers in Fig. 3.2 consist solely of multiple couplers, the electrical performance of these layers precisely reflects the characteristics of the designed couplers in their respective layers.



### 3.6 Design of waveguide phase shifters

Phase shifter is two-ports component to acting as a phase overrun or retard, counterpart to inductive phase shifters and capacitive phase shifters, respectively. In beam-switching matrices, often the absolute phase output does not make any sense, but the relative one will work out.

The schematic diagrams of both capacitive and inductive phase shifters employed in the 2-D 3×3-way Nolen matrix are presented in Fig. 3.10. It is important to note that the phase shifters not only provide the desired phase shifting values but also compensate for the transmission phase of the couplers they are connected to. Therefore, the phase shifting values indicated as  $0^\circ$ ,  $90^\circ$ , and  $180^\circ$  in Fig. 3.2 can function as both progressive (inductive) phase shifters and laggy (capacitive) phase shifters.

The capacitive phase shifter design incorporates an expanded broad side area ( $w_{PS} > a_i$ ) and utilizes several irises placed across the broad wall. On the other hand, the inductive phase shifter design features a shortened broad side area ( $w_{PS} < a_i$ ) and employs irises positioned along the side walls. Various parameters, including the length ( $l_{PS}$ ) of the phase shifter, the number ( $n$ ) of irises, the length ( $t_{PS}$ ) and depth ( $r_{PS}$ ) of the irises, and the distance ( $d_{PS}$ ) between the irises, can be adjusted to achieve the desired phase shifting value.

To simplify the design process and reduce the number of variables, the phase shifters are intentionally designed with longitudinal symmetry. This approach ensures that the performance optimization of the phase shifters can be achieved effectively. Mode-matching techniques are utilized to fine-tune the performance of the phase shifters, which consist of only a few segments with a normal rectangular cross-section.

### 3.7 Experimental results of 2-D 3×3-way Nolen matrix

Fig. 3.11 provides a comprehensive view of the 3-D inner waveguide cavities within the proposed 2-D 3 × 3-way Nolen matrix, offering additional insights into the interconnection between various components depicted in Fig. 3.2. To ensure smooth connectivity, oblique waveguides are employed to connect adjacent layers. Furthermore,

measures have been taken to suppress higher modes in the input/output ports of each component, ensuring the dominance of the TE<sub>10</sub> mode with a suppression level below -40 dB. The introduction of oblique waveguides to connect input ports with the 1st layer does not have any significant impact on the overall matrix performance in terms of phase difference. However, it is essential to compensate for the phase imbalance introduced by other oblique waveguides using the phase shifters in the 3rd and 5th layers. Notably, the oblique waveguides connecting the 1st and 2nd layers are intentionally designed to avoid introducing additional phase imbalance. In order to accommodate the constraints imposed by the milling drill during the fabrication process, certain rounded edges have been incorporated into the components. These rounded edges have been carefully examined and verified to have no discernible impact on the matrix's performance. It is worth mentioning that the radius of the drill used in this particular manufacturing process is 0.3 mm, which is significantly smaller than the size of each component.

Fig. 3.12 showcases the manufactured 2-D 3×3-way Nolen matrix, complete with a transformer, which facilitates the transition from a coaxial line to a waveguide for testing purposes. The fabrication process involved milling several individual aluminum plates to match the shape of the inner waveguide cavities, followed by assembling these plates together using screws. The transformer, specifically designed with 8×8 ports, allows for compatibility with matrices requiring a greater number of ports. In the case of the 2-D 3×3-way Nolen matrix, only 9 ports are utilized out of the transformer's full capacity. For the coaxial line to waveguide transition at 28.25 GHz, a schematic representation and dimensional parameters are provided in Fig. 3.13 and Table 3.4, respectively. Notably, a three-stage ridged waveguide transition is employed to effectively suppress any reflections that may arise during the transition process.

The fabricated 2-D 3×3-way Nolen matrix boasts an impressive complete matrix body, measuring 60.0 mm × 60.0 mm × 241.3 mm, which includes the additional transition connecting the output waveguides of the transformer to the input waveguides of the matrix. With a weight of 2.55 kg, the matrix showcases its robust construction. Delving into its design, the 2-D 3×3-way Nolen matrix incorporates a meticulous 6.9 mm element

spacing between adjacent output ports ( $a \times b = 5.78 \text{ mm} \times 2.47 \text{ mm}$ ) across two transverse dimensions. This spacing translates to approximately  $0.65\lambda$  at the center frequency of 28.25 GHz, accompanied by a total aperture size of  $2.1\lambda \times 1.28\lambda$ . These precise dimensions demonstrate the meticulous attention to detail in the construction of the matrix. Compared to the conventional symmetrical 2-D Butler matrix, the proposed 2-D 3×3-way Nolen matrix diverges from symmetry along the transverse axes. As a consequence, the integration of numerous oblique waveguides becomes essential to connect the constituent components. This departure from symmetry contributes to the slightly larger physical dimensions of the matrix body when juxtaposed with a previously reported 2-D one-body Butler matrix of a similar size [3-11]. Nevertheless, it is crucial to acknowledge that the larger dimensions are not a limitation of the concept itself but rather a consequence of the chosen mechanical design approach, employing multiple plates. Future advancements in manufacturing techniques, such as the utilization of 3D printing [3-12], hold promise for offering enhanced design flexibility and the potential for even further refinements in the construction of such matrices.

The simulation results of the complete 18-port matrix are beautifully displayed in Fig. 3.14, offering insights into the performance when incidence is applied from Port 1, Port 4, and Port 9. These examples correspond to the boresight beam, a 1-D tilted beam, and a 2-D tilted beam, respectively. The results showcase the output amplitude, reflection, and phase difference with reference to Port 10, unveiling the matrix's remarkable capabilities. Upon closer examination of Fig. 3.14, it becomes evident that the deviation of the output signal amplitude from the theoretical value of -9.54 dB remains within a range of 1.9 dB for all ports. Only a small portion of the frequency band, near 27.65 GHz, sees  $S_{17,4}$  slightly extend the range to 2.5 dB, approaching a value near -12 dB. However, such deviations are minimal and do not significantly impact the overall performance. Remarkably, the reflections and isolations from the input ports are impressively suppressed below -15 dB across the bandwidth, ensuring excellent signal integrity. The only exception is  $S_{59}$ , which slightly exceeds this criterion in the higher half of the operating bandwidth, reaching -13 dB at 28.85 GHz. Nonetheless, this value remains well

within acceptable limits for the intended applications. When considering insertion loss, the largest value is observed from Port 9, spanning the entire bandwidth at 0.86 dB. It is noteworthy that this includes the contribution from conductor loss, which accounts for 0.50 dB of the total. This insight allows for a comprehensive assessment of the matrix's performance in terms of signal attenuation. Turning our attention to the relative transmission phases with reference to Port 10, the outputs from Port 11 to Port 18 demonstrate remarkable adherence to the theoretical standard values. These values hover around  $0^\circ$ ,  $-120^\circ$ , and  $-240^\circ$ , with digressions of no more than  $\pm 30^\circ$  over the analyzed bandwidth. This exceptional phase consistency further highlights the matrix's reliability and precision in achieving the desired beam-switching capabilities. In summary, the exemplary simulation results portrayed in Fig. 3.14 unveil the impressive performance of the 18-port matrix, showcasing its ability to deliver accurate output amplitudes, excellent reflections and isolations, minimal insertion loss, and consistent transmission phases.

When the device is directly radiating from the output ports, it transforms into a 9-port network, which undergoes simulation and measurement to validate its performance. To ensure a fair comparison with the simulated data, post-processing techniques are employed to eliminate the impact of the coaxial line to waveguide transformer. Fig. 3.15 presents exemplary results, showcasing both the simulated and measured data, for incidence from Port 1 to Port 9.

The overall agreement between the measurement results and simulation results is commendable. In most cases, the reflection and isolation levels remain below the -10 dB threshold, providing confidence in the device's performance, except for  $S_{74}$ ,  $S_{84}$  and  $S_{59}$  which marginally go above -10 dB over the considered frequency bandwidth. However, discrepancies are observed in Fig. 3.15 compared to the reflection and isolation results shown in Fig. 3.14. This can be attributed to two primary factors. Firstly, the direct radiating output ports are not perfectly matched to free space, which is a known limitation associated with open-ended waveguides. This imperfection can contribute to some degradation in the reflection and isolation levels. Secondly, the dominant factor affecting

performance degradation is the strong coupling between adjacent output ports with a spacing of  $0.65\lambda$ . Particularly, there is significant coupling among the ports aligned along the direction of the electrical field of the  $TE_{10}$  mode. This strong port-to-port coupling leads to an ascending in reflection and isolation at the input ports. Despite these degradation factors, the observed levels are still considered acceptable for the intended applications. The advantages of having closely-spaced elements outweigh the minor impairment in the grating lobes level. It is important to note that these factors do not significantly hinder the overall performance of the device and its suitability for the target applications.

To thoroughly examine the radiation capabilities of the proposed 2-D  $3\times 3$ -way Nolen matrix, a series of far field measurements is conducted using a spherical scanner, as illustrated in Fig. 3.16. In this setup, the output aperture of the matrix directly radiates into free space without any additional antennas being used as loads. To evaluate the realized gain, the measured data is meticulously processed with respect to a standard gain horn antenna. During the measurement setup, the distance between the output aperture of the matrix and the waveguide probe is set at a suitable 22 cm. This distance ensures the requirement of the far field region condition, meeting the necessary condition for accurate characterization. By adhering to such guidelines, the radiation performance of the 2-D  $3\times 3$ -way Nolen matrix can be thoroughly assessed and analyzed.

Despite a constraint imposed by the mechanical arm, the scanning range for the radiation pattern evaluation is set from  $-30^\circ$  to  $90^\circ$ . Although this range is limited, it still able to adequately cover the primary radiation directions of each beam. Furthermore, to align with the slightly downward beam direction of Ports 2, 5, and 8, the matrix body is flipped accordingly, optimizing the alignment of these beams. Fig. 3.17 showcases contour plots of the realized gain at a level 3.9 dB below the peak for each radiation beam at a frequency of 28.25 GHz. The variables  $k_x$  and  $k_y$  represent  $\sin\theta\cos\varphi$  and  $\sin\theta\sin\varphi$ , respectively, where  $\theta$  and  $\varphi$  correspond to the elevation and azimuth angles in standard spherical coordinates. As observed in Fig. 3.17, beams 4, 5, 6, 7, 8, and 9 generate grating lobes in the  $k_y$  direction, which is parallel to the electrical field at the

output apertures. The grating lobe contours are visible at a level of -3.9 dB in the  $k_y$  direction, as the beamwidth of the radiating open-ended rectangular waveguides is wider in the  $k_y$  (E-plane) direction than in the  $k_x$  (H-plane) direction. It is important to note that future improvements can be made by adjusting the design of the radiating elements at the output ports to enhance the symmetry of the radiation pattern, addressing any limitations that may arise in practical applications.

Fig. 3.18 displays the radiation patterns at the center frequency of 28.25 GHz, focusing on a fixed value of  $k_x$  and varying  $k_y$ , which corresponds to quasi E-plane of the peak of each beam. The purpose is to showcase the main lobe along with its  $k_y$ -aligned grating lobes. Overall, the measurement results align closely with the simulation results, demonstrating good agreement between them. It is worth noting that in the measured radiation pattern for Beam 8, as shown in Fig. 18(b), the level of the grating lobe is slightly lower than that observed in the simulation. As a result, the measured grating lobe for Beam 8 does not appear in Fig. 17. Nonetheless, these minor discrepancies do not significantly impact the overall performance of the 2-D 3×3-way Nolen matrix, and the radiation patterns remain consistent with the expected behavior.

Table 3.5 provides detailed information on the peak realized gain for each beam at frequencies 27.65 GHz, 28.25 GHz, and 28.85 GHz. At the center frequency of 28.25 GHz, the measurement and simulation results demonstrate good overall agreement, with the largest deviation of approximately 1 dB observed for Beam 4. This is nevertheless acceptable considering for a low gain antenna condition. The boresight beam exhibits the maximum realized gain, with 15.5 dBi in the measurement and 15.7 dBi in the simulation. Conversely, the minimum realized gain corresponds to Beam 6, with 12.0 dBi in the measurement, with 3.5dB scan loss, and to Beam 9, with 12.7 dBi in the simulation, with 3dB scan loss. The scan loss of each beam is ascribed with non-isotropic radiation from an open-ended waveguide, and it is expected to be mitigated by future employment of external antenna with a conical beam to cover all main lobes. With the exception of Port 1, which has a pointing direction get proximity to the zenith resulting in naturally larger errors in the angle  $\varphi$  values, the beam peak directions in both simulation and

measurement align closely. However, there is a discrepancy of  $14^\circ$  in the  $\theta$  angle for Port 9 at 27.65 GHz. Despite this deviation, the agreement between the simulated and measured values for the peak realized gain and beam peak directions remains satisfactory.

The frequency dependence of the realized gain for each beam is detailly showcased in Fig. 3.19. Across the entire frequency bandwidth, most of the measurement results align closely with the simulations for the majority of the beams, with deviations of no more than 1 dB. With the exception that Beam 4 exhibits a difference of 1.6 dB at 27.95 GHz, while Beam 6 shows a 1.4 dB deviation at 28.85 GHz. These slight disparities can be attributed to a combination of factors, including manufacturing and assembly errors, as well as measurement uncertainties. However, such deviations do not undermine the overall agreement between the measured and simulated results.

Table 3.6 presents an elaborate comparison between various 2-D beam-switching matrices and the innovative 2-D  $3 \times 3$ -way Nolen matrix proposed in this research. Previous works such as [3-13] and [3-14] have explored planarized cascading of couplers in substrate integrated transmission lines, achieving similar functionality to that of a two-plane coupler. The main novelty of the matrix design in this study lies in its pioneering use of a two-plane waveguide coupler with unequal output division and the implementation of a 2-D Nolen matrix based on a one-body waveguide structure. In terms of performance, this work holds a significant advantage over other matrices in terms of low power imbalance and insertion loss. Compared to the 2-D hollow waveguide  $4 \times 4$ -way Butler matrix [3-11], the physical size of the proposed matrix is relatively larger. This excessive size can be attributed to two factors.

Firstly, in the transverse plane, a  $60.0 \text{ mm} \times 60.0 \text{ mm}$  exterior profile is selected to accommodate the  $19.6 \text{ mm} \times 16.3 \text{ mm}$  aperture area and to ensure good connection with the transformer (with a size of  $120 \text{ mm} \times 120 \text{ mm}$ ). However, it's important to note that this limitation stems from the test setup rather than the matrix configuration, and future works can potentially reduce the exterior profile further.

Secondly, in the longitudinal direction, as depicted in Fig. 3.11, four segments of oblique waveguides totaling 107.47 mm in length are introduced. Two segments are used

to connect the constituent components from the 1<sup>st</sup> to 5<sup>th</sup> layers, while the other two segments are employed to connect the input or output ports with the matrix. The presence of these lengthy oblique waveguides is necessary to address the broad side wall (5.78 mm) of the input or output port for each component in the matrix. This broad side wall corresponds to a cut-off frequency very close to 27.65 GHz, requiring the inclusion of long oblique waveguides with a moderate slope to effectively suppress reflections. These design constraints can be overcome in future iterations by exploring alternative manufacturing techniques that offer higher integration flexibility, especially those additive manufacturing techniques.

### **3.8 Conclusion remarks**

This chapter has presented an innovative 2-D one-body 3×3-way hollow-waveguide Nolen matrix, introducing a novel two-plane unequal division coupler operating in the Ka-band from 27.65 GHz to 28.85 GHz, corresponding to a fractional bandwidth of 4.1%. The proposed two-plane unequal division coupler demonstrates excellent performance, with transmission coefficients exhibiting variations within  $\pm 0.5$  dB in amplitude and  $\pm 10^\circ$  in phase over the considered frequency range.

The designed 2-D 3 × 3-way Nolen matrix showcases promising electrical characteristics, with simulation results revealing a maximum output port power imbalance of 2.5 dB and a maximum insertion loss of 0.86 dB across the analyzed bandwidth. To verify the radiation performance, far field measurements were conducted, and the realized gain was evaluated with reference to a standard horn antenna. At the center frequency, the maximum realized gain of the 2-D 3×3-way Nolen matrix is achieved at the boresight (Beam 1), measuring 15.5 dBi in the measurement and 15.7 dBi in the simulation. The minimum realized gain in the measurement is observed for the 2-D tilted Beam 6, measuring 12.0 dBi, while in the simulation, it is observed for another 2-D tilted Beam 9, measuring 12.7 dBi. The scan loss in the tilted beams is expected to be compensated by employing more isotropic radiation elements in future applications.



Significantly, this research marks the first reported instance of a 2-D one-body hollow-waveguide Nolen matrix with a port number other than  $2^n$ . It also introduces the utilization of a two-plane coupler with unequal output division within a beam-switching matrix network. Although the frequency bandwidth of the designed two-plane coupler and 2-D  $3 \times 3$ -way Nolen matrix is limited, it suffices to demonstrate the concept effectively. Future endeavors will explore a recently proposed method to enhance the bandwidth of two-plane couplers [3-8] and apply it to broaden the bandwidth of the 2-D  $3 \times 3$ -way Nolen matrix discussed in this research. The present work serves as a foundation for future studies on 2-D one-body hollow-waveguide matrices with different beam numbers in either dimension, including 5, 6, 7, 9, and beyond.

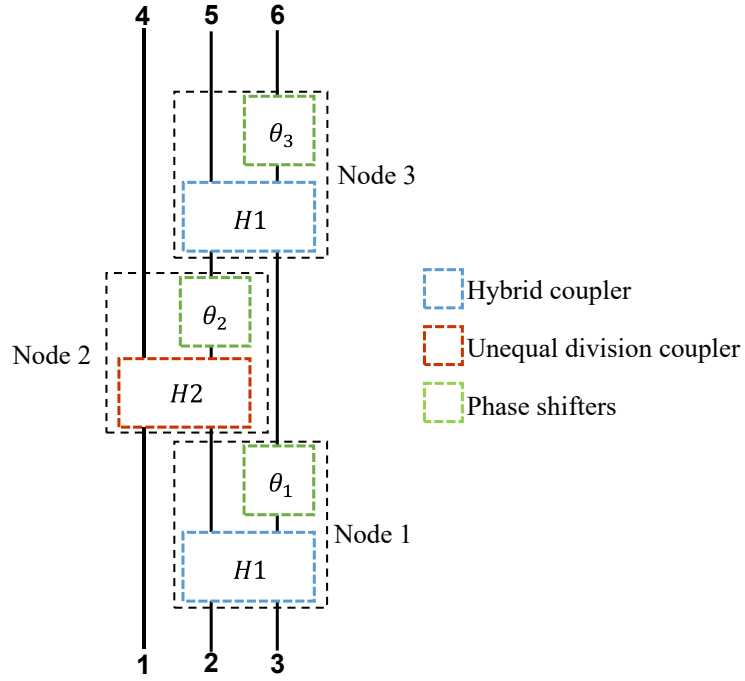


**Fig. 3.1.** 1-D 3-way Nolen matrix

**TABLE 3.1**  
**Port assignments of 1-D 3-way Nolen matrix**

$[\varphi_1, \varphi_2, \varphi_3]$	$\theta_1$	$\theta_2(\theta_3)$
$\left[0, \frac{-2\pi}{3}, \frac{2\pi}{3}\right]$	0	$\frac{\pi}{2}$
$\left[\frac{-2\pi}{3}, 0, \frac{2\pi}{3}\right]$	$\frac{\pi}{3}$	$\frac{-\pi}{6}$
$\left[\frac{-2\pi}{3}, \frac{2\pi}{3}, 0\right]$	$\frac{-2\pi}{3}$	$\frac{-\pi}{6}$
$\left[0, \frac{2\pi}{3}, \frac{-2\pi}{3}\right]$	$\pi$	$\frac{\pi}{2}$
$\left[\frac{2\pi}{3}, \frac{-2\pi}{3}, 0\right]$	$\frac{-\pi}{3}$	$\frac{-5\pi}{6}$
$\left[\frac{2\pi}{3}, 0, \frac{-2\pi}{3}\right]$	$\frac{2\pi}{3}$	$\frac{-5\pi}{6}$

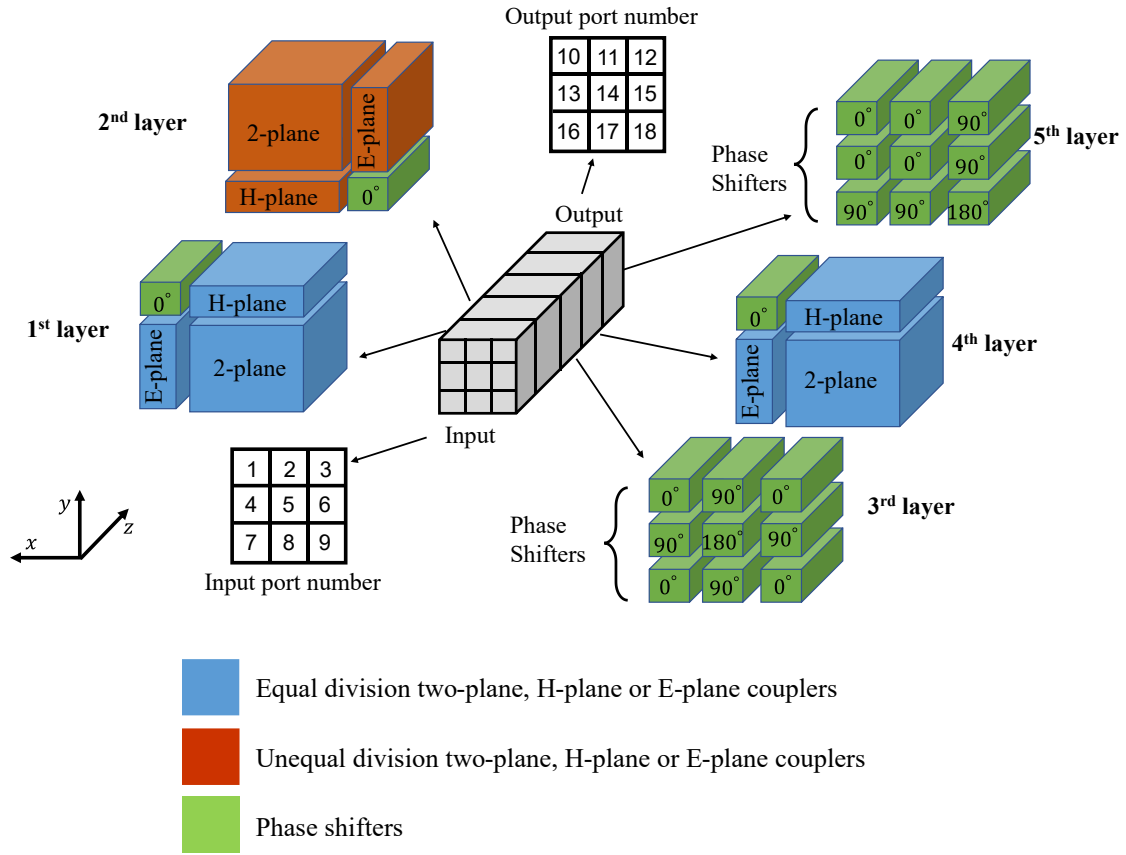


**Fig. 3.2.** 2-D one-body 3×3-way Nolen matrix.

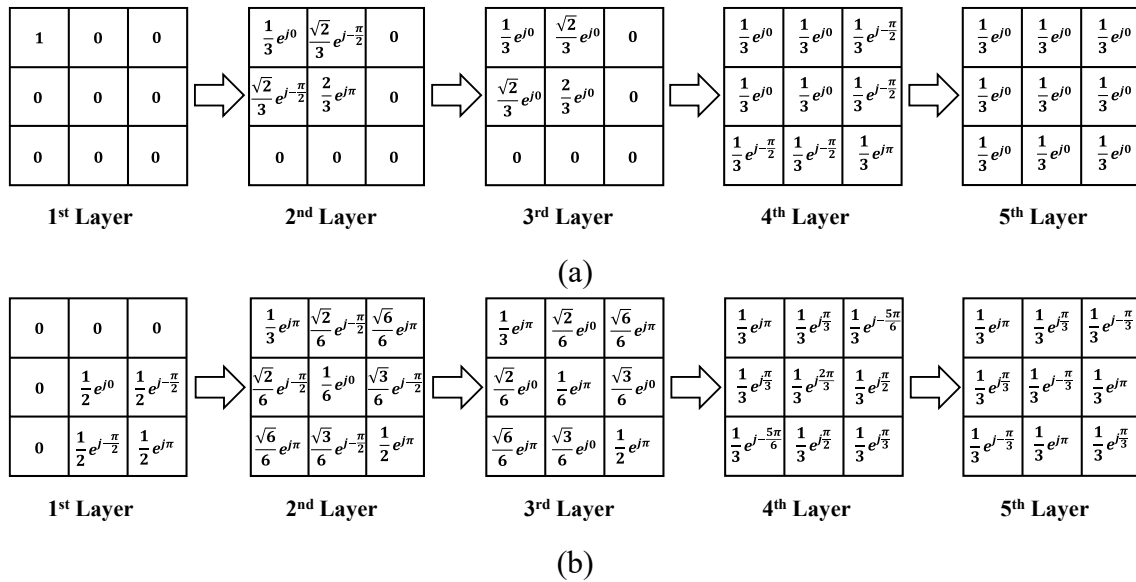
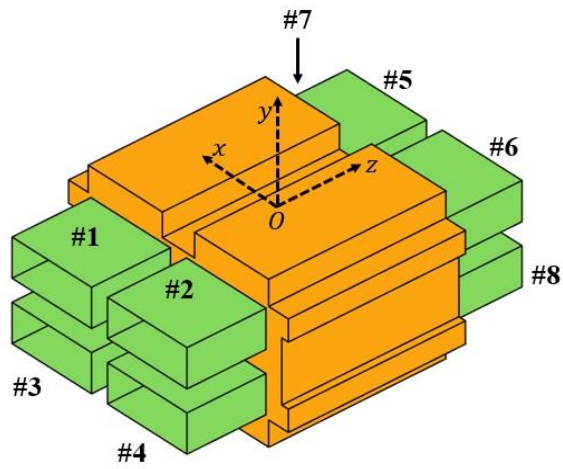
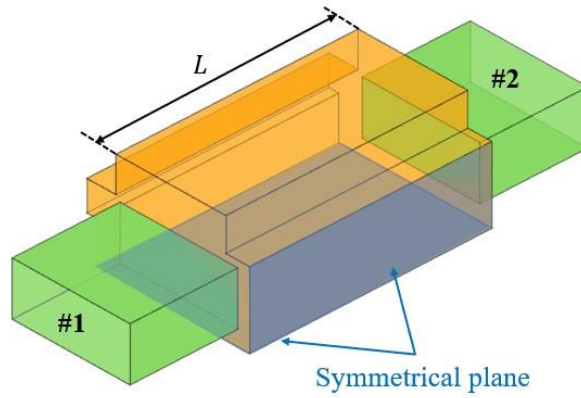


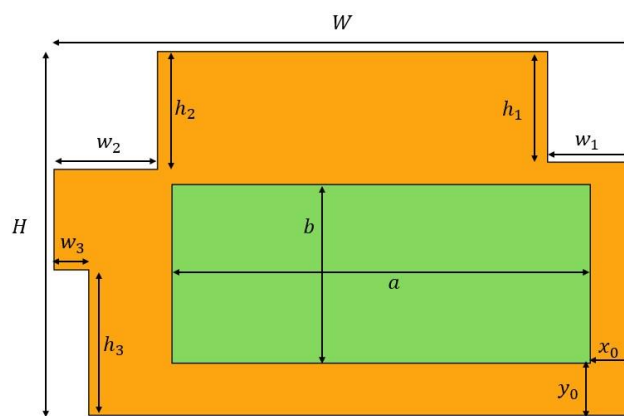
**Fig. 3.3.** Details of the beamforming steps in the 2-D 3×3-way Nolen matrix with ideal complex signals at the output of each layer corresponding to unitary input signal (a) at Port 1 and (b) at Port 5.



(a) Side view of the full model.



(b) Perspective view of the quarter model in the first quadrant.



(c) Cross section of the quarter model.

**Fig. 3.4.** Two-plane unequal division coupler model.

**TABLE 3.2**  
**Dimensional parameters of the quarter model of two-plane coupler (Unit:mm)**

(A)

$L$	$W$	$H$	$a$	$b$	$x_0$	$y_0$
11.44	7.99	5.03	5.78	2.47	0.58	0.72
$h_1$	$h_2$	$h_3$	$w_1$	$w_2$	$w_3$	
1.53	1.63	2.01	1.17	1.43	0.48	

(B)

$L$	$W$	$H$	$a$	$b$	$x_0$	$y_0$
11.04	8.20	5.28	5.78	2.47	0.55	0.71
$h_1$	$h_2$	$h_3$	$w_1$	$w_2$	$w_3$	
1.26	0.98	0.71	2.21	2.33	0.40	

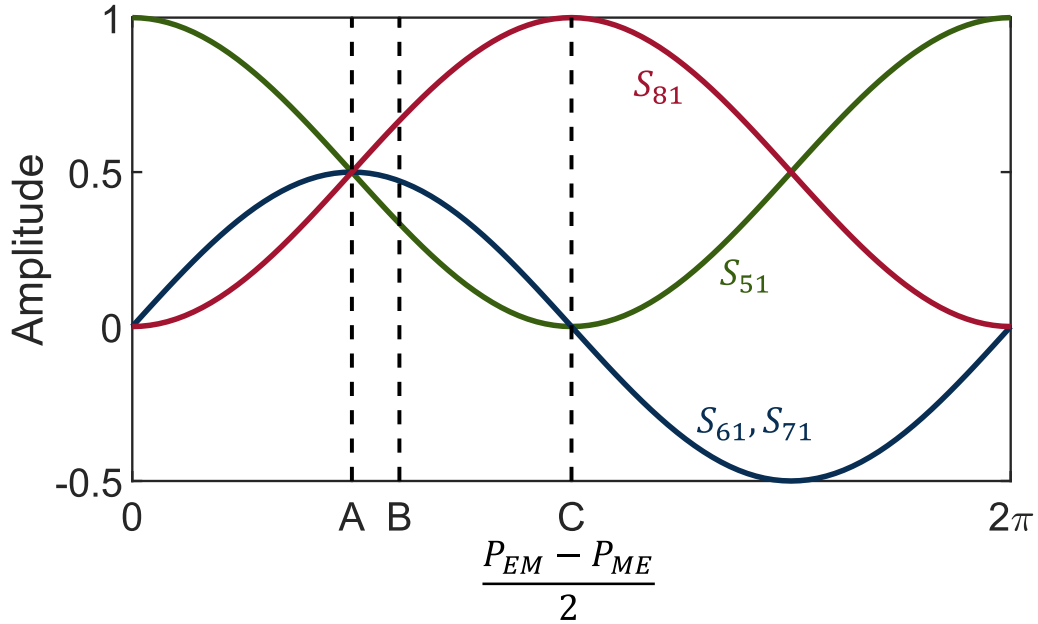
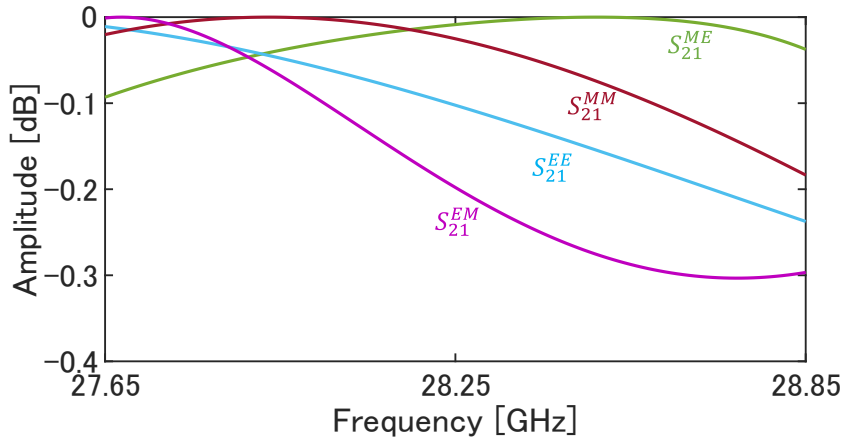
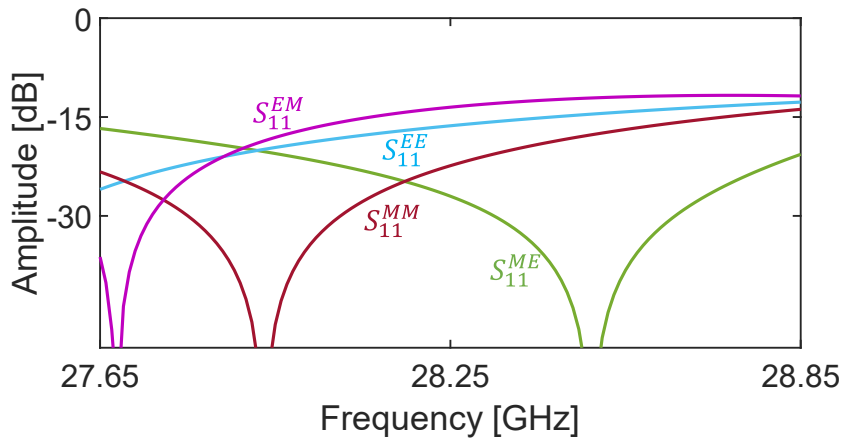


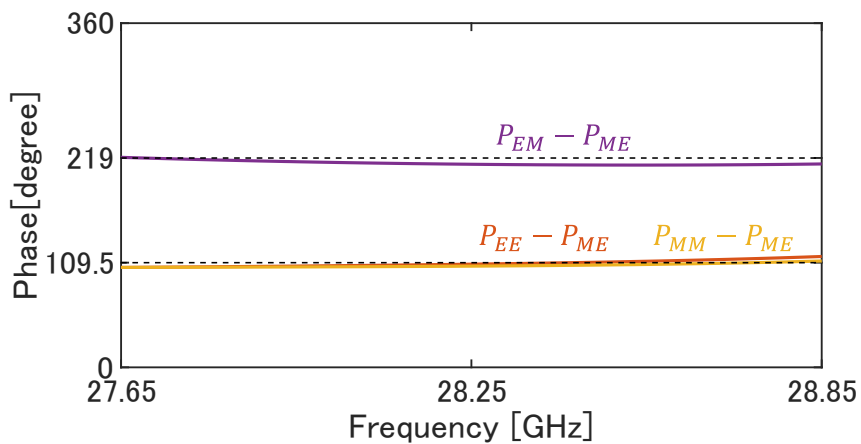
**Fig. 3.5.** Variation of output amplitudes.  $A = \pi/2$ ,  $B = \arccos(-1/3)$ ,  $C = \pi$



(a) Amplitude of the quarter coupler model assigned with ME, EE, MM, EM boundary conditions at the symmetrical planes.

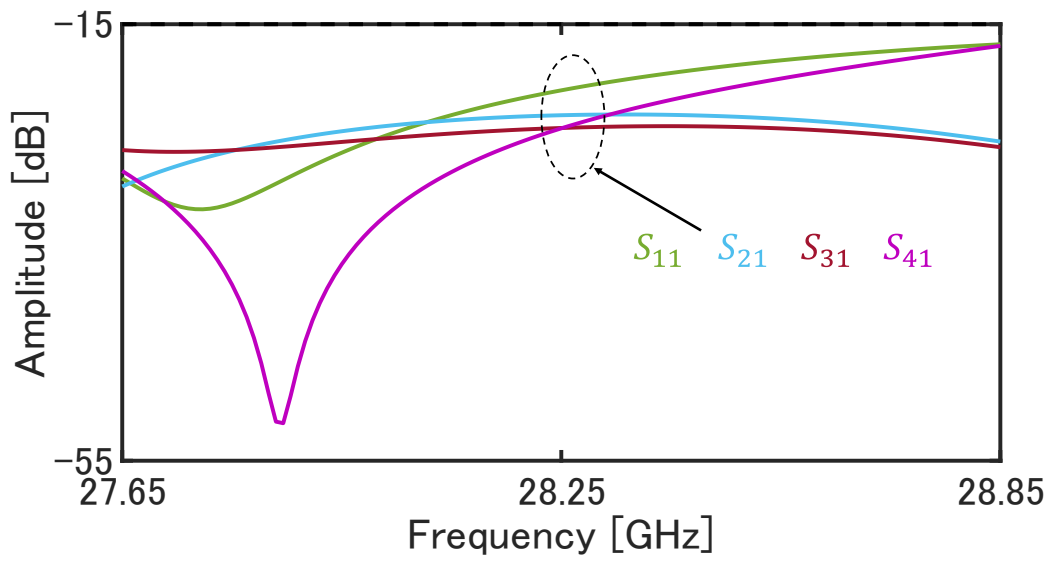


(b) Reflection of the quarter coupler model assigned with ME, EE, MM, EM boundary conditions at the symmetrical planes.

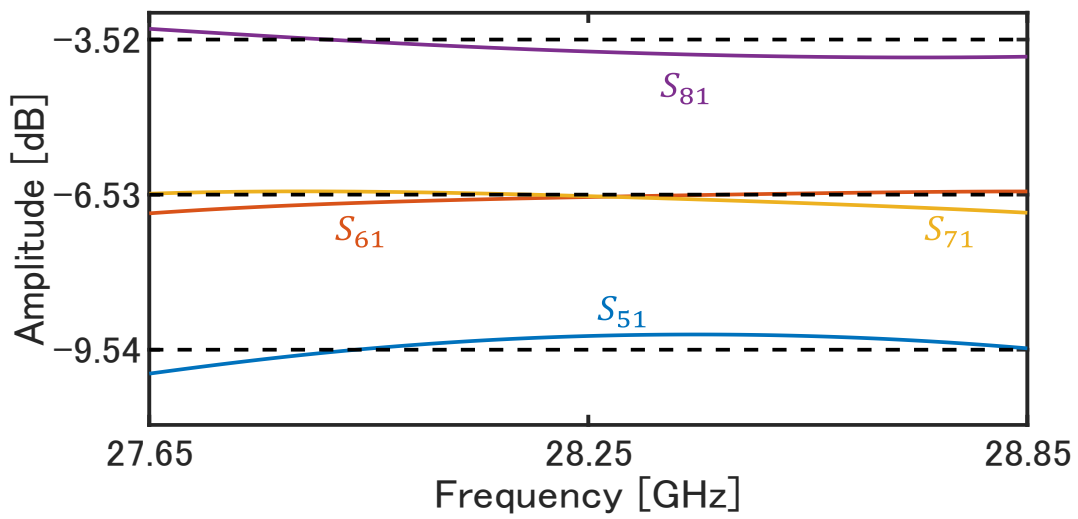


(c) Relative phases of the quarter coupler model assigned with EE, MM, EM boundary conditions with reference to model with ME boundary conditions.

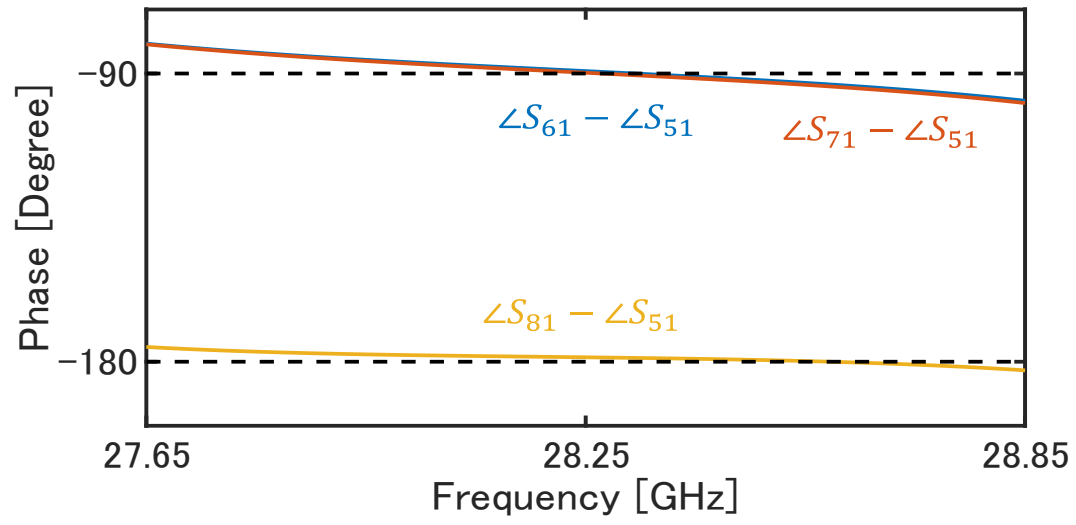
**Fig. 3.6.** Transmission coefficients of the quarter model of the proposed unequally divided two-plane coupler.



(a) Input ports reflection and isolation.



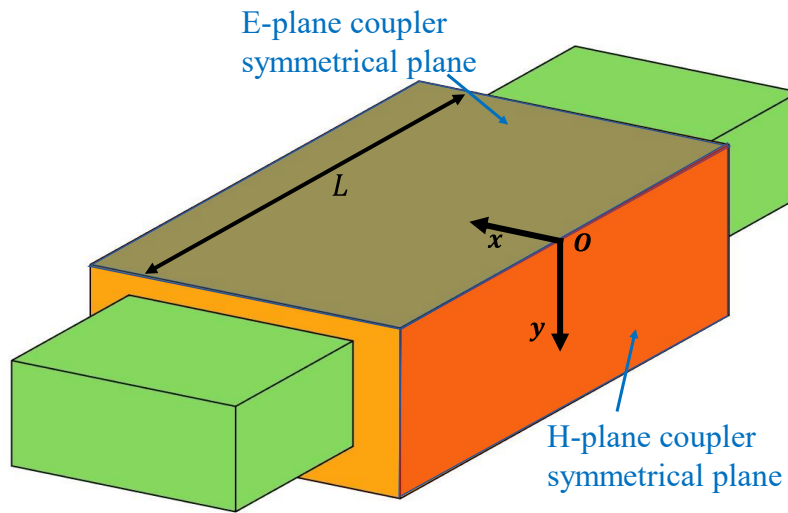
(b) Transmission amplitude.



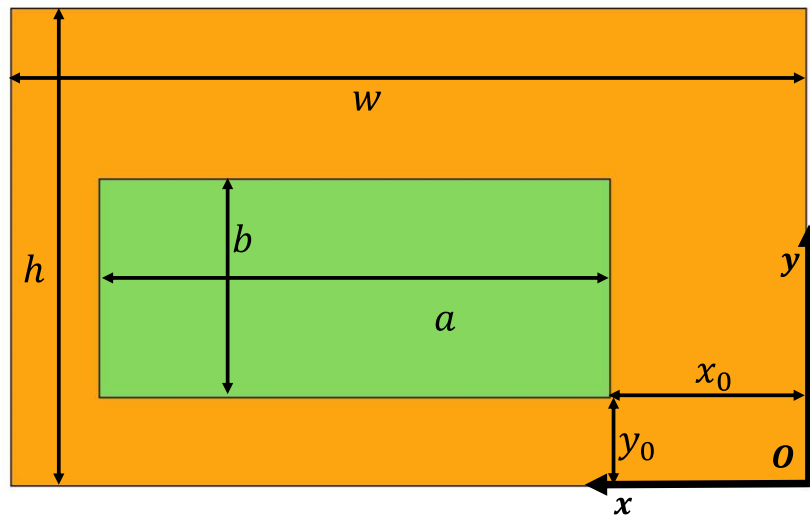
(c) Transmission phase compared with  $S_{51}$ .

**Fig. 3.7.** S-parameters of the two-plane unequal division coupler in the 2<sup>nd</sup> layer of the entire matrix.





(a) Side view.



(b) Cross-section.

**Fig. 3.8.** Schematic of the half model of the H-plane or E-plane coupler.

**TABLE 3.3**  
**Dimensional parameters of half model of one-plane couplers (Unit:mm)**

(A) H-plane equal

$L$	$w$	$h$	$x_0$	$y_0$
10.90	7.01	4.33	0.95	1.83

(B) H-plane unequal

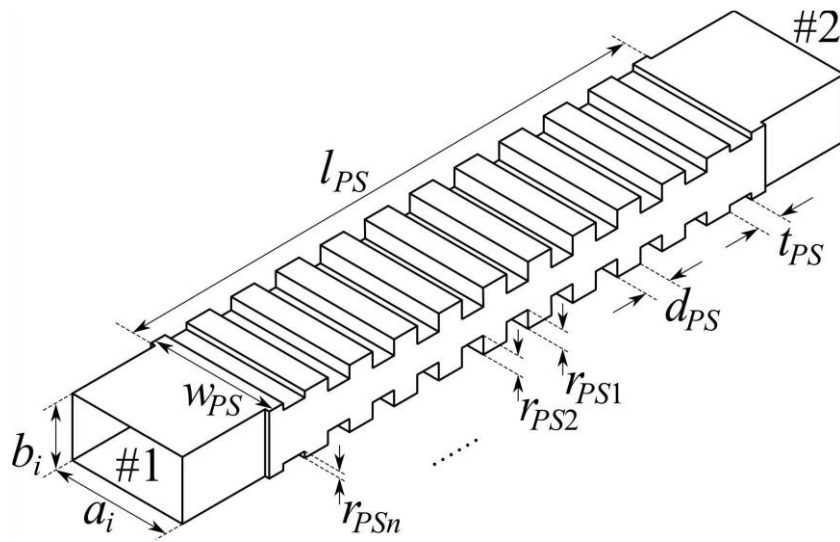
$L$	$w$	$h$	$x_0$	$y_0$
15.44	7.48	4.16	1.16	1.49

(C) E-plane equal

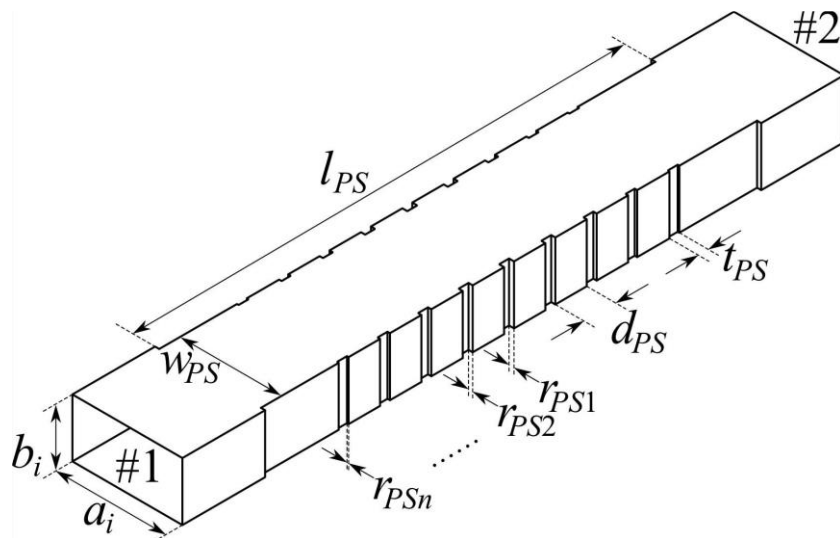
$L$	$w$	$h$	$x_0$	$y_0$
12.46	10.22	4.87	0.63	1.73

(D) E-plane unequal

$L$	$w$	$h$	$x_0$	$y_0$
11.98	10.87	4.18	1.05	0.67



(a) Capacitive phase shifter.



(b) Inductive phase shifter.

**Fig. 3.9.** Schematic of proposed waveguide phase shifters for use in the 2-D  $3 \times 3$ -way Nolen matrix.

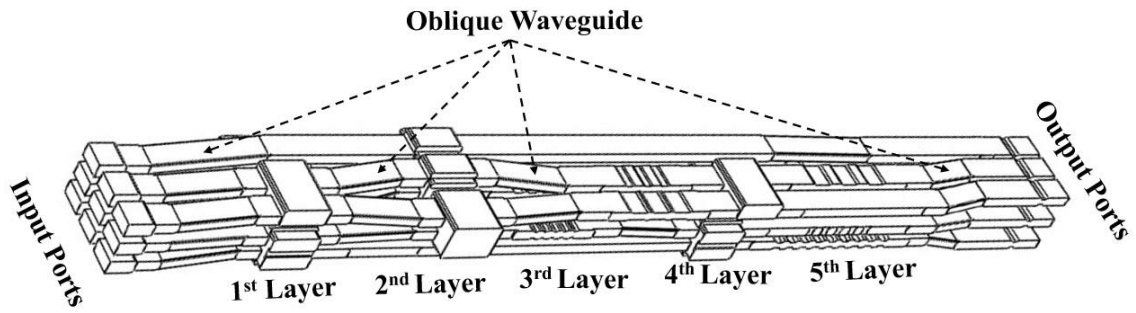
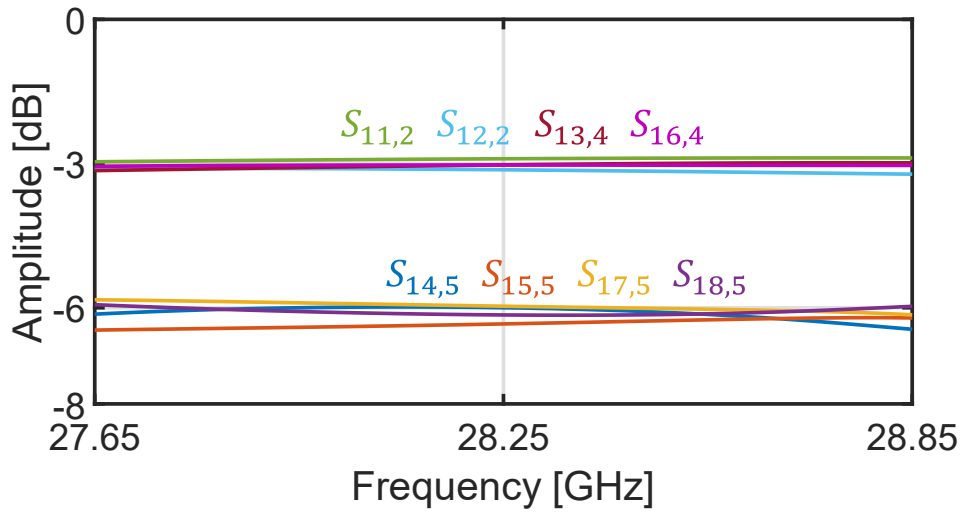
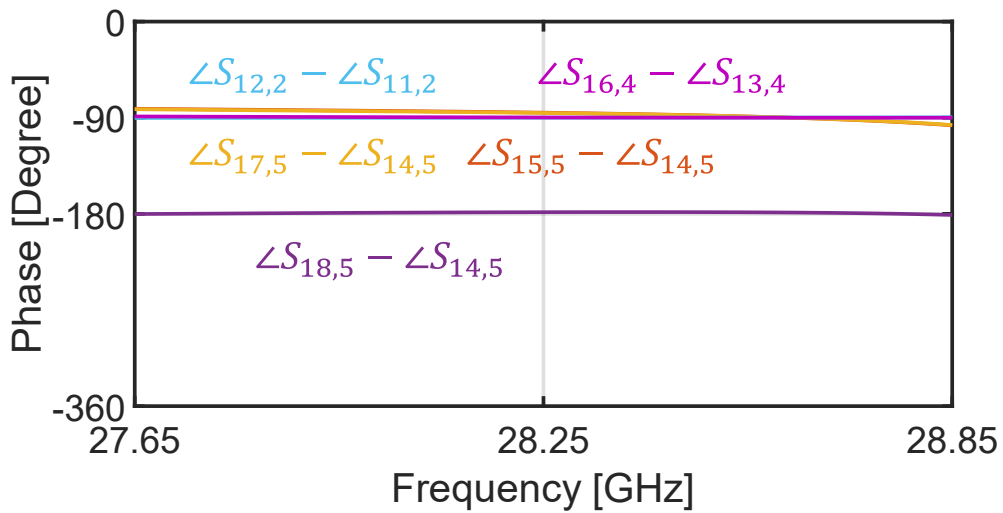


**Fig. 3.10.** Perspective view of the 3-D inner waveguide cavities of the proposed 2-D  $3 \times 3$ -way Nolen matrix.



(a1) Amplitude output on the 1<sup>st</sup> or 4<sup>th</sup> layer.



(a2) Phase output on the 1<sup>st</sup> or 4<sup>th</sup> layer.

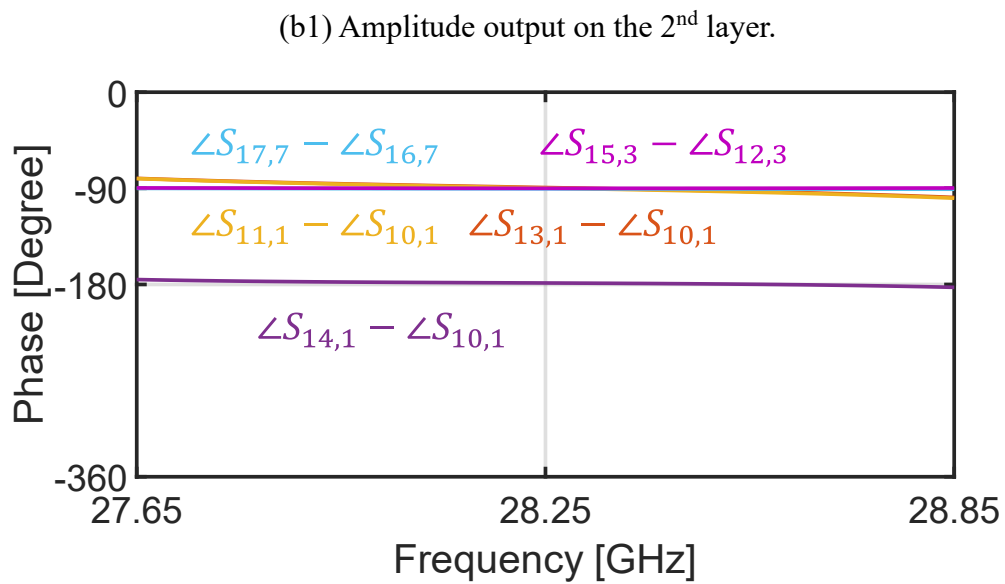
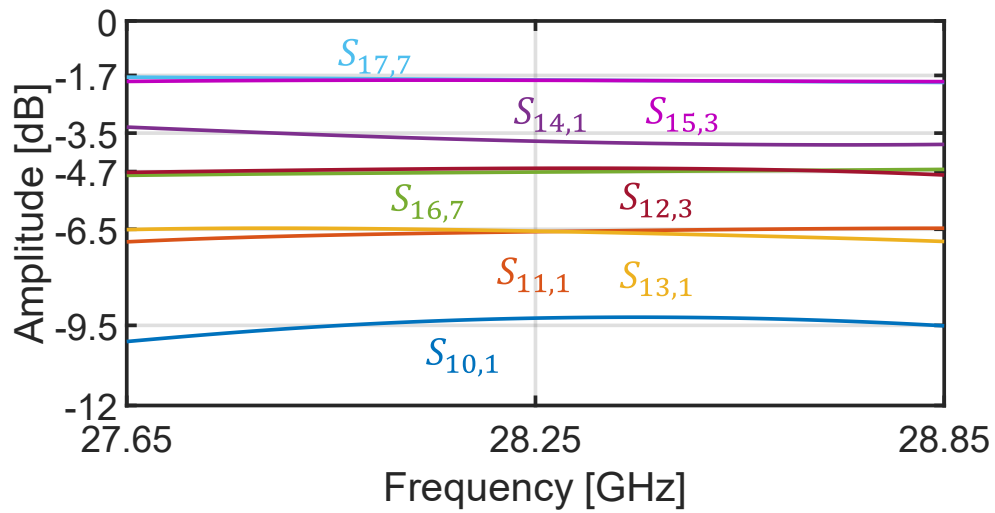
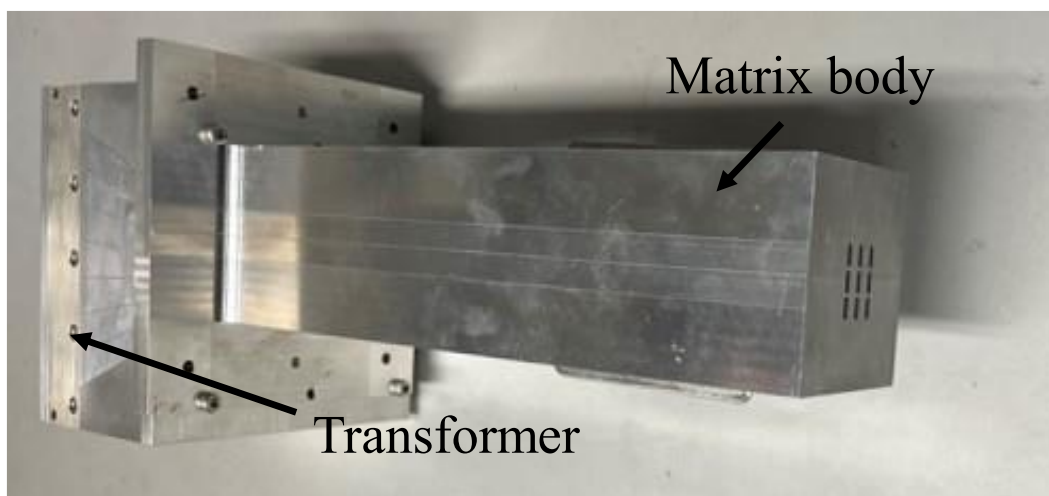
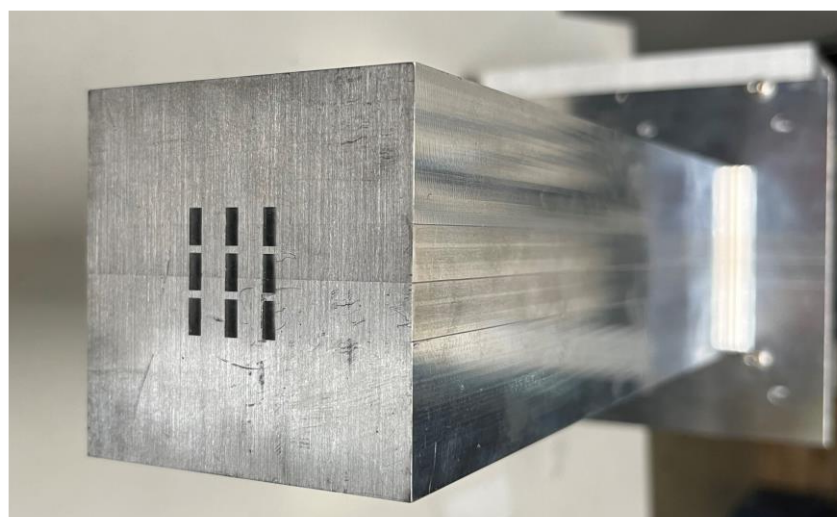


**Fig. 3.11.** Transition of the coupler layers in the 2-D 3×3-way Nolen matrix.



(a) Overview.



(b) Output aperture.

**Fig. 3.12.** Manufactured 2-D  $3 \times 3$ -way Nolen matrix.

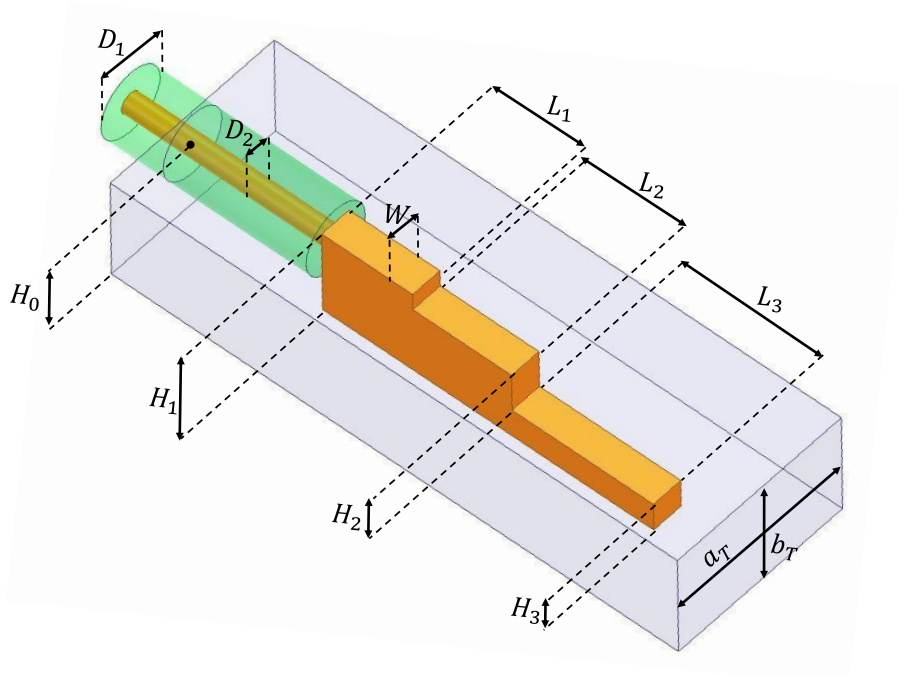
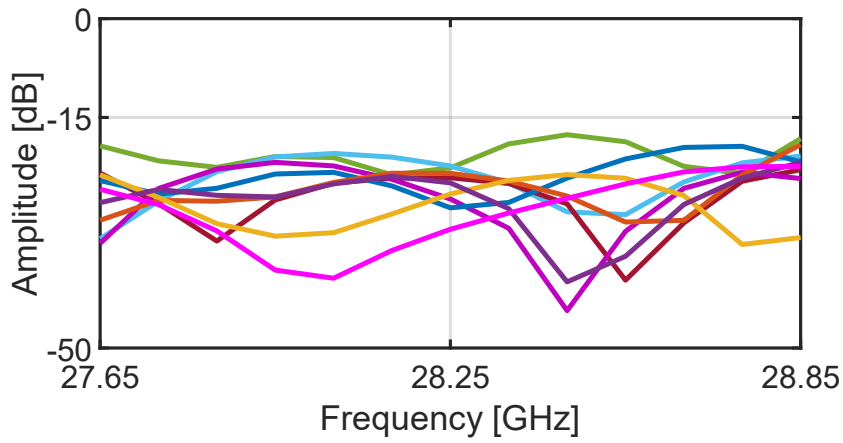


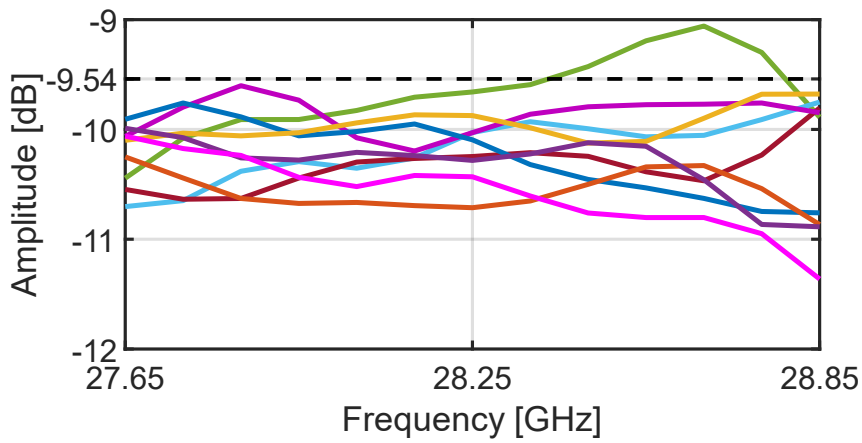
**Fig. 3.13.** Schematic of a coaxial line to waveguide transition working around 28.25GHz.  
Orange: metal, Green: PTFE.

**TABLE 3.4**  
**Dimensional parameters of the coaxial line-waveguide transition (Unit:mm)**

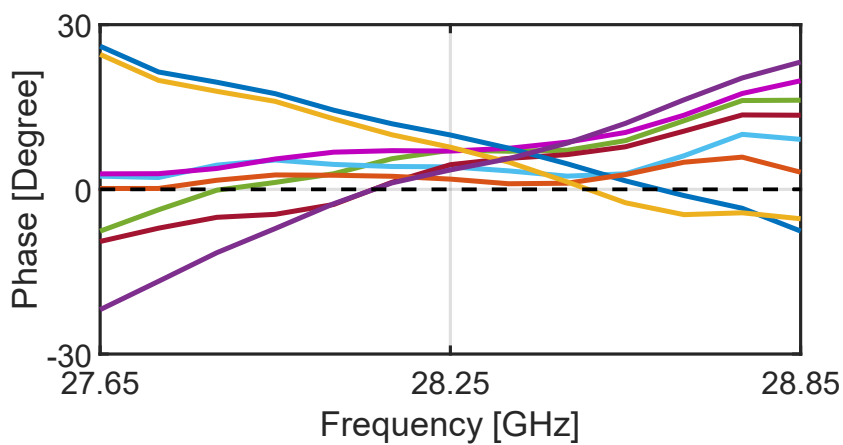
$D_1$	$D_2$	$H_0$	$H_1$	$H_2$	$H_3$
2.16	0.66	2.20	2.83	1.30	0.96
$L_1$	$L_2$	$L_3$	$a_T$	$b_T$	$W$
2.93	3.18	4.55	6.00	3.40	1.00



(a) Reflection and isolations corresponding to incidence from Port 1.

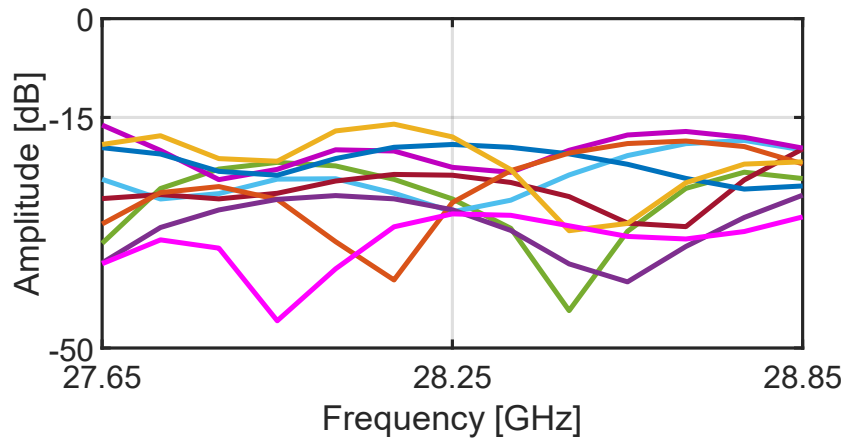


(b) Amplitude output corresponding to incidence from Port 1.

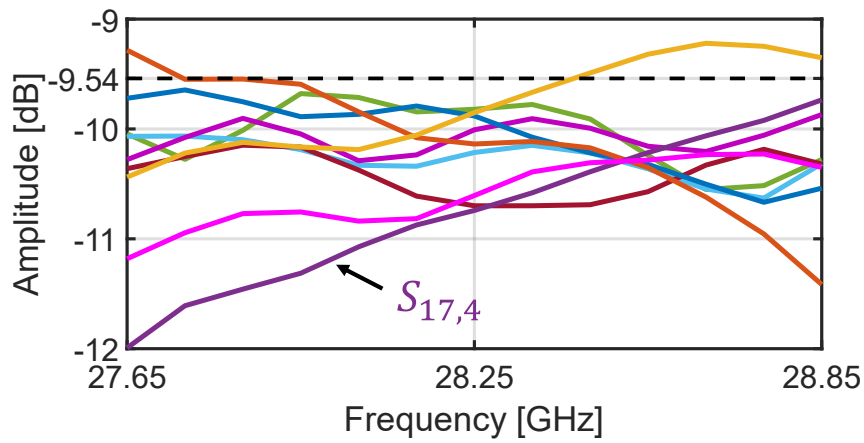


(c) Phase output corresponding to incidence from Port 1.

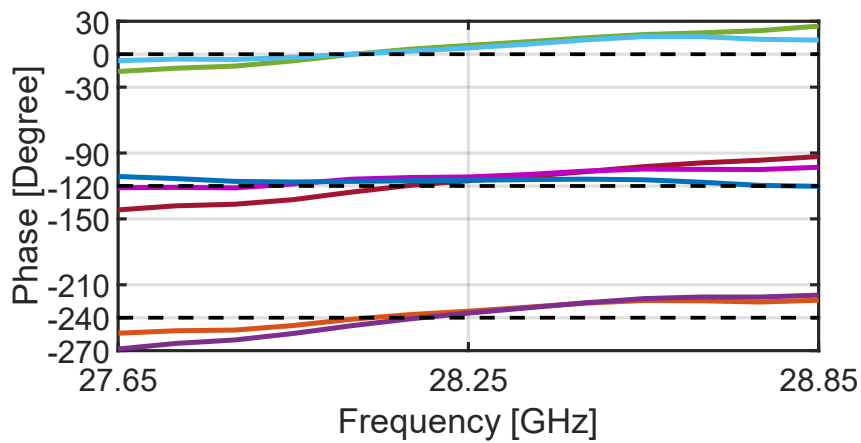




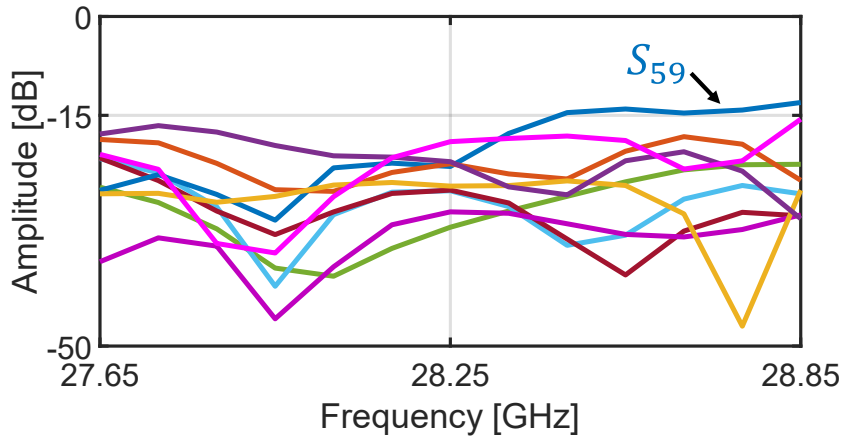
(a2) Reflection and isolations corresponding to incidence from Port 4.



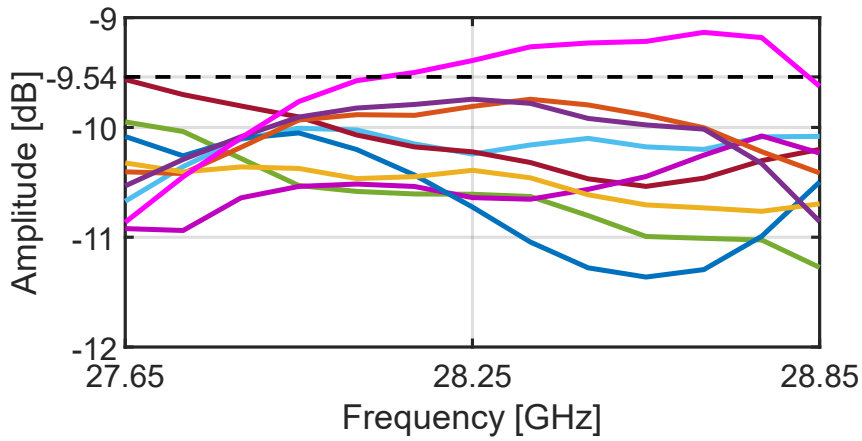
(b2) Amplitude output corresponding to incidence from Port 4.



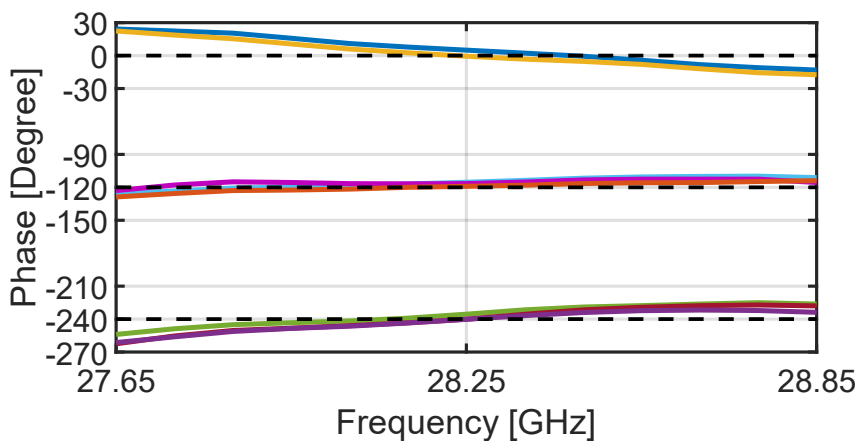
(c2) Phase output corresponding to incidence from Port 4.



(a3) Reflection and isolations corresponding to incidence from Port 9.

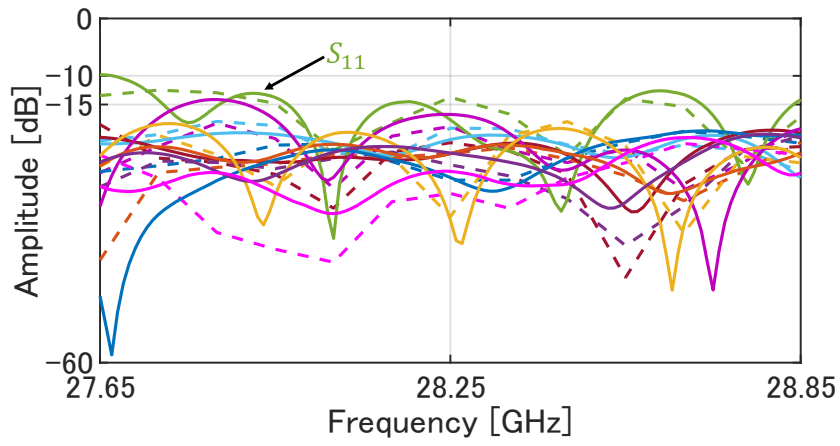


(b3) Amplitude output corresponding to incidence from Port 9.

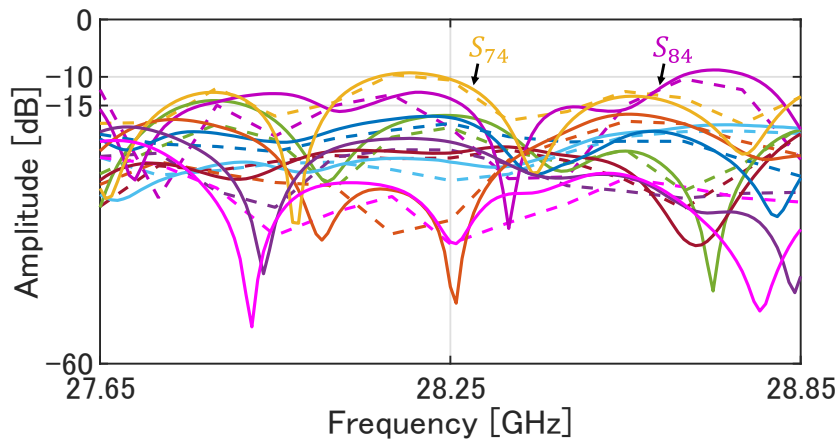


(c3) Phase output corresponding to incidence from Port 4.

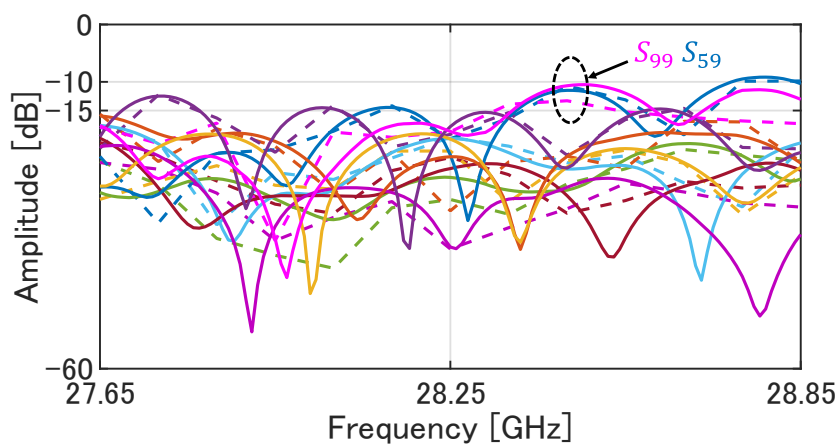
**Fig. 3.14.** S-parameters for the simulated 18-port 2-D 3×3-way Nolen matrix in terms of input ports reflection and isolation coefficients, and output ports transmission amplitude and relative phase to signal at Port 10.



(a) Incidence from Port 1.



(b) Incidence from Port 4.



(c) Incidence from Port 9.

**Fig. 3.15.** Reflection and isolation coefficients at the input ports when the output ports are radiating in free space. Solid line: measurements. Dotted line: simulations.

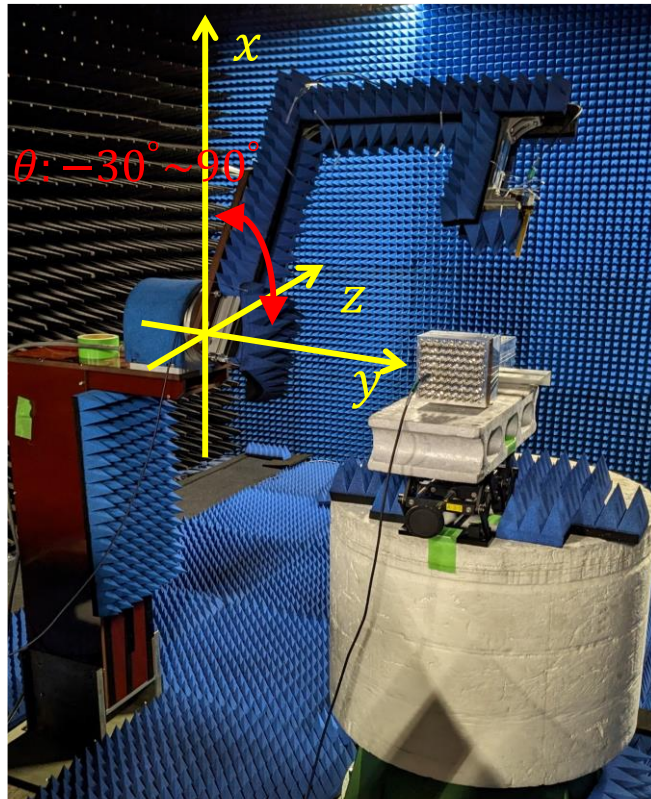


**Fig. 3.16.** Spherical scanning measurement system.

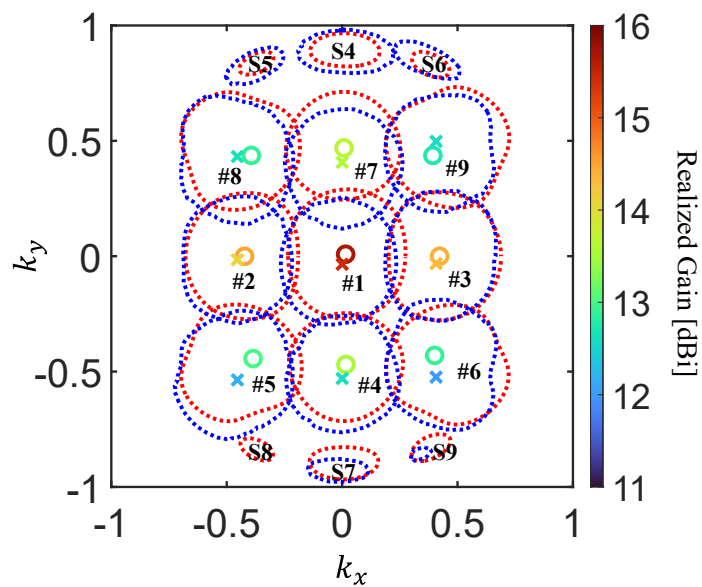
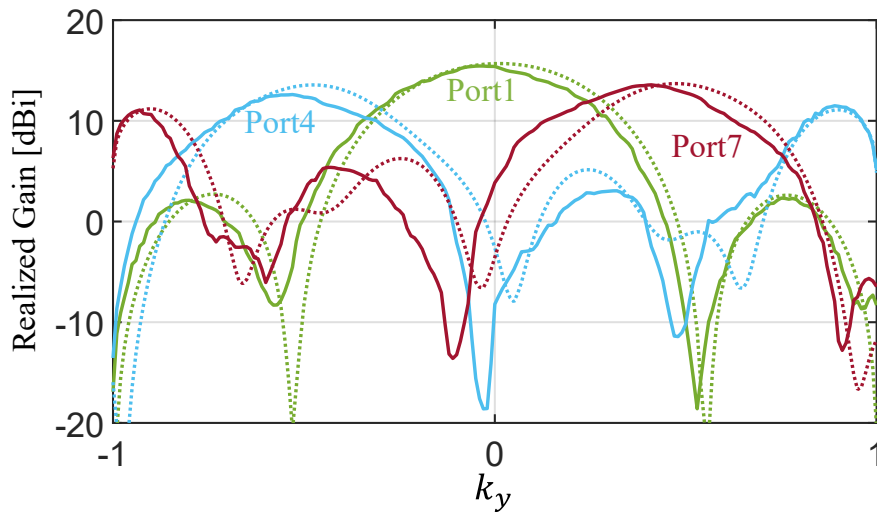


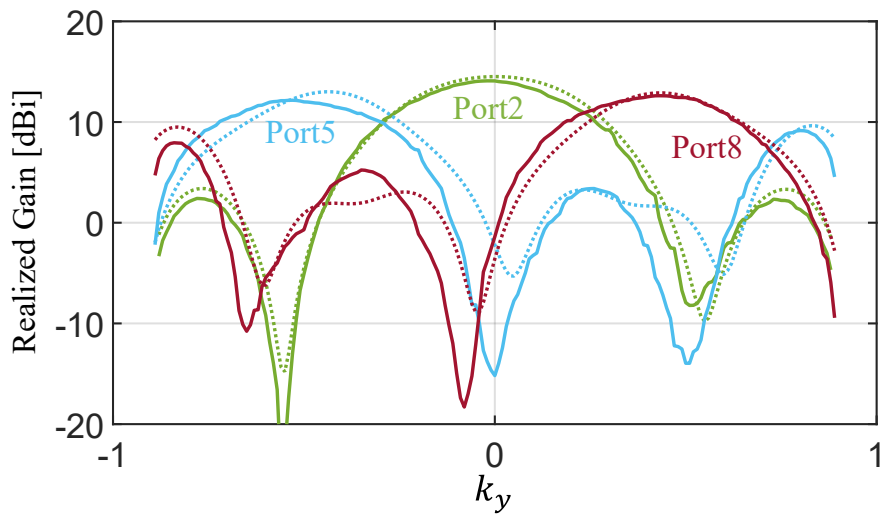
**Fig. 3.17.** Contour plots of radiation beams at 3.9 dB below peak values, with red dotted lines for simulation and blue dotted lines for measurements. Simulated and measured beam peak angular directions are marked with o and x, respectively. “#” and “S” markers stand for main beams and grating lobes, respectively.

**TABLE 3.5**  
**Realized gain of each beam**

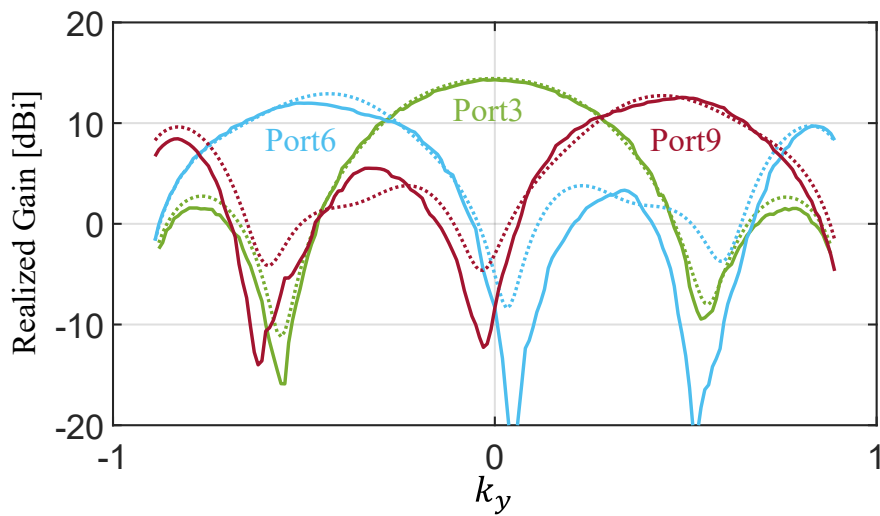
Port No.	27.65GHz				28.25GHz				28.85GHz			
	Gain (dBi)		$[\theta, \varphi]$ (deg.)		Gain (dBi)		$[\theta, \varphi]$ (deg.)		Gain (dBi)		$[\theta, \varphi]$ (deg.)	
	Mea.	Sim.	Mea.	Sim.	Mea.	Sim.	Mea.	Sim.	Mea.	Sim.	Mea.	Sim.
1	14.5	15.1	[-4, 90]	[2, 29]	15.5	15.7	[-2, 90]	[1, 29]	15.3	15.9	[-3, 18]	[1, 80]
2	12.8	13.4	[-27, 0]	[-26, -1]	14.1	14.5	[-27, 2]	[-25, 0]	13.7	14.2	[-27, 4]	[-25, 1]
3	13.1	13.3	[24, 0]	[26, -2]	14.3	14.4	[24, 4]	[25, 0]	13.9	14.4	[24, -2]	[25, -1]
4	12.6	13.7	[-37, 90]	[-29, 92]	12.6	13.6	[-32, 90]	[-28, 92]	13.1	13.5	[-32, 90]	[-28, 90]
5	12.0	12.6	[-45, 50]	[-35, 50]	12.2	13.0	[-44, 50]	[-36, 49]	11.4	12.2	[-45, 50]	[-37, 47]
6	11.5	12.0	[-40, 129]	[-36, 131]	12.0	12.9	[-42, 128]	[-36, 133]	10.5	12.0	[-39, 130]	[-36, 133]
7	13.7	14.0	[24, 90]	[29, 89]	13.6	13.7	[24, 90]	[28, 89]	13.4	13.2	[24, 90]	[29, 89]
8	12.2	12.4	[40, 135]	[35, 131]	12.6	12.9	[39, 136]	[36, 132]	11.7	12.3	[37, 133]	[36, 132]
9	12.0	11.5	[40, 52]	[54, 46]	12.6	12.7	[40, 51]	[36, 48]	12.3	12.8	[39, 50]	[36, 47]



(a) Port 1, 4 and 7.



(b) Port 2, 5 and 8.



(c) Port 3, 6 and 9.

**Fig. 3.18.** Radiation pattern at center frequency 28.25 GHz. Solid line: measurements. Dotted line: simulations.

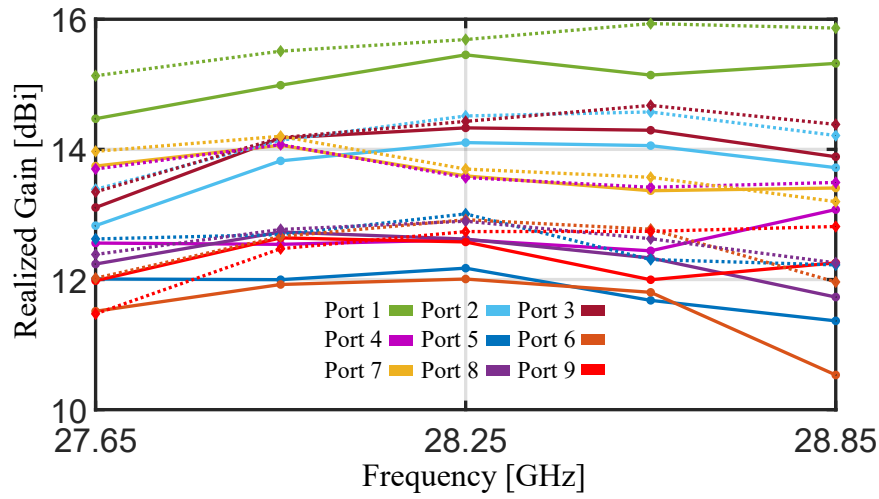


**Fig. 3.19.** Realized gain of each beam versus frequency, with measurement results in solid lines and simulation results in dotted lines.

**TABLE 3.6**  
**Comparison with other related works**

	2-D 3×3	2-D 3×3	2-D 4×4 Butler	2-D 4×4 Butler	2-D 4×4	Proposed 2-D
Performance	Nolen matrix [3-9]	matrix [3-10]	matrix [3-13]	matrix [3-14]	Butler matrix [3-11]	3×3 Nolen matrix
Frequency	6GHz	28GHz	2.4GHz	10GHz	22GHz	28GHz
Transmission	Microstrip line	SIW	Microstrip line	SIW	Waveguide	Waveguide
One-body structure	No	No	No	No	Yes	Yes
Use two-plane coupler	No	No	No	No	Yes	Yes
Coupler division ratio	Unequal and equal	Equal	Equal	Equal	Equal	Unequal and equal
Insertion loss (IL)	N.A.	N.A.	1.8dB	4dB	1.5dB	0.86dB
Output amplitude imbalance (IL included)	N.A.	N.A.	3dB	>6dB	4.8dB	2.5dB
Bandwidth	N.A.	7.1%	16.7%	N.A.	2%	4.1%
Physical size ( $\lambda^3$ )	N.A.	N.A.	1.6*1.6*0.004	22*16.7*0.03	3.45*3.45*14.0	5.65*5.65*23.02

## References

- [3-1] J. Nolen, "Synthesis of multiple beam networks for arbitrary illuminations" Bendix Corp, 1965.
- [3-2] N. J. G. Fonseca, "Printed S-Band  $4 \times 4$  Nolen Matrix for Multiple Beam Antenna Applications," *IEEE Trans. Antennas Propag.*, vol. 57, no. 6, pp. 1673-1678, June 2009.
- [3-3] J. Butler and R. Lowe, "Beam-forming matrix simplifies design of electronically scanned antennas," *Electron. Des.*, vol. 9, pp. 170–173, Apr. 1961.
- [3-4] J. Hirokawa and N. J. G. Fonseca, "Generalized one-dimensional parallel switching matrices with an arbitrary number of beams," *IEEE J. Microwaves*, vol. 1, no. 4, pp. 975-988, Oct. 2021.
- [3-5] F. Alessandri, M. Giordano, M. Guglielmi, G. Martirano and F. Vitulli, "A new multiple-tuned six-port Riblet-type directional coupler in rectangular waveguide," *IEEE Trans. Microw. Theory Techn.*, vol. 51, no. 5, pp. 1441-1448, May 2003.
- [3-6] T. Tomura, D. -H. Kim, M. Wakasa, Y. Sunaguchi, J. Hirokawa and K. Nishimori, "A 20-GHz-Band  $64 \times 64$  Hollow waveguide Two-Dimensional Butler Matrix," *IEEE Access*, vol. 7, pp. 164080-164088, 2019.
- [3-7] M. Wakasa, D.-H. Kim, T. Tomura, and J. Hirokawa, "Wideband Design of a Short-Slot 2-Plane Coupler by the Mode Matching/FEM Hybrid Analysis considering the Structural Symmetry," *IEICE Trans. Commun.*, vol. E102-B, No.5, pp.1019-1026, May 2019.
- [3-8] S. Chen, T. Tomura, J. Hirokawa, K. Ito, M. Suga, Y. Shirato, D. Uchida, and N. Kita, "Design for Operation in Two Frequency Bands by Division of the Coupled Region in a Waveguide 2-Plane Coupler," *IEICE Trans. Commun.*, vol. E105-C, No.12, pp.729-739, Dec. 2022.
- [3-9] H. Ren, H. Zhang, Y. Jin, Y. Gu, and B. Aridong, "A novel 2-D  $3 \times 3$  Nolen matrix for 2-D beamforming applications," *IEEE Trans. Microw. Theory Techn.*, vol. 67, no. 11, pp. 4622–4631, Nov. 2019.
- [3-10] J.-W. Lian, Y.-L. Ban, J.-Q. Zhu, K. Kang, and Z. Nie, "Compact 2-D scanning multibeam array utilizing the SIW three-way couplers at 28 GHz," *IEEE Antennas Wireless Propag Lett.*, vol. 17, no. 10, pp. 1915–1919, Oct. 2018.
- [3-11] D.-H. Kim, J. Hirokawa, and M. Ando, "One-body 2-D Beam-switching Butler Matrix with Waveguide Short-slot 2-plane Couplers," *IEICE Trans. Electron.*, vol. E100-C, no.10, pp.-, Oct. 2017.
- [3-12] O. A. Peverini, M. Lumia, G. Addamo, G. Virone and N. J. G. Fonseca, "How 3D-Printing Is Changing RF Front-End Design for Space Applications," *IEEE J. Microwaves*, vol. 3, no. 2, pp. 800-814, April 2023.
- [3-13] K. Ding and A. A. Kishk, "2-D Butler matrix and phase-shifter group," *IEEE Trans. Microw. Theory Techn.*, vol. 66, no. 12, pp. 5554-5562, Dec. 2018



- [3-14] J. -W. Lian, Y. -L. Ban, H. Zhu and Y. J. Guo, "Uniplanar Beam-Forming Network Employing Eight-Port Hybrid Couplers and Crossovers for 2-D Multibeam Array Antennas," *IEEE Trans. Microw. Theory Techn.*, vol. 68, no. 11, pp. 4706-4718, Nov. 2020.

# Chapter 4 Two-dimensional hollow waveguide 6×4-way beam-switching matrix

## 4.1 Introduction remarks

Butler matrices have gained widespread popularity among researchers due to their relatively simple design, by leveraging the key advantages that only half of the 1-D matrices need to be designed, attributing to their inherent symmetry. The seminal work by Butler and Turner [4-1] suggested that 2-D beam switching can be achieved by cascading 1-D beam switching matrices along two directions. The symmetries in 2-D matrices allow for reducing the design complexity to a quarter portion of the complete structure, with the remaining portions being mirror-like duplicates.

However, standard Butler matrices are limited to beam numbers as  $2^n$ . In contrast, the Nolen matrix [4-2][4-3] offers the flexibility to accommodate any number of beams. Designing an asymmetrical  $n$ -way Nolen matrix involves the composition of  $n(n-1)/2$  units with couplers having various values, leading to a complex design process. Additionally, the original Nolen matrix design is typically not wideband due to its series-fed configuration.

To address these challenges, a generalized 1-D matrix with an arbitrary number of beams was introduced in [4-4], representing an improvement over the parallel Nolen matrix design presented in [4-5]. This enhanced design yields a more compact configuration, combining the strengths of both the Butler matrix and the Nolen matrix. Following the methodology proposed in [4-4], a 1-D  $2n$ -way matrix can be constructed, encompassing all  $(2n)!$  permutations of beam assignments and associated adjacent output phase differences by adjusting the values of the phase shifters. Through careful selection of the phase shifter values, some of the solutions exhibit a symmetrical structure, offering the advantage of reducing design complexity.

This chapter presents the design of a novel two-dimensional (2-D) 6×4-way hollow waveguide beam-switching matrix operating at 28.25 GHz, with a fractional bandwidth

of 7.1%. It marks the first time that a 2-D one-body hollow waveguide beam-switching matrix is proposed, featuring different numbers of beams in two orthogonal directions. To reduce overall dimensions, this matrix partially incorporates two-plane couplers.

A prototype of the complete matrix is fabricated and subjected to measurement using a planar scanning near-field setup, validating the accuracy of the simulation results. At the center frequency of 28.25 GHz, the beam with the smallest tilting angle exhibits the highest directivity, achieving a simulated value of 21.1 dBi and a measured value of 21.3 dBi. Conversely, the beam with the largest tilting angle experiences the lowest directivity, with a simulated value of 16.0 dBi and a tilting angle of  $52^\circ$  from the boresight, resulting in a worst-case scan loss of 5.1 dB. It is important to note that the measured value in this specific case is slightly overestimated due to the limitations of the planar near-field test setup, which has a greater impact on the most tilted beams. Despite this, the radiation patterns demonstrate good agreement, confirming that the proposed matrix is a promising candidate for applications that demand symmetric beam coverage.

## 4.2 1-D 6-way and 4-way matrices

A remarkable characteristic of a  $2n$ -way generalized parallel symmetrical matrix is its symmetrical port assignment,

$$p(k) = -p(2n + 1 - k) \quad (4-1)$$

Here  $p$  and  $k$  mean the phase difference among adjacent output ports and the input port number with incident signal, respectively.

Drawing upon the original model presented in [4-4], the employed symmetrical 1-D 6-way and 4-way matrix configurations are derived by strategically adjusting the positions of phase shifters. Each quadrature coupler is uniquely characterized by an angle  $\theta_i$ , which plays a crucial role in defining its transmission matrix,

$$T_i = \begin{pmatrix} \cos \theta_i & -j \sin \theta_i \\ -j \sin \theta_i & \cos \theta_i \end{pmatrix} \quad (4-2)$$

For different port assignments of the 6-way and 4-way matrices, the coupling ratio of each quadrature coupler is fixed. By reviewing the 6-way matrix in Fig. 4.1(a), the structure can be a mirror-like self-duplication of 3-way Nolen matrices, by referring to [4-4], and the following condition is verified,

$$\varphi_3^6 = \varphi_4^6 \quad (4-3)$$

The proposed 6-way matrix and 4-way matrix configurations are associated with specific values of phase shift, denoted as  $\varphi_i^6$  and  $\varphi_i^4$ , respectively. These values, along with their corresponding port assignments, are provided in Table I. It is worth noting that while there are numerous possible permutations of symmetrical port assignments for the  $2^n(n!)$  matrix configurations [4-4], the enforced symmetrical configuration in the 6-way and 4-way matrices yield only four distinct solutions, as outlined in Table I. Because all the quadrature couplers employed in the 6-way and 4-way matrix configurations are deemed to not introduce transmission phase, phase shifters should additionally make up for the transition phase of couplers they are connecting with. With regard to the 4-way matrix in Fig. 4.1(b), the first port assignment in Table I(b) is equivalent to that of the conventional 4-way Butler matrix, based on account of the topology in this paper where we assume that all couplers, including crossovers ( $\theta_2=\pi/2$ ), as reflected on Eq. (4-2), have a  $90^\circ$  phase delay in the crossing path, while all the crossovers in a Butler matrix have no phase differences between the two output ports.

### 4.3 Configuration of 2-D 6×4-way matrix

The design of the 2-D 6×4-way matrix involves a hierarchical arrangement, as depicted in Fig. 4.2(a). The initial step entails placing the 6-way matrices horizontally (in the H-plane) and stacking them vertically (in the E-plane). These horizontally-placed matrices are connected to vertically-placed 4-way matrices, which are stacked horizontally. Each layer of the 6-way matrices is designated as  $H_n$ , representing the transmission matrix

specific to that layer. Similarly, the layers of the 4-way matrices are denoted as  $V_n$ , signifying the transmission matrix associated with each layer.

The transmission of the entire cascaded 2-D 6×4-way matrix can be expressed as,

$$T = H_1H_2H_3H_4H_5H_6H_7H_8H_9V_1V_2V_3V_4V_5V_6 \quad (4-4)$$

Considering the commutativity between the vertically-stacked and horizontally-stacked layers,

$$H_iV_k = V_kH_i \quad (4-5)$$

Consequently, 5005 permutations can be derived adjusting the order of each layer. To properly merge phase shifter layers in the 6-way matrix and 4-way matrix, the following transmission is adopted into the design,

$$T = (H_1V_1)H_2V_2(H_3V_3)H_4H_5H_6H_7V_4H_8V_5(H_9V_6) \quad (4-6)$$

The parentheses denote 2-D structure like two-plane coupler and merged phase shifters in two dimensions. In case with no pre-condition of fabrication limitation,  $H_2V_2$ ,  $H_7V_4$  and  $H_8V_5$  layers can also adopt two-plane couplers to further miniaturize the overall matrix body. Fig.4.2(b) provides a detailed perspective view of the three-dimensional (3-D) inner waveguide cavities of all the components comprising the 2-D 6×4-way matrix. This matrix operates at a center frequency of 28.25 GHz. In the  $(H_1V_1)$  layer, two-plane Hybrid couplers are employed. These couplers are with specific physical parameters, as outlined in [4-6]. The remaining couplers in the matrix are conventional H-plane or E-plane couplers. To ensure optimal performance, the input/output ports of each component are carefully designed to suppress higher modes, achieving attenuation levels below -40 dB. It should be noted that although the structure could be further simplified and miniaturized by incorporating more two-plane couplers, certain constraints associated with the CNC milling process have influenced the design choices. The frequency bandwidth of the targeted application is from 27.25 GHz to 29.25 GHz, corresponding to a 7.1% fractional bandwidth, which is difficult to achieve with the two-plane coupler

having rectangular notches. Hence the two-plane coupler with arbitrary shape of coupled region in [4-6] should be introduced to achieve the range of coupling needed while maintaining the targeted bandwidth. Unfortunately, this design approach is not compatible with the current CNC milling process combined with the mechanical design of the overall assembly, particularly when it involves cutting waveguides through their E-planes. As a matter of this, only at the first layer ( $H_1V_1$ ), two-plane coupler structure is introduced. To overcome this fabrication limitation, advanced manufacturing technologies such as 3-D printing [4-7] may be adopted in future iterations. Before the layer ( $H_1V_1$ ), a segment of oblique waveguides is introduced to realize a transition from the input ports to the matrix body, the size and spacing of which correspond to those of an existing 64-port coaxial-to-waveguide transformer, used for test purposes. The designed 2-D  $6 \times 4$ -way matrix only utilizes 24 ports of the transformer, while the remaining ones are left unconnected.

In this design, the 1<sup>st</sup> port assignment in the 6-way matrix and 1<sup>st</sup> port assignment in the 4-way matrix, as specified in Table 4.1, are utilized alongside their corresponding phase shift values. However, it is important to note that the phase shifters in layers ( $H_3V_3$ ),  $H_6$ , and ( $H_9V_6$ ) serve a dual purpose. They not only introduce the desired phase shift value as per the design requirements but also compensate for the transmission phase introduced by the couplers and oblique waveguides they are connected to.

#### **4.4 Experimental results of 2-D $6 \times 4$ -way matrix**

The performance evaluation of the 2-D  $6 \times 4$ -way matrix is conducted in two stages. The first stage involves analyzing the S-parameters of the complete 48-port network through simulation. The second stage focuses on assessing the radiation characteristics of the open-ended 24-port network. In this configuration, the output ports radiate directly into free space without the use of external antennas. Both simulation and measurement techniques are employed to verify the radiation performance. It is important to note that the extensive nature of a comprehensive experimental verification for the entire matrix is time-consuming. Therefore, measurements were primarily conducted in the most relevant configuration, which corresponds to the radiating scenario.

The input and output ports of the 2-D 6×4-way matrix, as depicted in Fig. 4.3, are numbered from 1 to 24 and 25 to 48, respectively. In order to validate the performance of the entire matrix, the analysis focuses on investigating cases where incidence is from a quarter of the input ports. Specifically, the performance is thoroughly examined for Port 1, 2, 3, 7, 8, and 9, as defined in Fig. 4.3(a). This approach takes into account the 2-D symmetry of the matrix with respect to the transverse directions, allowing for comprehensive validation of its functionality.

Fig. 4.4 presents the S-parameters of the 48-port network over a frequency range of 27.25 GHz to 29.25 GHz, considering incidence from Port 1 and Port 9 as examples. The parameters examined include reflection and isolations at the input ports, output amplitudes, and phase differences with reference to Port 25 of Ports 26, 27, 28, 29 and 30 in the horizontal and Ports 31, 37 and 43 in the vertical directions.

In Fig. 4.4(a1), the reflections and isolations at the input ports are mostly suppressed below -15 dB, with a few exceptions that reach a higher level but still remain below -10 dB. Moving to Fig. 4.4(a2), the output amplitudes are centered around -13.8 dB, which corresponds to the expected value in decibels for equal power division across 24 ports. Although some outputs exhibit larger deviations, even dipping below -20 dB, it is important to note that these deviations are expected to have minimal impact on the overall field distribution and radiation performance, considering the collective behavior of all 24 ports.

In Fig. 4.4(a3) and (a4), the phase differences with reference to Port 25 remain stable and closely aligned with the ideal distribution, except for values in the vertical direction for incidence from Port 1 in the upper frequency range analyzed. It is interesting to observe that although the simulated values deviate from the theoretical ones, the trend is consistent across all reported ports (Ports 31, 37, and 43). This suggests that the deviation originates solely from the reference Port 25. Similarly to the amplitude dispersion, these larger deviations affecting only a few ports are anticipated to have limited impact on the overall phase distribution at the output ports, and consequently on the radiation performance.

Utilizing the S-parameters obtained from the comprehensive model, the performance of the 2-D 6×4-way matrix by examining additional crucial indicators such as insertion loss and conductor loss can be assessed. The insertion loss ( $IL$ ) corresponding to incidence from Port  $n$  is defined as,

$$IL_n = 1 / \sum_{i=25}^{48} |S_{in}|^2 \quad (4-7)$$

While the conductor loss ( $CL$ ) corresponding to incidence from Port  $n$  is,

$$CL_n = 1 / \sum_{i=1}^{48} |S_{in}|^2 \quad (4-8)$$

Fig. 4.5 provides the insertion loss and conductor loss of the proposed 2-D 6×4-way matrix over the entire operational bandwidth. The matrix is constructed using aluminum as the material, with a known electrical conductivity of 38,000,000 S/m. The total length of the matrix, including the transition from the input ports to the layer ( $H_1V_1$ ) as depicted in Fig. 4.2, measures approximately 650 mm. The numerical results demonstrate that the conductor loss remains consistently stable, averaging around 0.6 dB throughout the frequency range. This value is comparable to previous studies [4-8][4-9], also demonstrating the reliabilities of the results. Furthermore, the insertion loss of the matrix is generally below 2 dB, highlighting its excellent signal transmission capabilities. While Port 4 exhibits slightly higher values to break through this threshold, reaching around 2.2 dB at the upper frequency 29.25 GHz, it remains within a reasonable deviation. This minor variation is not anticipated to significantly impact the radiation performance of the matrix.

Fig. 4.6 shows a comprehensive overview of the reflections and isolations at the input ports when the output ports of the matrix are directly radiating into free space. The presented data has been carefully post-processed to eliminate the influence of the insertion loss introduced by the coaxial-to-waveguide transformer. It is important to note that the open-ended waveguides at the output ports have dimensions of 6.8 mm×3.21 mm, with a spacing of 7.8 mm (equivalent to  $0.73\lambda$ ) in the H-plane and 6.9 mm (equivalent to  $0.65\lambda$ ) in the E-plane directions. Considering the closely-spaced nature of the output ports,



strong port-to-port coupling is anticipated. This coupling can potentially result in differences in the reflections and isolations compared to the ideal matched conditions depicted in Fig. 4.5(a1) and (b1). As a consequence, the data presented in Fig. 4.6 provides a more realistic representation of the actual operating performance of the matrix. Notably, the reflections and isolations at the input ports, as depicted in Fig. 4.6, remain consistently below -10 dB. This demonstrates the matrix's effectiveness in suppressing unwanted signal reflections and maintaining a high level of isolation among the input ports. By taking into account the actual operating conditions, these results offer valuable insights into the matrix's performance in real-world scenarios.

Fig. 4.7 presents the setup used for planar scanning near-field measurements to verify the radiation performance of the proposed 2-D 6×4-way matrix. The measurements are conducted in a controlled environment, with the matrix loaded inside a chamber surrounded by absorbers to minimize unwanted reflections. To ensure stability and precise positioning of the matrix during the measurements, specialized fixtures are employed to securely support the matrix body. These fixtures not only provide mechanical support but also maintain the desired alignment and orientation of the matrix.

Fig. 4.8 showcases the contour plots at -3.9 dB below the peak directivity of each beam at the central frequency of 28.25 GHz, offering a comprehensive visual representation of the radiation characteristics of the 2-D 6×4-way matrix. The contours exhibit the spatial distribution of the main lobes as well as the grating lobes for each beam. The values associated with the peak directivity, as well as the corresponding elevation and azimuth angles, are summarized in Table 4.2. The definitions of  $k_x$  and  $k_y$  are  $\sin \theta \cos \varphi$  and  $\sin \theta \sin \varphi$ , respectively. The largest directivity corresponds to Beam 2 with 21.3 dBi in measurement and 21.1 dBi in simulation. The minimum directivity is 17.7 dBi reached by Beam 1 in measurement, with a tilted angle of  $34^\circ$  deviating from zenith, with 3.4dB scan loss, while in simulation, it is 16.0 dBi obtained at Beam 7, inclining  $52^\circ$  from zenith corresponding to 5.1 dB scan loss. Scan loss for all beams is expected to be compensated by future employment of more isotropic external antenna in lieu of open-ended waveguide.

Upon close examination of Fig. 4.8, it becomes evident that the contour shapes of the main lobes for each beam demonstrate remarkable consistency between the measurement and simulation results. This high level of agreement is further confirmed by the values provided in Table 4.2, where the angular deviations in elevation and azimuth angles between the measured and simulated data remain within a narrow range of  $5^\circ$  or less. Regarding the presence of grating lobes, Beams 1 and 7 exhibit grating lobes primarily in the  $k_x$  direction, while Beams 8 and 9 generate grating lobes in the  $k_y$  direction. Notably, the grating lobes associated with Beams 1 and 7 are barely discernible at the -3.9 dB level in the measurement. Analyzing the directivity values, Beams 1, 2, 3, and 8 exhibit excellent agreement between the simulation and measurement data, with deviations of no more than 0.9 dB. Beam 9 demonstrates a slightly larger discrepancy of 1.7 dB, while Beam 7 displays the largest deviation of up to 3.8 dB. The deviation for Beam 7 can be attributed to the challenges associated with accurately measuring large-angle tilted beams using planar scanning near-field techniques. These challenges arise from truncation effects, especially as Beam 7 corresponds to significant phase differences in two orthogonal directions of the matrix, as in the H-plane of  $5\pi/6$  and in the E-plane of  $-3\pi/4$ , both of which stand for the largest phase differences in either direction of the matrix. In order to provide a comprehensive view of the radiation pattern,

Fig. 4.9 presents the full contour map of all 24 beams, achieved by mirror-duplicating quarter 6 beams. This visualization offers a holistic understanding of the radiation characteristics, highlighting the symmetry and spatial position for all beams. Crossover of each adjacent beam, especially lined in  $k_y$  direction can be observed. This is mainly attributed to array factor, as number of elements in  $k_x$  direction as 6 is larger than that in  $k_y$  direction as 4, leading to wider beamwidth in  $k_y$  direction and subsequent higher crossover level. And radiation element adopted as open-ended waveguide in this design may have a minor influence as well, since it is not ideally isotropic radiation source, and it could lead to strong port-to-port coupling at output port, which will potentially affect array factor. Further decreasing of distance of each radiation element in  $k_y$  direction would be expected to improve crossover level among adjacent beams. Meanwhile,

antenna array with triangular lattice of beams will showcase much lower crossover level than rectangular lattice of beams. This methodology could be introduced in future improvement of this 2-D 6×4-way matrix by externally introducing some network to convert rectangular lattice of beams to triangular lattice of beams.

The radiation patterns at the center frequency 28.25GHz, are given in Fig. 4.10 for selected quarter 6 beams, by fixing  $k_x$  of peak for each beam and scanning along the  $k_y$  direction(quasi E-plane), or alternatively fixing  $k_y$  of peak for each beam and scanning along the  $k_x$  direction(quasi H-plane). The beam shapes and trends in measurement are concurring well with those in simulation. The sidelobe levels of Beams 1 and 7, as observed in Fig. 4.10(a) and (c), exhibit lower values in the measurement data compared to the simulation. This reduction in sidelobe levels ultimately leads to the sidelobes in Fig. 4.8 disappearing. This is mainly due to low accuracy by planar-scanning near field measurement for large angle tilted beam, as known as truncation effect.

Table 4.3 provides a detailed comparison of this work with other related works, particularly putting emphasis on the comparison of waveguide-type matrices to show the difference on performance as a function of the numbers of beams. Compared with the 2-D 4×4-way Butler matrix in [4-8] and the 2-D 8×8-way Butler matrix in [4-9], the proposed 2-D 6×4-way matrix has intermediate insertion loss, which is justifiable as a result of corresponding number of ports and as well as the network complexity.

Table 4.3 presents a comprehensive comparison between this study and other relevant works, with a particular focus on waveguide-type matrices. The comparison highlights the performance differences observed across various beam numbers, as compared with the 2-D 4×4-way Butler matrix in [4-8] and the 2-D 8×8-way Butler matrix in [4-9], the proposed 2-D 6×4-way matrix has intermediate insertion loss, which is justifiable as a result of corresponding number of ports and as well as the network complexity.

## 4.5 Conclusion remarks

This chapter has introduced a 2-D hollow waveguide 6×4-way beam switching matrix working from 27.25 GHz to 29.25 GHz, counterpart to a 7.1% fractional bandwidth. This

is the first time that a 2-D waveguide beam-switching matrix is proposed with different number of beams in two orthogonal directions. Attributing to the 2-D symmetry in the transverse directions, the design complexity of the 2-D 6×4-way matrix is significantly reduced to quarter solely.

The 2-D 6×4-way matrix demonstrates excellent performance, with insertion loss ranging up to a maximum of 2.2 dB across the entire operational bandwidth. The radiation performance of the matrix is verified through planar scanning near-field measurements, providing valuable insights into its directivity characteristics.

The highest directivity is achieved by Beam 2, with an impressive value of 21.3 dBi in measurement and 21.1 dBi in simulation. On the other hand, Beam 1 exhibits the minimum directivity in measurement, reaching 17.7 dBi, accompanied by a tilted angle of 34° with reference to the boresight, corresponding to a scan loss of 3.4 dB. In simulation, the minimum directivity of 16.0 dBi is obtained for Beam 7, which is inclined at an angle of 52° relative to the boresight, resulting in a scan loss of 5.1 dB. It is worth noting that Beam 7 showcases the largest discrepancy 3.8dB between measurement and simulation, with the measured results showing 19.8 dBi in directivity, 1.5 dB in scan loss, and a tilted angle of 48° with reference to the boresight. The scan loss observed in the tilted beam configuration can be potentially compensated in future applications through the utilization of isotropic radiation elements.

This 2-D 6×4-way matrix may be improved in future works by embracing alternative manufacturing techniques and capitalizing on the specific fabrication on two-plane couplers, such as 3-D printing [4-7], to enable further physical miniaturization and complexity reduction by employing more two-plane couplers to replace the conventional H-plane and E-plane couplers.

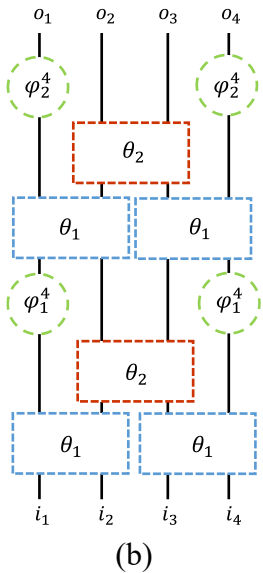
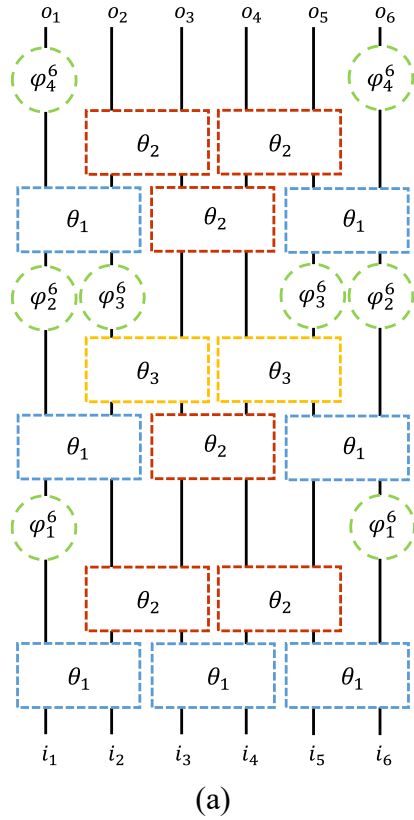


**Fig. 4.1.** (a) 6-way matrix. (b) 4-way matrix.  $\theta_1 = \pi/4$ ,  $\theta_2 = \pi/2$  and  $\theta_3 = \arccos(-1/3)$  in Eq. (4-2)

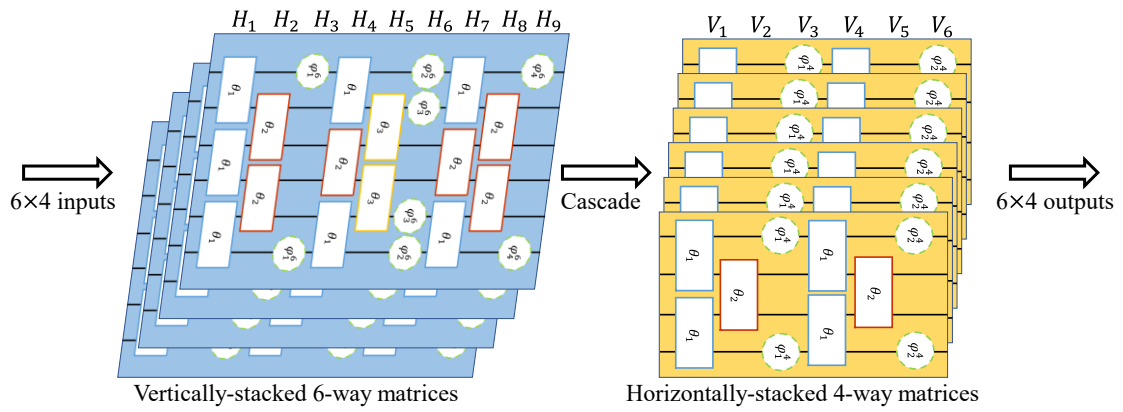
**TABLE 4.1**  
**Port assignments with corresponding phase shifters**

(A) 6-way matrix

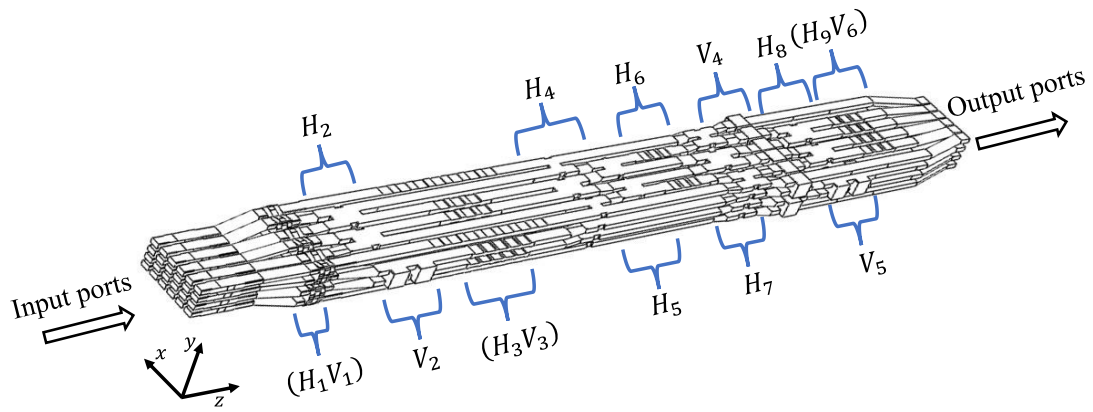
$[p_1, p_2, p_3, p_4, p_5, p_6]$	$\varphi_1^6$	$\varphi_2^6$	$\varphi_3^6(\varphi_4^6)$
$[\frac{5\pi}{6}, \frac{-\pi}{6}, \frac{-3\pi}{6}, \frac{3\pi}{6}, \frac{\pi}{6}, \frac{-5\pi}{6}]$	0	$\frac{-5\pi}{6}$	$\frac{-\pi}{3}$
$[\frac{\pi}{6}, \frac{-5\pi}{6}, \frac{-3\pi}{6}, \frac{3\pi}{6}, \frac{5\pi}{6}, \frac{-\pi}{6}]$	0	$\frac{5\pi}{6}$	$\frac{\pi}{3}$
$[\frac{-\pi}{6}, \frac{5\pi}{6}, \frac{-3\pi}{6}, \frac{3\pi}{6}, \frac{-5\pi}{6}, \frac{\pi}{6}]$	$\pi$	$\frac{-5\pi}{6}$	$\frac{-\pi}{3}$
$[\frac{-5\pi}{6}, \frac{\pi}{6}, \frac{-3\pi}{6}, \frac{3\pi}{6}, \frac{-\pi}{6}, \frac{5\pi}{6}]$	$\pi$	$\frac{5\pi}{6}$	$\frac{\pi}{3}$

(B) 4-way matrix

$[p_1, p_2, p_3, p_4]$	$\varphi_1^4$	$\varphi_2^4$
$[\frac{\pi}{4}, \frac{-3\pi}{4}, \frac{3\pi}{4}, \frac{-\pi}{4}]$	$\frac{-\pi}{4}$	$\frac{\pi}{2}$
$[\frac{3\pi}{4}, \frac{-\pi}{4}, \frac{\pi}{4}, \frac{-3\pi}{4}]$	$\frac{\pi}{4}$	$-\frac{\pi}{2}$
$[\frac{-\pi}{4}, \frac{3\pi}{4}, \frac{-3\pi}{4}, \frac{\pi}{4}]$	$\frac{-3\pi}{4}$	$\frac{-\pi}{2}$
$[\frac{-3\pi}{4}, \frac{\pi}{4}, \frac{-\pi}{4}, \frac{3\pi}{4}]$	$\frac{3\pi}{4}$	$\frac{\pi}{2}$



(a)



(b)

**Fig. 4.2.** (a) Direct cascading of vertically-stacked 6-way matrices and horizontally-stacked 4-way matrices. (b) Perspective view of 3-D inner waveguide cavities of the proposed 2-D 6x4-way matrix.

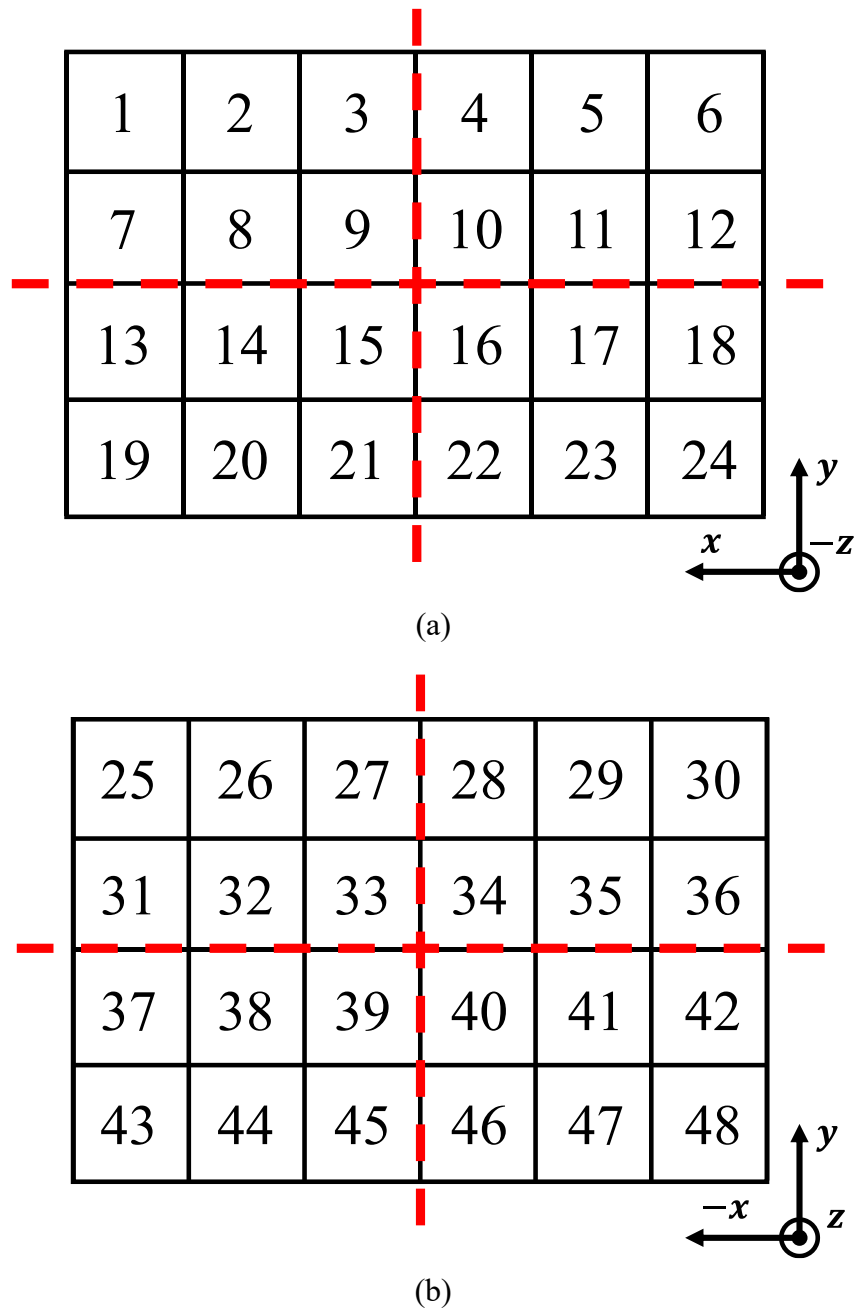
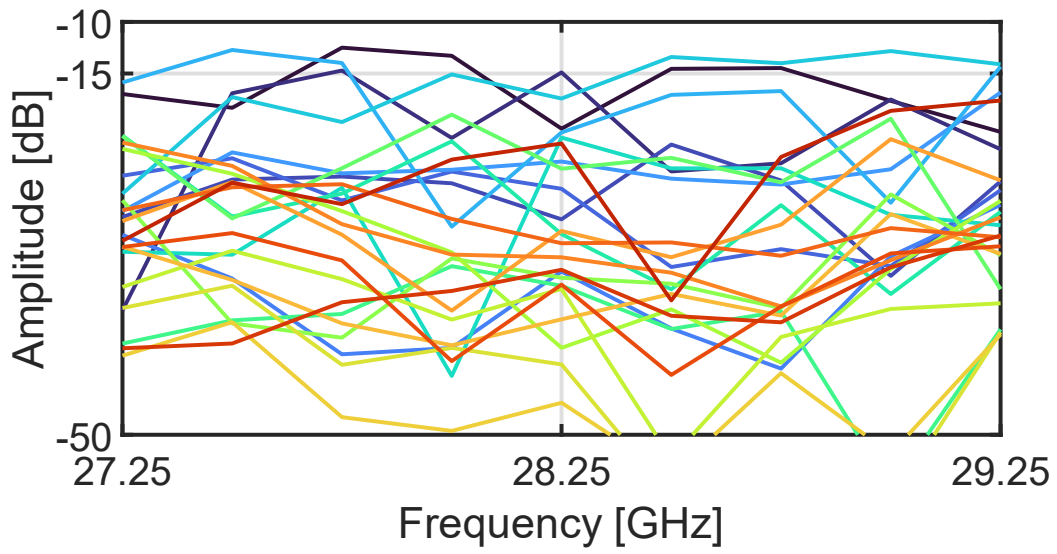
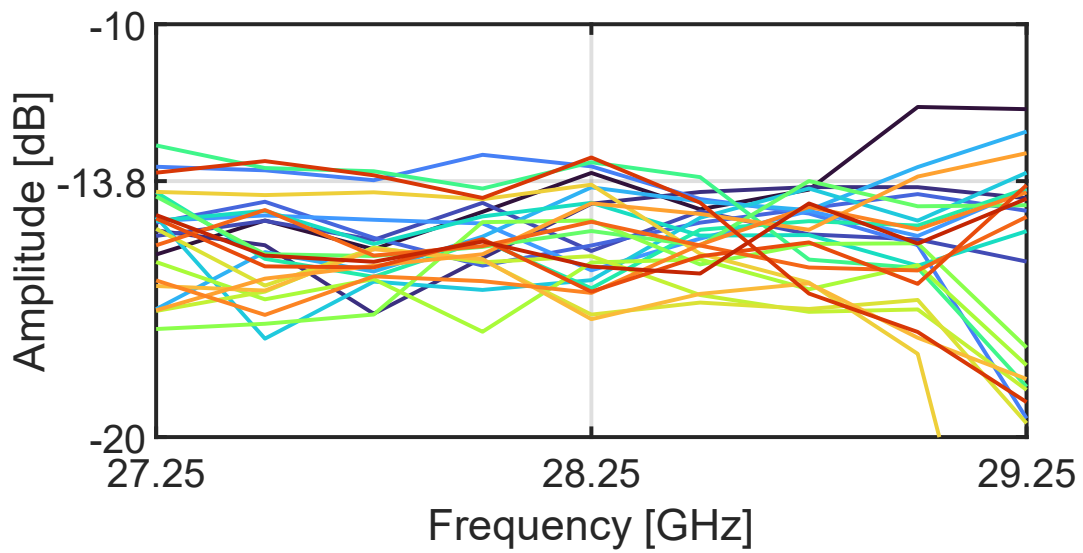


**Fig. 4.3.** Port numbering of (a) input ports and (b) output ports. Red dotted line: symmetrical axes.

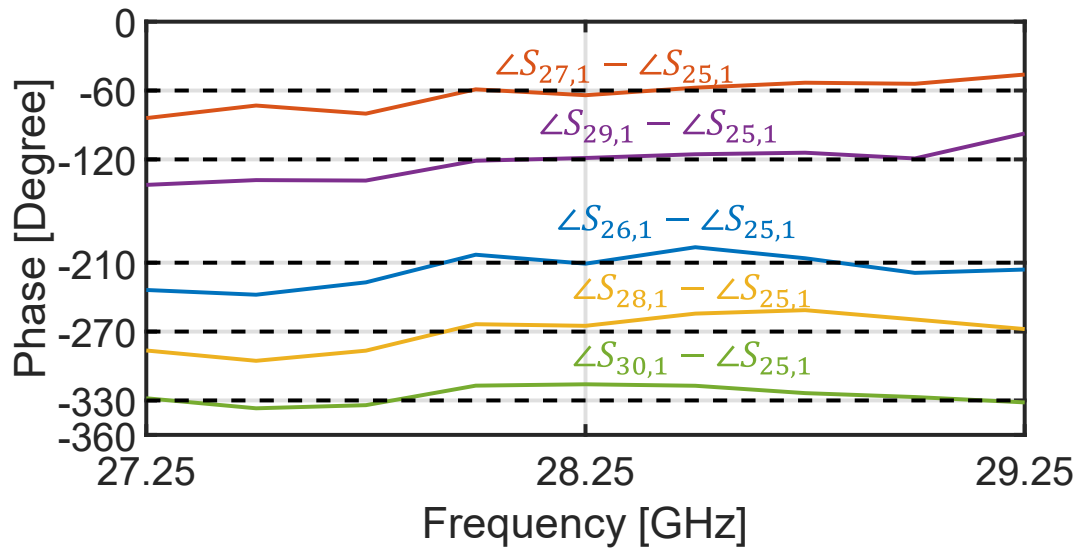




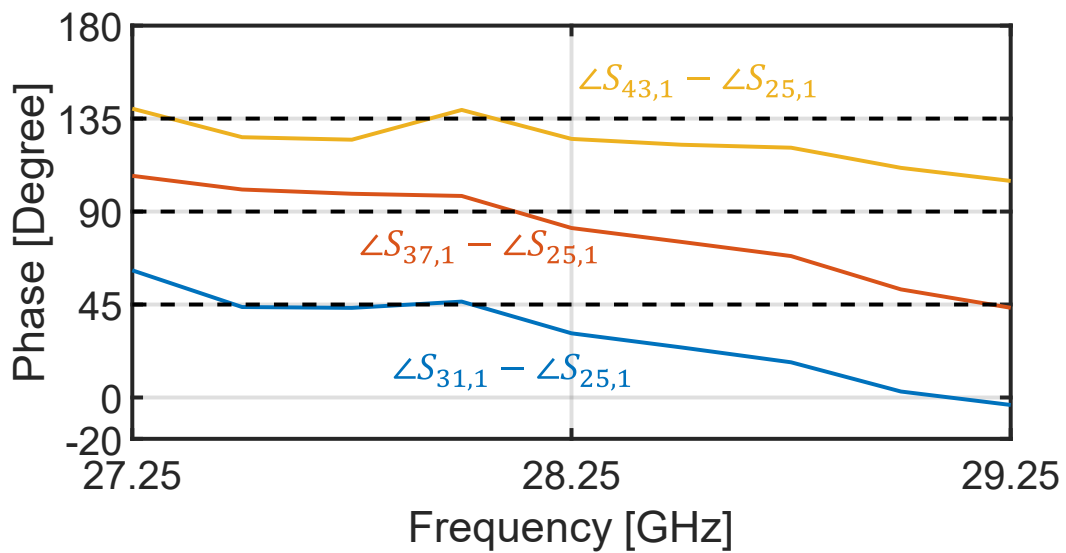
(a1) Reflection and isolations corresponding to incidence from Port 1.



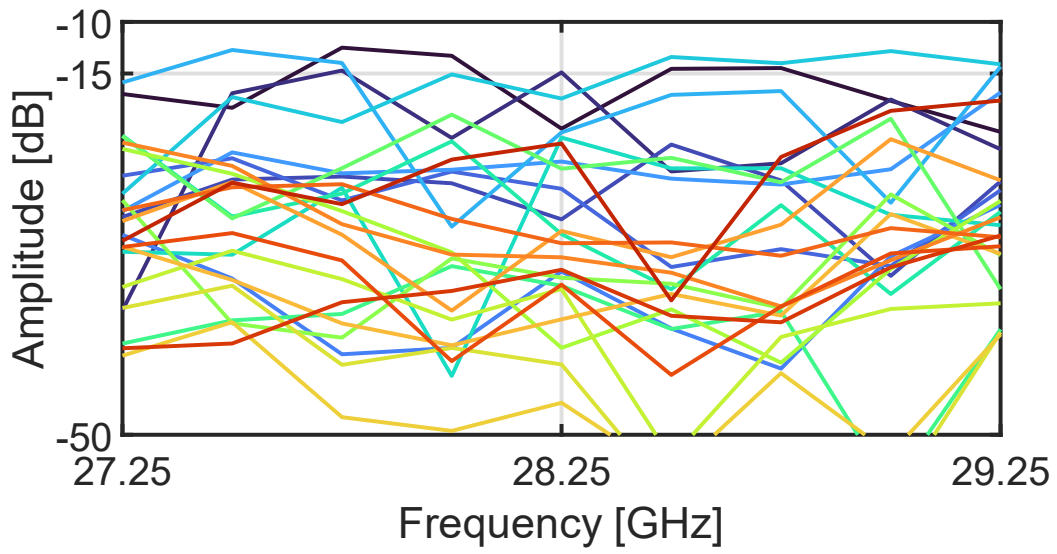
(a2) Output amplitude corresponding to incidence from Port 1.



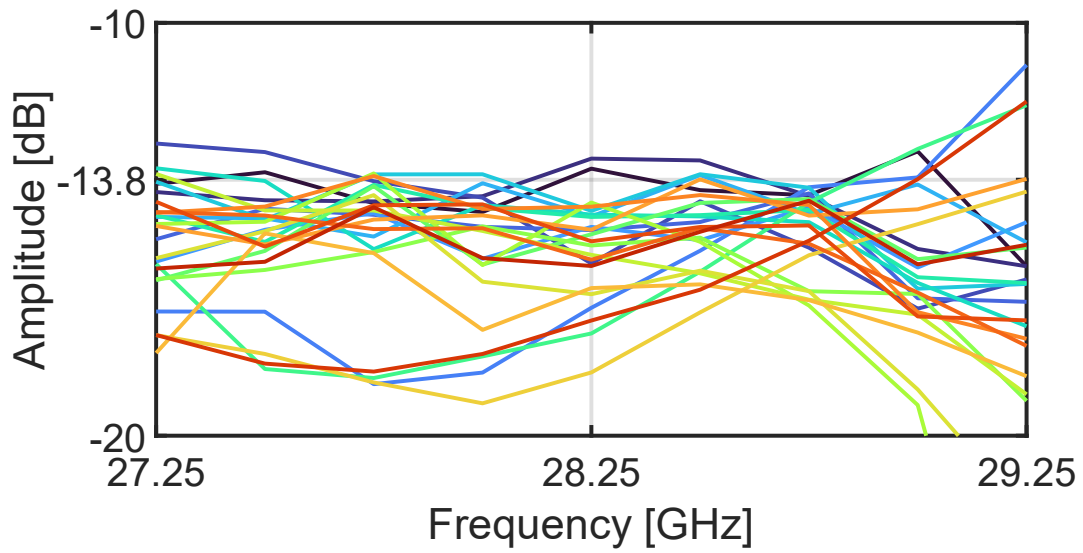
(a3) Phase difference with reference to Port 25 in the horizontal direction corresponding to incidence from Port 1.



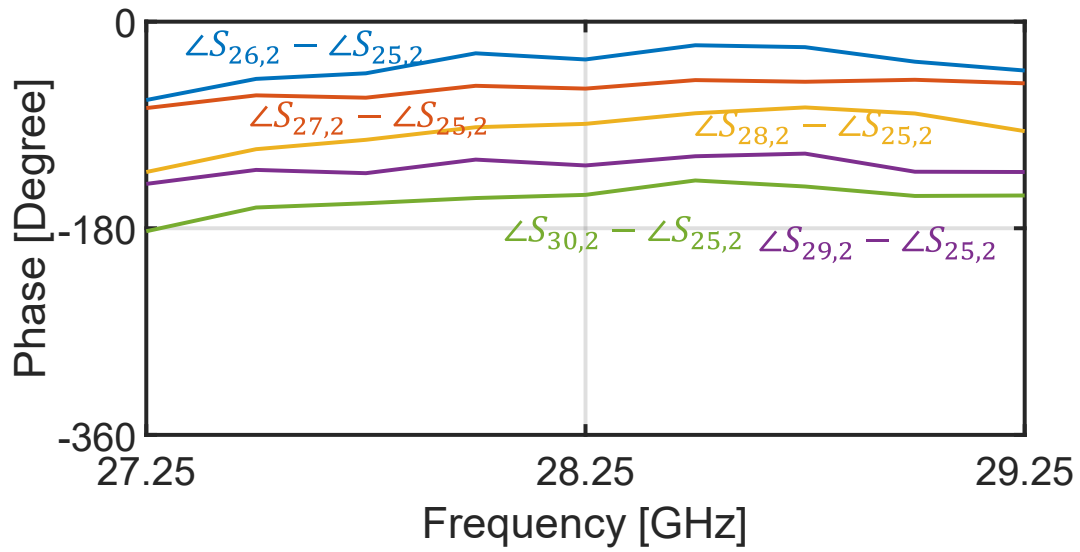
(a4) Phase difference with reference to Port 25 in the vertical direction corresponding to incidence from Port 1.



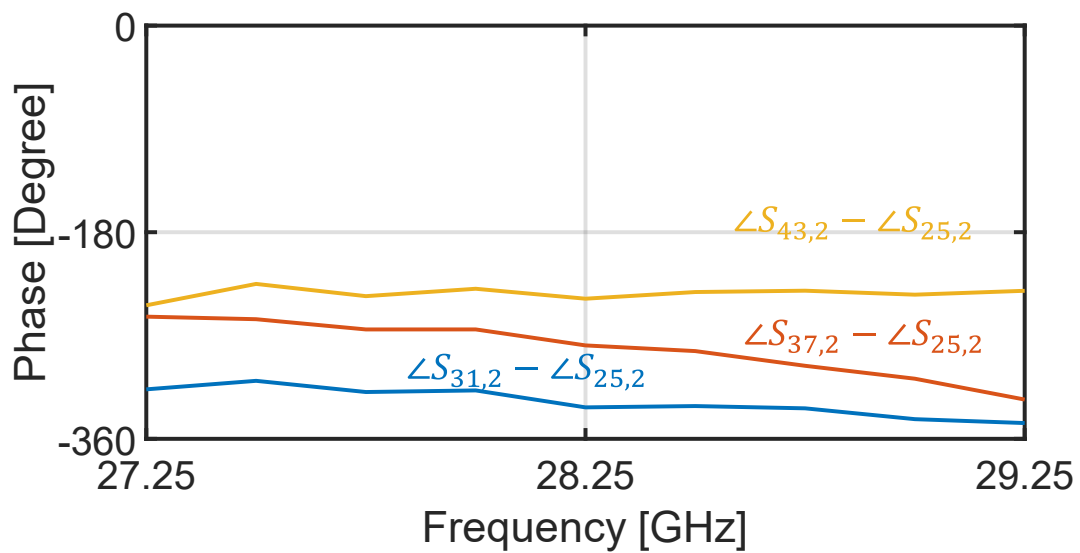
(b1) Reflection and isolations corresponding to incidence from Port 2.



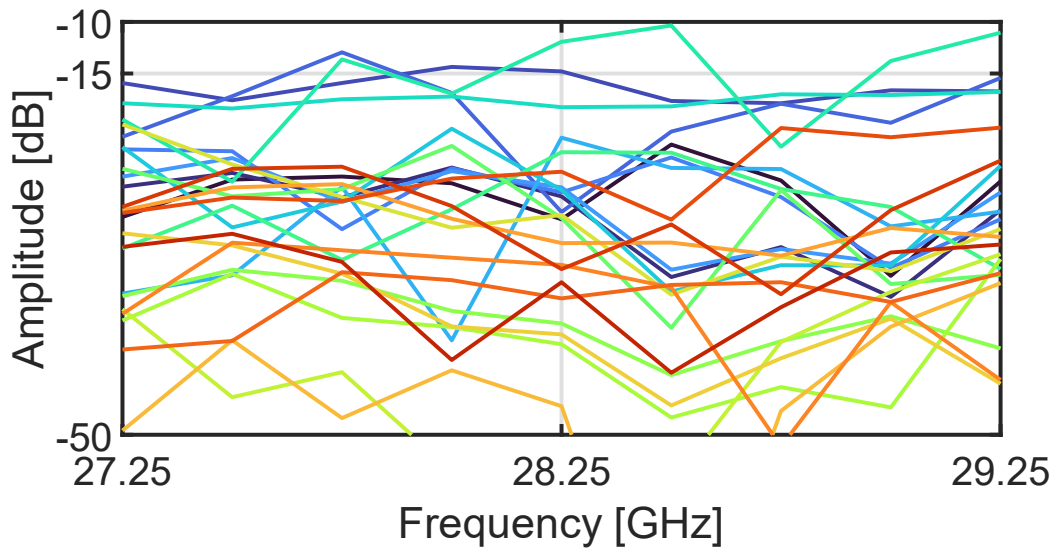
(b2) Output amplitude corresponding to incidence from Port 2.



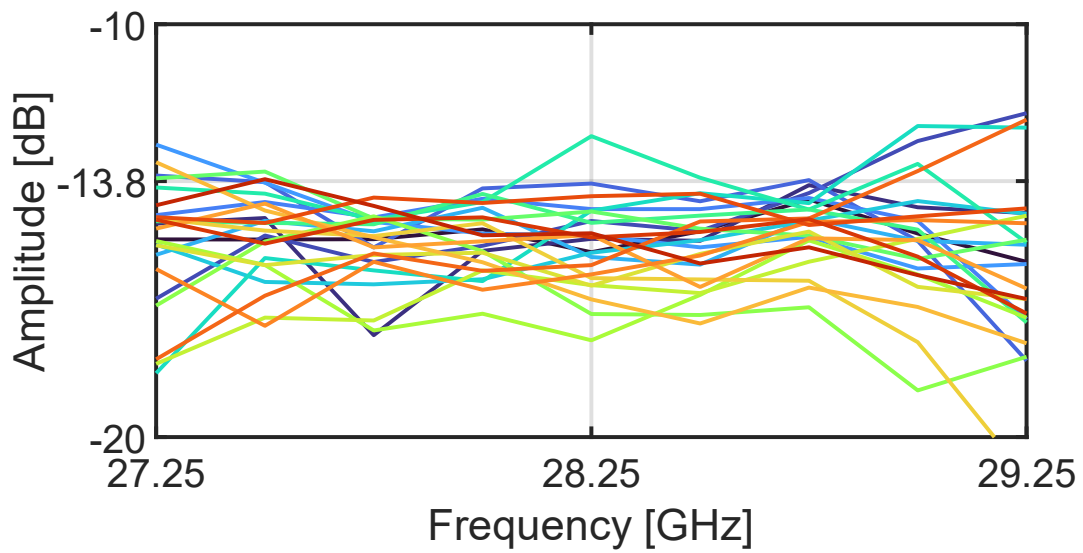
(b3) Phase difference with reference to Port 25 in the horizontal direction corresponding to incidence from Port 2.



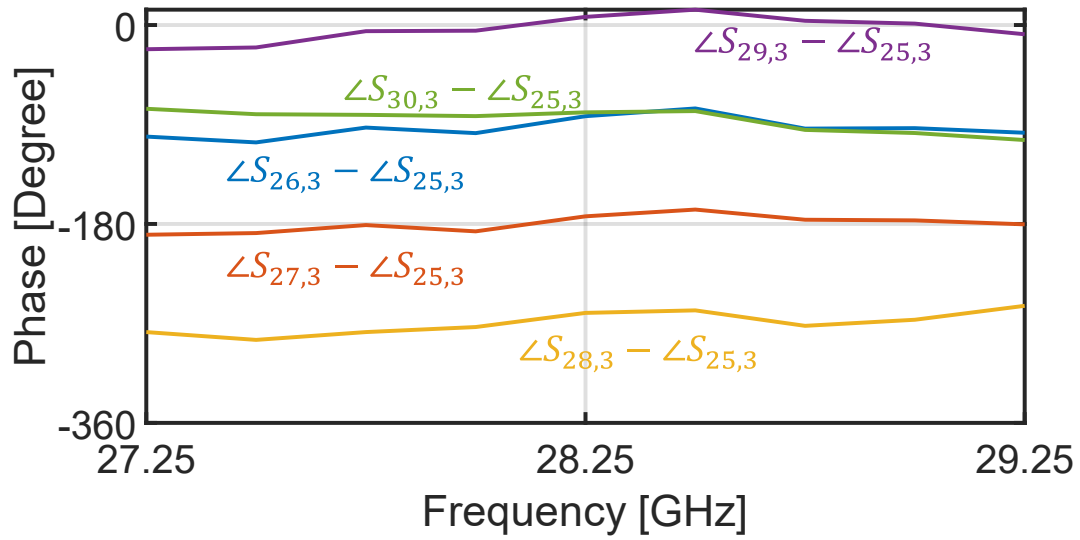
(b4) Phase difference with reference to Port 25 in the vertical direction corresponding to incidence from Port 2.



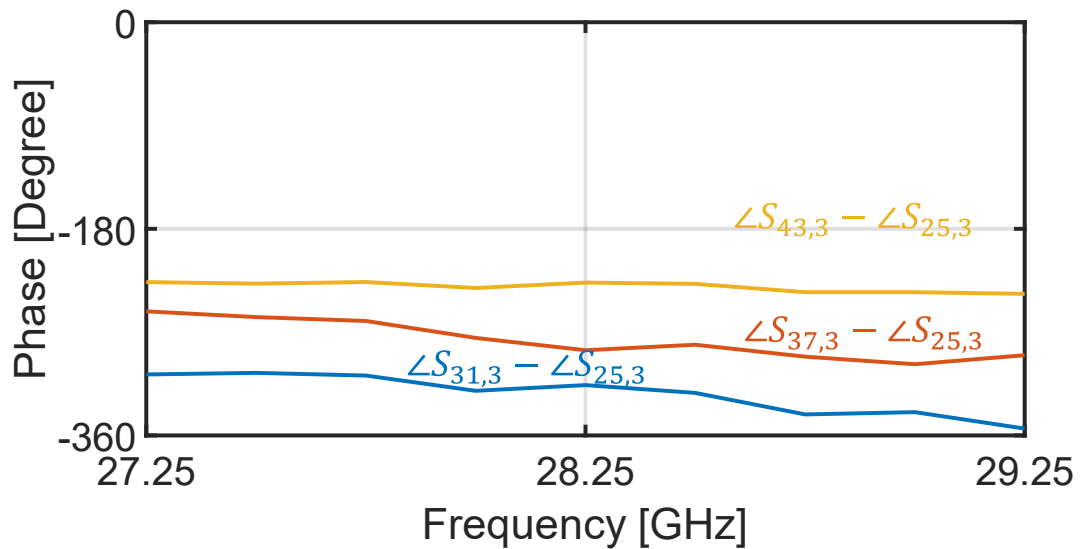
(c1) Reflection and isolations corresponding to incidence from Port 3.



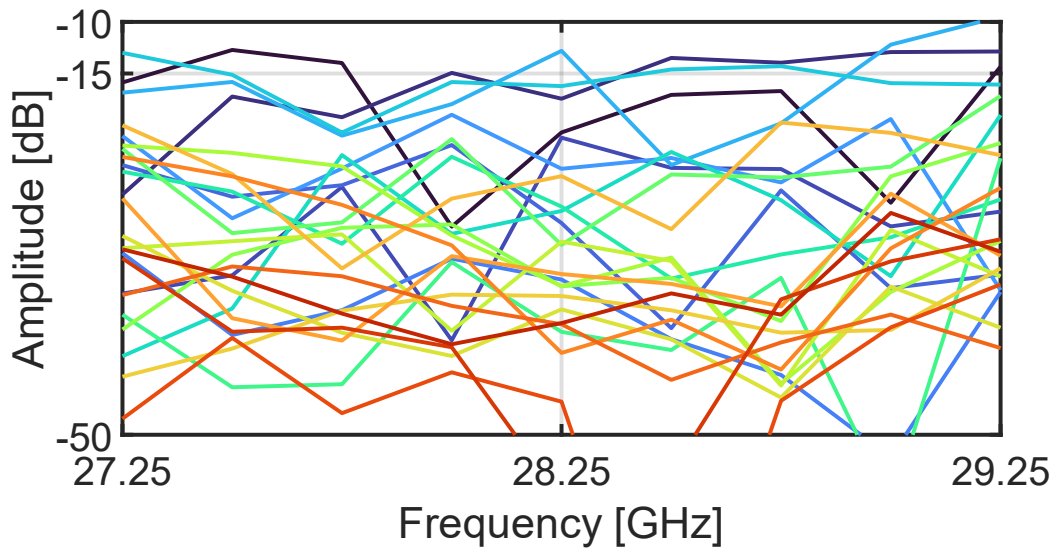
(c2) Output amplitude corresponding to incidence from Port 3.



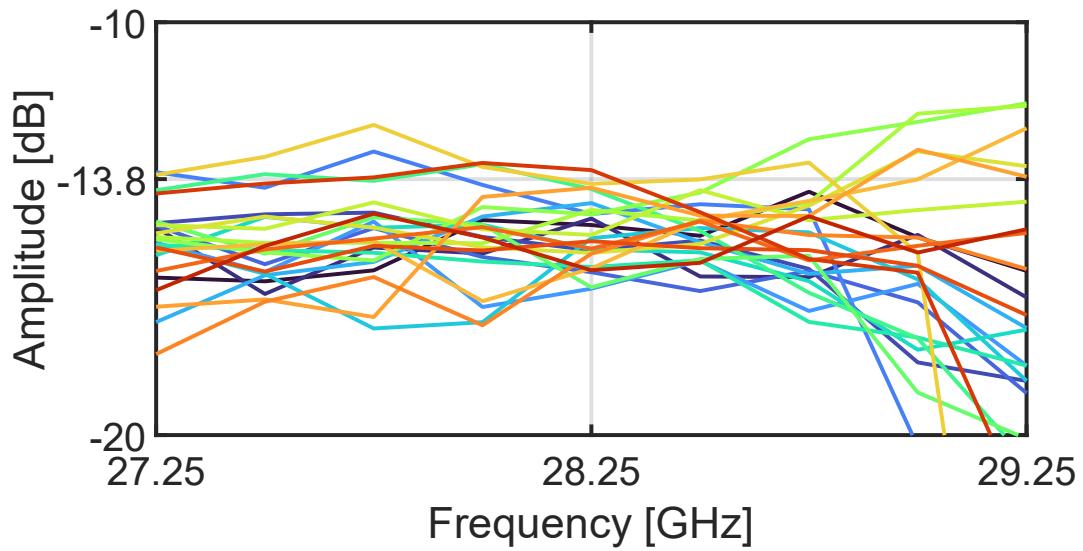
(c3) Phase difference with reference to Port 25 in the horizontal direction corresponding to incidence from Port 3.



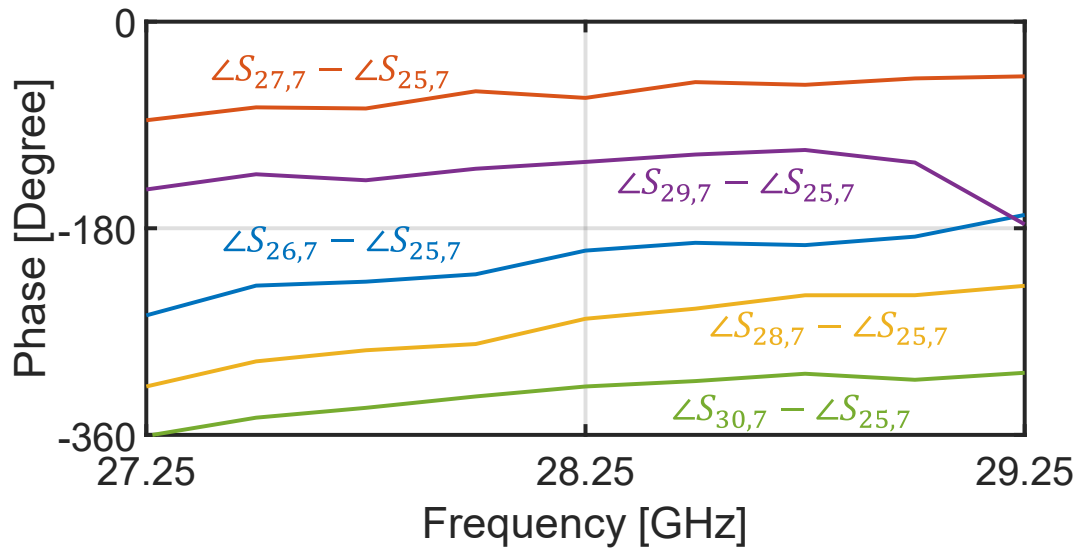
(c4) Phase difference with reference to Port 25 in the vertical direction corresponding to incidence from Port 3.



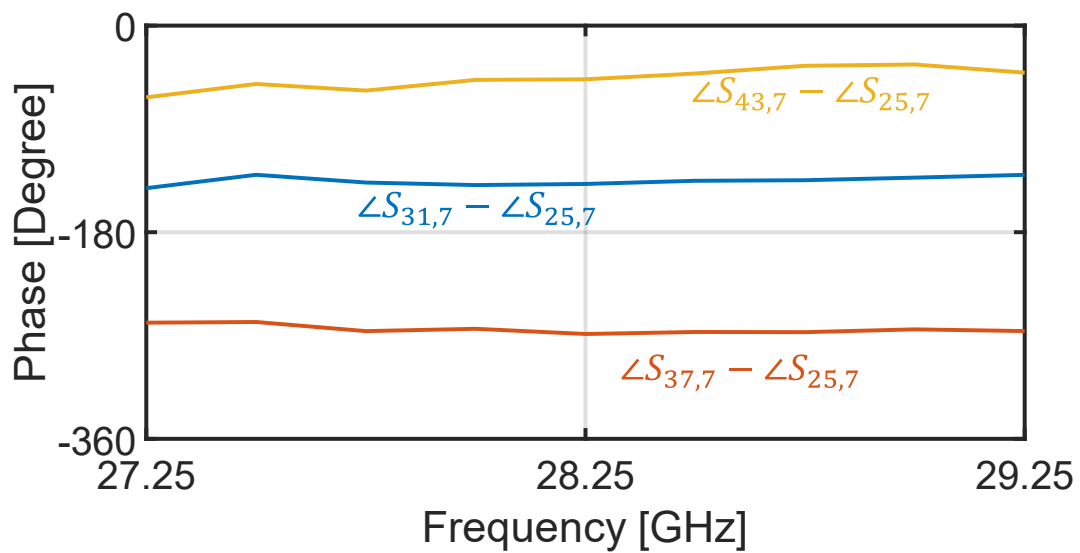
(d1) Reflection and isolations corresponding to incidence from Port 7.



(d2) Output amplitude corresponding to incidence from Port 7.

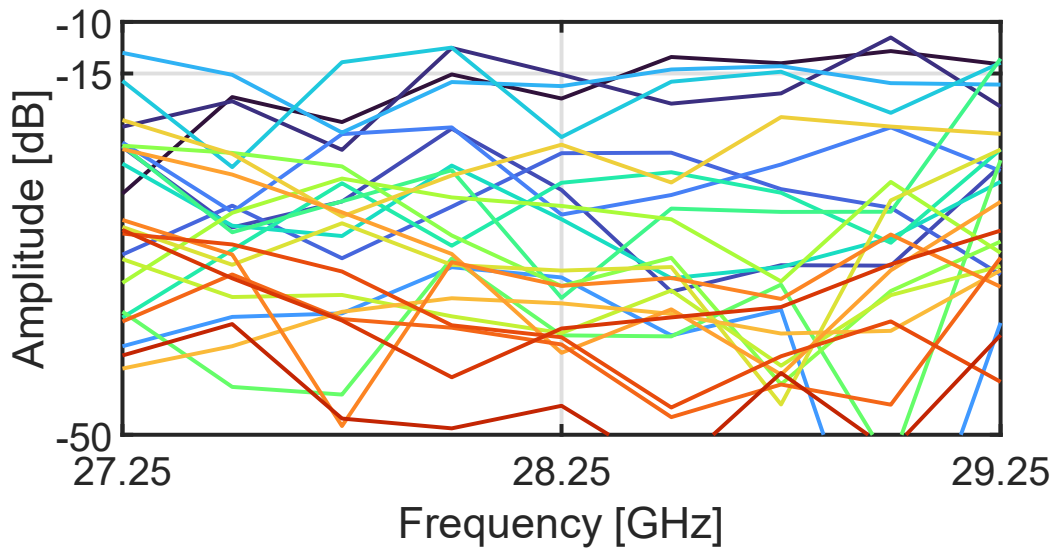


(d3) Phase difference with reference to Port 25 in the horizontal direction corresponding to incidence from Port 7.

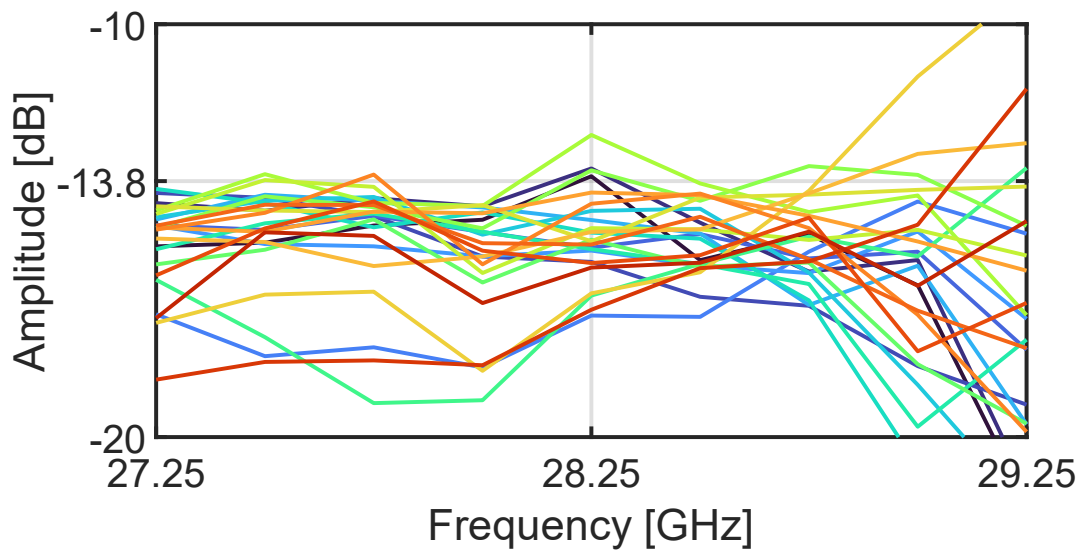


(d4) Phase difference with reference to Port 25 in the vertical direction corresponding to incidence from Port 7.

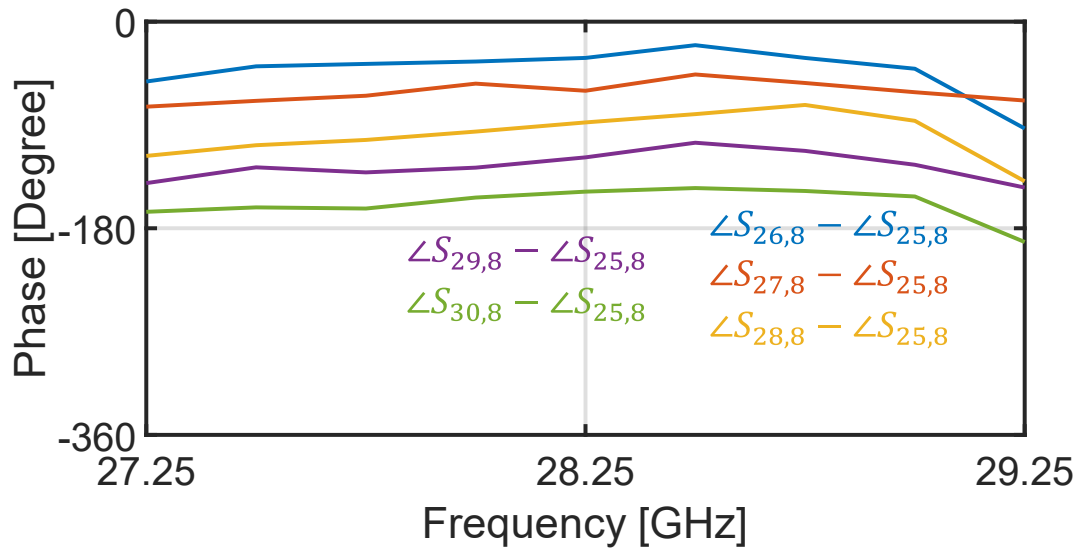




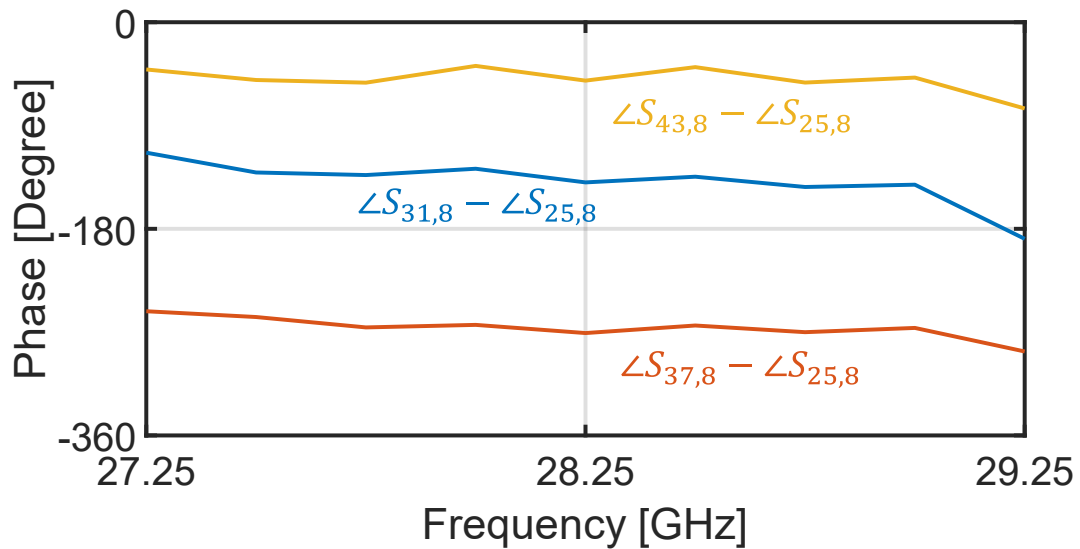
(e1) Reflection and isolations corresponding to incidence from Port 8.



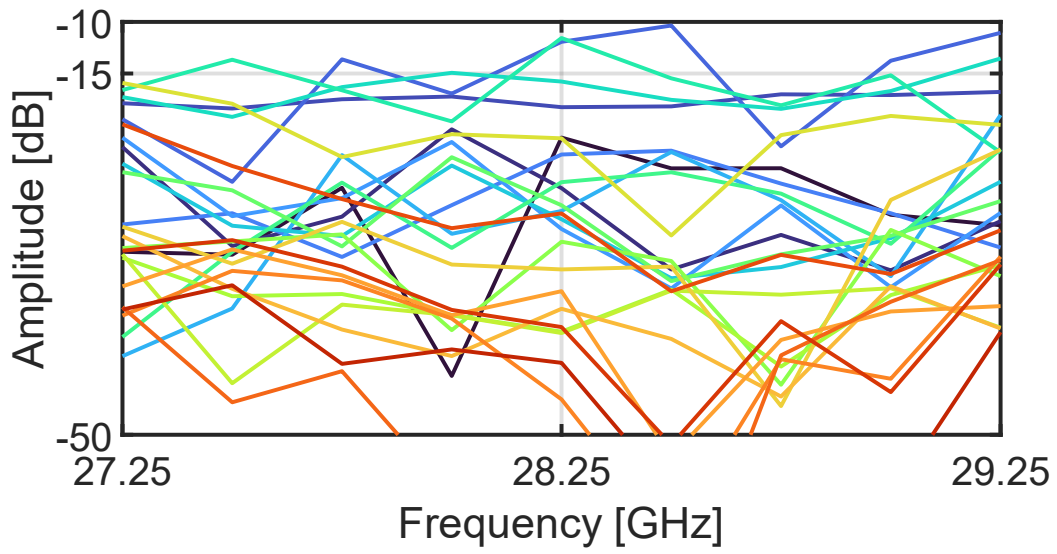
(e2) Output amplitude corresponding to incidence from Port 8.



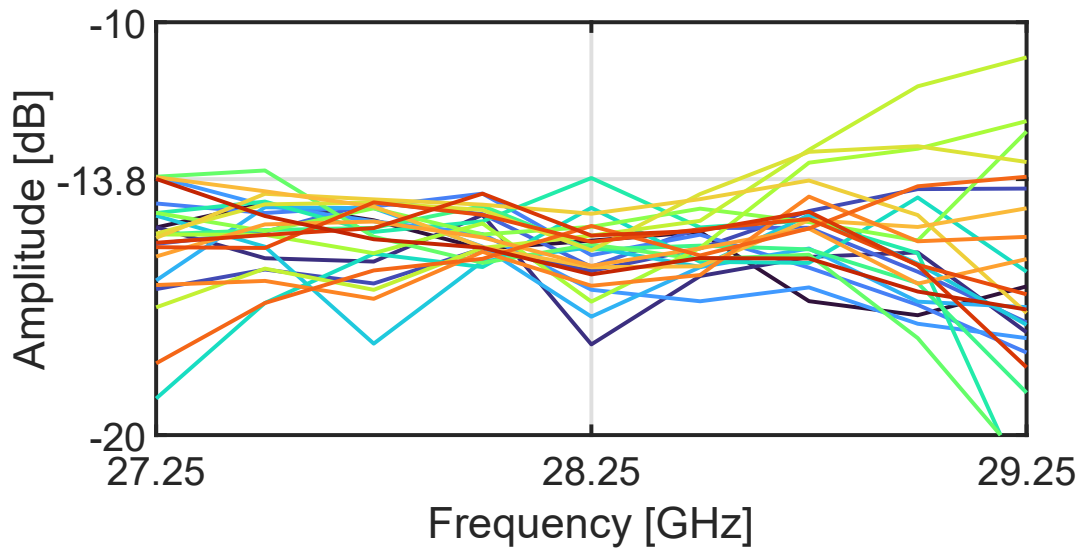
(e3) Phase difference with reference to Port 25 in the horizontal direction corresponding to incidence from Port 8.



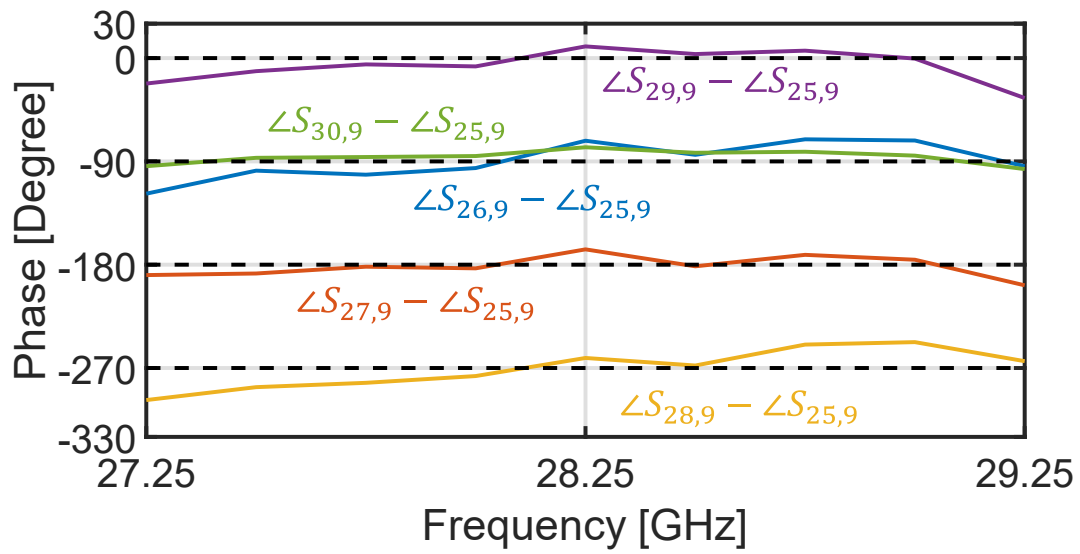
(e4) Phase difference with reference to Port 25 in the vertical direction corresponding to incidence from Port 8.



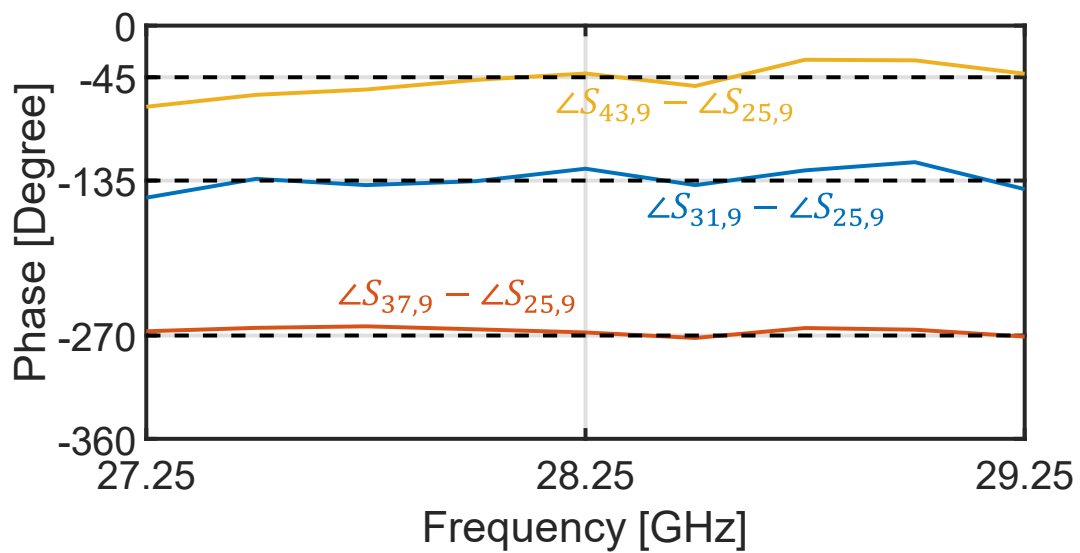
(f1) Reflection and isolations corresponding to incidence from Port 9.



(f2) Output amplitude corresponding to incidence from Port 9.

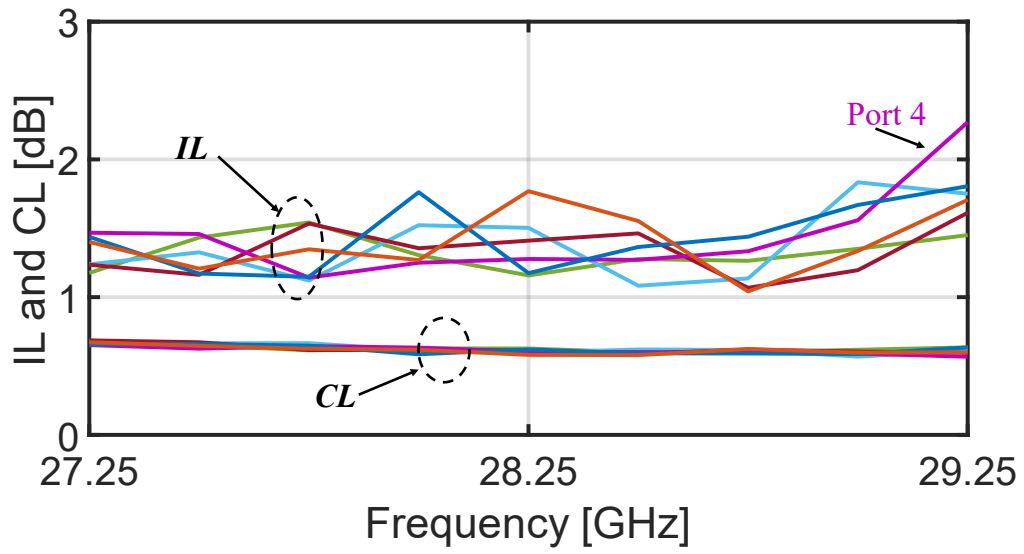


(f3) Phase difference with reference to Port 25 in the horizontal direction corresponding to incidence from Port 9.

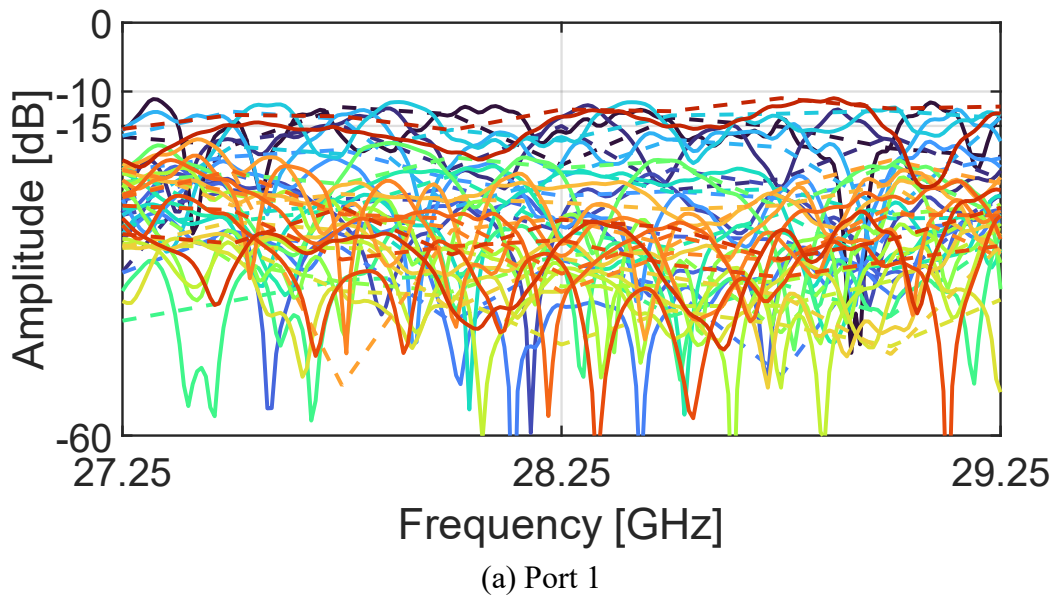


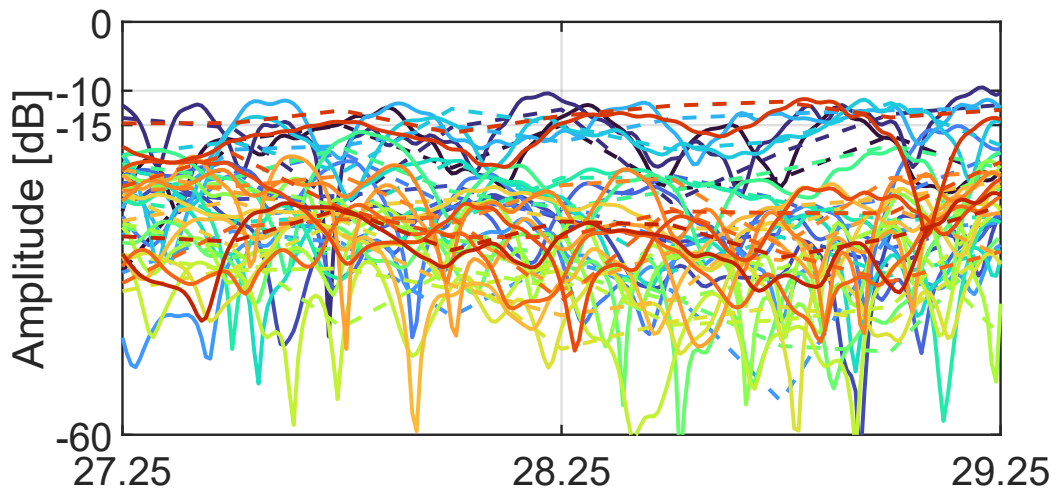
(f4) Phase difference with reference to Port 25 in the vertical direction corresponding to incidence from Port 9.

**Fig. 4.4.** S-parameters of the 48-port network for incidence from Port 1, 2, 3, 7, 8 and 9.

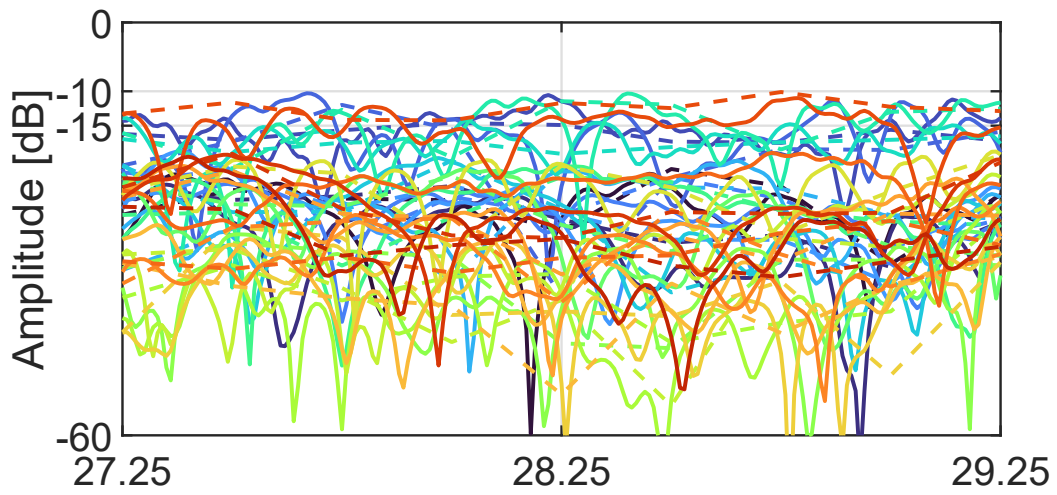


**Fig. 4.5.** Insertion loss and conductor loss of the 2-D 6×4-way matrix.

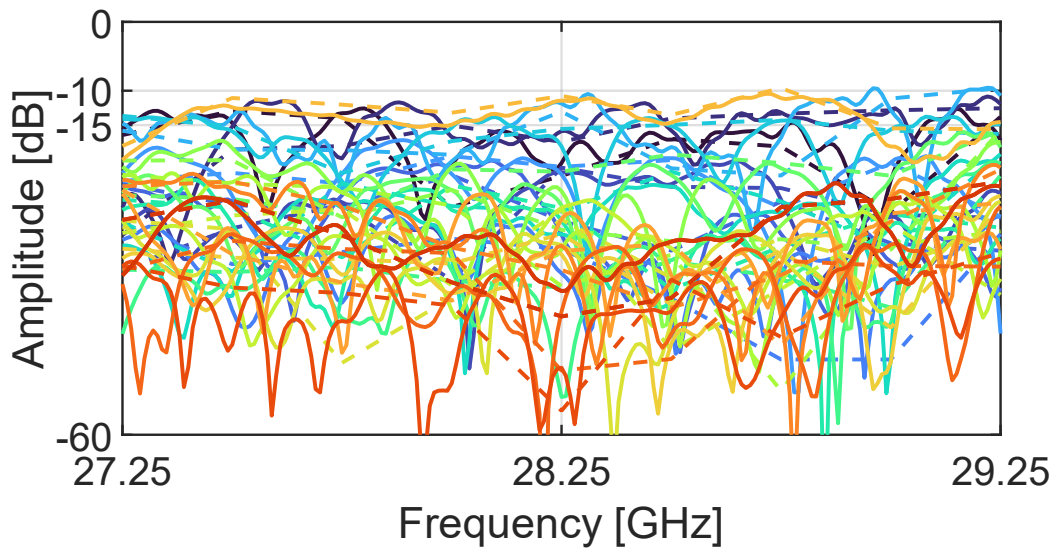




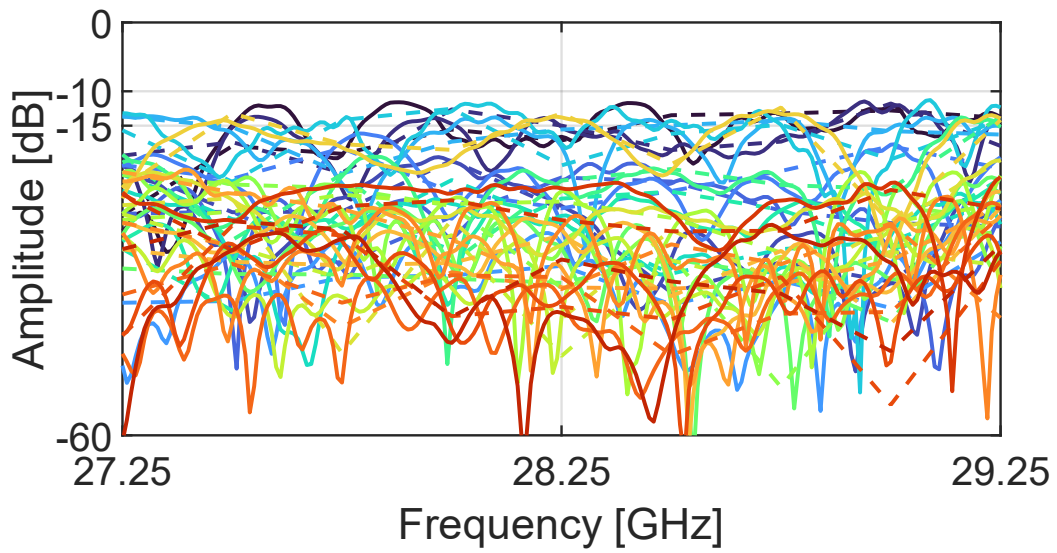
(b) Port 2



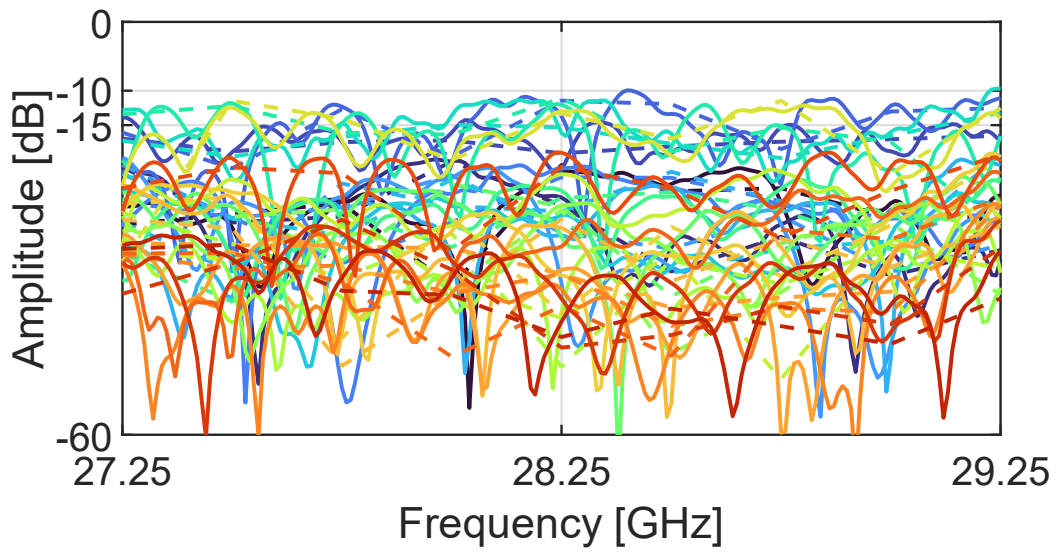
(c) Port 3



(d) Port 7



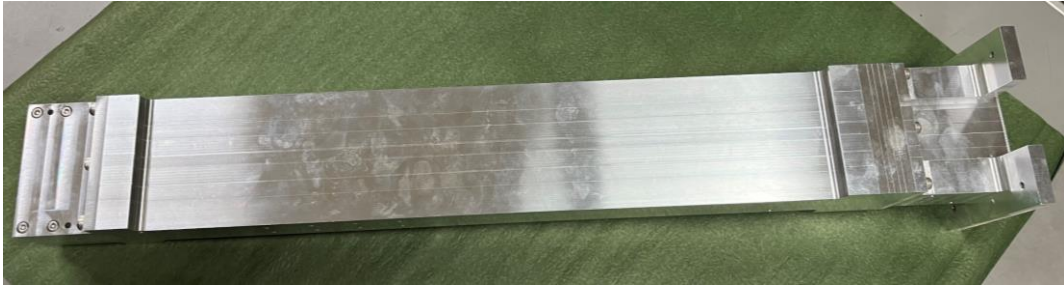
(e) Port 8



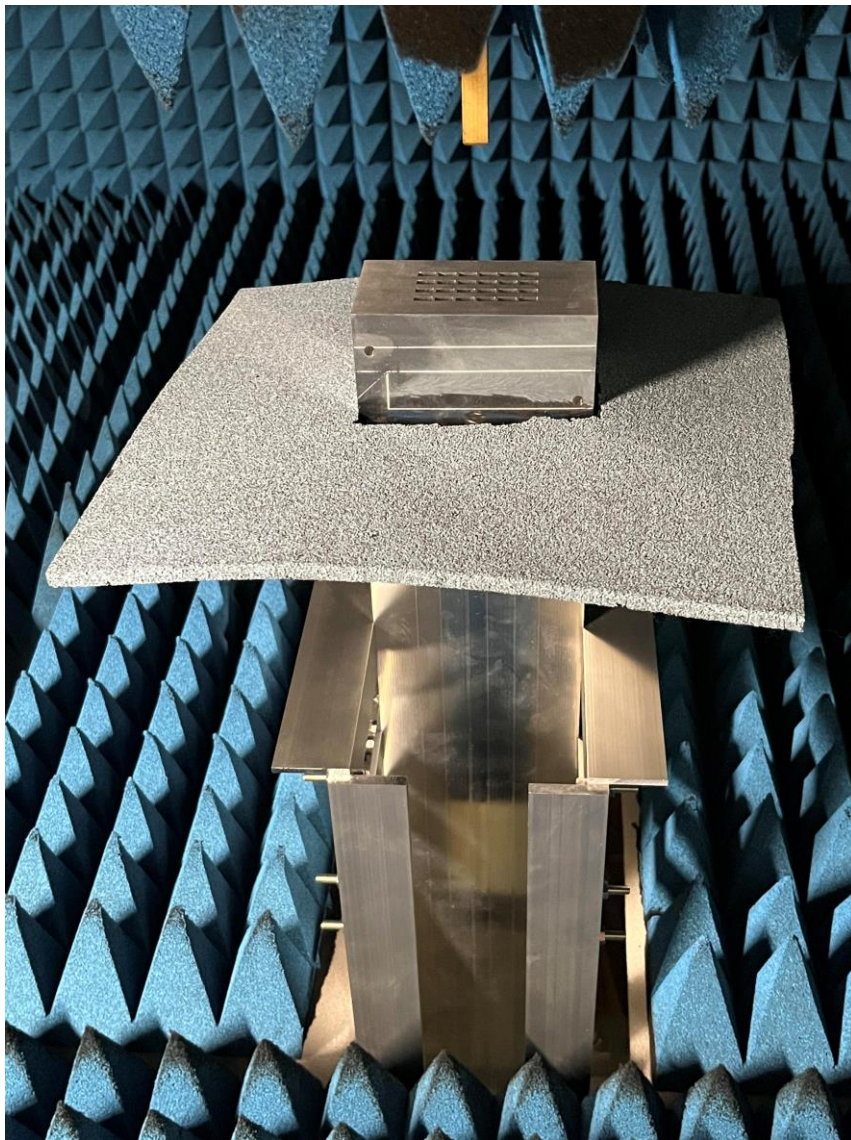
(f) Port 9

**Fig. 4.6.** Reflection and isolation performances of the 2-D 6×4-way matrix when the output ports are directly radiating into free space for incidence from each port. Solid line: measurement. Dotted line: simulation.





(a)



(b)

**Fig. 4.7.** Planar scanning near field measurement setup. (a) Matrix body. (b) Near field measurement cabin.

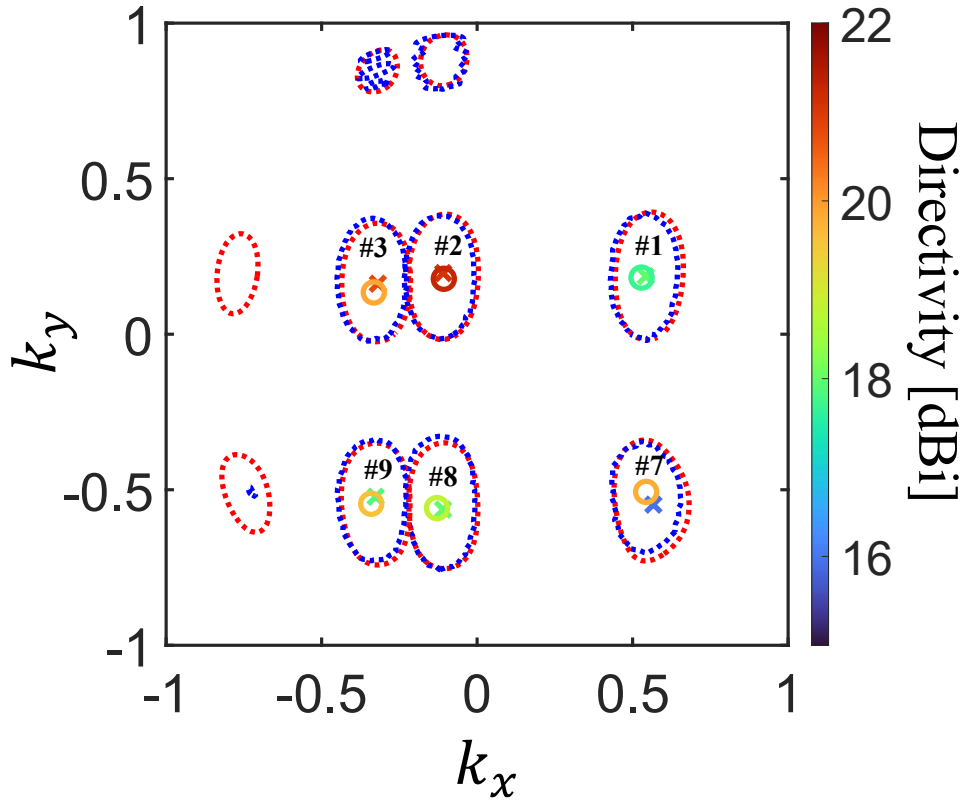


**Fig. 4.8.** Contour plots at 3.9 dB below the peak directivity for the six tested beams of the complete 2-D 6×4-way matrix at 28.25 GHz. O: peaks in measurement. X: peaks in simulation. Blue: measurement. Red: simulation.

**TABLE 4.2**  
**Directivity of each tested beam at 28.25 GHz**

Port No.	Dir. (dBi)		[ $\theta$ , $\varphi$ ] (deg.)	
	Meas.	Sim.	Meas.	Sim.
1	17.7	18.0	[34, 19]	[35, 19]
2	21.3	21.1	[12, 121]	[13, 119]
3	19.9	20.8	[21, 158]	[21, 153]
7	19.8	16.0	[-48, 137]	[-52, 136]
8	18.8	18.0	[-35, 77]	[-35, 79]
9	19.6	17.9	[-40, 58]	[-38, 58]

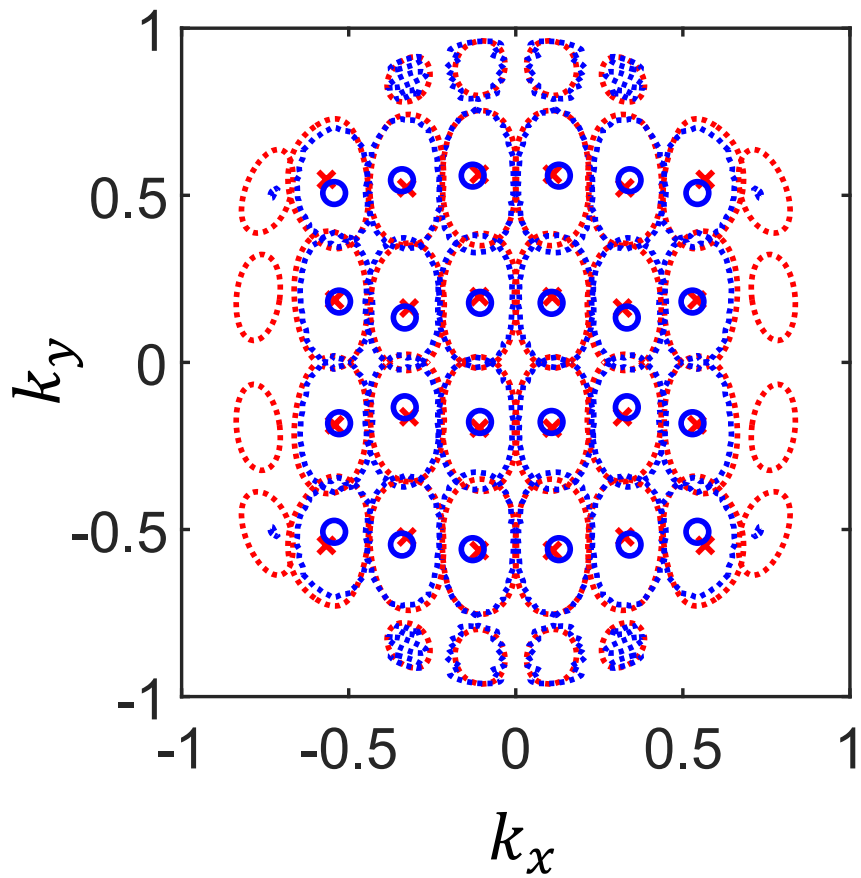
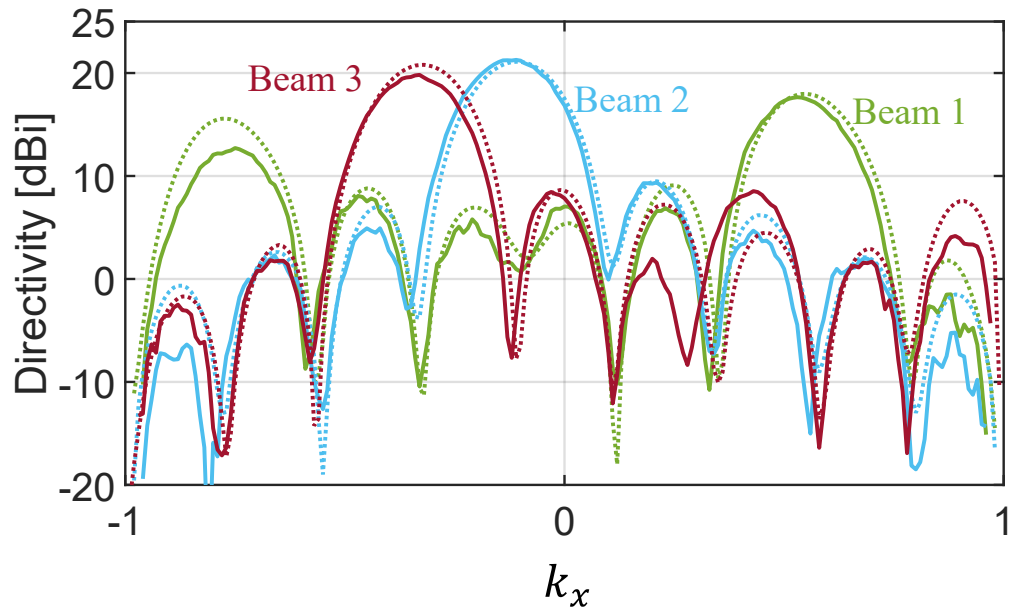
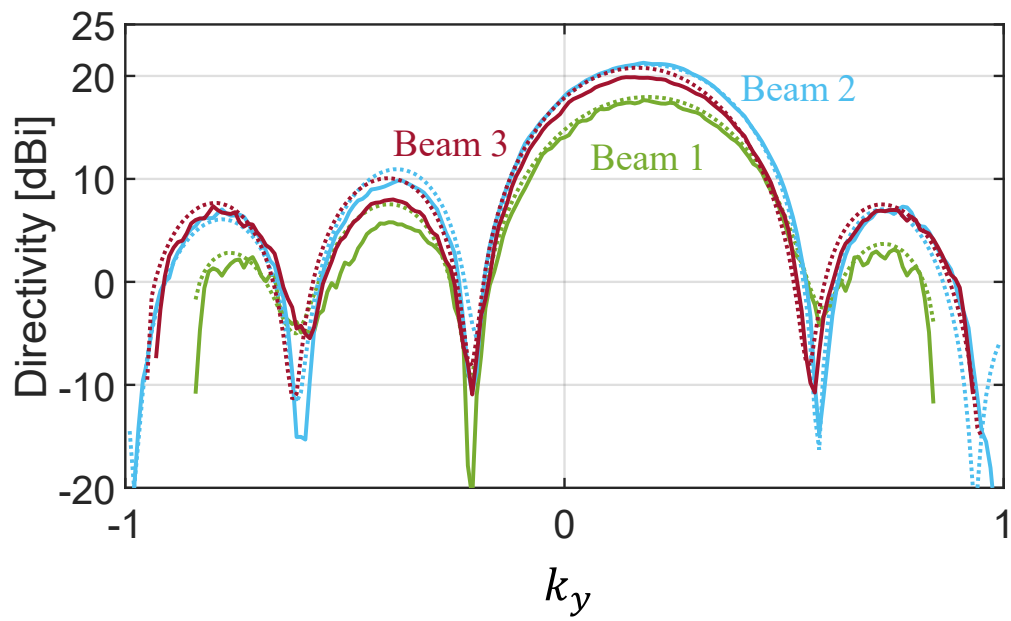


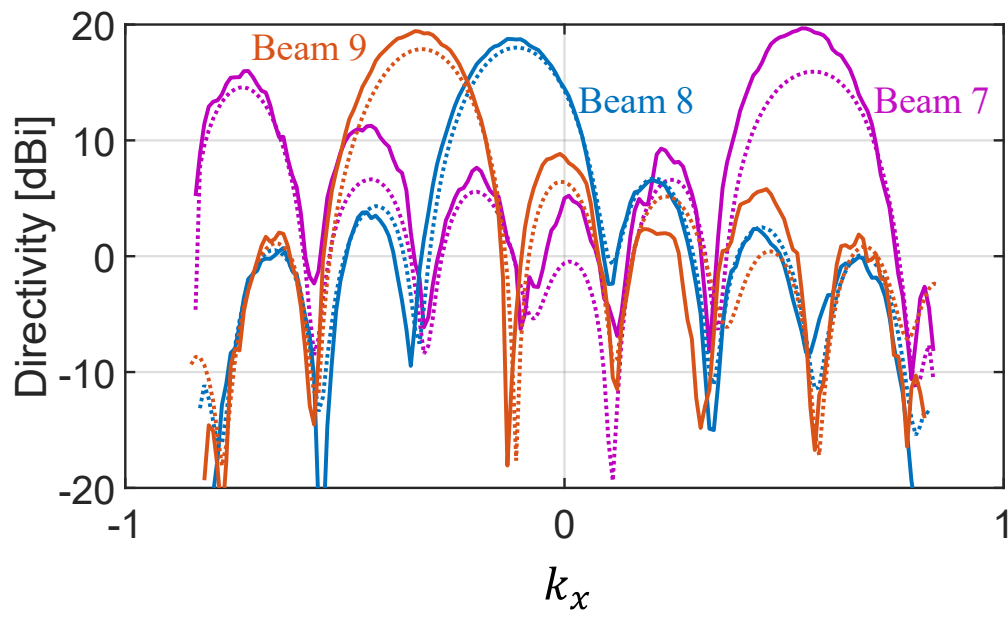
**Fig. 4.9.** Contour plots at 3.9 dB below the peak directivity of all the beams of the complete 2-D  $6 \times 4$ -way matrix at 28.25 GHz. O: peaks in measurement by mirror-like duplicating of six tested beams. X: peaks in simulation. Blue: measurement. Red: simulation.



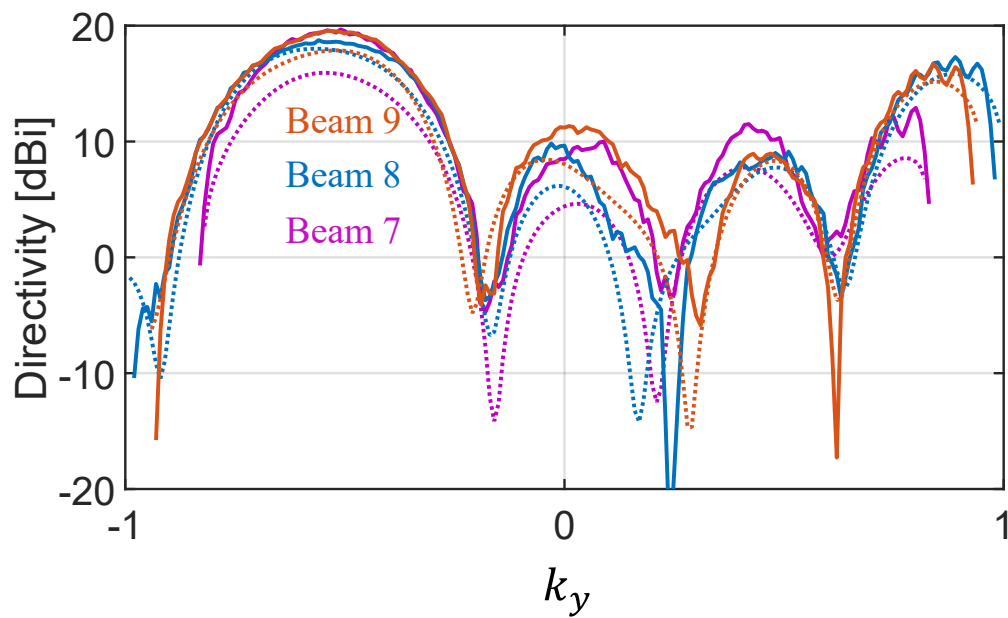
(a) Beams 1, 2 and 3 in  $k_x$ -plane.



(b) Beams 1, 2 and 3 in  $k_y$ -plane.



(c) Beams 7, 8 and 9 in  $k_x$ -plane.



(d) Beams 7, 8 and 9 in  $k_y$ -plane.

**Fig. 4.10.** Radiation patterns at 28.25 GHz.

**TABLE 4.3**  
**Comparison with related works on 2-D beam-switching matrices**

Matrix size	2-D 4×4 [4-10]	2-D 4×4 [4-11]	2-D 4×4 [4-8]	2-D 8×8 [4-9]	2-D 6×4 This work
Frequency	2.4 GHz	10 GHz	22 GHz	19.5 GHz	28 GHz
Technology	Microstrip line	SIW	Waveguide	Waveguide	Waveguide
Number of ports	16	16	16	64	24
One-body structure	No	No	Yes	Yes	Yes
Use of two-plane couplers	No	No	Yes	Yes	Partially
Worst-case insertion loss (IL)	1.8 dB	4.0 dB	1.5 dB	5.0 dB	2.2 dB
Bandwidth	16.7 %	N.A.	2.0 %	5.1%	7.1%

## References

- [4-1] J. Butler and R. Lowe, "Beam-forming matrix simplifies design of electronically scanned antennas," *Electron. Des.*, vol. 9, pp. 170–173, Apr. 1961.
- [4-2] J. Nolen, "Synthesis of multiple beam networks for arbitrary illuminations" Bendix Corp, 1965.
- [4-3] N. J. G. Fonseca, "Printed S-Band  $4 \times 4$  Nolen Matrix for Multiple Beam Antenna Applications," *IEEE Trans. Antennas Propag.*, vol. 57, no. 6, pp. 1673-1678, June 2009.
- [4-4] Jiro Hirokawa and N. J. G. Fonseca, "Generalized one-dimensional parallel switching matrices with an arbitrary number of beams," *IEEE J. Microwaves*, vol. 1, no. 4, pp. 975-988, Oct. 2021.
- [4-5] T. Djerafi, N. J. G. Fonseca and K. Wu, "Broadband Substrate Integrated Waveguide  $4 \times 4$  Nolen Matrix Based on Coupler Delay Compensation," *IEEE Trans. Microw. Theory Techn.*, vol. 59, no. 7, pp. 1740-1745, July 2011.
- [4-6] S. Chen, T. Tomura, J. Hirokawa, K. Ito, M. Suga, Y. Shirato, D. Uchida, and N. Kita, "Design for Operation in Two Frequency Bands by Division of the Coupled Region in a Waveguide 2-Plane Coupler," *IEICE Trans. Commun.*, vol. E105-C, No.12, pp.729-739, Dec. 2022.
- [4-7] O. A. Peverini, M. Lumia, G. Addamo, G. Virone and N. J. G. Fonseca, "How 3D-Printing Is Changing RF Front-End Design for Space Applications," *IEEE J. Microwaves*, vol. 3, no. 2, pp. 800-814, April 2023.
- [4-8] D.-H. Kim, J. Hirokawa, and M. Ando, "One-body 2-D Beam-switching Butler Matrix with Waveguide Short-slot 2-plane Couplers," *IEICE Trans. Electron.*, vol. E100-C, no.10, pp.-, Oct. 2017.
- [4-9] T. Tomura, D. -H. Kim, M. Wakasa, Y. Sunaguchi, J. Hirokawa and K. Nishimori, "A 20-GHz-Band  $64 \times 64$  Hollow waveguide Two-Dimensional Butler Matrix," *IEEE Access*, vol. 7, pp. 164080-164088, 2019.
- [4-10] K. Ding and A. A. Kishk, "2-D Butler matrix and phase-shifter group," *IEEE Trans. Microw. Theory Techn.*, vol. 66, no. 12, pp. 5554-5562, Dec. 2018
- [4-11] J. -W. Lian, Y. -L. Ban, H. Zhu and Y. J. Guo, "Uniplanar Beam-Forming Network Employing Eight-Port Hybrid Couplers and Crossovers for 2-D Multibeam Array Antennas," *IEEE Trans. Microw. Theory Techn.*, vol. 68, no. 11, pp. 4706-4718, Nov. 2020.

# Chapter 5 Conclusion

## 5.1 Summary of preceding chapters

This Ph.D. dissertation is dedicated to the development of hollow waveguide-based beam-switching matrices and the refinement for the working mechanism of two-plane couplers those are instrumental in multibeam matrices networks.

Chapter 1 gave a brief introduction concerning background, application and development of beam forming networks, including beam-switching matrices and lens-based antennas. And the motivation of this dissertation is mentioned up, which focuses on the exploration of two-plane coupler realizing arbitrary coupling ratios and 2-D beam-switching matrices with beam numbers other than  $2^n$  and with different number of beams in two orthogonal directions.

Chapter 2 conducted a comprehensive theoretical analysis to investigate the working principles of a two-plane coupler capable of achieving arbitrary coupling ratios in both the H-plane and E-plane directions. The fundamental equation (2-7) was identified as the core mechanism governing the behavior of the two-plane coupler, establishing a solid theoretical foundation for its design and implementation. To validate the theoretical analysis, a specific two-plane coupler centered at the 28.25 GHz band was designed with a coupling ratio of  $\sqrt{2}:2:1\sqrt{2}$ , which can be deconstructed as  $1:\sqrt{2}$  in the H-plane direction and  $\sqrt{2}:1$  in the E-plane direction. The performance of this coupler was evaluated through comprehensive simulation and measurement campaigns over a frequency range of 27 GHz to 29.5 GHz, corresponding to an impressive 8.85% fractional bandwidth. Substantially, the results of the simulation and measurement demonstrated good agreement for the proposed two-plane coupler across the entire bandwidth. The reflections at the input and output ports were effectively suppressed, achieving levels below -15 dB. The output amplitudes exhibited minimal deviations, with variations of no more than 2 dB. Additionally, the phase differences remained within 20 degrees throughout the frequency range. Importantly, this work represents the first instance of a two-plane coupler designed with different coupling ratios in the H-plane and E-plane



directions, showcasing the novelty and uniqueness of the theoretical analysis.

Chapter 3 has presented an innovative 2-D one-body  $3 \times 3$ -way hollow-waveguide Nolen matrix, introducing a novel two-plane unequal division coupler operating in the Ka-band from 27.65 GHz to 28.85 GHz, corresponding to a fractional bandwidth of 4.1%. The proposed two-plane unequal division coupler demonstrates excellent performance, with transmission coefficients exhibiting variations within  $\pm 0.5$  dB in amplitude and  $\pm 10^\circ$  in phase over the considered frequency range. The designed 2-D  $3 \times 3$ -way Nolen matrix showcases promising electrical characteristics, with simulation results revealing a maximum output port power imbalance of 2.5 dB and a maximum insertion loss of 0.86 dB across the analyzed bandwidth. To verify the radiation performance, far field measurements were conducted, and the realized gain was evaluated with reference to a standard horn antenna. At the center frequency, the maximum realized gain of the 2-D  $3 \times 3$ -way Nolen matrix is achieved at the boresight (Beam 1), measuring 15.5 dBi in the measurement and 15.7 dBi in the simulation. The minimum realized gain in the measurement is observed for the 2-D tilted Beam 6, measuring 12.0 dBi, while in the simulation, it is observed for another 2-D tilted Beam 9, measuring 12.7 dBi. The scan loss in the tilted beams is expected to be compensated by employing more isotropic radiation elements in future applications. Significantly, this research marks the first reported instance of a 2-D one-body hollow-waveguide Nolen matrix with a port number other than  $2^n$ . It also introduces the utilization of a two-plane coupler with unequal output division within a beam-switching matrix network. Although the frequency bandwidth of the designed two-plane coupler and 2-D  $3 \times 3$ -way Nolen matrix is limited, it suffices to demonstrate the concept effectively. The present work serves as a foundation for future studies on 2-D one-body hollow-waveguide matrices with different beam numbers in either dimension, including 5, 6, 7, 9, and beyond.

Chapter 4 has introduced a 2-D hollow waveguide  $6 \times 4$ -way beam switching matrix working from 27.25 GHz to 29.25 GHz, counterpart to a 7.1% fractional bandwidth. This is the first time that a 2-D waveguide beam-switching matrix is proposed with different number of beams in two orthogonal directions. Attributing to the 2-D symmetry in the

transverse directions, the design complexity of the 2-D 6×4-way matrix is significantly reduced to quarter solely. The 2-D 6×4-way matrix demonstrates excellent performance, with insertion loss ranging up to a maximum of 2.2 dB across the entire operational bandwidth. The radiation performance of the matrix is verified through planar scanning near-field measurements, providing valuable insights into its directivity characteristics. The highest directivity is achieved by Beam 2, with an impressive value of 21.3 dBi in measurement and 21.1 dBi in simulation. On the other hand, Beam 1 exhibits the minimum directivity in measurement, reaching 17.7 dBi, accompanied by a tilted angle of 34° with reference to the boresight, corresponding to a scan loss of 3.4 dB. In simulation, the minimum directivity of 16.0 dBi is obtained for Beam 7, which is inclined at an angle of 52° relative to the boresight, resulting in a scan loss of 5.1 dB. It is worth noting that Beam 7 demonstrates the largest discrepancy 3.8dB between measurement and simulation, with the measured results showing 19.8 dBi in directivity, 1.5 dB in scan loss, and a tilted angle of 48° with reference to the boresight. The scan loss observed in the tilted beam configuration can be potentially compensated in future applications through the utilization of isotropic radiation elements.

## 5.2 Remarks for future study

Based on the study and research of this doctoral dissertation, here comes up some perspective on potential future works:

1. Apply for two-plane coupler having different coupling ratios in H-plane and E-plane directions into two-dimensional beam switching matrices. As Chapter 2 of this dissertation has completely accomplished theoretical analysis together with experimental verification of two-plane coupler following arbitrary coupling ratio, its practical application can be expected.
2. To further broaden the bandwidth of two-plane couplers. As two-plane coupler can significantly reduce the physical size compared to conventional H-plane and E-plane couplers, however, its bandwidth performance is still to be broadened to fit in future applications. There might be two efficient methods to enhance the

bandwidth of two-plane couplers:

- a) By introducing asymmetrical structure about the longitudinal directions. In preceding journals and this dissertation, symmetry about longitudinal direction of two-plane coupler is always assigned to diminish design complexity. However, this might restrict possible enhancement of two-plane coupler on bandwidth and other performances. Though there will be accompanying longer analysis time for the optimization, introducing asymmetrical structure about longitudinal direction could be a good way to improve its bandwidth.
  - b) By proposing input or output (I/O) waveguides with irregular shape. As depicted in all reported research up to days, I/O waveguide of two-plane couplers are always defaulted as normal rectangular shape, which is deemed not necessary. Breakthroughs of this limitation may yield unanticipated benefits on bandwidth enhancements.
3. To accomplish theoretical work of  $2N$ -way 1-D beam-switching matrices with symmetrical configuration. As depicted in Chapter 4, the 6-way and 4-way symmetrical matrices are utilized to construct 2-D  $6 \times 4$ -way matrix with two-dimensional symmetry, which significantly decreases the designing complexity. However, a rigorous theoretical analysis of the configuration of 1-D  $2N$ -way matrix with symmetry is still needing explorations, including the prediction of components parameter like couplers and phase shifters.

# Appendix A

## Wave equations

According to Maxwell equations in non-source region

$$\nabla \cdot \mathbf{E} = 0 \quad (\text{A-1})$$

$$\nabla \cdot \mathbf{H} = 0 \quad (\text{A-2})$$

$$\nabla \times \mathbf{E} = -j\omega\mu\mathbf{H} \quad (\text{A-3})$$

$$\nabla \times \mathbf{H} = j\omega\varepsilon\mathbf{E} \quad (\text{A-4})$$

The wave equations can be established separately for TE-mode and TM-mode scenarios.

### ● TE-mode

For TE(H)-mode, based on  $\nabla \cdot (\nabla \times \mathbf{A}) = 0$ , and  $\nabla \times (\nabla \cdot \mathbf{f}) = 0$

$$\mathbf{E} = -j\omega\mu\nabla \times \Psi_h \quad (\text{A-5})$$

$$\mathbf{H} = k^2\Psi_h + \nabla\varphi_h \quad (\text{A-6})$$

$$k^2 = \omega^2\mu\varepsilon = \left(\frac{2\pi f}{c}\right)^2 \quad (\text{A-7})$$

Based on Lorentz condition  $\nabla \cdot \boldsymbol{\psi}_h = \varphi_h$ ,

$$\mathbf{H} = k^2\Psi_h + \nabla\nabla \cdot \Psi_h \quad (\text{A-8})$$

As well as the equation for  $\boldsymbol{\psi}_h$

$$\nabla^2\Psi_h + k^2\Psi_h = 0 \quad (\text{A-9})$$

For TE-mode, there are no longitudinal electric field component,

$$\Psi_{hi} = \vec{z}\psi_{hu}\exp(\mp\gamma_{hu}z) \quad (\text{A-10})$$

$$\nabla_{\vec{t}}^2\psi_{hu} + k_c^2\psi_{hu} = 0 \quad (\text{A-11})$$

$$\gamma_{hu}^2 + k^2 = k_{cu}^2 \quad (\text{A-12})$$

Here  $u$  signifies the order of mode, and  $t$  means transverse. Then the expressions for TE-mode in terms of electric and magnetic fields are,

$$\mathbf{E}_{hi}^{\pm} = \pm \mathbf{e}_{thu} \exp(\mp \gamma_{hu} z) \quad (\text{A-13})$$

$$\mathbf{H}_{hi}^{\pm} = \{\pm \mathbf{h}_{thu} + \mathbf{h}_{zhu}\} \exp(\mp \gamma_{hu} z) \quad (\text{A-14})$$

Here  $z$  means longitudinal direction. Lower-case letters mean basic function(vector) of each mode. And below restrictions should be complied with,

$$\mathbf{e}_{thi} = -Z_{hu} \vec{\mathbf{z}} \times \mathbf{h}_{thu} \quad (\text{A-15})$$

$$\mathbf{h}_{thi} = -\frac{\sqrt{Y_{hu}}}{k_{cu}} \nabla_t \psi_{hu} \quad (\text{A-16})$$

$$\mathbf{h}_{zhi} = \vec{\mathbf{z}} \frac{\sqrt{Y_{hu}} k_{cu}}{\gamma_u} \psi_{hu} \quad (\text{A-17})$$

$$Z_{hi} = \frac{1}{Y_{hu}} = \frac{j z_0 \mu k_0}{\gamma_{hu}} \quad (\text{A-18})$$

Here  $z_0$  stand for wave impedance in free space, while  $k_0$  means wave number in free space.

### ● TM-mode

For TM(E)-mode, similarly, it could be derived as

$$\mathbf{H} = -j\omega\mu\nabla \times \boldsymbol{\Psi}_e \quad (\text{A-19})$$

$$\mathbf{E} = k^2 \boldsymbol{\Psi}_e + \nabla \varphi_e \quad (\text{A-20})$$

$$k^2 = \omega^2 \mu \varepsilon \quad (\text{A-21})$$

Still, based on Lorentz condition  $\nabla \cdot \boldsymbol{\Psi}_e = \varphi_e$ ,

$$\mathbf{E} = k^2 \boldsymbol{\Psi}_e + \nabla \nabla \cdot \boldsymbol{\Psi}_e \quad (\text{A-22})$$

As well as the equation for  $\boldsymbol{\Psi}_e$

$$\nabla^2 \Psi_e + k^2 \Psi_e = 0 \quad (\text{A-23})$$

To satisfy TM-mode condition,

$$\Psi_{ei} = \vec{z} \psi_h \exp(\mp \gamma_{eu} z) \quad (\text{A-24})$$

$$\nabla_t^2 \psi_{eu} + k_c^2 \psi_{eu} = 0 \quad (\text{A-25})$$

$$\gamma_{eu}^2 + k^2 = k_{eu}^2 \quad (\text{A-26})$$

Then the expressions for electric and magnetic field are,

$$\mathbf{H}_{eu}^\pm = \pm \mathbf{h}_{teu} \exp(\mp \gamma_{eu} z) \quad (\text{A-27})$$

$$\mathbf{E}_{eu}^\pm = \{\pm \mathbf{e}_{teu} + \mathbf{e}_{zeu}\} \exp(\mp \gamma_{eu} z) \quad (\text{A-28})$$

$$\mathbf{h}_{thu} = Y_{eu} \vec{z} \times \mathbf{e}_{thu} \quad (\text{A-29})$$

$$\mathbf{e}_{thu} = -\frac{\sqrt{Z_{hu}}}{k_{cu}} \nabla_t \psi_{eu} \quad (\text{A-30})$$

$$\mathbf{h}_{zhi} = \vec{z} \frac{\sqrt{Z_{hu}} k_{cu}}{\gamma_{eu}} \psi_{eu} \quad (\text{A-31})$$

$$Z_{eu} = \frac{1}{Y_{eu}} = -\frac{j z_0 \gamma_{eu}}{\epsilon k_0} \quad (\text{A-32})$$

The definition of  $z_0$  and  $k_0$  are same to TE-mode condition. More details can be referred to [A-1][A-2].

# Appendix B

## Mode-matching

Taking the normal condition model as Fig.B.1 as reference, the electrical field and magnetic field in both regions can be expressed as:

$$\mathbf{E}_1 = \sum_i A_{1i} \mathbf{E}_{1i}^+ + \sum_i B_{1i} \mathbf{E}_{1i}^- \quad (\text{B-1})$$

$$\mathbf{H}_1 = \sum_i A_{1i} \mathbf{H}_{1i}^+ + \sum_i B_{1i} \mathbf{H}_{1i}^- \quad (\text{B-2})$$

$$\mathbf{E}_2 = \sum_i A_{2i} \mathbf{E}_{2i}^- + \sum_i B_{2i} \mathbf{E}_{2i}^+ \quad (\text{B-3})$$

$$\mathbf{H}_2 = \sum_i A_{2i} \mathbf{H}_{2i}^- + \sum_i B_{2i} \mathbf{H}_{2i}^+ \quad (\text{B-4})$$

Here the mode number  $i$  is to represent all TE-mode and TM-mode number described by  $u$ . Define the boundary  $S = S_1 \cap S_2 = S_1$ ,  $S^* = S_2 - S_1 \cap S_2$  and based on continuity at the boundary,

$$\begin{aligned} \vec{\mathbf{z}} \times \mathbf{E}_2 &= \vec{\mathbf{z}} \times \mathbf{E}_1 \quad (S) \\ \vec{\mathbf{z}} \times \mathbf{E}_2 &= 0 \quad (S^*) \end{aligned} \quad (\text{B-5})$$

$$\vec{\mathbf{z}} \times \mathbf{H}_2 = \vec{\mathbf{z}} \times \mathbf{H}_1 \quad (S) \quad (\text{B-6})$$

By substituting equations (A-13)(A-14)(A-27)(A-28) into (B-5)(B-6),

$$\begin{aligned} \sum_i^{N_2} (A_{2i} + B_{2i}) \vec{\mathbf{z}} \times \mathbf{e}_{2ti} &= \sum_i^{N_1} (A_{1i} + B_{1i}) \vec{\mathbf{z}} \times \mathbf{e}_{1ti} \quad (S) \\ \sum_i^{N_2} (A_{2i} + B_{2i}) \vec{\mathbf{z}} \times \mathbf{e}_{2ti} &= 0 \quad (S^*) \end{aligned} \quad (\text{B-7})$$

$$\sum_i^{N_2} (-A_{2i} + B_{2i}) \vec{\mathbf{z}} \times \mathbf{h}_{2ti} = \sum_i^{N_1} (A_{1i} - B_{1i}) \vec{\mathbf{z}} \times \mathbf{h}_{1ti} \quad (S) \quad (\text{B-8})$$

For equation (B-7), taking consideration of orthogonality among modes, by multiplying  $\mathbf{h}_{2tj}$  and taking integration at area  $S_2$ , the left side of (B-7) turns to be,

$$\sum_i^{N_2} (A_{2i} + B_{2i}) \iint_{S_2} \mathbf{e}_{2ti} \times \mathbf{h}_{2tj} \cdot \vec{\mathbf{z}} dS = A_{2j} + B_{2j} \quad (\text{B-9})$$

The right side of (B-7) turns to be,

$$\sum_i^{N_2} (A_{1i} + B_{1i}) \iint_{S_1} \mathbf{e}_{1ti} \times \mathbf{h}_{2tj} \cdot \vec{\mathbf{z}} dS \quad (\text{B-10})$$

Combining (B-9) and (B-10),

$$\sum_i^{N_2} (A_{1i} + B_{1i}) \iint_{S_1} \mathbf{e}_{1ti} \times \mathbf{h}_{2tj} \cdot \vec{\mathbf{z}} dS = A_{2j} + B_{2j} \quad (\text{B-11})$$

Here  $j$  is varying from 1 to  $N_2$ . Similarly, by multiplying  $\mathbf{e}_{1tk}$  to (B-8),

$$\sum_i^{N_2} (-A_{2i} + B_{2i}) \iint_{S_1} \mathbf{e}_{1tk} \times \mathbf{h}_{2ti} \cdot \vec{\mathbf{z}} dS = A_{1k} - B_{1k} \quad (\text{B-12})$$

Here  $k$  is varying from 1 to  $N_1$ . (B-11) and (B-12) can be demonstrated in matrix format as,

$$\begin{aligned} X^T (A_1 + B_1) &= A_2 + B_2 \\ A_1 - B_1 &= X(-A_2 + B_2) \end{aligned} \quad (\text{B-13})$$

Here,

$$X_{ij} = \iint_{S_1} \mathbf{e}_{1ti} \times \mathbf{h}_{2tj} \cdot \vec{\mathbf{z}} dS \quad [N_1 \times N_2] \quad (\text{B-14})$$

$A_1$  and  $B_1$  are  $[N_1 \times 1]$  vectors and  $A_2$  and  $B_2$  are  $[N_2 \times 1]$  vectors. Table. B.1 gives a coupling condition for reference, some coupling condition would make no contribution as 0 [A-3]. As Fig.B.2 shows, to establish a counterpart from X-matrix to S-matrix, following conversion is needed:

$$\begin{aligned} \begin{bmatrix} b_1 \\ b_2 \end{bmatrix} &= \begin{bmatrix} F - I_{N_1} & FX \\ X^T F & X^T FX - I_{N_2} \end{bmatrix} \begin{bmatrix} a_1 \\ a_2 \end{bmatrix} \\ F &= 2(I_{N_1} + XX^T)^2 \end{aligned} \quad (\text{B-15})$$

Here  $I$  means unitary diagonal matrix.

When the reference plane is deviating from the discontinuous plane, as Fig.B.3 shows, transmission phase should be compensated to S-matrix as:



$$\begin{aligned}
S &= \begin{bmatrix} p_1^+ S_{11} p_1^- & p_1^+ S_{12} p_2^+ \\ p_2^- S_{21} p_1^- & p_2^- S_{22} p_2^+ \end{bmatrix} \\
p_1^\pm &= \text{diag}_{N_1} \{ \pm \gamma_u z_1 \} \quad u = 1 \dots N_1 \\
p_2^\pm &= \text{diag}_{N_2} \{ \pm \gamma_u z_2 \} \quad u = 1 \dots N_2
\end{aligned} \tag{B-16}$$

For a complex condition as Fig.B.4 depicts, when cross-section of Port 1 is not involved in Port 2, then it should be processed under the manner to calculate mode matching between  $S_1$  and  $S_2$ , then between  $S_2$  and  $S_3$ , by cascading these two results with the consideration that length of  $S_2$  region is 0.

More details for Mode matching can be referred to [A-4].

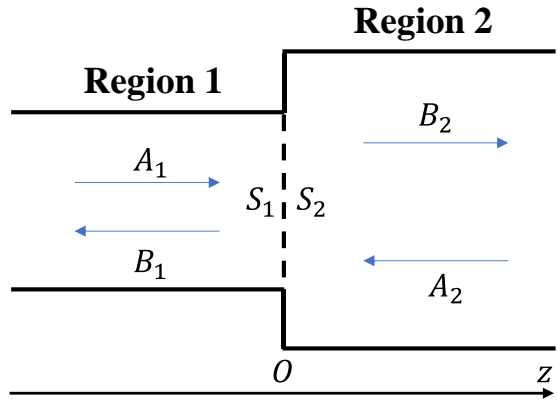


Fig. B.1. Schematic of mode matching model.

Table B.1 Coupling condition for mode matching when  $S_1 \in S_2$

$S_1 \backslash S_2$	TEM	TE	TM
TEM	Coupling	✘	Coupling
TE	Coupling	Coupling	Coupling
TM	✘	✘	Coupling

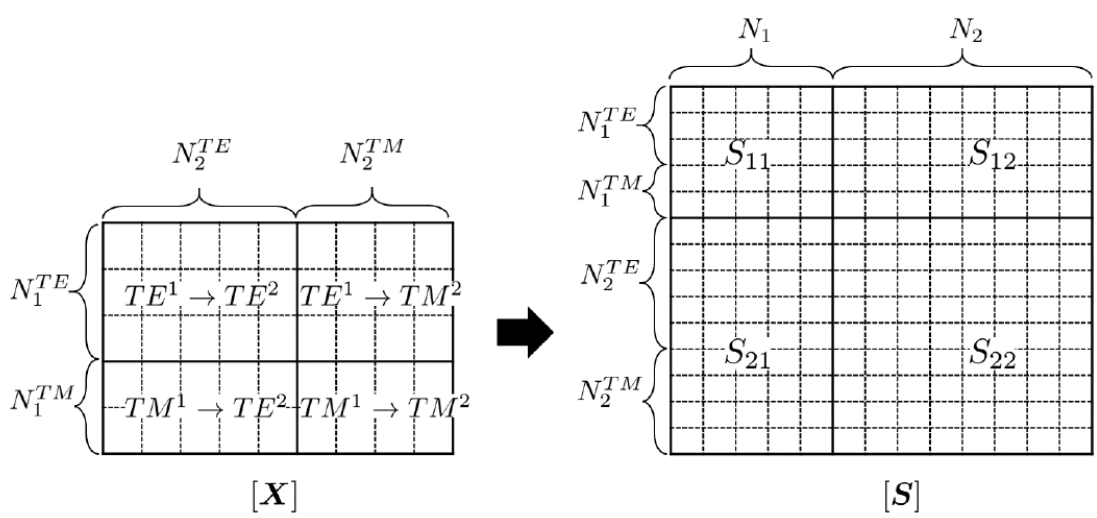
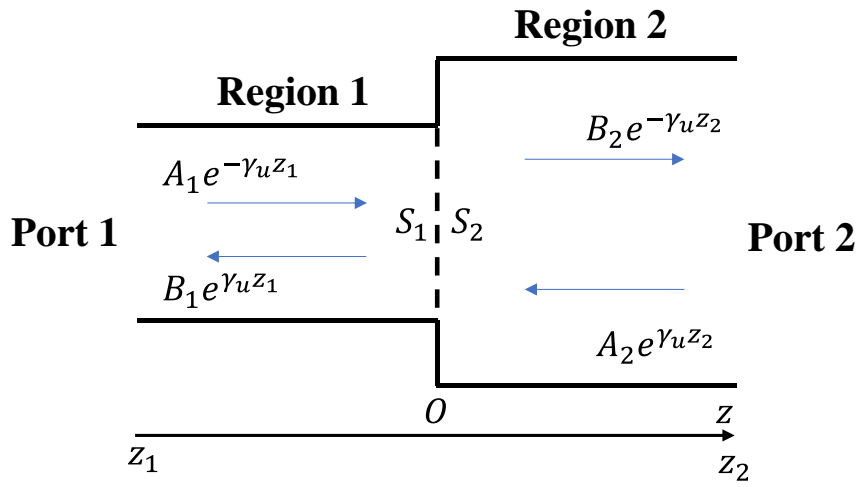
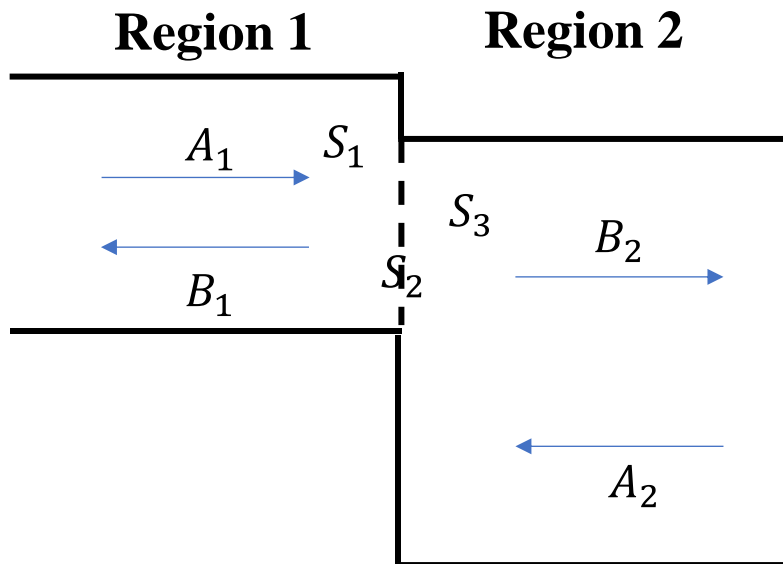


Fig. B.2. Conversion from X-matrix to S-matrix.



**Fig. B.3.** Schematic of mode matching model when reference plane deviates from discontinuous



**Fig. B.4.** Schematic when  $S_1$  is not covered by  $S_2$ .

# Appendix C

## 2-D Finite element method (FEM)

The transverse Helmholtz equation for TE-mode and TM-mode wave are

$$\nabla_t^2 \mathbf{E}_{ht} + k_c^2 \mathbf{E}_{ht} = 0 \quad (\text{C-1})$$

$$\nabla_t^2 \mathbf{H}_{et} + k_c^2 \mathbf{H}_{et} = 0 \quad (\text{C-2})$$

By multiplying weighting function  $\mathbf{W}_t$  and exerting integration at target area,

$$\int_S \mathbf{W}_t (\nabla_t^2 \mathbf{E}_{ht} + k_c^2 \mathbf{E}_{ht}) dS = 0 \quad (\text{C-3})$$

$$\int_S \mathbf{W}_t (\nabla_t^2 \mathbf{H}_{et} + k_c^2 \mathbf{H}_{et}) dS = 0 \quad (\text{C-4})$$

(C-3) and (C-4) could be converted to below weak form equations,

$$\int_S (\nabla_t \times \mathbf{W}_t) (\nabla_t \times \mathbf{E}_t) - k_c^2 \mathbf{W}_t \mathbf{E}_t dS = 0 \quad (\text{C-5})$$

$$\int_S (\nabla_t \times \mathbf{W}_t) (\nabla_t \times \mathbf{H}_t) - k_c^2 \mathbf{W}_t \mathbf{H}_t dS = 0 \quad (\text{C-6})$$

(C-5) and (C-6) indicate that electric field and magnetic field are given in same manipulation. Consequently, it is sufficient to investigate electric field only. Triangular mesh is deemed to be more fitting into complex area shape than rectangular mesh. The basis vector function for a single triangular mesh as shown in Fig.C.1, is given below,

$$\mathbf{w}_i = \frac{l_i}{\Delta^2} [\vec{x}(A_i - B_i y) - \vec{y}(C_i - B_i x)] \quad i = 1, 2, 3$$

$l_i$ : length of each edge

$$a_1 = x_2 y_3 - x_3 y_2 \quad a_2 = x_3 y_1 - x_1 y_3 \quad a_3 = x_1 y_2 - x_2 y_1$$

$$b_1 = y_2 - y_3 \quad b_2 = y_3 - y_1 \quad b_3 = y_1 - y_2$$

$$c_1 = x_3 - x_2 \quad c_2 = x_1 - x_3 \quad c_3 = x_2 - x_1$$

$$A_1 = a_1 b_2 - a_2 b_1 \quad A_2 = a_2 b_3 - a_3 b_2 \quad A_3 = a_3 b_1 - a_1 b_3$$

$$B_1 = b_1 c_2 - b_2 c_1 \quad B_2 = b_2 c_3 - b_3 c_2 \quad B_3 = b_3 c_1 - b_1 c_3$$

$$C_1 = c_1 a_2 - c_2 a_1 \quad C_2 = c_2 a_3 - c_3 a_2 \quad C_3 = c_3 a_1 - c_1 a_3$$

$$\Delta = x_1 b_1 + x_2 b_2 + x_3 b_3 \quad (\text{C-7})$$

Galerkin's method restrict weighting function to be same as basis function,

$$\mathbf{W}_t = \sum_{ele=1}^{N_{ele}} \sum_{i=1}^3 \mathbf{w}_i^{ele} \quad (\text{C-8})$$

$$\mathbf{E}_t = \sum_{ele=1}^{N_{ele}} \sum_{i=1}^3 E_i^{ele} \mathbf{w}_i^{ele} \quad (\text{C-9})$$

By substituting (C-8)(C-9) into (C-5),

$$\begin{bmatrix} K_{\nabla,11}^{ele} & K_{\nabla,12}^{ele} & K_{\nabla,13}^{ele} \\ K_{\nabla,21}^{ele} & K_{\nabla,22}^{ele} & K_{\nabla,23}^{ele} \\ K_{\nabla,31}^{ele} & K_{\nabla,32}^{ele} & K_{\nabla,33}^{ele} \end{bmatrix} \begin{bmatrix} E_1^{ele} \\ E_2^{ele} \\ E_3^{ele} \end{bmatrix} = k_c^2 \begin{bmatrix} K_{\bullet,11}^{ele} & K_{\bullet,12}^{ele} & K_{\bullet,13}^{ele} \\ K_{\bullet,21}^{ele} & K_{\bullet,22}^{ele} & K_{\bullet,23}^{ele} \\ K_{\bullet,31}^{ele} & K_{\bullet,32}^{ele} & K_{\bullet,33}^{ele} \end{bmatrix} \begin{bmatrix} E_1^{ele} \\ E_2^{ele} \\ E_3^{ele} \end{bmatrix} \quad (\text{C-10})$$

$$K_{\nabla,ij}^{ele} = \int_{S_{ele}} (\nabla \times \mathbf{w}_i) \cdot (\nabla \times \mathbf{w}_j) dS$$

$$K_{\bullet,ij}^{ele} = \int_{S_{ele}} \mathbf{w}_i \cdot \mathbf{w}_j dS$$

In rectangular coordinate, each of the calculation can be expanded as

$$\int_{S_{ele}} (\nabla \times \mathbf{w}_i) \cdot (\nabla \times \mathbf{w}_j) dx dy = \frac{4l_i l_j B_i B_j}{\Delta^4} \int_{S_{ele}} dx dy \quad (\text{C-11})$$

$$\begin{aligned} & \int_{S_{ele}} \mathbf{w}_i \cdot \mathbf{w}_j dx dy \\ &= \frac{4l_i l_j}{\Delta^4} \left[ \frac{\Delta(A_i A_j + C_i C_j)}{2} - (C_i B_j + C_j B_i) \int_{S_{ele}} x dx dy \right. \\ & \quad \left. - (A_i B_j + A_j B_i) \int_{S_{ele}} y dx dy \right] + B_i B_j \left( \int_{S_{ele}} x^2 dx dy + \int_{S_{ele}} y^2 dx dy \right) \end{aligned} \quad (\text{C-12})$$

The integration incorporated in (C-11) and (C-12) can be computed as

$$\int_{S_{ele}} dx dy = \frac{\Delta}{2}$$

$$\int_{S_{ele}} x dx dy = \frac{\Delta(x_1 + x_2 + x_3)}{6}$$

$$\int_{S_{ele}} y dx dy = \frac{\Delta(y_1 + y_2 + y_3)}{6}$$

$$\int_{S_{ele}} x^2 dx dy = \frac{\Delta(x_1^2 + x_2^2 + x_3^2 + x_1x_2 + x_1x_3 + x_2x_3)}{12}$$

$$\int_{S_{ele}} y^2 dx dy = \frac{\Delta(y_1^2 + y_2^2 + y_3^2 + y_1y_2 + y_1y_3 + y_2y_3)}{12}$$
(C-13)

Based on (C-11) and (C-12), the local mesh matrix for (C-10) can be derived. The next step is to connect each local mesh to construct overall global matrix, taking the Fig.C.2 as an example to connect two adjacent triangle meshes, the combined matrix can be described by considering continuity at shared common edge as,

$$\begin{bmatrix} K_{\nabla,11}^1 & K_{\nabla,12}^1 & K_{\nabla,13}^1 & 0 & 0 \\ K_{\nabla,21}^1 & K_{\nabla,22}^1 & K_{\nabla,23}^1 & 0 & 0 \\ K_{\nabla,13}^1 & K_{\nabla,23}^1 & K_{\nabla,33}^1 + K_{\nabla,11}^2 & -K_{\nabla,12}^2 & -K_{\nabla,13}^2 \\ 0 & 0 & -K_{\nabla,21}^2 & K_{\nabla,22}^2 & K_{\nabla,23}^2 \\ 0 & 0 & -K_{\nabla,31}^2 & K_{\nabla,32}^2 & K_{\nabla,33}^2 \end{bmatrix} \begin{bmatrix} E_1 \\ E_2 \\ E_3 \\ E_4 \\ E_5 \end{bmatrix}$$

$$= k_c^2 \begin{bmatrix} K_{\bullet,11}^1 & K_{\bullet,12}^1 & K_{\bullet,13}^1 & 0 & 0 \\ K_{\bullet,21}^1 & K_{\bullet,22}^1 & K_{\bullet,23}^1 & 0 & 0 \\ K_{\bullet,13}^1 & K_{\bullet,23}^1 & K_{\bullet,33}^1 + K_{\bullet,11}^2 & -K_{\bullet,12}^2 & -K_{\bullet,13}^2 \\ 0 & 0 & -K_{\bullet,21}^2 & K_{\bullet,22}^2 & K_{\bullet,23}^2 \\ 0 & 0 & -K_{\bullet,31}^2 & K_{\bullet,32}^2 & K_{\bullet,33}^2 \end{bmatrix} \begin{bmatrix} E_1 \\ E_2 \\ E_3 \\ E_4 \\ E_5 \end{bmatrix}$$
(C-14)

Additional boundary condition could be imposed to global matrix, such as PEC or PMC, to specific some of  $E_{ele}$ . For a global matrix with  $N_{ele}$  of edge,  $N_{ele}$  solutions for eigenvalue  $k_c$  with corresponding  $N_{ele}$  sorts of feature vectors can be derived to express the overall electrical field distribution within target 2-D area for TE-mode, and magnetic field can be deduced by (A-14)-(A-18). Similarly, starting from (C-6), for TM-mode, magnetic field distribution can be derived by FEM analysis, and electric field can be deduced by (A-28)-(A-32).

More details regarding 2-D FEM can be referred to [A-5].

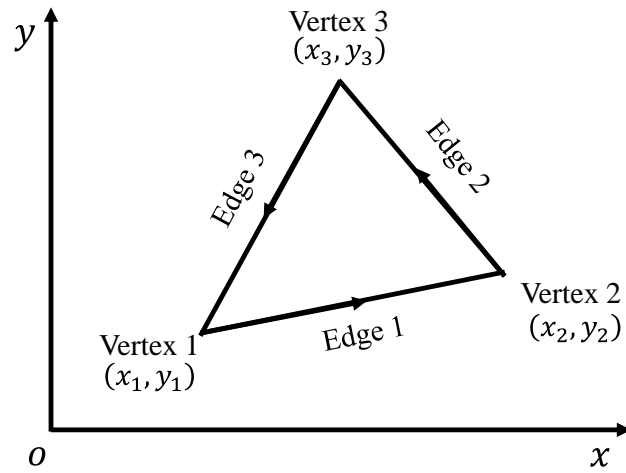


**Fig. C.1.** Schematic of a single triangular mesh.

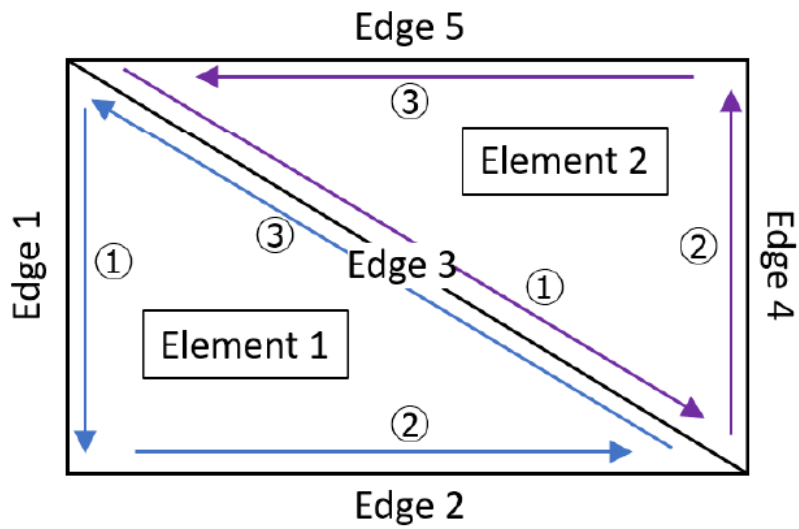


**Fig. C.2.** Connection of two adjacent triangle meshes.

## Appendix D

### FEM-Mode matching joint calculation

By taking the results by FEM into mode matching calculation, for TE-TE coupling condition,

$$\begin{aligned}
 X_{mn} &= \iint_S \mathbf{e}_{1thm} \times \mathbf{h}_{2thn} \cdot \vec{z} dS = \frac{1}{Z_{2hn}} \iint_S \mathbf{e}_{1thm} \cdot \mathbf{e}_{2thn} dS \\
 &= D_{mn} \sum_{ele=1}^{N_{ele}} \iint_{S_{ele}} \left( \sum_{i=1}^3 E_{1,im}^{ele} \mathbf{w}_i^{ele} \right) \left( \sum_{i=1}^3 E_{2,in}^{ele} \mathbf{w}_i^{ele} \right) dS \\
 &= D_{mn} \sum_{ele=1}^{N_{ele}} E_{1,m}^{ele} W_{\bullet}^{ele} E_{2,n}^{ele}
 \end{aligned}$$

$$D_{mn} = \sqrt{\frac{Z_{1,hm}}{Z_{2,hn}}} \cdot \frac{1}{\sqrt{\left( \iint_{S_{ele}} \mathbf{E}_{1thm} \cdot \mathbf{E}_{1thm} dS \right) \left( \iint_{S_{ele}} \mathbf{E}_{2thn} \cdot \mathbf{E}_{2thn} dS \right)}}$$

$$E^{ele} = \text{diag}\{E_1^{ele}, E_2^{ele}, E_3^{ele}\}$$

$$W_{\bullet}^{ele} = \begin{bmatrix} K_{\bullet,11}^{ele} & K_{\bullet,12}^{ele} & K_{\bullet,13}^{ele} \\ K_{\bullet,21}^{ele} & K_{\bullet,22}^{ele} & K_{\bullet,23}^{ele} \\ K_{\bullet,31}^{ele} & K_{\bullet,32}^{ele} & K_{\bullet,33}^{ele} \end{bmatrix}$$

(D-1)

For TM-TM coupling condition,

$$\begin{aligned}
 X_{mn} &= \iint_S \mathbf{e}_{1tem} \times \mathbf{h}_{2ten} \cdot \vec{z} dS = \frac{1}{Y_{1en}} \iint_S \mathbf{h}_{1tem} \cdot \mathbf{h}_{2ten} dS \\
 &= D_{mn} \sum_{ele=1}^{N_{ele}} \iint_{S_{ele}} \left( \sum_{i=1}^3 H_{1,im}^{ele} \mathbf{w}_i^{ele} \right) \left( \sum_{i=1}^3 H_{2,in}^{ele} \mathbf{w}_i^{ele} \right) dS \\
 &= D_{mn} \sum_{ele=1}^{N_{ele}} H_{1,m}^{ele} W_{\bullet}^{ele} H_{2,n}^{ele}
 \end{aligned}$$

$$D_{mn} = \sqrt{\frac{Y_{2,hm}}{Y_{1,hn}}} \cdot \frac{1}{\sqrt{\left( \iint_{S_{ele}} \mathbf{H}_{1tem} \cdot \mathbf{H}_{1tem} dS \right) \left( \iint_{S_{ele}} \mathbf{H}_{2ten} \cdot \mathbf{H}_{2ten} dS \right)}}$$



$$H^{ele} = \text{diag}\{H_1^{ele}, H_2^{ele}, H_3^{ele}\}$$

$$W_{\bullet}^{ele} = \begin{bmatrix} K_{\bullet,11}^{ele} & K_{\bullet,12}^{ele} & K_{\bullet,13}^{ele} \\ K_{\bullet,21}^{ele} & K_{\bullet,22}^{ele} & K_{\bullet,23}^{ele} \\ K_{\bullet,31}^{ele} & K_{\bullet,32}^{ele} & K_{\bullet,33}^{ele} \end{bmatrix}$$

(D-2)

For the TE-TM coupling condotion is,

$$\begin{aligned} X_{mn} &= \iint_S \mathbf{e}_{1thm} \times \mathbf{h}_{2ten} \cdot \vec{z} dS \\ &= D_{mn} \sum_{ele=1}^{N_{ele}} \iint_{S_{ele}} \left( \sum_{i=1}^3 E_{1,im}^{ele} \mathbf{w}_i^{ele} \right) \times \left( \sum_{i=1}^3 H_{2,in}^{ele} \mathbf{w}_i^{ele} \right) \cdot \vec{z} dS \\ &= D_{mn} \sum_{ele=1}^{N_{ele}} E_{1,m}^{ele} W_{\times}^{ele} H_{2,n}^{ele} \end{aligned}$$

$$D_{mn} = \frac{\sqrt{Z_{1,hm} Y_{2,en}}}{\sqrt{\left( \iint_{S_{ele}} \mathbf{E}_{1thm} \cdot \mathbf{E}_{1thm} dS \right) \left( \iint_{S_{ele}} \mathbf{H}_{2ten} \cdot \mathbf{H}_{2ten} dS \right)}}$$

$$E^{ele} = \text{diag}\{E_1^{ele}, E_2^{ele}, E_3^{ele}\}$$

$$H^{ele} = \text{diag}\{H_1^{ele}, H_2^{ele}, H_3^{ele}\}$$

$$W_{\times}^{ele} = \begin{bmatrix} K_{\nabla,11}^{ele} & K_{\nabla,12}^{ele} & K_{\nabla,13}^{ele} \\ K_{\nabla,21}^{ele} & K_{\nabla,22}^{ele} & K_{\nabla,23}^{ele} \\ K_{\nabla,31}^{ele} & K_{\nabla,32}^{ele} & K_{\nabla,33}^{ele} \end{bmatrix}$$

(D-3)

For TM-TE condition, there is no coupling,

$$X_{mn} = 0 \quad (D-4)$$

More details for FEM/MM hybrid calculation can be referred to [A-6][A-7].

# Appendix E

## Calibration mechanism

In this dissertation, ordinary conditions of beam-switching matrices connecting with transformers occurs, as depicted in Fig. E.1.

The measurement results  $S_{mea}$  can be expressed as

$$S_{mea} = \overrightarrow{TtoS}(T_{mea}) = \overrightarrow{TtoS}(T_{trans}T_{DUT}T_{trans}) \quad (E-1)$$

Where S means S-matrix, T means T-matrix and  $\overrightarrow{TtoS}$  represent transition form T-matrix to S-matrix, which can be demonstrated as,

$$S = \frac{1}{T_{11}} \begin{pmatrix} T_{21} & T_{11}T_{22} - T_{12}T_{21} \\ 1 & -T_{12} \end{pmatrix} \quad (E-2)$$

Similarly, the reverse operation  $\overrightarrow{StoT}$  to convert S-matrix to T-matrix is

$$T = \frac{1}{S_{21}} \begin{pmatrix} 1 & -S_{22} \\ S_{11} & S_{12}S_{21} - S_{11}S_{22} \end{pmatrix} \quad (E-3)$$

The measurement results will always include coaxial line-waveguide transition, which incorporate additional insertion loss, to properly exclude this influence and derive pure  $S_{DUT}$ ,

$$S_{DUT} = \overrightarrow{TtoS}(T_{trans}^{-1}\overrightarrow{StoT}(S_{mea})T_{trans}^{-1}) \quad (E-4)$$

To get S-parameters of transformer, TRL calibration method is usually utilized as shown in Fig.E.2, reflection at input port of network containing cascading of transformer and a termination load can be measured and expressed as

$$S_{11,CAL} = \frac{b_{1mea}}{a_{1mea}} = S_{11} + \frac{\Gamma S_{12}^2}{1-\Gamma S_{22}} \quad (E-5)$$

As a two-ports passive network, three unknown parameters  $S_{11}$ ,  $S_{12}$  and  $S_{22}$  are in

demand to solve, hence, three equations corresponding to three different termination loads need to be uploaded,

$$S_{11,CAL1} = S_{11} + \frac{\Gamma_1 S_{12}^2}{1 - \Gamma_1 S_{22}} \quad (\text{E-6a})$$

$$S_{11,CAL2} = S_{11} + \frac{\Gamma_2 S_{12}^2}{1 - \Gamma_2 S_{22}} \quad (\text{E-6b})$$

$$S_{11,CAL3} = S_{11} + \frac{\Gamma_3 S_{12}^2}{1 - \Gamma_3 S_{22}} \quad (\text{E-6c})$$

From (A-6), the S-parameters of transformer can be deduced,

$$S_{11} = \frac{\Gamma_1 S_{11,CAL3} - \Gamma_3 S_{11,CAL1} - \frac{\Gamma_3 (S_{11,CAL3} - S_{11,CAL1})}{\Gamma_2 (S_{11,CAL2} - S_{11,CAL1})} (\Gamma_1 S_{11,CAL2} - \Gamma_2 S_{11,CAL1})}{\Gamma_1 - \Gamma_3 - \frac{\Gamma_3 (S_{11,CAL3} - S_{11,CAL1})}{\Gamma_2 (S_{11,CAL2} - S_{11,CAL1})} (\Gamma_1 - \Gamma_2)} \quad (\text{E-7a})$$

$$S_{22} = \frac{\Gamma_2 (S_{11} - S_{11,CAL1}) - \Gamma_1 (S_{11} - S_{11,CAL2})}{\Gamma_1 \Gamma_2 (S_{11,CAL2} - S_{11,CAL1})} \quad (\text{E-7b})$$

$$S_{12} = S_{21} = \sqrt{\left(S_{22} - \frac{1}{\Gamma_1}\right) (S_{11} - S_{11,CAL1})} \quad (\text{E-7c})$$

Normal waveguide loads contain a PEC-short plate, and two plates with different length  $l_1$  and  $l_2$ , with their reflection coefficients as,

$$\Gamma_1 = -1 \quad (\text{E-8a})$$

$$\Gamma_2 = -e^{j\beta l_1} \quad (\text{E-8b})$$

$$\Gamma_3 = -e^{j\beta l_2} \quad (\text{E-8c})$$

Where  $\beta$  means waveguide wave number,

$$\beta = \sqrt{\left(\frac{2\pi}{\lambda}\right)^2 - \left(\frac{\pi}{a}\right)^2} \quad (\text{E-9})$$

Where  $a$  and  $\lambda$  signify broad wall of waveguide and free space wavelength.

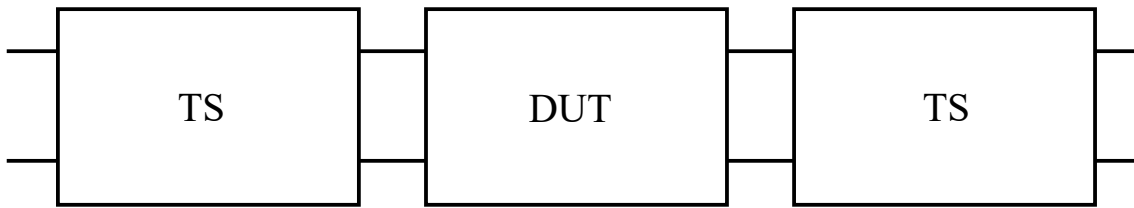


**Fig. E.1.** Measurement networks including DUT and transformers.

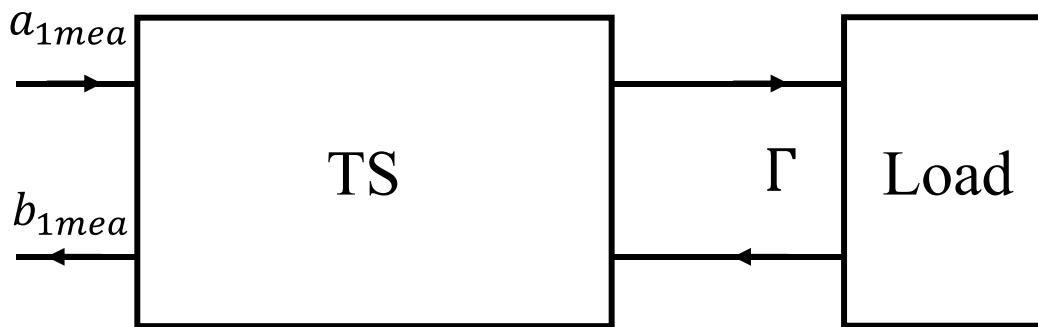


**Fig. E.2.** Calibration models for transformer.

## References

- [A-1] Balanis, C. A. (2012). *Advanced Engineering Electromagnetics* (2nd ed.). Wiley.
- [A-2] Collin, R. E. (1990). *Field Theory of Guided Waves* (2nd ed.). IEEE Press.
- [A-3] G. G. Gentili, "Properties of TE-TM mode-matching techniques," in *IEEE Transactions on Microwave Theory and Techniques*, vol. 39, no. 9, pp. 1669-1673, Sept. 1991.
- [A-4] M. Wakasa, D.-H. Kim, T. Tomura, and J. Hirokawa, "Wideband Design of a Short-Slot 2-Plane Coupler by the Mode Matching/FEM Hybrid Analysis considering the Structural Symmetry," *IEICE Trans. Commun.*, vol. E102-B, No.5, pp.1019-1026, May 2019.
- [A-5] Jin, J. M. (2014). *The Finite Element Method in Electromagnetics* (3rd ed.). Wiley.
- [A-6] R. Beyer and F. Arndt, "Efficient modal analysis of waveguide filters including the orthogonal mode coupling elements by an MM/FE method," in *IEEE Microwave and Guided Wave Letters*, vol. 5, no. 1, pp. 9-11, Jan. 1995.
- [A-7] D. Arena, M. Ludovico, G. Manara and A. Monorchio, "Analysis of waveguide discontinuities using edge elements in a hybrid mode matching/finite elements approach," in *IEEE Microwave and Wireless Components Letters*, vol. 11, no. 9, pp. 379-381, Sept. 2001.

# Acknowledgement

With heartfelt sincerity and profound appreciation, I express my deepest gratitude to the luminaries who have guided and supported me throughout my transformative journey of Ph.D. studies.

Foremost among them is the illustrious Prof. Jiro Hirokawa, a beacon of wisdom and mentorship. Under his esteemed supervision, I embarked on my Ph.D. studies as a cherished member of the revered Hirokawa lab. This profound experience has etched indelible imprints in the recesses of my mind, a treasure trove of knowledge and inspiration that will continuously shape my future endeavors in the most constructive and impactful ways.

I owe an immeasurable debt to the venerable Prof. Takashi Tomura. His technical guidance and support significantly dispel obstacles and difficulties that occasionally veiled my research, sustained me throughout the triumphant three years of my study.

I extend my thanks to the esteemed Dr. Nelson Fonseca from the European Space Agency. His invaluable technical advice and support infused my projects with a heightened sense of purpose and precision. Additionally, I wish to convey my heartfelt appreciation to Prof. Jiwei Lian, whose abundant auxiliary advice propelled my research to move forward.

To my cherished lab members, a kaleidoscope of benevolence, I owe a debt of thanks for their kindness and constant assistance. Together, we painted countless moments of splendid joyfulness that enriched my life immeasurably during my sojourn in the enchanting land of Japan.

Yet, I must not forget the cornerstone of my existence, my beloved parents Zhian Li and Xuemin Zhuang. Their selfless love and dedication have been the very bedrock upon which I built my dreams and aspirations. Their unwavering belief in my potential has been a source of boundless strength and inspiration.

Lastly, I reserve the greatest thanks for myself, acknowledging the tenacity and resilience that have defined my journey. In the presence of numerous challenges and difficulties, I found the strength and determination not to renunciate but to persevere. Through every trial and tribulation, I emerge stronger and more resolute than I was.

In this intricate weaving of thankfulness and boundless gratitude, I stand humbled and inspired, knowing that without the support, wisdom, and love of these exceptional individuals, my Ph.D. voyage would not have been as enriching and triumphant. With a heart brimming with appreciation, I embrace the future with newfound zeal and an

enduring commitment to making a difference in this vast tapestry of knowledge we call life.



# List of Publications

## Journal paper

[1] Qi Li, Jiro Hirokawa, Takashi Tomura, "Two-plane Waveguide Coupler with Arbitrary Coupling Ratio in the H-plane and E-plane Directions", DOI: 10.1049/mia2.12398, IET Microwaves, Antennas & Propagation.

[2] Qi Li, Jiro Hirokawa, Takashi Tomura, and Nelson J. G. Fonseca, "Two-dimensional One-body  $3 \times 3$ -way Hollow-waveguide Nolen Matrix using a Two-plane Unequal Division Coupler", DOI: 10.1109/TMTT.2023.3291759, IEEE Transactions on Microwave Theory and Techniques.

[3] Qi Li, Jiro Hirokawa, Takashi Tomura, Yuta Takahashi, Naoki Kita and Nelson J. G. Fonseca, "A Two-dimensional  $6 \times 4$ -way Hollow Waveguide Beam-switching Matrix", DOI: 10.1109/ACCESS.2023.3296477, IEEE ACCESS.

## International Conferences

[1] Qi Li, Jiro Hirokawa, Takashi Tomura, and Nelson J. G. Fonseca, "Design of a Waveguide Two-plane Hybrid Coupler with Nonuniform Division," IEEE AP-S URSI Intl. Symp., TH-UB.1P.6, Dec. 2021.

[2] Qi Li, Jiro Hirokawa, Takashi Tomura, and Nelson J. G. Fonseca, "A  $3 \times 3$ -way Hollow Waveguide Nolen Matrix Using a 2-plane Unbalanced Coupler," IEEE AP-S URSI Intl. Symp., WE-UB.2A.9, Jul. 2022.

[3] Qi Li, Jiro Hirokawa, and Takashi Tomura, "Design Method of a Hollow-waveguide Two-plane Coupler with Unequal Division Ratio along with Horizontal and Vertical Direction," URSI-JRSM, BP-3, Sep. 2022.

[4] Qi Li, Jiro Hirokawa, and Takashi Tomura, "Design of a Waveguide Two-Plane Coupler With a Different Division Ratio in Horizontal and Vertical Directions," Intl. Symp. Antennas Propag., CS11-5, Oct. 2022.

## **Domestic Conferences**

- [1] Qi Li, Jiro Hirokawa, Takashi Tomura, and Nelson J. G. Fonseca, "Design of a 2-plane Coupler with Unequal Division," IEICE General Conf., B-1-64, 2021-3.
- [2] Qi Li, Jiro Hirokawa, Takashi Tomura, and Nelson J. G. Fonseca, "A  $3 \times 3$ -way Hollow-waveguide Nolen Matrix Using a 2-plane Coupler with Unequal Power Division," IEICE General Conf., B-1-95, 2022-3.
- [3] Qi Li, Jiro Hirokawa, and Takashi Tomura, "Design of a Hollow-waveguide Two-plane Coupler with Unequal Division Ratio along with Horizontal and Vertical Directions," IEICE Commun. Conf., B-1-74, 2022-9.